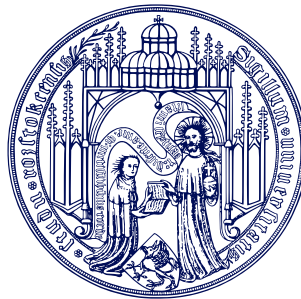# Perturbative Methods for the Computation of Resonant Cavity Eigenmodes Subject to Geometric Variations

Korinna Brackebusch
geboren am 05.12.1984 in Rostock

Dissertation
zur Erlangung des akademischen Grades
Doktor-Ingenieur (Dr.-Ing.)
der Fakultät für Informatik und Elektrotechnik
der Universität Rostock

Rostock, 5. September 2016

Gutachter:

Frau Prof. Dr. rer. nat. habil. Ursula van Rienen
(Universität Rostock)

Herr Prof. Dr.-Ing. Herbert De Gersem
(Technische Universität Darmstadt)

Herr Prof. Dr. Thomas Weis
(Technische Universität Dortmund)

Datum der Verteidigung:

11.November 2016

Abstract

Designing multicell accelerating cavities with best possible electromagnetic characteristics is a challenging task in computational electrical engineering. The deliberate modification of various shape parameters regarding different, partially contradicting optimization goals easily requires the modal analysis of an immense number of often only slightly different cavity geometries. The optimization is typically performed by an iterative variation of the structure's shape entailing a full eigenmode recomputation with a direct numerical solver for each modification. At this, the structure usually involves a problem with hundreds of thousands or more degrees of freedom. The resulting computational effort is enormous, forcing a tradeoff between design requirements and computational time. In most cases, this limits the observed frequency range, the number of optimization passes, or both. For the same reason, the effects of geometric imperfections are usually excluded from the optimization process, even though they may be of particular importance for the final design. The aim of this thesis is to introduce and validate two perturbative approaches that enable geometric parameter studies based on the eigenmodes of only one initial geometry, denoted as the *unperturbed* geometry. The two novel methods are called the *generalization of Slater's theorem* (GST) and the *expansion of a reduced eigenmode set* (ERES). Both techniques base on the concept to expand the eigenmodes of a modified and thus *perturbed* geometry in terms of the eigenmodes of the unperturbed geometry by analyzing the energy-related mutual interactions of the unperturbed eigenmodes inside the volume that is removed by the geometric modification. So, the methods require a direct numerical eigenmode computation only once for the unperturbed geometry. In contrast to conventional perturbative approaches, like Slater's theorem, which only provide the frequency shift that arises from a deformation, the here presented approaches also allow for the determination of the electromagnetic fields of the perturbed eigenmodes and thereby of all electromagnetic properties. This thesis describes the theory of both perturbative methods and discusses several validation and application examples. The results show that particularly the generalization of Slater's theorem accurately computes the eigenmodes of single-cell and multicell structures over a wide frequency range for both small and large geometric perturbations. Concluding, the perturbative methods allow for an efficient investigation of the electromagnetic characteristics of a vast number of different cavity structures exceeding the limitations of conventional straightforward methods.

Zusammenfassung

Der Entwurf mehrzelliger Hohlraumresonatoren mit bestmöglichen elektromagnetischen Parametern ist eine anspruchsvolle Aufgabe der rechnergestützten Elektrotechnik. Die gezielte Veränderung verschiedener Geometrie-Parameter hinsichtlich unterschiedlicher, sich teilweise widersprechender Optimierungsziele erfordert die Modalanalyse einer enormen Anzahl, sich häufig nur wenig unterscheidender Geometrien. Typischerweise wird die Optimierung mittels einer iterative Modifizierung der Strukturform durchgeführt, wobei jede Änderung eine vollständige Neuberechnung der Eigenmoden mithilfe eines direkten numerischen Lösers nach sich zieht. Dabei besitzt die Struktur üblicherweise Hunderttausende oder mehr Freiheitsgrade. Der resultierende Berechnungsaufwand ist enorm und erzwingt einen Kompromiss zwischen den Design-Anforderungen und der Rechenzeit. In den meisten Fällen beschränkt dies den untersuchten Frequenzbereich, die Anzahl der Optimierungsdurchläufe oder beides. Aus dem gleichen Grund wird üblicherweise auf eine Untersuchung der Effekte geometrischer Unsicherheiten verzichtet, obwohl diese von erheblicher Bedeutung für das endgültige Design sein können. Das Ziel der vorliegenden Arbeit ist die Einführung und Validierung zweier störungstheoretischer Ansätze, welche es erlauben, geometrische Parameterstudien basierend auf den Eigenmoden von nur einer Ausgangsgeometrie, welche als *ungestörte* Geometrie bezeichnet wird, durchzuführen. Die beiden neuartigen Methoden tragen die englischen Namen *Generalization of Slater's Theorem* (GST) sowie *Expansion of a Reduced Eigenmode Set* (ERES). Beide Verfahren beruhen auf der Idee die Eigenmoden einer veränderten und somit *gestörten* Geometrie als Funktionsreihe aus den ungestörten Eigenmoden zu entwickeln, basierend auf den energetischen Wechselwirkungen der ungestörten Moden innerhalb des Volumens, das durch die geometrische Modifikation entfernt wird. Die Methoden erfordern somit nur einmalig für die ungestörte Geometrie eine direkte numerische Berechnungen der Eigenmoden. Im Gegensatz zu konventionellen störungstheoretischen Ansätzen, wie Slaters Theorem, die lediglich den Frequenzversatz bestimmen können, der infolge einer Deformation entsteht, ermöglichen die hier vorgestellten Verfahren auch eine Berechnung der elektromagnetischen Felder der gestörten Eigenmoden und somit aller elektromagnetischer Eigenschaften. Die vorliegende Arbeit beschreibt die theoretischen Grundlagen beider Methoden und diskutiert verschiedene Validierungs- und Anwendungsbeispiele. Die Ergebnisse zeigen, dass insbesondere die Methode namens Generalization of Slater's Theorem die Eigenmoden ein- und mehrzelliger Strukturen, sowie für kleine und große geometrische Störungen, präzise über einen breiten Frequenzbereich berechnen kann. Abschließend kann festgestellt werden, dass störungstheoretische Methoden eine effiziente Untersuchung der elektromagnetischen Charakteristika einer Vielzahl unterschiedlicher Hohlraumresonatoren ermöglichen und somit die Beschränkungen konventioneller direkter Verfahren überwinden.

Für Großmutti und Großvati

Danksagung

Die vorliegende Arbeit wäre nicht ohne die Untersützung einiger wichtiger Menschen entstanden. Hiermit möchte ich mich bedanken bei:

- Prof. Dr. Ursula van Rienen für die gute Zusammenarbeit und das in mich gesetzte Vertrauen sowie die Möglichkeit diese Arbeit zu verwirklichen,

- Prof. Dr. Herbert De Gersem und Prof. Dr. Thomas Weis für die Übernahme der externen Gutachten,

- meinen (Ex)Kollegen aus der Arbeitsgruppe Theoretische Elektrotechnik, insbesondere Dr. Christian Bahls, Andrea Böhme, Dr. Thomas Flisgen, Dr. Tomasz Galek, Petra Gefken, Dr. Anne Grünbaum, Dr. Dirk Hecht, Johann Heller, Mirjana Holst, Dr. Aleksandar Markovic, Dr. Carsten Potratz, Dr. Gisela Pöplau, Franziska Reimann, Dr. Christian Schmidt, Dawei Zheng und Ulf Zimmermann für viele fachliche und auch weniger fachliche Diskussionen,

- meinen Kollegen vom Helmholtz-Zentrum Berlin und der Technischen Universität Dortmund, insbesondere Benjamin Isbarn, Prof. Dr. Jens Knobloch, Dr. Axel Neumann, Bernard Riemann, Malte Sommer und Prof. Dr. Thomas Weis,

- Maja Gudat, Dr. Bernhard Himmel und Kathrin Krebs für organisatorische und technische Hilfestellung,

- Philipp und Silvia für den besten italienischen Kaffee aller Zeiten und einen guten Start in den Tag,

- meinen Freunden aus Rostock und dem Rest der Welt für viele schöne Erlebnisse; den Kletterern unter ihnen zusätzlich für das Sichern meines Überlebens bis zur Fertigstellung dieser Arbeit,

- meiner Familie für die uneingeschränkte Unterstützung; meinen Eltern dabei besonders für die Förderung (stoische Erduldung) meines Forscherdrangs, der sich bereits in jungen Jahren durch zu Testzwecken geopferte Einrichtungsgegenstände, zerrissene Kleidung und unterwegs verloren gegangene Gummistiefel manifestierte.

Thesis Statements

of the dissertation

Perturbative Methods for the Computation of Resonant Cavity Eigenmodes Subject to Geometric Variations

by Korinna Brackebusch

1. The optimization and robustness analysis of radio frequency cavities demand a rigorous investigation of their electromagnetic characteristics subject to geometric variations, typically involving extensive parameter studies.

2. A conventional straightforward analysis of the electromagnetic properties based on repetitive eigenmode computations requires an enormous computational effort. This usually limits the observed frequency range, the number of optimization passes, or both.

3. Alternatively to the direct repetitive eigenmode computations, perturbative methods allow to deduce the eigenmodes of a vast number of different cavity shapes from the eigenmodes of only one initial geometry. The eigenmodes of a modified (perturbed) geometry are expanded in terms of the eigenmodes of the initial (unperturbed) geometry, based on the energy-related mutual interactions of the unperturbed eigenmodes inside the deformed volume. Solely the eigenmodes of the unperturbed geometry need to be computed with a direct numerical solver. Thereby, the computational effort for parameter studies can be significantly reduced.

4. The number of computable perturbed modes is necessarily smaller than the number of used unperturbed modes since the unperturbed geometry can exclusively be deformed inwardly. The larger the extent of the perturbation, the less modes can be expanded.

5. The first perturbative method, called *generalization of Slater's theorem* (GST), features a sort of compensatory mechanism to fulfill the requirement of a reduced number of computable perturbed modes since the number of computed perturbed modes is identical to the number of unperturbed modes. The discrepancy is compensated by a corresponding number of irregular, partially complex-valued mode pairs, each constituting just one actual mode.

6. The regular GST modes accurately reproduce the frequencies and electromagnetic fields of the perturbed eigenmodes of single-cell and multicell structures over a wide frequency range. The irregular mode pairs possess a diminished accuracy which may noticeable interfere the fields of affected modes. However, only in case of comparatively large perturbations a relevant impairment occurs. For realistic geometric variations, the irregular modes arise only for extremely high frequencies, constituting solely a minor or negligible drawback.

7. The second method, called *expansion of a reduced eigenmode set* (ERES), inherently provides the correct number of computed perturbed modes. The method thereby a priori evades the generation of irregular deficient modes. The ERES-based eigenmodes converge step-like and noticeably slower than the GST eigenmodes. Hence, ERES requires a distinctly higher number of expansion modes to obtain the same accuracy as GST.

8. One of the main restrictions for applying perturbative methods to real-life radio frequency structures is the limited number of computable unperturbed modes. Thus, GST is the preferable method since it provides a more reliable and higher accuracy than ERES.

9. Especially for multicell cavities, the efficiency of the methods can further be improved by a suitable choice and segmentation of the unperturbed geometry, allowing for a simultaneously performance optimization and robustness analysis regarding geometric imperfections.

10. The number of unperturbed modes required for a sufficient accuracy of the perturbative methods is primarily determined by the relative perturbation extent and the frequency of the highest mode to be computed. The larger the modification, the faster converges the expansion.

11. In case of multicell cavities subject to very small perturbations even GST requires an extremely high number of unperturbed modes to accurately expand the electromagnetic fields. An adjustment of the interaction terms of the unperturbed modes enhances the converge of GST and thereby considerably reduces the number of necessary modes. The adjustment is performed segment-wise based on the ratio of the deformed to the unperturbed volume.

Contents

List of Figures

List of Tables

List of Acronyms

AKS	advanced Krylov subspace
BEM	boundary element methods
BBU	beam breakup
bERLinPro	Berlin Energy Recovery Linac Project
CEM	computational electromagnetics
CST MWS	CST Microwave Studio®
DOF	degree of freedom
EM	electromagnetic
ERES	expansion of a reduced eigenmode set
FEM	finite element method
FIT	finite integration technique
GST	generalization of Slater's theorem
HEM	hybrid electric and magnetic
HOM	higher order mode
IA	interaction
JD	Jacobi-Davidson
linac	linear accelerator
LFD	Lorentz force detuning
LOM	lower order mode
MRE	mean relative error
NC	normal conducting
ODE	ordinary differential equation
PBA	perfect boundary approximation
PDE	partial differential equation
PEC	perfect electric conducting
PM	perturbative method
PMC	perfect magnetic conducting
RF	radio frequency
SC	superconducting
ST	Slater's theorem
TE	transverse electric
TEM	transverse electromagnetic
TM	transverse magnetic

List of Symbols

Symbol	Unit	Description
a_{kj}	Hz^2	electric coupling term of the k-th and j-th unperturbed mode (GST)
$\mathbf{A}$	Hz^2	electric coupling matrix of the unperturbed eigenmodes (GST)
$A_{\ell,\nu}$	1	relative field amplitude of the ℓ-th passband mode in ν-th cell of a multicell resonator
b_{kj}	Hz^2	magnetic coupling term of the k-th and j-th unperturbed mode (GST)
$\mathbf{B}$	Hz^2	magnetic coupling matrix of the unperturbed eigenmodes (GST)
$\mathbf{B}(\mathbf{r},t)$	Vs/m^2	magnetic flux density
c_0	m/s	speed of light in vacuum
c_ν	1	coefficient of the basis function in the ν-th element (FEM)
C_i	A s/V	capacitance of i-th eigenmode (equivalent circuit)
C_{cp_i}	A s/V	coupling capacitance of i-th eigenmode (equivalent circuit)
$\mathbf{D}(\mathbf{r},t)$	As/m^2	electric flux density
$\mathbf{D}_\omega$	Hz	diagonal matrix of unperturbed angular eigenfrequencies
$\mathbf{D}_{\widetilde{\omega}}$	Hz	diagonal matrix of perturbed angular eigenfrequencies
$\mathbf{D}_{\psi_e}$	1	eigenvalue matrix of the matrix $\mathbf{G}_e$ (ERES)
$\widehat{\mathbf{D}}_{\psi_e}$	1	truncated eigenvalue matrix of the matrix $\mathbf{G}_e$ (ERES)
e	1	Euler's constant
$e^{\mathrm{t}}(t)$	1	time functions of the steady-state electric field
$e_i^{\mathrm{t}}(t)$	1	time functions of the electric field of the i-th unperturbed eigenmode
$\widetilde{e}_i^{\mathrm{t}}(t)$	1	time functions of the electric field of the i-th perturbed eigenmode
$e_k(t)$	1	time expansion function of the electric field in terms of the k-th mode
$e_{ik}(t)$	1	time expansion function for the electric field of the i-th perturbed eigenmode in terms of the k-th unperturbed eigenmode
$\widetilde{e}_k(t)$	1	time expansion function of the perturbed electric field in terms of the k-th perturbed eigenmode
$\mathbf{E}(\mathbf{r},t)$	V/m	electric field
$\mathbf{E}_i(\mathbf{r})$	V/m	stationary electric field of the i-th (unperturbed) eigenmode
$\mathbf{E}_{i,T}(\mathbf{r})$	V/m	transverse stationary electric field of the i-th (unperturbed) mode
$\mathbf{E}_{i,z}(\mathbf{r})$	V/m	longitudinal stationary electric field of the i-th (unperturbed) mode
$\mathbf{E}_{\mathrm{GST}}(\mathbf{r})$	V/m	GST-based perturbed stationary electric field
$\mathbf{E}_{\mathrm{Ref}}(\mathbf{r})$	V/m	stationary (perturbed) electric reference field
$\mathbf{E}_{z,\mathrm{GST}}(\mathbf{r})$	V/m	GST-based perturbed longitudinal stationary electric field
$\mathbf{E}_{z,\mathrm{Ref}}(\mathbf{r})$	V/m	(perturbed) longitudinal stationary electric reference field
E_{acc}	V/m	average accelerating electric field
E_{max}	V/m	maximal magnitude of the electric field
$E_{\mathrm{peak,sf}}$	V/m	peak surface electric field
$E_{\mathrm{peak,ax}_\nu}$	V/m	peak axial electric fields in the ν-th cell of a multicell resonator
$\widetilde{\mathbf{E}}_i(\mathbf{r})$	V/m	stationary electric field of the i-th perturbed eigenmode
$\mathbf{F}_{\mathrm{L}}(\mathbf{r},t)$	N	Lorentz force
f	Hz	temporal (unperturbed) frequency

f_{CST}	Hz	frequency computed with CST MWS
f_{ERES}	Hz	ERES-based perturbed frequency
f_{GST}	Hz	GST-based perturbed frequency
$f_{\max}$	Hz	frequency of the highest unperturbed eigenmode
f_{Ref}	Hz	(perturbed) reference frequency
$f_{i_{\mathrm{GSTirr}}}$	Hz	frequency of the first mode of the i-th irregular GST mode pair
$f_{i_{\mathrm{GSTirr}}+1}$	Hz	frequency of the second mode of the i-th irregular GST mode pair
$\overline{f}_{i_{\mathrm{GSTirr}}}$	Hz	mean frequency of the i-th irregular GST mode pair
$\overline{f}_{i_{\mathrm{GST}}}$	Hz	mean GST-based frequency of the i-th perturbed eigenmodes depending on the number of modes
$\overline{f}_{i_{\mathrm{ERES}}}$	Hz	mean ERES-based frequency of the i-th perturbed eigenmodes depending on the number of modes
$\widetilde{f}_i$	Hz	frequency of the i-th perturbed eigenmode
$f(\mathbf{r})$	var.	sought function (FEM)
$g_{e_{kj}}$	1	electric interaction term of the k-th and j-th unperturbed mode (GST)
$g_{h_{kj}}$	1	magnetic interaction term of the k-th and j-th unperturbed mode (GST)
$\mathbf{G}_e$	1	electric interaction matrix of the unperturbed eigenmodes (GST)
$\mathbf{G}_h$	1	magnetic interaction matrix of the unperturbed eigenmodes (GST)
G_i	Ω	geometry constant of the i-th eigenmode
$h^{\mathrm{t}}(t)$	1	time functions of the steady-state magnetic field
$h_i^{\mathrm{t}}(t)$	1	time functions of the magnetic field of the i-th unperturbed eigenmode
$\widetilde{h}_i^{\mathrm{t}}(t)$	1	time functions of the magnetic field of the i-th perturbed eigenmode
$h_k(t)$	1	time expansion function of the magnetic field in terms of the k-th eigenmode
$h_{ik}(t)$	1	time expansion function for the magnetic field of the i-th perturbed eigenmode in terms of the k-th unperturbed eigenmode
$\widetilde{h}_k(t)$	1	time expansion function of the perturbed magnetic field in terms of the k-th perturbed eigenmode
$\mathbf{H}(\mathbf{r},t)$	A/m	magnetic field
$\mathbf{H}_i(\mathbf{r})$	V/m	stationary magnetic field of the i-th (unperturbed) eigenmode
$\mathbf{H}_{\mathrm{GST}}(\mathbf{r})$	V/m	GST-based stationary (perturbed) magnetic field
$\mathbf{H}_{\mathrm{Ref}}(\mathbf{r})$	V/m	(perturbed) stationary magnetic reference field
$H_{\max}$	V/m	maximal magnitude of the magnetic field
$H_{\mathrm{peak,sf}}$	A/m	peak surface magnetic field
$H_{\mathrm{crit,rf}}$	A/m	RF critical magnetic field
$\widetilde{\mathbf{H}}_i(\mathbf{r})$	V/m	stationary magnetic field of the i-th perturbed eigenmode
i	1	index
i_{defi}	1	index of the first deficient perturbed eigenmode
$i_{\max}$	1	index of the unperturbed mode with highest frequency
i_{mode}	1	mode index
$\mathbf{I}$	1	identity matrix
$\mathbf{J}(\mathbf{r},t)$	A/m^2	electric current density
$\mathbf{J}_{\mathrm{cc}}(\mathbf{r},t)$	A/m^2	convection current density

$\mathbf{J}_{\text{ic}}(\mathbf{r}, t)$	A/m^2	impressed current density
$\mathbf{J}_{\sigma}(\mathbf{r}, t)$	A/m^2	conduction current density
$\mathbf{J}_{\text{S}}(\mathbf{r}, t)$	A/m	surface current density
j	1	index
$\jmath$	1	complex unit
k	1/m	angular wave number
k_T	1/m	transverse wave number
k_x	1/m	wave number in x-direction
k_y	1/m	wave number in y-direction
k_z	1/m	longitudinal wave number
k_{φ}	1/m	azimuthal wave number
k_{ρ}	1/m	radial wave number
k_i	1/m	angular wave number of the i-th (unperturbed) eigenmode
k_{cp_i}	1	cell-to-cell coupling constant of the i-th eigenmode
k	1	index
l	1	index
L	m	length
L_{cell}	m	cell length
L_i	V s/A	inductance of i-th eigenmode (equivalent circuit)
$\widetilde{L}$	m	perturbed length
m	1	azimuthal mode index
$\check{\mathbf{M}}$	var.	mass matrix
n	1	radial mode index
$\mathbf{n}$	1	outward-oriented unit surface normal vector
$\mathbf{n}_z$	1	unit vector in z-direction
N_{b}	1	number of basis functions (FEM)
N_{cell}	1	number of cells in a multicell resonator
N_{dof}	1	number of degrees of freedom
$N_{\text{ia}_{\nu}}$	1	number of modes in the ν-th set of interacting eigenmodes
N_{k_i}	1	algebraic multiplicity of the eigenvalue k_i
N_{modes}	1	number of unperturbed eigenmodes
$\widetilde{N}_{\text{modes}}$	1	number of computable perturbed eigenmodes
$\widehat{N}_{\text{modes}}$	1	number of computed perturbed eigenmodes (ERES)
N_{elem}	1	number of volume elements (discretization of ΔV)
N_{mc}	1	number of mesh cells
N_{segm}	1	number of segments (geometry partitioning)
$N_{\text{step}\lambda}$	1	number of steps per wavelength
o	1	polynomial order of basis function (FEM)
p	1	longitudinal mode index
P_{wall_i}	W	wall power losses of the i-th eigenmode
P'_{wall_i}	W/m	wall power losses of the i-th eigenmode per unit length
P_{ext_i}	W	external power losses of the i-th eigenmode
P_{tot_i}	W	total power losses of the i-th eigenmode

q	A s	electric charge
q_Ω	A s	total electric charge in the domain Ω
q_{kj}	W	PMC interaction term of the k-th and j-th unperturbed mode (GST)
$q_{e_{kj}}$	J	electric energy part of the PMC interaction term of the k-th and j-th unperturbed eigenmode (GST)
$q_{e_{kj[\nu]}}$	J	electric energy part of the PMC interaction term of the k-th and j-th unperturbed eigenmode inside the ν-th volume segment (GST)
$q_{h_{kj}}$	J	magnetic energy part of the PMC interaction term of the k-th and j-th unperturbed eigenmode (GST)
$q_{h_{kj[\nu]}}$	J	magnetic energy part of the PMC interaction term of the k-th and j-th unperturbed eigenmode inside the ν-th volume segment (GST)
$\mathbf{Q}$	W	PMC interaction term matrix (GST)
Q_{0_i}	1	unloaded quality factor of the i-th eigenmode
Q_{ext_i}	1	external quality factor of the i-th eigenmode
Q_{L_i}	1	loaded quality factor of the i-th eigenmode
r	var.	residual (FEM)
$\mathbf{r}$	m	position vector
$\mathbf{r}_\nu$	m	center of the ν-th volume element
r_{sh_i}	Ω/m	effective shunt impedance per unit length of the i-th eigenmode
R_{sh_i}	Ω	shunt impedance of the i-th eigenmode
$R_{\parallel_i}$	Ω	longitudinal shunt impedance of the i-th eigenmode
$R_{\perp_i}$	Ω	transverse shunt impedance of the i-th eigenmode
R_{S}	Ω	surface resistance of a cavity
R_{sh_i}/Q_{0_i}	Ω	R-over-Q of the i-th eigenmode
$R_{\parallel_i}/Q_{0_i}$	Ω	longitudinal R-over-Q of the i-th eigenmode
$R_{\perp_i}/Q_{0_i}$	Ω	transverse R-over-Q of the i-th eigenmode
R	m	radius
R_{eq}	m	equator radius
R_{iris}	m	iris radius
$\widetilde{R}$	m	perturbed radius
s_{kj}	W	PEC interaction term of the k-th and j-th unperturbed mode (GST)
$s_{e_{kj}}$	J	electric energy part of the PEC interaction term of the k-th and j-th unperturbed eigenmode (GST)
$s_{e_{kj[\nu]}}$	J	electric energy part of the PEC interaction term of the k-th and j-th unperturbed eigenmode inside the ν-th volume segment (GST)
$s_{h_{kj}}$	J	magnetic energy part of the PEC interaction term of the k-th and j-th unperturbed eigenmode (GST)
$s_{h_{kj[\nu]}}$	J	magnetic energy part of the PEC interaction term of the k-th and j-th unperturbed eigenmode inside the ν-th volume segment (GST)
$\mathbf{S}$	W	PEC interaction term matrix (GST)
$\mathbf{S}_e$	J	electric energy part of the PEC interaction term matrix
$\mathbf{S}_h$	J	magnetic energy part of the PEC interaction term matrix
$\check{\mathbf{S}}$	var.	stiffness matrix
$\mathbf{S}(\mathbf{r}, t)$	W/m^2	Poynting vector
S	m^2	(unperturbed) surface

S_{pec}	m^2	(unperturbed) PEC surface
S_{pmc}	m^2	(unperturbed) PMC surface
$\widetilde{S}$	m^2	perturbed surface
$\widetilde{S}_{\text{pec}}$	m^2	perturbed PEC surface
$\widetilde{S}_{\text{pmc}}$	m^2	perturbed PMC surface
t	s	time
$u_{\text{e}}(\mathbf{r}, t)$	J/m^3	electric energy density
$u_{\text{m}}(\mathbf{r}, t)$	J/m^3	magnetic energy density
U_i	J	total electromagnetic energy of the i-th (unperturbed) eigenmode
$\widetilde{U}_i$	J	total electromagnetic energy of the i-th perturbed eigenmode
$\mathbf{v}(\mathbf{r}, t)$	m/s	velocity
$\mathbf{v}_{e_k}, \widehat{\mathbf{v}}_{e_k}$	1	k-th eigenvector of the matrix $\mathbf{G}_e$ (ERES)
$\mathbf{V}_e$	1	eigenvector matrix of the matrix $\mathbf{G}_e$ (ERES)
$\widehat{\mathbf{V}}_e$	1	truncated eigenvector matrix of the matrix $\mathbf{G}_e$ (ERES)
$\widehat{\mathbf{V}}_h$	1	truncated eigenvector matrix of the matrix $\mathbf{G}_h$ (ERES)
V_{acc}	V	accelerating voltage of the accelerating mode
$V_{\|_i}$	V	longitudinal accelerating voltage of the i-th eigenmode
$V_{\perp_i}$	V	transverse accelerating voltage of the i-th eigenmode
V	m^3	(unperturbed) volume
V_ν	m^3	volume of the ν-th segment (geometry partitioning)
V_{elem_ν}	m^3	volume of the ν-th volume element
$V_{\text{elem}_{\text{min}}}$	m^3	limit for minimal volume size of a volume element
$\widetilde{V}$	m^3	perturbed volume
$w_\nu(\mathbf{r})$	var.	test function of the ν-th element (FEM)
$\mathbf{W}_e$	1	orthogonal extension matrix for the electric field (ERES)
$\mathbf{W}_h$	1	orthogonal extension matrix for the magnetic field (ERES)
x	m	x-coordinate in Cartesian coordinate system
$x_{\text{Ell,eq}}$	m	longitudinal equator ellipse parameter
$x_{\text{Ell,iris}}$	m	longitudinal iris ellipse parameter
y	m	y-coordinate in Cartesian coordinate system
$y_{\text{Ell,eq}}$	m	radial equator ellipse parameter
$y_{\text{Ell,iris}}$	m	radial iris ellipse parameter
z	m	z-coordinate in Cartesian coordinate system, longitudinal coordinate in circular-cylindrical coordinate system
Z_{S}	Ω	surface impedance
$\mathbf{Z}_e$	1	final ancillary matrix for the electric field (ERES)
$\mathbf{Z}_h$	1	final ancillary matrix for the magnetic field (ERES)
α	1/m	attenuation constant
α_{ik}	1	expansion coefficient for the electric field of the i-th perturbed eigenmode in terms of the k-th unperturbed eigenmode
$\boldsymbol{\alpha}_i$	1	vector of expansion coefficients for the electric field of the i-th perturbed eigenmode
$\alpha_{i_{\text{dom}}}$	1	electric expansion coefficient of the dominant expansion mode of the i-th perturbed eigenmode

$\overline{\boldsymbol{\alpha}}_{i_{\mathrm{GSTirr}}}$	1	mean electric expansion coefficient of the i-th irregular GST mode pair
$\boldsymbol{\mathcal{A}}$	1	electric expansion matrix
β	1/m	phase constant
β_{ik}	1	expansion coefficient for the magnetic field of the i-th perturbed eigenmode in terms of the k-th unperturbed eigenmode
$\boldsymbol{\beta}_i$	1	vector of expansion coefficients for the magnetic field of the i-th perturbed eigenmode
$\beta_{i_{\mathrm{dom}}}$	1	magnetic expansion coefficient of the dominant expansion mode of the i-th perturbed eigenmode
$\overline{\boldsymbol{\beta}}_{i_{\mathrm{GSTirr}}}$	1	mean magnetic expansion coefficient of the i-th irregular GST mode pair
$\boldsymbol{\mathcal{B}}$	1	magnetic expansion matrix
γ	1/m	propagation constant
δ_{ik}	1	Kronecker delta
$\Delta\rho$	m	polar radial step size
Δz	m	longitudinal step size
$\Delta\varphi$	rad	azimuthal step size
Δf	Hz	frequency shift between perturbed and unperturbed frequency
Δf_{GST}	Hz	GST-based frequency shift between perturbed and unperturbed frequency
Δf_{Ref}	Hz	reference frequency shift between perturbed and unperturbed frequency
ΔL	m	extent of length perturbation
$\Delta\widehat{N}_{\mathrm{modes}}$	1	difference between number of unperturbed and perturbed modes (ERES)
ΔR	m	extent of radius perturbation
ΔS	m^2	original unperturbed surface part corresponding to the deformed surface part
ΔS_{pec}	m^2	original unperturbed PEC surface part
ΔS_{pmc}	m^2	original unperturbed PMC surface part
$\Delta\widetilde{S}$	m^2	deformed part of the perturbed surface
$\Delta\widetilde{S}_{\mathrm{pec}}$	m^2	deformed part of the perturbed PEC surface
$\Delta\widetilde{S}_{\mathrm{pmc}}$	m^2	deformed part of the perturbed PMC surface
ΔV	m^3	volume removed by the perturbation
ΔV_{pec}	m^3	removed volume with PEC boundaries
ΔV_{pmc}	m^3	removed volume with PMC boundaries
ΔV_ν	m^3	removed volume in the ν-th segment
$\Delta\xi/\xi$	1	relative perturbation extent
ε	F/m	permittivity
ε_0	F/m	vacuum permittivity
ε_r	1	relative permittivity
ϵ_{EV}	1	eigenvalue truncation accuracy (ERES)
η_{ff}	%	field flatness
$\kappa_{\mathbf{A}}$	var.	condition number of the matrix $\mathbf{A}$

$\varkappa$	1	GST adjustment constant
$\varkappa_\nu$	1	GST adjustment constant of the ν-th volume segment
λ	m	wavelength
λ_i	m	wavelength of the i-th (unperturbed) eigenmode
λ_{min}	m	minimal wavelength of the highest unperturbed eigenmode
$\widetilde{\lambda}_i$	m	wavelength of the i-th perturbed eigenmode
$\widetilde{\lambda}_{i_{\mathrm{defi}}}$	m	wavelength of the first deficient perturbed eigenmode
μ	H/m	permeability
μ_0	H/m	vacuum permeability
μ_r	1	relative permeability
ν	1	index
ϕ_{e}	rad	phase of the electric field
ϕ_{h}	rad	phase of the magnetic field
φ	rad	polar angle, azimuth
φ_0	rad	polarization angle of an eigenmode
$\Delta\varphi$	rad	polarization angle shift between degenerate eigenmodes
$\partial\Omega_{\mathrm{com}}$	var.	boundary of computational domain
$\partial\Omega_{\mathrm{com,pec}}$	var.	PEC boundary of computational domain
$\partial\Omega_{\mathrm{com,pmc}}$	var.	PMC boundary of computational domain
$\partial\Omega_{\mathrm{pec}}$	m^2	surface of a perfect conductor
$\partial\Omega_{\mathrm{pmc}}$	m^2	surface of an insulator conductor
$\partial\Omega_{\mathrm{pipe}}$	m^2	port surface(s) of a resonator to beam pipe(s)
$\partial\Omega_{\mathrm{res}}$	m^2	complete closed surface of a resonator
$\partial\Omega_{\mathrm{wall}}$	m^2	wall surface of a resonator
ρ	m	polar radius
$\rho(\mathbf{r},t)$	As/m^3	electric charge density
σ	S/m	electric conductivity
σ_{wall}	S/m	electric wall conductivity
σ_i	var.	i-th singular value of a matrix
ω	rad/s	angular frequency
ω_{acc}	rad/s	angular frequency of the accelerating mode
ω_{co}	rad/s	angular cutoff frequency of a waveguide
ω_i	rad/s	angular frequency of the i-th (unperturbed) eigenmode
$\omega_{i,\ell}$	Hz	angular frequency of the ℓ-th passband mode in i-th band
$\widetilde{\omega}_i$	rad/s	angular frequency of the i-th perturbed eigenmode
Ω_{com}	var.	computational domain
Ω_ℓ	rad	phase advance per cell of the ℓ-th passband mode
Ω_{res}	m^3	domain of resonator
ψ_{e_k}	1	k-th eigenvalue of the matrix $\mathbf{G}_e$ (ERES)
$\psi_\nu(\mathbf{r})$	var.	basis function of the ν-th element (FEM)
∇	1/m	Nabla operator
Δ	1/m^2	Laplacian operator
Δ_T	1/m^2	transverse Laplacian operator

Chapter 1

Introduction

The analysis of linear and time-invariant radio frequency (RF) resonant structures with ports is a challenging task in computational electrical engineering. The modeling of complex structures such as superconducting (SC) multicell cavities is computationally demanding and the design process usually requires a multitude of geometric modifications for identifying the final design with superior electromagnetic (EM) properties. These repetitive recomputations of the structure's properties result in a tremendous computational expense. This thesis proposes two new perturbative approaches enabling for an efficient realization of geometric parameter studies of the EM eigenmodes of complex, linear and time-invariant RF structures. Based on one initially defined structure geometry, the eigenmodes of this so-called *unperturbed* geometry are computed with a freely selectable technique. Subsequently, the eigenmodes of a modified, *perturbed* structure can be expanded in terms of the eigenmodes of the unperturbed geometry. For this, the energy-related mutual interactions of the complete set of unperturbed eigenmodes are analyzed inside the volume that is removed by the geometric modification. The eigensystem of the resulting interaction matrix provides the frequencies and the expansion coefficients of the eigenmodes of the respective perturbed geometry. The methods allow to investigate an arbitrary number of differently varied geometries and is applicable to RF structures with perfect electric conducting (PEC) or perfect magnetic conducting (PMC) boundaries. Their development is mainly motivated by the design of superconducting RF structures associated with particle accelerator applications. The treatment of boundaries with a finite conductivity is not in the focus of this work. Likewise, the effects of surface material defects are not regarded. Nevertheless, lossless models of RF structures with a high finite surface conductivity provide a profound understanding of the underlying EM effects, particularly during the design process. The objectives of this thesis are the derivation of the methods' fundamentals, their effective and efficient implementation, the validation of their applicability and the demonstration of the achievable efficiency enhancement.

1.1 Structure of this Thesis

This thesis is organized as follows: The next section of this chapter gives a brief introduction into the fundamental aspects of superconducting RF structures in the framework

of particle accelerators. The following two sections outline the problem statement of this thesis, describing the essential importance of geometric variations in the context of RF structures and the drawback of conventional approaches for their investigation. Chapter 2 provides a summary of the electromagnetic field theory relevant for the understanding of the functional principle of RF structures and the fundamentals of the perturbative methods. Chapter 3 initially outlines the basics of normal mode expansion and Slater's cavity perturbation theorem, which form the basis for a profound understanding of the subsequent detailed derivation of the two novel perturbative methods, the generalization of Slater's theorem and the expansion of a reduced eigenmode set. Chapter 4 briefly explains the main aspects of the implementation of the novel methods and the most relevant procedures for an enhancement of their accuracy and efficiency. Chapter 5 discusses and compares their basic properties regarding accuracy, required effort and spectrum of application based on several simple validation examples while Chapter 6 focuses on the methods' applicability to practically relevant cavity structures. Chapter 7 concludes the thesis with a discussion of the results.

Scalar quantities are written in italic, non-bold typeface while vector and tensor quantities are written in non-italic, bold typeface. Complex quantities are additionally indicated by an underlining.

1.2 Particle Accelerators and Superconducting RF Cavities

Particle accelerators exploit the interaction of electric charges with electromagnetic fields. There is a variety of different technical principles regarding the use of static, low frequency and RF fields. Nowadays, the scope of applications are numerous [1, Ch. 1]. Accelerators are widely used in industrial applications such as x-ray radiography and lithography, material testing or ion implantation and play further an important role in medical treatment particularly for radiation therapy of cancer. Accelerators are also sources of incoherent and coherent radiation for a wide application variety in basic and applied physics research. But primarily, they are known as essential research tools in nuclear and high energy physics. Their significance in fundamental research substantially promoted the technological advance of accelerators. In particle colliders or fixed target setups, bunches of charged particles, like electrons or the considerably heavier protons, are accelerated to high kinetic energies and brought to collision. Several types of detectors analyze the subatomic particles formed by the collision providing information about the dynamics and structure of matter.

Resonant cavities are the fundamental devices for the energy input in modern particle accelerators. Their basic design depends on the particle velocity. High-beta accelerating structures, where the particles travel almost at speed of light, are generally cylindrical cavities or rotationally symmetric cavities with a rounded shape whereas accelerators for low-beta charged particles possess a different design evolved from a coaxial transmission line [2, Sec. 1.1]. High-beta accelerators for very high beam energies become long and very costly. Therefore, a high energy input per length is desired. This requires high electric field strengths which can only be provided by metal RF multicell cavities since electrostatic

fields are limited by field emission effects and voltage breakdown. In normal conducting (NC) copper cavities, the achievable field strength is limited by the surface losses. The fundamental advantage of superconducting (SC) cavities is their extremely low surface resistance. While NC structures typically possess an intrinsic quality factor of 10^4 to 10^5, SC cavities made of niobium or niobium alloys reach values of 10^9 to 10^{11} [2], [3]. Cooled down to a temperature of about $2\,\mathrm{K}$, they have a surface resistivity of only 100 to $10\,\mathrm{n\Omega}$. Especially for applications demanding continuous wave fields of high strength, solely SC structures are economically viable due to the significantly reduced energy requirements. This thesis focusses on high-beta superconducting RF cavities.

1.3 Cavity Design and Geometric Variations

In general, an infinite number of EM resonances, called eigenmodes, can exist inside a resonant cavity, each identified by its respective resonant frequency and field distribution. For particle acceleration the $\mathrm{TM}_{0,1,0_\pi}$ mode is used since it provides a maximal axial electric field and a phase advance of π from cell to cell. The shape of the cavity determines the EM characteristics of each mode, so an optimal design is crucial for the best possible accelerating performance. However, there are a multitude of contradicting optimization goals and the most suitable design depends on the specific application of the accelerator. Regarding only the accelerating mode, a high gradient is desirable for an effective acceleration. But the achievable axial electric field is limited by the maximally maintainable surface fields which are proportional to the accelerating field. A too high magnetic surface field may cause a thermal breakdown of the superconductivity [2, Ch. 11] which must be avoided at all cost. Likewise, a too high electric surface field increases the risk of field emission which can lead to an avalanche-like increase of free electrons, called *multipacting*. Multipacting is a resonant process at which the electrons absorb the RF power impeding to increase the field strength by raising the RF input power [2, Ch. 10]. The ratios of the peak surface fields to the accelerating field can be minimized by a suitable mid-cell shape. By the introduction of a curved shape, noticeable improvements were achieved in the last decades. Nowadays, a multitude of basic cell designs like elliptical, reentrant, low loss or spline cavities exists [3], [4], [5], [6], each of them modifiable by several geometric parameters (e.g. seven parameters for an elliptical cell shape). The multitude of different basic shapes demonstrates not only the importance of a shape optimization but also the complexity of the task. The process becomes even more complicated if the complete multicell structure is considered. Here, first of all the flatness of the accelerating field is of importance since an optimal acceleration is solely achieved if the particles gain an equal kick in each cell [2, Ch. 7]. For this purpose, again an iterative tuning of the end-cells is required. In addition, the intrinsic quality factor of the accelerating mode should be as high as possible in order to minimize RF losses.

One of the main issues for multicell cavities is the existence of *higher order modes* (HOMs). All modes whose frequency is higher than the one of the accelerating mode are denoted as HOMs. Charged particles traversing the structure can generate a broadband excitation of HOMs entailing so-called *wakefields* which are time-dependent superpositions of these modes [7], [8], [9], [10], [11, Ch. 19]. The excitation of a wakefield creates

additional cryogenic losses by extracting energy from the particle beam and heating the cavity walls. In addition, the wakefields persist inside the structure for a certain time and thus may interact with following bunches of charged particles. In SC cavities with their very low surface losses, the wakefield energy almost exclusively reduces by external port losses, identified by the external quality factors of the modes. So, the wakefields may decay very slowly and interfere with trailing particles. *Single-bunch effects* are caused by short-range wakefields which are generated by the particles at the head of a bunch and affect the particles in its tail. Varying longitudinal wakefields can create an energy spread within the bunch degrading the beam focusing. Transverse wakefields deflect the particles at the tail leading to a beam emittance growth. HOMs that can cause transverse wakefields are therefore also denoted as deflecting modes. *Coupled-bunch instabilities* by long-range wakefields can be even more dangerous than single-bunch instabilities since they affect following bunches and have a self-amplifying effect. Deflecting modes which are excited by off-axis particles can lead to a further deflection of following particles, which in turn amplify the mode excitation. If the process is not counteracted, it creates a *beam breakup* (BBU) resulting in a loss of the beam. HOMs with a very weak coupling to the beam pipes or neighboring cavities cannot leave the cavity and thus have very high external quality factors. Such *trapped* modes can be extremely dangerous for the beam stability if they possess a high interaction capability with the beam, specified by their shunt impedance. Hence, an adequate damping of the higher order modes is essential to reduce the quality factors of potentially dangerous modes and thereby avoid a resonant buildup of beam-induced wakefields. For this purpose, HOM couplers are applied which allow all modes but the accelerating mode to pass. There are three major types of HOM couplers: waveguide, coaxial and beam tube couplers [2, Ch. 16], [12], [13], [14]. A large aperture radius also facilitates the damping but may also decrease the shunt impedance of the accelerating mode. As a consequence, the transition between cavity and beam pipe as well as the position, orientation and shape of the HOM coupler have to be included in the cavity optimization process. At this, a rigorous modal analysis is absolutely necessary for an identification of dangerous modes and an adaptation of the cavity design [4], [15].

Despite nowadays elaborate technological manufacturing precision and high technical standards a discrepancy between the actual and the ideal cavity design can never be prevented. Fabrication tolerances and deformations due to operational demands may noticeably change the EM properties. Especially in accelerators with many cavities, such geometric imperfections have a vital role in the choice of the structure [16, Ch. 2]. Geometric deformations may impair the field flatness [17] or increase the adverse effects of HOMs. For instance, an eccentricity of the ideally cylindrical profile may lead to an increased transverse coupling of the wakefields [18]. Further, additionally to the internally trapped HOMs, which do not couple to the beam pipe waveguide modes and exist already for the ideally shaped cavity, externally trapped modes can emerge [19]. Such HOMs may arise in chains of cavities due to the different frequency band shift of each cavity, caused by imperfections. For a cavity in the middle of the chain, the modes at the ends of a passband can fall into the stop bands of neighboring cavities and thus be trapped. Particularly trapped modes are very sensitive to small geometric changes. But the detuning of HOMs may also improve the beam stability by eliminating long range synchronous modes [19].

The cavity fabrication [3] starts with the deep drawing of half-cells. Two half-cells each

are electron-beam welded at their irises to a so-called dumbbell which is additionally stabilized by welding a stiffening ring around the iris. Based on a frequency measurement the length of each dumbbell is then trimmed at its equator to correct the accelerating mode frequency. The HOM frequencies are usually not examined. Subsequently, $N_{\text{cell}} - 1$ dumbbells and two further half-cells are welded to a N_{cell}-cell cavity. The cavity wall thickness is further multiple times reduced during the production by chemical or electro-polishing and cleaning. Every fabrication step contributes to the geometric deviations from the perfect shape with the result that the geometry of each cell and thus of each cavity is different. The effects of production-related imperfections may be tested after the completion of the cavity. However, during operation the cavity is subject to further deforming factors which are partially difficult to predict. Firstly, the cool-down to operating temperature leads to a cavity length change. Furthermore, the cavity geometry dynamically changes. The cavity wall thickness is limited by the ability to cool it down by the cryo-modules and thus has a certain mechanical instability which makes the cavity susceptible to microphonics and Lorentz force detuning [2, Ch. 19], [20]. *Microphonics detuning* includes ambient noise generating a spectrum of mechanical vibrations that cause a variation of the resonant frequencies. *Lorentz force detuning* (LFD) describes the contraction, a simultaneous stretching and compression, of the cavity during operation due to the interaction of the cavity with the RF magnetic field. LFD distorts the EM fields and is relevant for a high accelerating field strength and for pulsed accelerators. Frequency tuners are used to adjust the accelerating mode frequency of the imperfect cavity after installation. Additionally they dynamically tune the cavity during operation using piezoelectric actuators to compensate microphonics and LFD but also amplitude, phase or beam current variations. For this purpose, typically a slow main tuner and a fast fine tuner are applied.

The deformations resulting from fabrication imperfections and operational demands lie in the range of tens of micrometers up to millimeters while the frequencies have a sensitivity of some MHz/mm [3], [18], [19], [21]. Several publications proved the importance of a HOM survey regarding the effects of realistic deformations by numerical and experimental data [3], [18], [20], [22], [23], [24]. For instance, both simulated and measured results displayed noticeable differences for the frequencies and external quality factors of HOMs.

1.4   State of the Art and Problem Statement

The previous section elucidated that a rigorous broadband computation of the EM properties is of major importance for an optimal and robust cavity design since the EM fields are highly sensitive to geometric modifications. The resolution of the applied method must cope with the size of the deformations and the regarded frequency range. But at the same time it has to allow for an investigation of a vast number of different designs. The optimization of the mid-cell shape for the maximization of the accelerating field is subject to at least two limiting constraints, the electric and magnetic surface fields, and depends on even more variable geometric parameters. This multi-dimensional problem already may involve a considerable computational effort. The analysis of the complete multicell structure regarding field flatness and HOM properties is even more expensive, in particular if

additional devices like input or HOM couplers have to be included. The numerical models of such structures involve a higher number of degrees of freedoms. In addition to this, the frequency bands of multicell cavities are more densely populated with modes. Thus, also a larger number of modes has to be investigated for an appropriate HOM analysis. However, the investigation of the effects of unavoidable geometric imperfections by far surpasses the optimization demands due to the statistical nature of the deformations. A vast amount of randomly generated design variations has to be considered for the complete structure in order to obtain a realistic sensitivity estimation. This is aggravated by the fact that imperfections generally involve asymmetric deformations which often further increase the computational expenses for the modeling.

The EM characteristics of a cavity can be determined by computing the EM fields in time or frequency domain. The time domain analysis, involving a field excitation by waveguide ports, is the most rigorous and most accurate method to compute the EM fields and particularly their external quality factors [15], [25]. However, the application of time domain methods is inconvenient for SC cavities due to large time constants arising from the modes' high quality factors. The results may even be wrong if the simulation time is too short or the mesh used for the discretization of the structure creates parasitic resonances [15]. In frequency domain, the EM properties of guided wave systems are often described by scattering parameters [26, Ch. 3], [27, Ch. 4]. But scattering parameters do not provide information about the field distributions inside the cavities and thus cannot yield all required quantities. The most common approach of modeling a RF cavity is a modal analysis of the steady-state EM fields of a respective ideal resonator with PEC or PMC boundaries. The eigenmode concept is very useful for the analysis of RF structures allowing for the determination of all relevant EM characteristics. In addition, the effects of traveling waves, such as external energy losses may be determined a posteriori by modal approaches [15], [28], [29]. There are also algorithms for the eigenmode computation with open boundary conditions which directly include external losses [30], [31]. However, they involve the solution of complex eigenvalue problems causing high computational expenses.

The standard approach for performing geometric parameter studies of the EM characteristics is the execution of lossless eigenmode computations combined with an iterative modification of the structure's shape. The major drawback of this straight forward approach is that each geometric modification necessitates a complete recomputation of the eigenmodes regardless of its extent. The resulting computational effort is enormous, forcing a tradeoff between design requirements and computational time. In literature a large variety of studies concerning the EM properties of superconducting RF cavities by means of numerical eigenmode computations exists, for instance [4], [5], [32], [33], [34], [35]. Most of them solely perform an optimization regarding the perfectly shaped cavity whereas the effects of geometric imperfections are excluded from the investigation, even though they may be of particular importance for the final design. Moreover, often merely the modes within a relatively small frequency range are analyzed. Thus, dangerous modes with a higher frequency may be not be detected. Likewise, the number of optimization steps is often limited by the computational demands.

Extensive direct parameter studies may only be realized by supercomputers and massive parallel computing. However, only a few facilities worldwide possess the necessary technical resources [31], [36]. There are several alternative approaches to efficiently esti-

mate the effects of geometric variations. An example for computing the frequency shift based on the mode sensitivity is given in [21]. But the determined sensitivities are only valid for the specific geometry and variations of limited extent. Furthermore, such approaches also require direct computations in order to obtain the sensitivities. A shape determination algorithm for solving unknown perturbations through a least square minimization is presented in [37]. It bases on a forward eigenmode computation by means of a mesh distortion method [38]. Mesh distortion methods reduce the computational effort for the solution of the eigenvalue problem. But nevertheless, they require a recomputation for every geometric variation and thus are not suitable for complex parameter studies. An eigenmode solver that directly yields the frequency sensitivities and further computes the effect of LFD by a stochastic response surface method based on the uncertainty concept is demonstrated in [39]. Disadvantageously, the computation of the EM field distributions is not considered. So, EM quantities such as quality factors cannot be obtained. The same applies to the often applied Slater's cavity perturbation theorem [28, Sec. III.7]. It allows for a computation of the frequency shifts caused by a geometric deformation but does not account for the field distributions. Another perturbative approach enables the approximation of both the frequencies and the EM fields of a deformed cavity by using the eigenvalue and eigenvector derivatives [40]. The derivatives are determined based on modal superposition methods or direct methods. But according to [40], the method's major drawback is that precise results can demand a high effort similar to the one of a direct computation.

The here presented perturbative methods offer an efficient approach to tackle the problem of geometric parameter studies. They allow for the computation of the eigenmodes and the derived EM properties for a vast number of different cavity designs based on the eigenmodes of just one initial design. The fundamental idea of the methods is to expand the eigenmodes of a modified, perturbed structure in terms of the orthogonal eigenmodes of the initial, unperturbed geometry. Hence, inefficient repetitive computations are avoided and the limitations of conventional methods exceeded. Particularly in case of extensive studies, the methods can significantly reduce the computational demands and thus are very suitable for a performance optimization of multicell structures with a simultaneous investigation of shape imperfections. Their application is motivated by the following advantages:

- The methods enable the computation of both the frequencies and field distributions over a wide frequency range and thereby the determination of integral cavity characteristics.

- They require a conventional numerical eigenmode computation only once for the initial, unperturbed geometry. At this, the eigenmodes can be computed with a freely selectable technique.

- Once the eigenmodes of the unperturbed resonator are computed, the eigenmodes of an arbitrary number of modified geometries can be determined with a very low effort. So, geometric parameter studies are less computationally demanding and may be performed on a larger scale.

- The eigenmodes of a structure with symmetry breaking elements, like tuned end-cells or wall deformations, can be derived from the eigenmodes of a symmetric unperturbed structure. This may lead to a significant reduction of the degrees of freedom and thereby to a further efficiency improvement as well as to an expansion of the computable frequency range.

- By a suitable partitioning of the unperturbed geometry into segments, each segment can be individually modified. In this way, the computational effort is further reduced.

- The methods are applicable to arbitrary RF structures with PEC or PMC boundaries and are suitable for automation.

Chapter 2

Electromagnetic Field Theory

This chapter provides a brief survey of the basic equations of electromagnetic (EM) field theory that describe the functional principle of radio frequency (RF) accelerating structures and form the basis for the perturbative methods in Chapter 3. Subsequently, the most relevant figures of merit for characterization of RF accelerating structures are introduced.

2.1 Maxwell's Equations

James Clark Maxwell (1831-1879) reviewed and collated the most important laws on electric and magnetic phenomena, established by different scientists over several decades by empirical and theoretical investigations. He was the first person formulating a complete set of equations describing the behavior of electromagnetic phenomena [41]. Later, the equations were reformulated into the present-day form by Oliver Heaviside (1850-1925). This set of equations is formally known as *Maxwell's Equations*.

2.1.1 General Maxwell's Equations

Maxwell's equations can be written either in integral or differential form. The integral representation is given by

$$\oiint_{\partial\Omega} \mathbf{B}(\mathbf{r},t)\cdot \mathrm{d}\mathbf{A} = 0, \tag{2.1}$$

$$\oiint_{\partial\Omega} \mathbf{D}(\mathbf{r},t)\cdot \mathrm{d}\mathbf{A} = \iiint_{\Omega} \rho(\mathbf{r},t)\,\mathrm{d}V, \tag{2.2}$$

$$\oint_{\partial S} \mathbf{E}(\mathbf{r},t)\cdot \mathrm{d}\mathbf{s} = -\iint_{S} \frac{\partial}{\partial t}\mathbf{B}(\mathbf{r},t)\cdot \mathrm{d}\mathbf{A}, \tag{2.3}$$

$$\oint_{\partial S} \mathbf{H}(\mathbf{r},t)\cdot \mathrm{d}\mathbf{s} = \iint_{S} \left(\frac{\partial}{\partial t}\mathbf{D}(\mathbf{r},t) + \mathbf{J}(\mathbf{r},t)\right)\cdot \mathrm{d}\mathbf{A}, \tag{2.4}$$

where $\mathbf{D}(\mathbf{r}, t)$ denotes the *electric flux density* (unit: As/m^2), $\rho(\mathbf{r}, t)$ the *electric charge density* (unit: As/m^3), $\mathbf{B}(\mathbf{r}, t)$ the *magnetic flux density* (unit: Vs/m^2), $\mathbf{E}(\mathbf{r}, t)$ the *electric field strength* (unit: V/m), $\mathbf{H}(\mathbf{r}, t)$ the *magnetic field strength* (unit: A/m) and $\mathbf{J}(\mathbf{r}, t)$ the *electric current density* (unit: A/m^2). The electric and magnetic field strength are also known as electric and magnetic field intensity, or electric and magnetic field for short. The spatial and time dependence of the quantities is indicated by the *position* $\mathbf{r}$ (unit: m) and the *time t* (unit: s). Further, dV, d$\mathbf{A}$ and d$\mathbf{s}$ compose the infinitesimal volume, area and line element. *Gauss's law for the magnetic field* (2.1) states that the total magnetic flux through the closed boundary $\partial\Omega$ of a domain Ω is always zero. It thereby implies the non-existence of magnetic charges. *Gauss's law for the electric field* (2.2) requires the total electric flux through the closed boundary $\partial\Omega$ of a domain Ω to be equal to the total electric charge enclosed by $\partial\Omega$. *Faraday's law of induction* (2.3) expresses that the negative time derivative of the total magnetic flux through a bounded surface S is equal to the integral of the electric field along the closed contour ∂S of the surface S, i.e a time-varying magnetic field involves a non-conservative electric field. *Ampère's circuital law extended by Maxwell's hypothesis of displacement current* (2.4) states that the total current through a surface S, formed by the time derivative of the total electric flux and the electric current density, is equal to the integral of the magnetic field along the contour ∂S.

While the integral form of Maxwell's equations is more appropriate for understanding the physical meaning of the equations, the differential representation is often more suitable for mathematical considerations. The equations (2.1) - (2.4) can be transformed into differential form by applying the divergence theorem (A.3) and Stokes' theorem (A.4)

$$\boldsymbol{\nabla} \cdot \mathbf{B}(\mathbf{r}, t) = \quad 0, \tag{2.5}$$

$$\boldsymbol{\nabla} \cdot \mathbf{D}(\mathbf{r}, t) = \quad \rho(\mathbf{r}, t), \tag{2.6}$$

$$\boldsymbol{\nabla} \times \mathbf{E}(\mathbf{r}, t) = -\frac{\partial}{\partial t} \mathbf{B}(\mathbf{r}, t), \tag{2.7}$$

$$\boldsymbol{\nabla} \times \mathbf{H}(\mathbf{r}, t) = \quad \frac{\partial}{\partial t} \mathbf{D}(\mathbf{r}, t) + \mathbf{J}(\mathbf{r}, t). \tag{2.8}$$

The relation between electric charge density and electric current density, can be restated from (2.6) and (2.8) as

$$\iint_{\partial\Omega} \mathbf{J}(\mathbf{r}, t) \cdot \mathrm{d}\mathbf{A} = -\frac{\partial}{\partial t} \underbrace{\iiint_{\Omega} \rho(\mathbf{r}, t) \, \mathrm{d}V}_{q_\Omega} \tag{2.9}$$

by applying (A.6). The equation of continuity (2.9) shows that a transport of charged particles from a domain Ω leads to a reduction of the *total domain charge q_Ω* (unit: A s) by a current flow through its surface and thereby clarifies the conservation of charge in Maxwell's equations.

In media, the phenomena of conduction, polarization and magnetization influence the behavior of the electromagnetic fields. They have to be taken into account by additional constitutive relations and parameters. In general, the constitutive parameters are scalars or tensors that can be spatially, time- and temperature-dependent as well as a function of the field strengths. However, in the following equations, the constitutive parameters are

only referred as scalars without any dependences (σ, ε and μ) to avoid an unnecessarily complex notation. Despite this simplified notation, the actual possible dependences must still be regarded. The total electric current density consists of three, partially material-dependent, components

$$\mathbf{J}(\mathbf{r},t) = \underbrace{\sigma\mathbf{E}(\mathbf{r},t)}_{\mathbf{J}_\sigma(\mathbf{r},t)} + \underbrace{\mathbf{v}(\mathbf{r},t)\,\rho(\mathbf{r},t)}_{\mathbf{J}_{\mathrm{cc}}(\mathbf{r},t)} + \mathbf{J}_{\mathrm{ic}}(\mathbf{r},t)\,. \tag{2.10}$$

The *conduction current density* $\mathbf{J}_\sigma(\mathbf{r},t)$ only occurs in conducting media and obeys Ohm's law. It is proportional to the electric field strength by the proportionality factor of the *electric conductivity* σ (unit: S/m). In contrast, the *convection current density* $\mathbf{J}_{\mathrm{cc}}(\mathbf{r},t)$ reflects the effects of moving charged particles with a *velocity* $\mathbf{v}(\mathbf{r},t)$ (unit: m/s) in insulators or dielectrics. The third component, the *impressed current density* $\mathbf{J}_{\mathrm{ic}}(\mathbf{r},t)$, is field-independent and represents currents excited by external sources. The electric flux density $\mathbf{D}(\mathbf{r},t)$ depends on the electric field strength $\mathbf{E}(\mathbf{r},t)$ and the polarization induced by $\mathbf{E}(\mathbf{r},t)$. Similarly, the magnetic flux density $\mathbf{B}(\mathbf{r},t)$ is determined by the magnetic field strength $\mathbf{H}(\mathbf{r},t)$ and the magnetization due to $\mathbf{H}(\mathbf{r},t)$. The relations are described by

$$\mathbf{D}(\mathbf{r},t) = \underbrace{\varepsilon_0\varepsilon_r}_{\varepsilon}\,\mathbf{E}(\mathbf{r},t)\,, \tag{2.11}$$

$$\mathbf{B}(\mathbf{r},t) = \underbrace{\mu_0\mu_r}_{\mu}\,\mathbf{H}(\mathbf{r},t)\,. \tag{2.12}$$

The *permittivity* ε (unit: F/m) is the product of the *vacuum permittivity* $\varepsilon_0 = 8.85418782 \cdot 10^{-12}$ F/m and the *relative permittivity* ε_r. The *permeability* μ (unit: H/m) is the product of the *vacuum permeability* $\mu_0 = 4\pi \cdot 10^{-7}$ H/m and the *relative permeability* μ_r. In any case, ε_0 and μ_0 are constant scalars and define the *speed of light in vacuum* c_0 by the following relation

$$c_0 = \frac{1}{\sqrt{\mu_0\varepsilon_0}}\,. \tag{2.13}$$

In homogeneous media, all constitutive parameters are spatially independent. In anisotropic media, the conduction, the polarization and/or the magnetization are directionally dependent. In this case, σ, ε_r and/or μ_r become tensors of rank two. In addition, anisotropic media described by symmetric tensors are called reciprocal. Dispersive media cannot polarize or magnetize instantaneously and thereby show a frequency-dependent behavior. Thus, in dispersive media, $\mathbf{J}_\sigma(\mathbf{r},t)$, $\mathbf{D}(\mathbf{r},t)$ and/or $\mathbf{B}(\mathbf{r},t)$ are not only determined by the present value of the respective field strength but also by its time derivatives. In non-linear materials, σ, ε_r and/or μ_r themselves depend upon the field strengths. The hysteresis of ferromagnetic materials is a prominent example for a non-linear medium [42]. For the sake of completeness, it must be mentioned that a cross coupling between electric and magnetic field may occur in bi-isotropic and bi-anisotropic media. Such media can be polarized by a magnetic field and magnetized by an electric field [43]. A detailed description of the electromagnetic properties of matters is provided in [44, Ch. 2]. In this thesis, only linear, homogeneous, time-invariant (non-dispersive), isotropic, charge-free and source-free materials are considered, since the investigated RF structures like cavities, beam pipes,

waveguides and couplers are evacuated or filled with air. Beam effects are only regarded a posteriori. Hence, inside the structures $\rho(\mathbf{r}, t) = 0$, $\sigma = 0$ and $\mathbf{J}_{\text{ic}}(\mathbf{r}, t) = \mathbf{0}$ while ε and μ are constant scalars. RF ferrite cavities [45], waveguides with energy absorbing materials [46], laser plasma accelerators [47], [48] or other devices applied in accelerator physics that consist of more complex materials are not part of this thesis.

In the context of particle acceleration, the effect of an EM field on a particle carrying the charge q is of particular interest. It is described by the *Lorentz force* $\mathbf{F}_{\text{L}}(\mathbf{r}, t)$ (unit: N) [26, Ch. 1]

$$\mathbf{F}_{\text{L}}(\mathbf{r}, t) = q\big(\mathbf{E}(\mathbf{r}, t) + \mathbf{v}(\mathbf{r}, t) \times \mathbf{B}(\mathbf{r}, t)\big). \tag{2.14}$$

For a positive charge, the electric force acts in the same direction as the electric field whereas the magnetic force is perpendicular to the direction of the particle velocity and the magnetic flux. Thus, electric fields are particularly suitable for accelerating particles and magnetic fields for deflecting them. More generally formulated, the velocity $\mathbf{v}(\mathbf{r}, t)$ is the temporal change of particle position $\frac{\partial}{\partial t}\mathbf{r}$.

2.1.2 Maxwell's Equations for Time-Harmonic Electromagnetic Fields

Steady-state alternating fields that sinusoidally oscillate at an *angular frequency* ω (unit: rad/s) are called *time-harmonic* fields and are of particular importance in electromagnetic field theory involving the phenomena of waves in linear media. Time-harmonic fields can be represented as complex quantities, called phasors, to simplify mathematical considerations [26, Ch. 1]. The instantaneous quantity is defined as the real part of the corresponding complex quantity that has a time dependence proportional to $\mathrm{e}^{\jmath\omega t}$. The electric field $\mathbf{E}(\mathbf{r}, t)$ can for instance be expressed in terms of a *complex electric field* $\underline{\mathbf{E}}(\mathbf{r}, t)$

$$\mathbf{E}(\mathbf{r}, t) = \Re\{\underline{\mathbf{E}}(\mathbf{r}, t)\} = \Re\left\{\mathrm{e}^{\jmath(\omega t + \phi_{\text{e}})}\underline{\mathbf{E}}(\mathbf{r})\right\}. \tag{2.15}$$

As apparent from (2.15), the time-harmonic vector $\underline{\mathbf{E}}(\mathbf{r}, t)$ is identified as a product of two distinct functions, a spatial vector function $\underline{\mathbf{E}}(\mathbf{r})$ and a time-dependent scalar function with the frequency ω and the *phase* ϕ_{e}. Consequently, the time derivative of $\underline{\mathbf{E}}(\mathbf{r}, t)$ is

$$\frac{\partial}{\partial t}\underline{\mathbf{E}}(\mathbf{r}, t) = \jmath\omega\underline{\mathbf{E}}(\mathbf{r}, t). \tag{2.16}$$

The phasor representation, as demonstrated in (2.15) - (2.16) for the electric field $\mathbf{E}(\mathbf{r}, t)$, can be applied to every other time-harmonic quantity, provided that its components have the same frequency and a constant phase shift. Otherwise a separation into a purely spatially and a purely time-dependent function is not possible. However, any transient field or source, involving time variations in arbitrary forms, can be expressed as a superposition of sinusoidal functions of different frequencies according to Fourier's theorem [49, Ch. 1] which in turn may be transformed into a complex form. Beside the angular frequency ω, that describes the rate of the phase change, there exists a different frequency term, the *temporal frequency* f (unit: Hz). It states the number of oscillations per unit time and is related to ω by

$$\omega = 2\pi f. \tag{2.17}$$

For time-harmonic complex fields, the equations (2.1) – (2.4) become the *frequency-domain Maxwell's equations*

$$\boldsymbol{\nabla} \cdot \underline{\mathbf{B}}(\mathbf{r}, t) = \quad 0, \tag{2.18}$$
$$\boldsymbol{\nabla} \cdot \underline{\mathbf{D}}(\mathbf{r}, t) = \quad \rho(\mathbf{r}, t), \tag{2.19}$$
$$\boldsymbol{\nabla} \times \underline{\mathbf{E}}(\mathbf{r}, t) = -\jmath\omega\underline{\mathbf{B}}(\mathbf{r}, t), \tag{2.20}$$
$$\boldsymbol{\nabla} \times \underline{\mathbf{H}}(\mathbf{r}, t) = \quad \jmath\omega\underline{\mathbf{D}}(\mathbf{r}, t) + \underline{\mathbf{J}}(\mathbf{r}, t). \tag{2.21}$$

In the context of eigenmodes, that will be introduced in Section 2.2, the definition of complex electromagnetic field vectors will be further concretized.

2.1.3 Energy Conservation in the Electromagnetic Field

The conservation of energy in the electromagnetic field is described by *Poynting's theorem* [26, Ch. 1], [44, Ch. 1], which is directly derived from Maxwell's equations as described in Appendix A.4.2. Poynting's theorem in integral form is

$$\oiint_{\partial\Omega} \left(\mathbf{E}(\mathbf{r}, t) \times \mathbf{H}(\mathbf{r}, t)\right) \cdot \mathrm{d}\mathbf{A} = -\iiint_{\Omega} \left(\overbrace{\mathbf{H}(\mathbf{r}, t) \cdot \frac{\partial}{\partial t}\mathbf{B}(\mathbf{r}, t)}^{\frac{\partial}{\partial t}u_{\mathrm{m}}(\mathbf{r}, t)} + \overbrace{\mathbf{E}(\mathbf{r}, t) \cdot \frac{\partial}{\partial t}\mathbf{D}(\mathbf{r}, t)}^{\frac{\partial}{\partial t}u_{\mathrm{e}}(\mathbf{r}, t)} \right) \mathrm{d}V$$
$$- \iiint_{\Omega} \sigma E^2(\mathbf{r}, t)\,\mathrm{d}V - \iiint_{\Omega} \mathbf{E}(\mathbf{r}, t) \cdot \left(\mathbf{J}_{\mathrm{cc}}(\mathbf{r}, t) + \mathbf{J}_{\mathrm{ic}}(\mathbf{r}, t)\right)\,\mathrm{d}V. \tag{2.22}$$

Here, $u_{\mathrm{e}}(\mathbf{r}, t)$ is the instantaneous *electric energy density* (unit: J/m^3) and $u_{\mathrm{m}}(\mathbf{r}, t)$ the instantaneous *magnetic energy density* (unit: J/m^3). The left side of (2.22) is the total power flow through the closed surface $\partial\Omega$ of the domain Ω while the right-hand side states energy increases or decreases inside the domain. The first two terms on the right-hand side characterize the time-dependent changes of the stored electric and magnetic energy, the third term constitutes Joule energy losses in the form of heat and the last term describes a gain or loss of energy due to an impressed electric field strength or a movement of charged particles through the surface. The cross product of electric and magnetic field

$$\mathbf{S}(\mathbf{r}, t) = \mathbf{E}(\mathbf{r}, t) \times \mathbf{H}(\mathbf{r}, t), \tag{2.23}$$

that describes the power flow per unit area at any point in space, is also denoted as the *time-domain Poynting vector* $\mathbf{S}(\mathbf{r}, t)$ (unit: W/m^2). For linear, homogeneous, isotropic and time-invariant media, the changes of energy densities per unit time $\mathrm{d}t$ become

$$\mathrm{d}\big(u_{\mathrm{e}}(\mathbf{r}, t)\big) = \frac{1}{2}\mathrm{d}\big(\mathbf{E}(\mathbf{r}, t) \cdot \mathbf{D}(\mathbf{r}, t)\big) = \frac{1}{2}\mathrm{d}\big(\varepsilon E^2(\mathbf{r}, t)\big), \tag{2.24}$$

$$\mathrm{d}\big(u_{\mathrm{m}}(\mathbf{r}, t)\big) = \frac{1}{2}\mathrm{d}\big(\mathbf{H}(\mathbf{r}, t) \cdot \mathbf{B}(\mathbf{r}, t)\big) = \frac{1}{2}\mathrm{d}\big(\mu H^2(\mathbf{r}, t)\big) \tag{2.25}$$

and equation (2.22) simplifies to

$$
\oiint_{\partial\Omega} \big(\mathbf{E}(\mathbf{r},t) \times \mathbf{H}(\mathbf{r},t)\big) \cdot \mathrm{d}\mathbf{A} =
$$
$$
-\iiint_{\Omega} \left(\frac{\partial}{\partial t}\Big(\frac{\varepsilon}{2}E^2(\mathbf{r},t) + \frac{\mu}{2}H^2(\mathbf{r},t)\Big) + \sigma E^2(\mathbf{r},t) + \mathbf{E}(\mathbf{r},t) \cdot \big(\mathbf{J}_{\mathrm{cc}}(\mathbf{r},t) + \mathbf{J}_{\mathrm{ic}}(\mathbf{r},t)\big) \right)\mathrm{d}V. \tag{2.26}
$$

Time-harmonic electromagnetic fields can also be described by the *complex Poynting vector*

$$
\underline{\mathbf{S}}(\mathbf{r}) = \frac{1}{2}\big(\underline{\mathbf{E}}(\mathbf{r}) \times \underline{\mathbf{H}}(\mathbf{r})^*\big). \tag{2.27}
$$

The additional prefactor arises from the sinusoidal time behavior of the fields [26]. The real part of $\underline{\mathbf{S}}(\mathbf{r},t)$ is equal to the time-average of the power flux density while the imaginary part is equal to the reactive power flux density. Applying complex quantities, (2.22) transforms into the *frequency-domain Poynting's theorem*

$$
\oiint_{\partial\Omega} \frac{\underline{\mathbf{E}}(\mathbf{r}) \times \underline{\mathbf{H}}(\mathbf{r})^*}{2} \cdot \mathrm{d}\mathbf{A} = -2\jmath\omega \iiint_{\Omega} \left(\overbrace{\frac{\underline{\mathbf{H}}(\mathbf{r})^* \cdot \underline{\mathbf{B}}(\mathbf{r})}{4}}^{\underline{u}_{\mathrm{m}}(\mathbf{r})} - \overbrace{\frac{\underline{\mathbf{E}}(\mathbf{r}) \cdot \underline{\mathbf{D}}(\mathbf{r})^*}{4}}^{\underline{u}_{\mathrm{e}}(\mathbf{r})} \right)\mathrm{d}V
$$
$$
- \iiint_{\Omega} \frac{\sigma E^2(\mathbf{r})}{2}\,\mathrm{d}V - \iiint_{\Omega} \underline{\mathbf{E}}(\mathbf{r}) \cdot \frac{\underline{\mathbf{J}}_{\mathrm{cc}}(\mathbf{r})^* + \underline{\mathbf{J}}_{\mathrm{ic}}(\mathbf{r})^*}{2}\,\mathrm{d}V. \tag{2.28}
$$

Equation (2.26) likewise transforms into

$$
\oiint_{\partial\Omega} \frac{\underline{\mathbf{E}}(\mathbf{r}) \times \underline{\mathbf{H}}(\mathbf{r})^*}{2} \cdot \mathrm{d}\mathbf{A} = -2\jmath\omega \iiint_{\Omega} \left(\frac{\mu H^2(\mathbf{r})}{4} - \frac{\varepsilon E^2(\mathbf{r})}{4} \right)\mathrm{d}V - \iiint_{\Omega} \frac{\sigma E^2(\mathbf{r})}{2}\,\mathrm{d}V
$$
$$
- \iiint_{\Omega} \underline{\mathbf{E}}(\mathbf{r}) \cdot \frac{\underline{\mathbf{J}}_{\mathrm{cc}}(\mathbf{r})^* + \underline{\mathbf{J}}_{\mathrm{ic}}(\mathbf{r})^*}{2}\,\mathrm{d}V. \tag{2.29}
$$

It must be pointed out that $E(\mathbf{r})$ and $H(\mathbf{r})$ are the magnitudes of the stationary fields $\underline{\mathbf{E}}(\mathbf{r})$ and $\underline{\mathbf{H}}(\mathbf{r})$ which are not to be confused with the instantaneous magnitudes of $\mathbf{E}(\mathbf{r},t)$ and $\mathbf{H}(\mathbf{r},t)$. The first term on the right-hand side of (2.29) is purely imaginary, i.e. it does not create losses, involving only the time-depending conversion between electric and magnetic energy in the EM field. Thus, the time-average energies stored in the electric and the magnetic field are identical.

2.1.4 Wave Equations

Faraday's law of induction (2.7) and Ampère's circuital law extended by Maxwell's hypothesis of displacement current (2.4) are two coupled vector differential equations of first order, describing the interactions between electric fields and magnetic fields. To obtain a

solution for $\mathbf{E}(\mathbf{r}, t)$ and $\mathbf{H}(\mathbf{r}, t)$, it is often more suitable to combine the two equations. In a linear, homogeneous, isotropic and time-invariant media, this is achieved by transferring Maxwell's equations into the so-called *wave equations* [26, Ch. 1] (see Appendix A.4.3) which contain either the electric or the magnetic field. The wave equations are four-dimensional hyperbolic vector partial differential equations (PDEs) of second order and emphasize the wave nature of the time-varying EM fields. The *inhomogeneous generalized wave equations* of the electric and magnetic field are

$$\Delta\mathbf{E}(\mathbf{r}, t) - \mu\sigma\frac{\partial}{\partial t}\mathbf{E}(\mathbf{r}, t) - \mu\varepsilon\frac{\partial^2}{\partial t^2}\mathbf{E}(\mathbf{r}, t) = \frac{\boldsymbol{\nabla}\rho(\mathbf{r}, t)}{\varepsilon} + \mu\frac{\partial}{\partial t}\big(\mathbf{J}_{\mathrm{cc}}(\mathbf{r}, t) + \mathbf{J}_{\mathrm{ic}}(\mathbf{r}, t)\big), \quad (2.30)$$

$$\Delta\mathbf{H}(\mathbf{r}, t) - \mu\sigma\frac{\partial}{\partial t}\mathbf{H}(\mathbf{r}, t) - \mu\varepsilon\frac{\partial^2}{\partial t^2}\mathbf{H}(\mathbf{r}, t) = -\boldsymbol{\nabla} \times \big(\mathbf{J}_{\mathrm{cc}}(\mathbf{r}, t) + \mathbf{J}_{\mathrm{ic}}(\mathbf{r}, t)\big). \quad (2.31)$$

The first term on the left-hand sides of (2.30) and (2.31) can be interpreted as the rate of spatial change of the respective field, the second term represents its damping part and third term its oscillating part. The right-hand sides of the equations comprise the sources of the fields. In a further non-conducting, charge- and source-free medium, with $\rho(\mathbf{r}, t) = 0$, $\sigma = 0$ and $\mathbf{J}_{\mathrm{ic}}(\mathbf{r}, t) = 0$, (2.30) and (2.31) become the *homogeneous wave equations*

$$\Delta\mathbf{E}(\mathbf{r}, t) - \mu\varepsilon\frac{\partial^2}{\partial t^2}\mathbf{E}(\mathbf{r}, t) = \mathbf{0}, \quad (2.32)$$

$$\Delta\mathbf{H}(\mathbf{r}, t) - \mu\varepsilon\frac{\partial^2}{\partial t^2}\mathbf{H}(\mathbf{r}, t) = \mathbf{0} \quad (2.33)$$

where the damping terms and the source terms vanish. The *complex inhomogeneous wave equations* for time-harmonic EM fields are obtained by substituting the time derivative $\frac{\partial}{\partial t} = \jmath\omega$, resulting from (2.16), into (2.30) and (2.31)

$$\Delta\underline{\mathbf{E}}(\mathbf{r}, t) - (\jmath\omega\mu\sigma - \omega^2\mu\varepsilon)\underline{\mathbf{E}}(\mathbf{r}, t) = \frac{\boldsymbol{\nabla}\rho(\mathbf{r}, t)}{\varepsilon} + \jmath\omega\mu\big(\underline{\mathbf{J}}_{\mathrm{cc}}(\mathbf{r}, t) + \underline{\mathbf{J}}_{\mathrm{ic}}(\mathbf{r}, t)\big), \quad (2.34)$$

$$\Delta\underline{\mathbf{H}}(\mathbf{r}, t) - \underbrace{(\jmath\omega\mu\sigma - \omega^2\mu\varepsilon)}_{\underline{\gamma}^2}\underline{\mathbf{H}}(\mathbf{r}, t) = -\boldsymbol{\nabla} \times \big(\underline{\mathbf{J}}_{\mathrm{cc}}(\mathbf{r}, t) + \underline{\mathbf{J}}_{\mathrm{ic}}(\mathbf{r}, t)\big). \quad (2.35)$$

Here, the *propagation constant* $\underline{\gamma}$ (unit: $1/\mathrm{m}$) is introduced to clarify the traveling behavior of the wave [44, Sec. 4.3]. The quantity $\underline{\gamma}$ is defined as

$$\underline{\gamma} = \alpha + \jmath\beta \quad (2.36)$$

with

$$\alpha = \omega\sqrt{\mu\varepsilon}\sqrt{\frac{1}{2}\left(\sqrt{1 + \left(\frac{\sigma}{\omega\varepsilon}\right)^2} - 1\right)}, \quad (2.37)$$

$$\beta = \omega\sqrt{\mu\varepsilon}\sqrt{\frac{1}{2}\left(\sqrt{1 + \left(\frac{\sigma}{\omega\varepsilon}\right)^2} + 1\right)}. \quad (2.38)$$

The *attenuation constant* α represents the damping of the wave and the *phase constant* β the spatial change of its phase. The *complex homogeneous wave equations*

$$\Delta\underline{\mathbf{E}}(\mathbf{r}, t) + \omega^2\mu\varepsilon\underline{\mathbf{E}}(\mathbf{r}, t) = \mathbf{0}, \quad (2.39)$$
$$\Delta\underline{\mathbf{H}}(\mathbf{r}, t) + \omega^2\mu\varepsilon\underline{\mathbf{H}}(\mathbf{r}, t) = \mathbf{0} \quad (2.40)$$

are also known as the *vector Helmholtz equations*. Here, $\underline{\gamma}$ is purely imaginary and β becomes the *angular wave number* k (unit: 1/m)

$$k = \omega\sqrt{\mu\varepsilon} \tag{2.41}$$

that is often simply referred to as wave number. The angular wave number is related to the *wavelength* λ (unit: m) by

$$\lambda = \frac{2\pi}{\omega\sqrt{\mu\varepsilon}} = \frac{2\pi}{k}. \tag{2.42}$$

2.2 Electromagnetic Fields in Closed Structures

While in free space the time-harmonic electromagnetic fields can propagate as uniform plane waves, they become *guided waves* inside accelerating structures, confined by material boundaries [29, Ch. 5]. The boundary conditions imposed on a steady-state time-harmonic EM field by cavity or waveguide walls constitute a time-varying boundary value problem of the Helmholtz equations. By treating a cavity as an ideal resonator, such a problem can be transformed into a three-dimensional (3D) eigenvalue problem, in which the fields are *standing waves*, called *eigenmodes*. An ideal resonator is a lossless electromagnetic system completely enclosed by a short-circuit or open-circuit surface that forms an adiabatic system [26, Sec. 5.2]. The term *resonator* is often equivalently used as the term *cavity* since they are closely related. But strictly speaking, a cavity, as referred to in accelerator physics, is no ideal resonator because it has ports for energy input, beam propagation and damping of higher order modes. The energy of eigenmodes whose frequency is higher than a port's cutoff frequency can propagate through the port and thus are actually guided waves. Nevertheless, the concept of eigenmodes is very useful for the analysis of RF structures allowing for the determination of several characteristics describing the cavity. The effects of propagating waves involving a gain or loss of energy can be taken into account by means of perturbation approaches based on the eigenmodes [28], [50], [51]. Likewise, the effects of wall losses due to a finite wall conductivity can be considered a posteriori by power loss methods [52].

2.2.1 Boundary Conditions

The *perfect electric conducting* (PEC) boundary condition describes the behavior of an EM field on the *surface of a perfect conductor* $\partial\Omega_{\mathrm{pec}}$ [26, Sec. 1.2]. It is also known as short-circuit surface, in analogy with the short-circuit condition in circuit theory. Inside a perfect conductor free charges cannot remain and all charges reside on its surface. Thus no electric field exists inside the conductor and the electric field tangentially to its boundary must be zero since it is continuous at the interface. In addition, the perpendicularity of electric and magnetic field implies that the normal magnetic field is also zero

$$\mathbf{n} \times \underline{\mathbf{E}}(\mathbf{r}) = \mathbf{0} \quad \text{and} \quad \mathbf{n} \cdot \underline{\mathbf{H}}(\mathbf{r}) = 0 \quad \text{at } \partial\Omega_{\mathrm{pec}}. \tag{2.43}$$

Here, $\mathbf{n}$ denotes the outward-oriented unit normal vector of the boundary (see Fig. 2.1). The *perfect magnetic conducting* (PMC) boundary condition, also called open-circuit surface or magnetic wall, describes the fields on the *surface of a perfect insulator* $\partial\Omega_{\mathrm{pmc}}$. There, the tangential magnetic field and accordingly the normal electric field vanish

$$\mathbf{n} \times \underline{\mathbf{H}}(\mathbf{r}) = \mathbf{0} \quad \text{and} \quad \mathbf{n} \cdot \underline{\mathbf{E}}(\mathbf{r}) = 0 \quad \text{at } \partial\Omega_{\mathrm{pmc}}. \tag{2.44}$$

Evidently, the conditions for the PEC boundary are dual to those for the PMC boundary. In the general case, neither the tangential electric nor the tangential magnetic field is zero. Such a boundary is called impedance surface and can be described by the *surface impedance* $\underline{Z}_{\mathrm{S}}$ (unit: Ω)

$$\underline{Z}_{\mathrm{S}}(\mathbf{r}, t) = \frac{\|\mathbf{n} \times \underline{\mathbf{E}}(\mathbf{r}, t)\|}{\|\mathbf{n} \times \underline{\mathbf{H}}(\mathbf{r}, t)\|} = \frac{\underline{E}_{\mathrm{tang}}(\mathbf{r}, t)}{\underline{J}_{\mathrm{S}}(\mathbf{r}, t)}, \tag{2.45}$$

which is the ratio of the two tangential fields. The tangential magnetic field at the boundary is equal to the *surface current density* $\underline{\mathbf{J}}_{\mathrm{S}}(\mathbf{r}, t)$ (unit: A/m). In structures where the shape, size, and constitutive material vary periodically along one direction, called periodic structures, steady-state EM fields show a cyclic spatial behavior and may be approached by periodic boundary conditions [26, Sec. 7.4].

Figure 2.1 shows the shape of a seven-cell resonator. The inner domain of the resonator is evacuated or filled with air and is thus non-conducting and has a constant permittivity ε and permeability μ. Its walls are considered as PEC boundaries which is a reasonable approximation for materials with a high electric conductivity σ_{wall}, as it is the case for superconducting cavities and to a certain extent also for copper cavities [53]. The ports of the resonator are represented by PEC or PMC boundaries. By regarding both settings independently, i. a. the coupling to neighboring cavities or beam pipes can be estimated [15].

2.2.2   Eigenmodes

In an ideal resonator, only standing waves oscillating sinusoidally with the same frequency and a fixed phase relation satisfy Maxwell's equations because of the completely closed, lossless boundary [26, Ch. 4], [28, Ch. III]. As a consequence, the complex EM field can
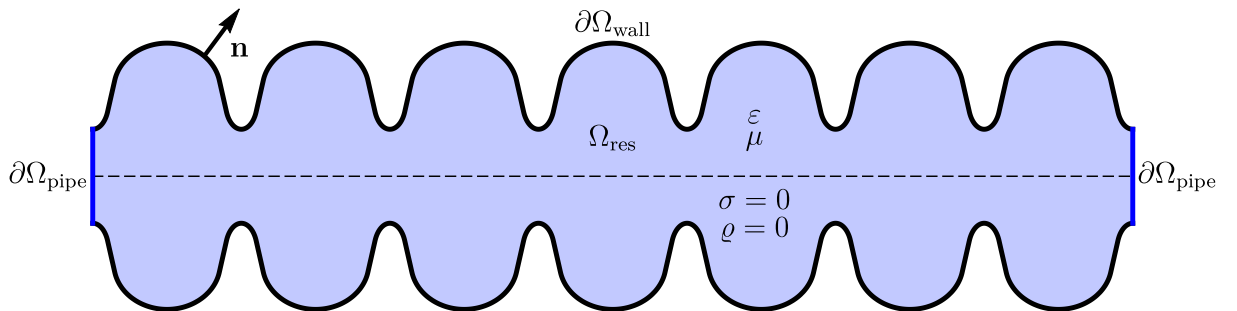
Figure 2.1: Shape of a rotationally symmetric resonator constructed of elliptical cells. The non-conducting inner domain Ω_{res} with the material parameters ε, μ, $\sigma = 0$ and $\rho = 0$ is enclosed by the boundary $\partial\Omega_{\mathrm{res}} = \partial\Omega_{\mathrm{wall}} \cup \partial\Omega_{\mathrm{pipe}}$.

be separated into a spatially dependent part, referred to as *stationary field*, and a time-independent part, referred to as *time function*. At that, the constant part of the field amplitude can be arbitrarily assigned to the spatially or the time-depending part. Within the scope of this thesis, the relation is now defined such that the spatially dependent part is a purely real-valued vector whereas the time function is a complex-valued scalar normalized to an absolute value of one, resulting in

$$\underline{\mathbf{E}}(\mathbf{r}, t) = \underbrace{e^{\jmath(\omega t + \phi_{\mathrm{e}})}}_{\underline{e}^{\mathrm{t}}(t)} \mathbf{E}(\mathbf{r}) , \qquad (2.46)$$

$$\underline{\mathbf{H}}(\mathbf{r}, t) = \underbrace{\jmath e^{\jmath(\omega t + \phi_{\mathrm{e}})}}_{\underline{h}^{\mathrm{t}}(t)} \mathbf{H}(\mathbf{r}) . \qquad (2.47)$$

The real *stationary electric field* $\mathbf{E}(\mathbf{r})$ and *stationary magnetic field* $\mathbf{H}(\mathbf{r})$ are of a physically easy to interpret form while the complex *electric time function* $\underline{e}^{\mathrm{t}}(t)$ and *magnetic time function* $\underline{h}^{\mathrm{t}}(t)$ do not affect the field magnitude by exclusively providing information about frequency and phase. Consequently, the temporal relation between electric and magnetic field is

$$\underline{h}^{\mathrm{t}}(t) = \jmath \underline{e}^{\mathrm{t}}(t) = e^{\jmath \frac{\pi}{2}} \underline{e}^{\mathrm{t}}(t) , \qquad (2.48)$$

i.e. the magnetic field has a phase advance of $\frac{\pi}{2}$ to the electric field. By applying the definitions (2.46) and (2.47) to the frequency-domain Maxwell's equations (2.18) - (2.21), the time dependences can be eliminated (see Appendix A.4.1), resulting in Maxwell's equations for a stationary EM field

$$\boldsymbol{\nabla} \cdot \mathbf{H}(\mathbf{r}) = 0, \qquad (2.49)$$
$$\boldsymbol{\nabla} \cdot \mathbf{E}(\mathbf{r}) = 0, \qquad (2.50)$$
$$\boldsymbol{\nabla} \times \mathbf{E}(\mathbf{r}) = \omega \mu \mathbf{H}(\mathbf{r}) , \qquad (2.51)$$
$$\boldsymbol{\nabla} \times \mathbf{H}(\mathbf{r}) = \omega \varepsilon \mathbf{E}(\mathbf{r}) . \qquad (2.52)$$

Equations (2.49)–(2.52) are an essential basis of the perturbative methods in this thesis. It must be pointed out that there is a sign change on the right-hand side of (2.51) compared to the original Faraday's law and that equations (2.49) – (2.52) are only valid with due regard to (2.46) and (2.47). The spatial and temporal separation of EM fields may be organized in a different way by other authors.

In an ideal resonator, the non-trivial solution of the Helmholtz equations

$$\Delta \mathbf{E}(\mathbf{r}) + k^2 \mathbf{E}(\mathbf{r}) = \mathbf{0}, \qquad (2.53)$$
$$\Delta \mathbf{H}(\mathbf{r}) + k^2 \mathbf{H}(\mathbf{r}) = \mathbf{0} \qquad (2.54)$$

is given by an infinite number of discrete real values for k. These values are called *eigenvalues* and are ordered ascendingly with respect to their magnitude as k_1, k_2, k_3, etc. For each specific eigenvalue k_i a corresponding three-dimensional vector function $\mathbf{E}_i(\mathbf{r})$ or $\mathbf{H}_i(\mathbf{r})$ exists that fulfills (2.53) or (2.54) and the related boundary conditions for the electric or magnetic field, respectively. These functions are called *eigenvectors* or eigenfunctions and represent the stationary fields corresponding to equations (2.46) and (2.47).

The electromagnetic field with the *angular eigenfrequency* $\omega_i = k_i/\sqrt{\mu\varepsilon}$, also called resonant frequency, and the field pattern $\mathbf{E}_i(\mathbf{r})$, $\mathbf{H}_i(\mathbf{r})$ is the *i*-th eigenmode or normal mode of the resonator, indicated by the *mode index i*. The eigenmode with the lowest possible eigenvalue k_1 is further denoted as *fundamental mode*. A distinct eigenvalue corresponds to exactly one eigenvector while an eigenvalue of the algebraic multiplicity $N_{k_i} > 1$ corresponds to N_{k_i} linearly independent eigenvectors. Eigenmodes with the same eigenvalue but different field patterns are called *degenerate modes*. All eigenvectors form a complete set of orthogonal basis functions, satisfying the following relations

$$\frac{\varepsilon}{2U_i} \iiint\limits_{\Omega_{\mathrm{res}}} \mathbf{E}_i(\mathbf{r}) \cdot \mathbf{E}_k(\mathbf{r}) \ \mathrm{d}V = \delta_{ik} = \begin{cases} 1 & i = k \\ 0 & i \neq k \end{cases}, \tag{2.55}$$

$$\frac{\mu}{2U_i} \iiint\limits_{\Omega_{\mathrm{res}}} \mathbf{H}_i(\mathbf{r}) \cdot \mathbf{H}_k(\mathbf{r}) \ \mathrm{d}V = \delta_{ik} = \begin{cases} 1 & i = k \\ 0 & i \neq k \end{cases}, \tag{2.56}$$

which are derived as described in Appendix A.4.4. Here, δ_{ik} denotes the *Kronecker delta*. According to (2.29), the *total electromagnetic energy of the i-th mode* U_i (unit: J) is defined as

$$U_i = \frac{\varepsilon}{2} \iiint\limits_{\Omega_{\mathrm{res}}} E_i{}^2(\mathbf{r}) \, \mathrm{d}V = \frac{\mu}{2} \iiint\limits_{\Omega_{\mathrm{res}}} H_i{}^2(\mathbf{r}) \, \mathrm{d}V. \tag{2.57}$$

By normalizing the amplitudes of $E_i(\mathbf{r})$ and $H_i(\mathbf{r})$ of each mode such that $U_i = 1\,\mathrm{J}$, the *orthogonal relations* (2.55) and (2.56) can be universalized to orthonormal ones. Based on the orthogonality relations, every continuous vector function with piecewise first and second order derivatives that satisfies the resonator boundary conditions can be expanded in an absolutely and uniformly convergent series in terms of the eigenvectors [26, Sec. 4.10]. Thus, the actual field inside the resonator may be expressed as a superposition of its eigenmodes.

In principle, there exist two independent types of solutions satisfying the Helmholtz equations (2.53) and (2.54). Firstly, *solenoidal* vector functions with

$$\boldsymbol{\nabla} \cdot \mathbf{E}(\mathbf{r}) = 0 \quad \mathrm{or} \quad \boldsymbol{\nabla} \cdot \mathbf{H}(\mathbf{r}) = 0, \tag{2.58}$$

and secondly, *irrotational* vector functions with

$$\boldsymbol{\nabla} \times \mathbf{E}(\mathbf{r}) = \mathbf{0} \quad \mathrm{or} \quad \boldsymbol{\nabla} \times \mathbf{H}(\mathbf{r}) = \mathbf{0}. \tag{2.59}$$

Thus, both the electric and the magnetic field patterns can be separated into a solenoidal and an irrotational part. However, according to the assumptions made in the scope of this thesis, solely solenoidal vector functions are relevant to the solutions discussed here since they satisfy Gauss's law for the electric and magnetic field (2.49), (2.50). Eigenmodes can further be differentiated with respect to their longitudinal field components, identified by the *longitudinal coordinate direction z*. A *transverse electric* (TE) mode has both transverse and longitudinal magnetic field components but only a transverse electric field component. Its longitudinal electric field E_z is zero. A *transverse magnetic* (TM) mode has

also both transverse and longitudinal electric field components. But in contrast, it has only a transverse magnetic field component and its longitudinal magnetic field H_z is zero. In multiply bounded resonators and waveguides with at least two separate conductors (see Fig. 2.3(b)), additionally *transverse electromagnetic* (TEM) modes can exist that have purely transverse electric and magnetic field components. TEM modes are also denoted as *principal modes*. In case of arbitrarily shaped boundaries, TE or TM modes usually cannot satisfy the boundary conditions and the modes are generally *hybrid electric and magnetic* (HEM) modes. Nevertheless, it is a common practice to refer to a HEM mode as a TE or TM mode if E_z or H_z is negligibly small or only occurs in close proximity to the boundaries. This is strictly speaking incorrect but often useful to categorize an eigenmode according to its resemblance to a true TE or TM mode of another resonator similar to the actual resonator.

In order to solve the vector Helmholtz equations, the three-dimensional vector PDEs can be reduced to three scalar PDEs based on an appropriately chosen coordinate system and by means of different approaches like the *method of Borgnis's potentials* [54], [55], the *method of Hertz's vector potentials* [55] or the *method of longitudinal components* [56]. If the boundaries of a resonator are exclusively perpendicular or parallel to the directions of a general orthogonal curvilinear coordinate system, the scalar partial differential equations can be furthermore reduced to scalar ordinary differential equations (ODEs) by applying the *method of separation of variables* [57]. Such a problem is called a *simple boundary value problem* and can be solved analytically resulting in orthogonal functions called *harmonics*. Two important simple resonator types are rectangular and cylindrical resonators, shown in Fig. 2.2. The *rectangular harmonics* and *cylindrical harmonics* describing the solution of the Helmholtz equations in Cartesian and circular-cylindrical coordinate systems, respectively, are presented in Appendix B. In case that the resonator boundaries cannot be described by an appropriate coordinate system, the boundary value problem is a complicated one. Such problems can be solved by means of approximation methods like *variational principles* [26, Sec. 4.11], [29, Sec. 5.11], [58, Ch. 2] or *field-matching tech-*

(a)   (b)
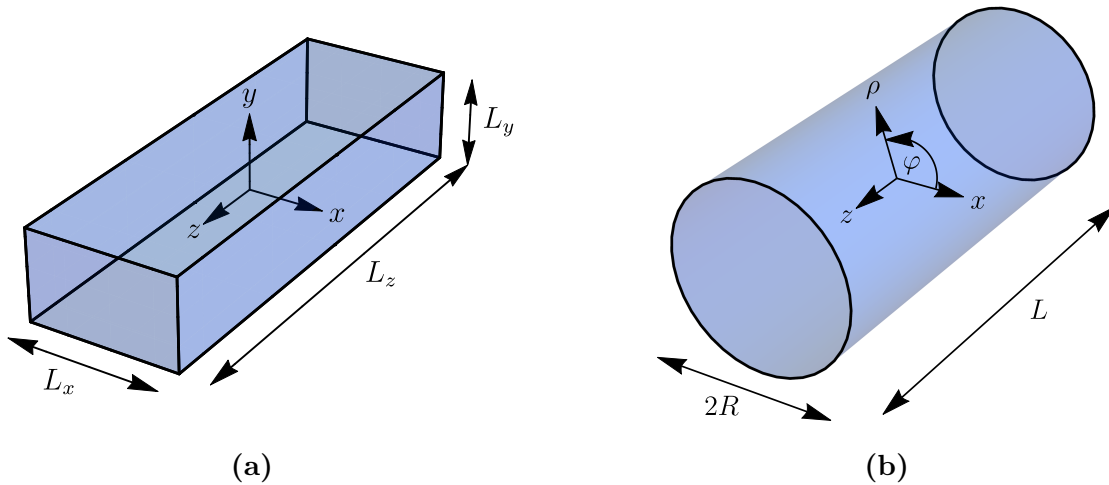
Figure 2.2: Two simple resonator types: (a) Rectangular resonator in a Cartesian coordinate system. (b) Cylindrical resonator in a circular-cylindrical coordinate system, also called pill-box resonator.

niques [26, Sec. 4.12], [59, Ch. 8] that are the basis of numerical computation techniques (see Section 2.3), or by means of perturbative methods as discussed in this thesis.

2.2.3 Two-dimensional Eigenvalue Problems

Besides longitudinally variant cavities as shown in Fig. 2.1, cavities and especially waveguides with a cross section that is uniform along the direction of particle propagation z (see Fig. 2.3) are of particular relevance for investigations of accelerating structures. For such cases, the three-dimensional eigenvalue problem can be reduced to a two-dimensional (2D) problem, as follows. By choosing a cylindrical coordinate system with the longitudinal coordinate direction z and two arbitrary orthogonal transverse coordinate directions, described by $\mathbf{r}_T$, the *Laplacian operator* Δ can be transformed into a *transverse Laplacian operator* Δ_T and the second-order partial derivatives with respect to z. The Helmholtz equations then become

$$\Delta_T \underline{\mathbf{E}}(\mathbf{r}, t) + \frac{\partial^2}{\partial z^2} \underline{\mathbf{E}}(\mathbf{r}, t) + k^2 \underline{\mathbf{E}}(\mathbf{r}, t) = \mathbf{0}, \tag{2.60}$$

$$\Delta_T \underline{\mathbf{H}}(\mathbf{r}, t) + \frac{\partial^2}{\partial z^2} \underline{\mathbf{H}}(\mathbf{r}, t) + k^2 \underline{\mathbf{H}}(\mathbf{r}, t) = \mathbf{0}. \tag{2.61}$$

In addition, every *scalar field component* $\underline{W}$ (in each spatial direction according to the determined coordinate system) of the electric and magnetic fields may be expressed as a product of scalar functions by applying the method of separation of variables

$$\underline{W}(\mathbf{r}, t) = \underline{W}_T(\mathbf{r}_T)\, \underline{W}_z(z)\, \underline{W}_t(t)\,. \tag{2.62}$$

By transforming the vector equations (2.60) and (2.61) into scalar equations for each component, applying (2.62) and eliminating the time dependences, each scalar equation can be expressed as

$$\frac{\Delta_T \underline{W}_T(\mathbf{r}_T)}{\underline{W}_T(\mathbf{r}_T)} + \frac{\frac{\partial^2}{\partial z^2} \underline{W}_z(z)}{\underline{W}_z(z)} + k^2 = 0. \tag{2.63}$$

(a)   (b)
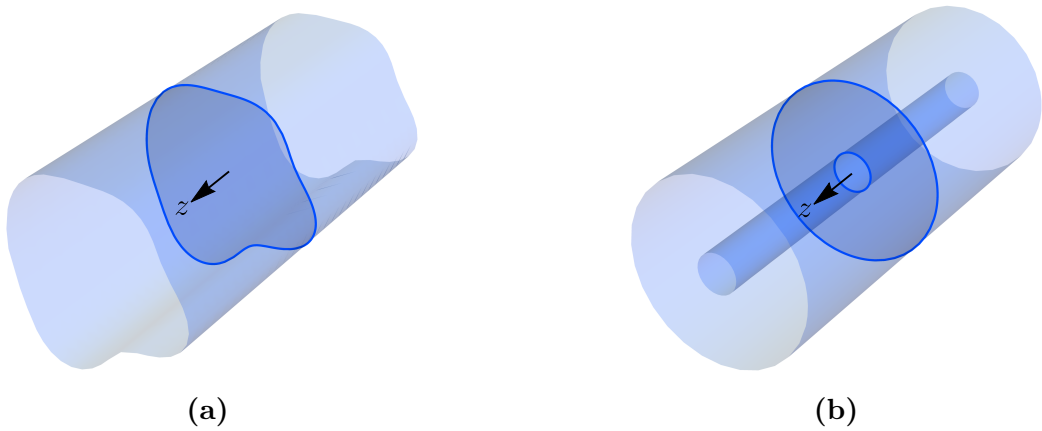
Figure 2.3: Infinitely long waveguides with a uniform cross section: (a) Waveguide with an arbitrarily shaped and simply connected cross section. (b) Double bounded coaxial waveguide.

Since k is a constant, (2.63) can be separated into two independent equations with respective to the transverse and longitudinal dependences

$$\frac{\Delta_T \underline{W}_T(\mathbf{r}_T)}{\underline{W}_T(\mathbf{r}_T)} + k_T^2 = 0 \quad \text{or} \quad \Delta_T \underline{W}_T(\mathbf{r}_T) + k_T^2 \underline{W}_T(\mathbf{r}_T) = 0, \tag{2.64}$$

$$\frac{\frac{\partial^2}{\partial z^2} \underline{W}_z(z)}{\underline{W}_z(z)} + k_z^2 = 0 \quad \text{or} \quad \frac{\partial^2}{\partial z^2} \underline{W}_z(z) + k_z^2 \underline{W}_z(z) = 0 \tag{2.65}$$

The wave number k is expressed in terms of a *transverse wave number* k_T and a *longitudinal wave number* k_z with

$$k^2 = k_T^2 + k_z^2. \tag{2.66}$$

Equation (2.64) is a two-dimensional eigenvalue problem determined by the boundaries of the cross section. The eigenvalues k_T of the corresponding 2D eigenmodes are positive real values in case of PEC and PMC boundaries like the eigenvalues of the 3D eigenmodes described in Subsection 2.2.2. Equation (2.65) is a one-dimensional (1D) eigenvalue problem with the general solution

$$\underline{W}_z(z) = \underline{W}_{z+} \mathrm{e}^{\jmath k_z z} + \underline{W}_{z-} \mathrm{e}^{-\jmath k_z z}. \tag{2.67}$$

For resonators with PEC or PMC longitudinal boundaries, the solution is restricted to real-valued sinusoidal function in the form of

$$\underline{W}_z(z) = W_{z,0} \sin\left(k_z z + \phi_{W_z}\right) \tag{2.68}$$

with discrete real values k_z. Infinitely long waveguides (see Fig. 2.3) are not bounded in longitudinal direction, consequently k_z and also k have continuous values. If $k > k_T$, the longitudinal wave number k_z is a real value as follows from (2.66) and the solution (2.67) represents undamped harmonic oscillations. Thus, eigenmodes with a real-valued k_z are traveling waves, called *propagating modes*. In contrast, eigenmodes with an imaginary k_z, called *evanescent modes*, attenuate exponentially in longitudinal direction. The critical state between propagation and attenuation is determined by the transverse wave number k_T that defines the *angular cutoff frequency* ω_{co} of a waveguide

$$\omega_{\mathrm{co}} = \frac{k_T}{\sqrt{\mu\varepsilon}}. \tag{2.69}$$

For waveguides that support TEM modes, like the coaxial line shown in Fig. 2.3(b), k_T is zero. So, modes for any frequency may propagate in them.

The concept of two-dimensional eigenmodes may not only be applied to simplify three-dimensional eigenvalue problems but is also an essential tool to describing the mode coupling at interfaces between cavities and subsequent cavities or beam pipes [26, Sec. 7.8], [60], [61]. By using the 2D eigenmodes as so-called *port modes*, the energy input or output through the ports of cavity can be considered. Furthermore, *concatenation methods* [62], [63] allow the computation of complex cavity structures by partitioning the structure into segments and concatenate the 3D eigenmodes of the segments by means of their port modes.

2.2.4   Categorization of Eigenmodes

It is often beneficial to categorize the eigenmodes of cavities according to their frequencies or according to certain characteristics of their EM fields. In the context of this thesis, this is evenly important for an efficient application of the perturbative methods (PMs). Depending on the their resonant frequency, the eigenmodes can be divided in *lower order modes* (LOMs) and *higher order modes* (HOMs). However, related to accelerating cavities the term HOM almost exclusively refers to impeding modes whose frequency is higher than the one of the accelerating mode and that can be excited by charged particles. To a certain extent, a mode may also be denoted as TE or TM-like according to its resemblance to an actual TE or TM mode. This classification indicates which are the dominant field components and thus if the mode rather can de-/accelerate or deflect particles. The modes in rotationally symmetric structures are further categorized by the sinusoidally azimuthal dependence of their fields

$$\mathbf{E}(\mathbf{r}), \mathbf{H}(\mathbf{r}) \propto \sin(m\varphi + \varphi_0) \tag{2.70}$$

by an *azimuthal index* m. The modes are accordingly denoted as *monopole* ($m = 0$), *dipole* ($m = 1$), *quadrupole* ($m = 2$) and so forth. While exclusively monopole modes are used for particle acceleration, dipole modes are especially critical for a beam deflection [2, Ch. 15]. All circularly asymmetric modes ($m \geq 1$) have a polarization degeneration [26, Sec. 5.4], i.e. each mode can exist with an arbitrary field *polarization angle* φ_0. The arbitrary orientation can be expressed as the combination of two orthogonal degenerate modes with a *polarization angle shift* $\Delta\varphi$ of

$$\Delta\varphi = \frac{\pi}{2m}. \tag{2.71}$$

Since the azimuthal dependences are analytically known, a rotationally symmetric structure constitutes a specific form of a 2D eigenvalue problem that can be solved by so-called *2.5D eigenmode solvers* like URMEL [64], URMEL-T [65], SUPERFISH [66], SuperLANS2 [67] or YACS [68]. It is also useful for the PMs to classify the modes as *even* or *odd* with regard to the symmetries of their field patterns arising from the symmetries of the resonator geometry. For simple resonator structures like rectangular or cylindrical resonators, moreover, each coordinate direction is related to a classification index (see Appendix B) determined by the number of local extrema in the respective direction.
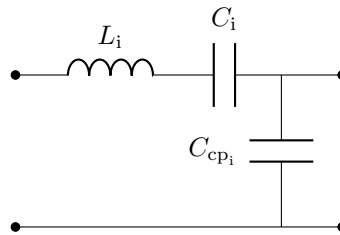
Figure 2.4: Simple electrically coupled equivalent circuit for the single cells of a multicell resonator: The i-th mode of the single-cell resonator is formed by an inductance L_i and a capacitance C_i which is coupled to the next cell by a capacitance C_{cp_i}.

State of the art cavities used for particle acceleration are almost exclusively multi-cell cavities. A multicell resonator consists of an array of N_{cell} often nearly identically shaped cells (see Fig. 2.1) that form a system of coupled oscillators. Hence, the characteristics of a multicell resonator may be described by an equivalent circuit model [2, Ch. 7], [69, Ch. 3] as the one shown in Fig. 2.4. Each eigenmode of the uncoupled single-cell resonator generates a set of N_{cell} modes in the multicell resonator within a definite frequency band, denoted as *passband*, that is close to the corresponding single-cell eigenfrequency $\omega_i = 1/\sqrt{L_i C_i}$. Consequently, each multicell mode can additionally be categorized by a *passband index* ℓ with $1 \leq \ell \leq N_{\text{cell}}$. The frequency $\omega_{i,\ell}$ of the ℓ-th passband mode based on the equivalent circuit in Fig. 2.4 is given by

$$\omega_{i,\ell} = \omega_i \sqrt{1 + 2\underbrace{\frac{C_{\text{cp}_i}}{C_i}}_{k_{\text{cp}_i}}\left(1 - \cos\left(\underbrace{\frac{\ell\pi}{N_{\text{cell}}}}_{\Omega_\ell}\right)\right)}. \tag{2.72}$$

So, the spacing between the passband frequencies increases the stronger the *cell-to-cell coupling constant* k_{cp_i} becomes. The quantity Ω_ℓ defines the *phase advance per cell* of each mode ℓ and can take values between zero and π. The characteristic phase advance is especially apparent in the relative field amplitude $A_{\ell,\nu}$ in the single cells ν

$$A_{\ell,\nu} \propto \sin\left(\ell\pi\left(\frac{2\nu - 1}{2N_{\text{cell}}}\right)\right), \tag{2.73}$$

as Fig. 2.5 illustrates for a six-cell resonator. For instance, the sign of the EM field of a π-mode inverts with each cell. For this reason, the $\text{TM}_{0,1,0_\pi}$-like mode is used for the particle acceleration. The smaller the cell-to-cell coupling k_{cp_i} of a passband is, the more similar are the field patterns in each cell to the one of the respective single-cell mode i, differing primarily in their relative amplitudes. However, the majority of the HOMs has a strong coupling, so their field patterns may significantly vary in each cell and for each passband mode, hardly resembling the single-cell pattern.
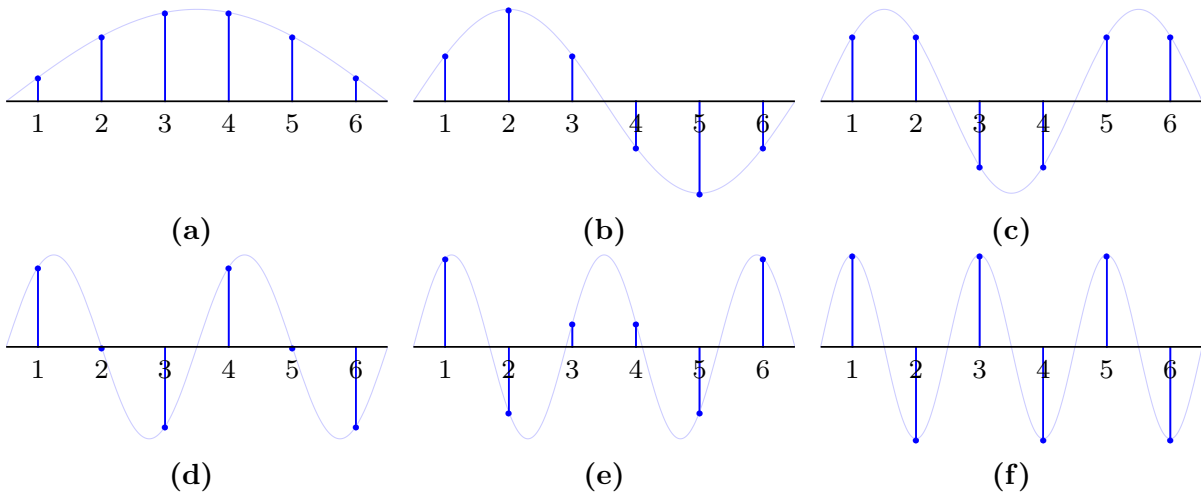
Figure 2.5: Relative amplitude $A_{\ell,\nu}$ of the EM field in each cell ν of a six-cell resonator for a passband of modes: (a) $\pi/6$-mode. (b) $\pi/3$-mode. (c) $\pi/2$-mode. (d) $2\pi/3$-mode. (e) $5\pi/6$-mode. (f) π-mode.

In the context of this thesis (see Subsection 4.4.2), a mode recognition algorithm was developed [70] to determine the modes' azimuthal index m as well as the radial and longitudinal regularities of their electric and magnetic fields. The algorithm further supports a distinction of TE and TM modes and the identification of the passband index ℓ for multicell cavities. A correct determination of the last two parameters principally depends on the complexity of the EM field patterns. Despite of these quantitative inaccuracies, the algorithm provides a suitable qualitative mode categorization.

2.3 Discrete Formulation of the Wave Equations

Analytical solutions for Maxwell's equations are only available for very simple geometries. For instance, the time-varying boundary value problems of the Helmholtz equations (2.39) and (2.40) considered in this thesis are analytically describable in terms of harmonics solely in case of simple boundary value problems as introduced in 2.2.2. For more complex geometries, an analytical solution can be found only in rare cases. With the advent of computers a large variety of numerical methods for tackling such electromagnetic problems developed, constituting the field of computational electromagnetics (CEM). These methods can treat large classes of EM problems. Several of them are presented in [71]. Most frequently used algorithms in frequency-domain are the finite element method (FEM), the boundary element method (BEM), and the finite integration technique (FIT). The BEM solely discretizes surfaces whereas FEM and FIT also discretize volumes. The majority of these numerical methods bases on a discretization of the domain, constituted by a *grid* (structured) or *mesh* (unstructured), that enables a discrete formulation of the continuous differential equations. The discretization necessarily requires a restriction to a finite domain, denoted as *solution* or *computational domain*, and the specification of proper field conditions on the domain boundary. Thereby caused discrepancies between discretized and actual boundary are referred to as *geometry error* whereas deviations arising from the approximation of the EM quantities are characterized by the *discretization error*. A *spatial discretization error* arises from an approximation of the exact spatial functions by, for instance, polynomial functions. In the context of time-domain EM problems, additionally a *temporal discretization* error is of relevance. Both spatial discretization and geometry error can be reduced by choosing a finer mesh. However, the finer the mesh, the higher the requirements regarding computing hardware and computational time. For this reason, a local mesh refinement in regions of interest or other mesh control techniques are often beneficial for the efficiency. An appropriate compromise between accuracy and computational demands can be identified by a mesh refinement study. The geometry error is additionally reducible by boundary refinement techniques like curved cells [72, Ch. 7] or partially filled mesh cells.

The finite element method is a standard method for the solution of (partial) differential equations. For the eigenmode computations in this thesis exclusively FEM-based solvers are used. Therefore, the basics of the methods are briefly outlined here using the example of the Helmholtz equation (2.39) for the electric field $\mathbf{E}(\mathbf{r}, t)$. A detailed description of the FEM fundamentals and implementational aspects are presented in [71, Ch. 6] and [73]. A major advantage of FEM is that it states a well-defined representation of the sought

function everywhere in the solution domain providing important properties concerning stability and convergence. Further, it supports the use of an unstructured mesh and curved elements allowing for an accurate and flexible discretization of complex structures. The discretization is usually done on triangular or hexahedral meshes, but a multitude of elements, for instance prisms, pyramids, or cubes for 3D, are applicable. Considering a problem in the form of

$$L[f(\mathbf{r})] = s \qquad \text{in } \Omega_{\text{com}} \tag{2.74}$$

with a linear operator L, the source s and the *sought function* $f(\mathbf{r})$ (scalar or vector) whose boundaries may be defined by a Dirichlet boundary condition

$$f(\mathbf{r}) = p \qquad \text{at } \partial\Omega_{\text{com1}}, \tag{2.75}$$

a Neumann boundary condition

$$f'(\mathbf{r}) = q \quad \text{at } \partial\Omega_{\text{com2}}, \tag{2.76}$$

or a Robin boundary condition

$$f'(\mathbf{r}) + \zeta f(\mathbf{r}) = q \quad \text{at } \partial\Omega_{\text{com3}}, \tag{2.77}$$

at first the solution domain Ω_{com} is subdivided into N_{mc} elements (mesh cells). The solution of $f(\mathbf{r})$ is then approximated by an expansion in terms of a finite number N_{b} of so-called *basis functions* $\psi_\nu(\mathbf{r})$

$$f(\mathbf{r}) = \sum_{\nu=1}^{N_{\text{b}}} c_\nu \psi_\nu(\mathbf{r}) \tag{2.78}$$

with the *basis function coefficients* c_ν. These basis functions are usually low order polynomials. After discretizing the solution domain and choosing appropriate $\psi_\nu(\mathbf{r})$, the *residual* r of the solution which defines the quality of the numerical solution (2.78)

$$r = L[f(\mathbf{r})] - s \tag{2.79}$$

is formed in order to minimize it. In general, it is not expedient to seek for a pointwise converging residual $r = 0$ since this may be a very complex task often leading to non-smooth solutions. Instead, a weighted residual is required to be zero which is formed based on a *variational (weak) formulation* of the governing equation (2.74)

$$\int_{\Omega_{\text{com}}} w_v(\mathbf{r}) \cdot L[f(\mathbf{r})] \, \mathrm{d}\Omega = \int_{\Omega_{\text{com}}} w_v(\mathbf{r}) \cdot s \, \mathrm{d}\Omega \qquad \forall \, w_v(\mathbf{r}) \,. \tag{2.80}$$

It is obtained by multiplying (2.74) by a *test function* $w_v(\mathbf{r})$ and integrating the term over the entire solution domain Ω_{com}. Setting the weighted residual to zero results in a sparse linear system of equations for which the unknowns c_ν are then determined.

Generally, each basis function $\psi_\nu(\mathbf{r})$ has non-zero values only in a few adjacent elements or even just one element. So, a *finite element* not only refers to a geometric element

but also to a local polynomial space defined in the element and a set of degrees of freedom (DOFs) defined on this space, conditioning the basis functions. Depending on the governing equation (2.74), boundary conditions (2.75) – (2.77) and involved quantities there are different types of basis functions and accordingly also different types of finite elements [73, Ch. 3] to provide a most suitable solution. At this, the DOFs of a finite element are determined by the spatial dimensions of the geometric element and the *polynomial order o* of its basis functions. *Nodal elements*, also denoted as Lagrange elements, are H^1-conforming elements commonly used in the context of scalar functions. A nodal basis function $\psi_\nu(\mathbf{r})$ is associated with a single node ν where $\psi_\nu(\mathbf{r})$ has a value of one whereas it is zero at all other nodes. For a linear Lagrange element ($o = 1$), involving so-called tent functions, the nodes are identical to its vertices, as Fig. 2.6 illustrates. For higher order polynomials, additional nodes are allocated along the edges, facets or inside the element matching the number of DOFs. Theoretically, nodal elements can also be applied to vector quantities by expressing each vector component separately in nodal basis functions. Hence, they could be used for solving the Helmholtz equations. However, this may cause non-physical solutions in the form of spurious modes [71, Sec. 6.5]. Curl-
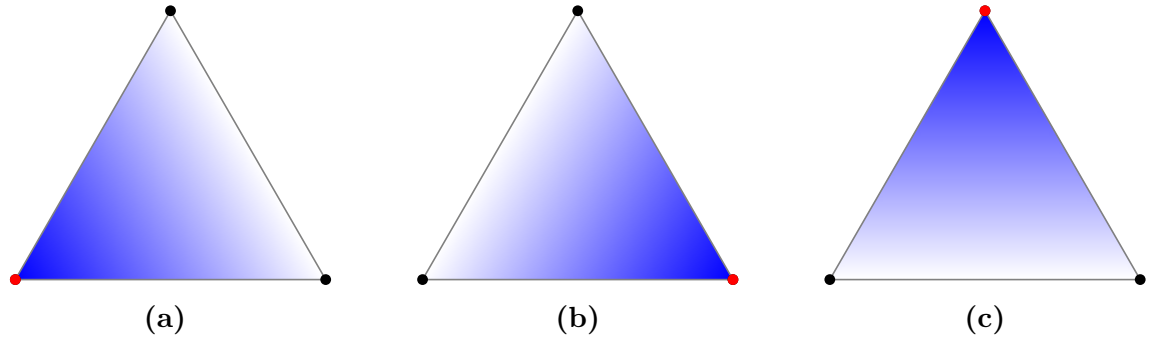
Figure 2.6: 2D triangle Lagrange H^1 element: The element vertices are displayed in black, its edges in gray. (a) – (c) The linear local scalar basis functions $\psi_\nu(\mathbf{r})$ ($o = 1$) are displayed in blue (value range: $0 =$ white to $1 =$ saturated) and associated to the respective nodal DOF (red).
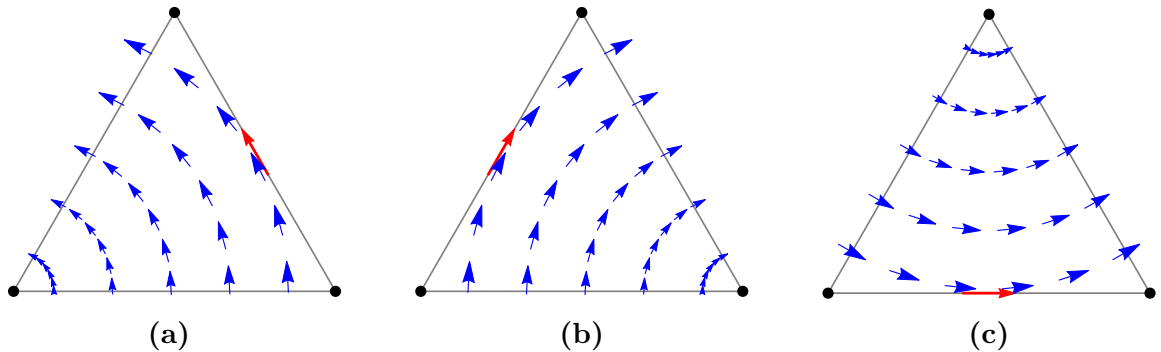
Figure 2.7: 2D triangle Nédélec H(curl) element of the first kind: The element vertices are displayed in black, its edges in gray. (a) – (c) The linear local vector basis functions $\boldsymbol{\psi}_\nu(\mathbf{r})$ ($o = 1$) are displayed in blue and associated to the respective DOF (red) on the edges' midpoints.

conforming elements, also referred to as *edge elements*, are considerably more suited for such problems. Their vector basis functions $\boldsymbol{\psi}_\nu$ are defined in such a way that they have continuous tangential components at the element edges while their normal components are allowed to be discontinuous. The DOFs of an edge element are thus associated with its edges. Figure 2.7 exemplarily shows a linear Nédélec element of the first kind for which the DOFs are defined by the tangential vector components at the midpoints of the edges. An additional advantage of edge elements is that they usually require substantially less DOFs for expanding a vector field than nodal elements. In order to apply edge elements to the Helmholtz equation (2.39) the Curl-Curl equation for $\mathbf{E}(\mathbf{r})$ is set as governing equation (2.74)

$$\boldsymbol{\nabla} \times \boldsymbol{\nabla} \times \mathbf{E}(\mathbf{r}) - k^2 \mathbf{E}(\mathbf{r}) = \mathbf{0} \quad \text{in } \Omega_{\text{com}} \tag{2.81}$$

instead of (2.39). The boundary conditions are accordingly given by

$$\mathbf{n} \times \mathbf{E}(\mathbf{r}) = \mathbf{0} \quad \text{at } \partial\Omega_{\text{com,pec}}, \tag{2.82}$$

$$\mathbf{n} \times \big(\boldsymbol{\nabla} \times \mathbf{E}(\mathbf{r})\big) = \mathbf{0} \quad \text{at } \partial\Omega_{\text{com,pmc}}. \tag{2.83}$$

The electric field $\mathbf{E}(\mathbf{r})$ is expanded in terms of vectorial edge basis functions $\boldsymbol{\psi}_\nu(\mathbf{r})$

$$\mathbf{E}(\mathbf{r}) = \sum_{\nu=1}^{N_{\text{b}}} c_\nu \boldsymbol{\psi}_\nu(\mathbf{r}) \tag{2.84}$$

and the weak formulation of (2.81) is also formed based on vector test functions $\mathbf{w}_v(\mathbf{r})$

$$\int_{\Omega_{\text{com}}} \mathbf{w}_v(\mathbf{r}) \cdot \big(\boldsymbol{\nabla} \times \boldsymbol{\nabla} \times \mathbf{E}(\mathbf{r})\big) \, \mathrm{d}\Omega = k^2 \int_{\Omega_{\text{com}}} \mathbf{w}_v(\mathbf{r}) \cdot \mathbf{E}(\mathbf{r}) \, \mathrm{d}\Omega. \tag{2.85}$$

The resulting equation (2.85) is transformed by applying the vector identity (A.7) and the divergence theorem (A.3) to its left-hand side

$$\int_{\Omega_{\text{com}}} \big(\boldsymbol{\nabla} \times \mathbf{w}_v(\mathbf{r})\big) \cdot \big(\boldsymbol{\nabla} \times \mathbf{E}(\mathbf{r})\big) \, \mathrm{d}\Omega - \oint_{\partial\Omega_{\text{com}}} \mathbf{w}_v(\mathbf{r}) \times \big(\boldsymbol{\nabla} \times \mathbf{E}(\mathbf{r})\big) \cdot \mathbf{n} \, \mathrm{d}\Gamma = k^2 \int_{\Omega_{\text{com}}} \mathbf{w}_v(\mathbf{r}) \cdot \mathbf{E}(\mathbf{r}) \, \mathrm{d}\Omega. \tag{2.86}$$

Here, the integration is partially expressed by an integral over the boundary $\partial\Omega_{\text{com}}$ of the solution domain. Separating the closed boundary integral over $\partial\Omega_{\text{com}}$ in (2.86) with respect to the PEC and PMC boundaries and applying further the vector formula (A.5), the integral can be written as

$$\oint_{\partial\Omega_{\text{com}}} \mathbf{w}_v(\mathbf{r}) \times \big(\boldsymbol{\nabla} \times \mathbf{E}(\mathbf{r})\big) \cdot \mathbf{n} \, \mathrm{d}\Gamma =$$

$$\int_{\partial\Omega_{\text{com,pec}}} \big(\mathbf{n} \times \mathbf{w}_v(\mathbf{r})\big) \cdot \big(\boldsymbol{\nabla} \times \mathbf{E}(\mathbf{r})\big) \, \mathrm{d}\Gamma + \int_{\partial\Omega_{\text{com,pmc}}} \big(\big(\boldsymbol{\nabla} \times \mathbf{E}(\mathbf{r})\big) \times \mathbf{n}\big) \cdot \mathbf{w}_v(\mathbf{r}) \, \mathrm{d}\Gamma. \tag{2.87}$$

The test functions are required to vanish on the parts of the boundary where the sought quantity is known, i.e. at Dirichlet boundaries. Hence, the tangential components of the $\mathbf{w}_\upsilon(\mathbf{r})$ have to vanish at the PEC surface in accordance with (2.82)

$$\mathbf{n} \times \mathbf{w}_\upsilon(\mathbf{r}) = \mathbf{0} \quad \text{at } \partial\Omega_{\text{com,pec}}. \tag{2.88}$$

This is guaranteed by setting the basis coefficients c_υ of involved boundary edges to zero. So, the Dirichlet boundary conditions (2.82) eliminate unknowns (DOFs) in the weak formulation whereas Neumann boundary conditions (2.83) or Robin boundary conditions maintain DOFs. For the particular case of an ideal resonator regarded here, the contribution of the curl of $\mathbf{E}(\mathbf{r})$ to (2.87) also vanishes at the PMC boundary since the Neumann condition (2.83) is homogeneous. Consequently, (2.87) is zero and (2.86) reduces to

$$\int\limits_{\Omega_{\text{com}}} \left(\boldsymbol{\nabla} \times \mathbf{w}_\upsilon(\mathbf{r})\right) \cdot \left(\boldsymbol{\nabla} \times \mathbf{E}(\mathbf{r})\right) \, \mathrm{d}\Omega = k^2 \int\limits_{\Omega_{\text{com}}} \mathbf{w}_\upsilon(\mathbf{r}) \cdot \mathbf{E}(\mathbf{r}) \, \mathrm{d}\Omega, \tag{2.89}$$

stating the weak formulation of (2.81). Substituting the basis function expansion (2.84) into the weak form (2.89) yields the linear system of equations

$$\sum_{\nu=1}^{N_{\text{b}}} c_\nu \underbrace{\int\limits_{\Omega_{\text{com}}} \left(\boldsymbol{\nabla} \times \mathbf{w}_\upsilon(\mathbf{r})\right) \cdot \left(\boldsymbol{\nabla} \times \boldsymbol{\psi}_\nu(\mathbf{r})\right) \, \mathrm{d}\Omega}_{\check{s}_{\upsilon\nu}} = k^2 \sum_{\nu=1}^{N_{\text{b}}} c_\nu \underbrace{\int\limits_{\Omega_{\text{com}}} \mathbf{w}_\upsilon(\mathbf{r}) \cdot \boldsymbol{\psi}_\nu(\mathbf{r}) \, \mathrm{d}\Omega}_{\check{m}_{\upsilon\nu}} \tag{2.90}$$

that constitutes a generalized linear eigenvalue problem with the matrix representation

$$\check{\mathbf{S}} \cdot \mathbf{c} = k^2 \, \check{\mathbf{M}} \cdot \mathbf{c}. \tag{2.91}$$

The matrix $\check{\mathbf{S}}$ is often referred to as *stiffness matrix* and $\check{\mathbf{M}}$ as *mass matrix*. Their coefficients $\check{s}_{\upsilon\nu}$ and $\check{m}_{\upsilon\nu}$ are determined by element-wise integration of the basis and test functions. Each eigenvalue of (2.91) yields the squared wave number k_i^2 of an eigenmode while the eigenvector $\mathbf{c}_i$ provides the expansion coefficients for the respective electric field pattern. The choice of the test functions $\mathbf{w}_\upsilon(\mathbf{r})$ for the weighting residual must fit the stated problem and the type of used finite elements. The most common weighted residual method is *Galerkin's method* where the test functions are chosen identical to the basis functions

$$\mathbf{w}_\upsilon(\mathbf{r}) = \boldsymbol{\psi}_\upsilon(\mathbf{r}), \tag{2.92}$$

so they have the same function space ensuring a minimal steady-state error [74, Sec. 4.3]. Additionally, Galerkin's method results in symmetric matrices $\check{\mathbf{S}}$ and $\check{\mathbf{M}}$ which facilitates the solving of (2.91). Due to the locality of the basis functions, the matrices are generally sparse. For 3D applications, the number of DOFs can be in the range of tens of thousands to several millions. Iterative solvers or multigrid methods are therefore most appropriate to solve the linear system of equations of large sparse matrices [71, Ch. 8].

2.4 Electromagnetic Cavity Characteristics

This section introduces the most important EM figures of merit [2, Ch. 2] to assess the effectiveness of a cavity in accelerating particles and its operation stability. Such characteristics allow for a comparison of different cavity geometries and a definition of optimization target parameters as well as maximally acceptable parameter tolerances in the cavity design process.

2.4.1 Accelerating Voltage, Peak Surface Fields and Field Flatness

According to the Lorentz force (2.14), charged particles traveling with the velocity $\mathbf{v}$ can only be supplied with energy without changing the direction of their motion by an electric field in $\mathbf{v}$-direction. For this reason, the $\mathrm{TM}_{0,1,0_\pi}$ mode is generally used for acceleration since it provides a maximal axial longitudinal electric field E_z. Its frequency ω_{acc} is synchronized to the transit time that a particle requires to traverse one cell with the length L_{cell} to guarantee that the field orientation changes exactly when the particle enters the next cell. The *accelerating voltage* V_{acc} (unit: V) defines the maximal energy that a particle gains during a transit normalized to its charge q

$$V_{\mathrm{acc}} = \left| \int_0^{L_{\mathrm{cell}}} E_z\big(0,0,z\big)\mathrm{e}^{\jmath\omega_{\mathrm{acc}}z/v}\,\mathrm{d}z \right| . \tag{2.93}$$

Often the *average accelerating electric field* E_{acc}, also known as the accelerating gradient,

$$E_{\mathrm{acc}} = \frac{V_{\mathrm{acc}}}{L_{\mathrm{cell}}} \tag{2.94}$$

is quoted instead of V_{acc}. A high gradient is desirable for an effective acceleration. However, the achievable gradient is limited by the maximally maintainable surface fields which are proportional to E_{acc}. The *peak surface magnetic field* $H_{\mathrm{peak,sf}}$ must be kept below the *RF critical magnetic field* $H_{\mathrm{crit,rf}}$ in SC cavities. Exceeding the critical value $H_{\mathrm{crit,rf}}$ may cause a thermal breakdown of the superconductivity [2, Ch. 11], known as *quench*, resulting in a severe chain reaction due to rapid Joule heating. The *peak surface electric field* $E_{\mathrm{peak,sf}}$ is restricted by the risk of field emission in wall regions of high electric field strength. Emitted electrons can lead to secondary electron emission entailing a resonant process, denoted as *multipacting* [2, Ch. 10], at that a large number of electrons builds up. The electrons not only absorb the RF power making it impossible to increase the cavity fields, but also create a large temperature rise when they hit the wall, potentially causing a thermal breakdown. For state of the art high-beta cavity structures, multipacting can generally be avoided by convenient cavity shapes and thus is primarily an issue for low-beta structures. In order to maximize the accelerating field E_{acc} it is essential to minimize the ratios $E_{\mathrm{peak,sf}}/E_{\mathrm{acc}}$, $H_{\mathrm{peak,sf}}/E_{\mathrm{acc}}$ by a suitable cavity shape.

In addition to a phase shift of π during the transit of one cell, the accelerating mode of a multicell cavity shall also provide an equal and thereby maximal acceleration in each cell

[2, Ch. 7]. This can be achieved by equalizing the maximal axial electric fields $E_{\text{peak,ax}_\nu}$ in all cells by a proper cell-to-cell and end-cell tuning, generating a so-called *flat* field. A flat field has further the advantage that it minimizes the peak surface fields. The amplitude matching can be measured by the *field flatness* η_{ff} (dimensionless) [17] which shall ideally reach $100\,\%$

$$\eta_{\text{ff}} = \left(1 - \frac{\max\limits_{\nu=1}^{N_{\text{cell}}}(E_{\text{peak,ax}_\nu}) - \min\limits_{\nu=1}^{N_{\text{cell}}}(E_{\text{peak,ax}_\nu})}{\dfrac{1}{N_{\text{cell}}} \sum\limits_{\nu=1}^{N_{\text{cell}}}(E_{\text{peak,ax}_\nu})} \right) \cdot 100\%. \tag{2.95}$$

2.4.2 Energy Dissipation and Quality Factors

In contrast to ideal resonators, real cavity structures are subject to different forms of energy dissipation. The finite conductivity of the cavity walls causes Joule losses by a current flow, even for SC cavities. The *wall power dissipation* P_{wall_i} (unit: W) of a mode i is described by the *surface resistance* R_{S} (unit: Ω) and the magnetic field inside the wall

$$P_{\text{wall}_i} = \frac{1}{2} \oiint\limits_{\partial\Omega_{\text{res}}} R_{\text{S}} \left| \mathbf{H}_i \right|^2 \mathrm{d}A. \tag{2.96}$$

In general, the finite conductivity creates non-orthogonal modes with both electric and magnetic tangential surface components, requiring to solve a complex-valued eigenvalue problem. However, since the surface resistance is relatively small for both SC (tens of $n\Omega$) and NC cavities ($m\Omega$), the wall losses P_{wall_i} can be determined in a very good approximation from the lossless eigenmode's surface field $\mathbf{H}_{i_{\text{sf}}}$. At this, the surface resistance R_{S} is characterized by the skin effect (skin depth) for NC and by the BCS theory or the London equations (London penetration depth) for SC cavities [2, Ch. 3-4], [58, Sec. 6.14]. The *unloaded quality factor* Q_{0_i} (dimensionless), also referred to as intrinsic quality factor, defines how many oscillation cycles it takes to dissipate the energy U_i stored in the mode

$$Q_{0_i} = \frac{\omega_i U_i}{P_{\text{wall}_i}} \tag{2.97}$$

if no further energy is supplied and the field decays exponentially. The higher the quality factor, the less energy is dissipated and the longer energy is preserved in the cavity. Supposing a constant R_{S}, Q_{0_i} is frequently expressed as

$$Q_{0_i} = \frac{1}{R_{\text{S}}} \underbrace{\frac{\omega_i \mu \iiint\limits_{\Omega_{\text{res}}} \left| \mathbf{H}_i \right|^2 \mathrm{d}V}{\oiint\limits_{\partial\Omega_{\text{res}}} \left| \mathbf{H}_i \right|^2 \mathrm{d}A}}_{G_i} \tag{2.98}$$

with the *geometry constant* G_i which is independent of the cavity size and thus allows to compare different cavity shapes. Due to the high cavity wall conductivity, a multitude

of perturbative techniques for determining the non-orthogonal lossy eigenmodes or their characteristics based on the orthogonal modes of the respective ideal resonator can be applied. Modal approaches [15], [28, Sec. III.3-4], [29, Sec. 5.10] not only allow to determine wall power losses but further characteristics such as the *lossy eigenfrequency* $\underline{\omega}_i$

$$\underline{\omega}_i = \omega_i \left(\sqrt{1 - \left(\frac{1}{2Q_{0_i}} \right)^2} + j\frac{1}{2Q_{0_i}} \right). \tag{2.99}$$

Two other examples are given by a technique to calculate the EM field propagation in waveguides with wall losses [52] and a variational method for the coupling of non-orthogonal modes in lossy waveguides and cavities [29, Sec. 5.3], [75].

The *loaded quality factor* Q_{L_i} describes the total power dissipation P_{tot_i} during the cavity operation

$$\frac{1}{Q_{\mathrm{L}_i}} = \frac{P_{\mathrm{tot}_i}}{\omega_i U_i} \approx \frac{1}{Q_{0_i}} + \frac{1}{Q_{\mathrm{ext}_i}} \tag{2.100}$$

including also the *external power losses* P_{ext_i} through ports like power couplers, HOM couplers or beam pipes by means of the *external quality factor* Q_{ext_i}

$$Q_{\mathrm{ext}_i} = \frac{\omega_i U_i}{P_{\mathrm{ext}_i}}. \tag{2.101}$$

The loaded cavity thus has a lower quality factor Q_{L_i} than the unloaded one. The external energy losses may likewise be determined by modal approaches [15], [28, Sec. III.5], [51]. Taking additionally the external losses into account, the lossy eigenfrequency $\underline{\omega}_i$ can also be defined based on the loaded quality factor Q_{L_i} as per (2.99). In general, the effects of energy transfer can be considered by describing the complete system of RF generator, cavity, couplers and other involved components by equivalent circuit models [69, Ch. 5]. A beam-induced power extraction is usually not regarded for Q_{L_i}, as in [2, Ch. 8], [69, Ch. 5], since the interaction between beam and EM fields induces a mutual energy transfer involving complex dynamic processes. Such processes like wakefield effects [2, Ch. 15], [7], [69, Ch. 11] or beam loading [2, Ch. 17], [69, Ch. 10] are not be discussed in this context.

2.4.3 Shunt Impedance

Optimally the accelerating mode shall provide a high acceleration, i.e. a maximal energy gain at minimal losses. The effectiveness of generating an axial accelerating field for a given ohmic power dissipation is determineed by the *shunt impedance* R_{sh_i} (unit: Ω) of a mode. Depending on the field of application, there are different definitions of R_{sh_i}. The accelerator definition is

$$R_{\mathrm{sh}_i} = \frac{V_{\mathrm{acc}_i}^2}{P_{\mathrm{wall}_i}}. \tag{2.102}$$

At this, V_{acc_i} is the accelerating voltage of the *i*-th mode as per (2.93). For long cavities, often the *effective shunt impedance* r_{sh_i} per unit length is a more suitable figure

$$r_{\mathrm{sh}_i} = \frac{V_{\mathrm{acc}_i}^2}{P'_{\mathrm{wall}_i}}, \tag{2.103}$$

where P'_{wall_i} defines the wall power losses per unit length. Especially NC cavities require a high R_{sh_i} for the accelerating mode since the minimization of wall power losses is a major concern. The ratio of the shunt impedance over the unloaded quality factor R_{sh_i}/Q_{0_i}, referred to as *R-over-Q*, defines a wall loss-independent measure of the acceleration efficiency with respect to the mode's stored energy and frequency

$$R_{\text{sh}_i}/Q_{0_i} = \frac{V_{\text{acc}_i}^2}{\omega_i U_i}. \tag{2.104}$$

R-over-Q characterizes the level of excitation of a mode i by the charged particles traversing the cavity and hence the level of beam-mode interaction. In literature [2, Ch. 2], [11, Ch. 15], the shunt impedance and R-over-Q are generally related to the cavity wall losses P_{wall_i}. However, it can also be expedient to define the quantities with respect to the total power dissipation P_{tot_i}. Since R-over-Q is loss-independent, it is not affected by the choice of losses. Therefore, R-over-Q is often a more suitable figure of merit than the shunt impedance. Additionally, it is independent of the cavity size and thus suitable for comparing different designs.

In contrast to the accelerating mode, for which a maximal $R_{\text{sh}_{\text{acc}}}$ and $R_{\text{sh}_{\text{acc}}}/Q_{0_{\text{acc}}}$ is desired, the R_{sh_i} and R_{sh_i}/Q_{0_i} values of HOMs shall be as low as possible to minimize the excitation of impeding wakefields. The quantity R_{sh_i} as per (2.102) exclusively refers to the on-axis longitudinal shunt impedance describing the de-/acceleration of particles by cavity monopole modes. If the beam is off-axis, the particles additionally excite transverse wakefields which in turn may deflect following particles possibly causing BBU instabilities. A more general definition of the *longitudinal accelerating voltage* $V_{\parallel_i}$ and the *transverse accelerating voltage* $V_{\perp_i}$ for a particle moving parallel but at a displacement (ρ_0, φ_0) to the axis is given by [9, Ch. 2]

$$V_{\parallel_i} = \left| \int_0^{L_{\text{cell}}} E_{i,z}(\rho_0, \varphi_0, z) e^{\jmath \omega_i z/v} \, \mathrm{d}z \right|, \tag{2.105}$$

$$V_{\perp_i} = \left| \int_0^{L_{\text{cell}}} \left(\mathbf{E}_{i,T}(\rho_0, \varphi_0, z) + \mu v (\mathbf{n}_z \times \mathbf{H}_i(\rho_0, \varphi_0, z)) \right) e^{\jmath \omega_i z/v} \, \mathrm{d}z \right|. \tag{2.106}$$

Here, $E_{i,z}$ describes the longitudinal and $\mathbf{E}_{i,T}$ the transverse electric field of the i-th mode. The corresponding off-axis *longitudinal shunt impedance* $R_{\parallel_i}$ and *transverse shunt impedance* $R_{\perp_i}$ are

$$R_{\parallel_i} = \frac{V_{\parallel_i}^2}{P_{\text{wall}_i}}, \tag{2.107}$$

$$R_{\perp_i} = \frac{V_{\perp_i}^2}{P_{\text{wall}_i}}. \tag{2.108}$$

The resulting R-over-Q values $R_{\parallel_i}/Q_{0_i}$ and $R_{\perp_i}/Q_{0_i}$ indicate the respective level of off-axis mode excitation.

Chapter 3

Perturbative Methods for Eigenmode Computation

A widely used practice within the scope of analyzing accelerating cavities is to express the electromagnetic field and related quantities inside a resonator as a sum of orthogonal normal modes. The concept of a normal mode expansion may not only be used to expand the field inside a resonator but also to express the field inside a cavity with ports involving an energy transfer. This chapter focuses on the specific application of normal mode expansion to resonator eigenmodes subject to geometric perturbations. At this, exclusively resonators with PEC and/or PMC walls filled with linear, homogeneous, time-invariant, isotropic, charge-free and source-free media are approached. The fundamental idea of the here presented perturbative methods (PMs) is to expand the eigenmodes inside a deformed resonator, denoted as the *perturbed* resonator, in terms of a series of known eigenmodes of an initial non-deformed resonator, denoted as the *unperturbed* resonator. In the following, a detailed derivation of three different PMs is presented: Slater's theorem (ST), the generalization of Slater's theorem (GST) and the expansion of a reduced eigenmode set (ERES).

3.1   Preliminary Considerations

This section gives a brief explanation of the fundamentals of normal mode expansion [28, Sec. III.2], [76] followed by a description of necessary definitions and relations concerning the unperturbed and perturbed quantities.

3.1.1   Series Expansion in Terms of Normal Modes

Any divergence-free, continuous vector field inside a resonator with PEC or PMC boundaries may be reproduced as a sum of the normal modes that were introduced in Subsection 2.2.2. Thus, the complete electromagnetic field inside the resonator can be defined

as

$$\underline{\mathbf{E}}(\mathbf{r}, t) = \sum_{k=1}^{\infty} \underline{e}_k(t)\, \mathbf{E}_k(\mathbf{r}), \tag{3.1}$$

$$\underline{\mathbf{H}}(\mathbf{r}, t) = \sum_{k=1}^{\infty} \underline{h}_k(t)\, \mathbf{H}_k(\mathbf{r}) \tag{3.2}$$

with the complex-valued, purely time-depending functions $\underline{e}_k(t)$, $\underline{h}_k(t)$ and the real-valued, purely space-depending stationary fields $\mathbf{E}_k(\mathbf{r})$, $\mathbf{H}_k(\mathbf{r})$. Accordingly, Maxwell's equations in the form of (2.48) – (2.52) are valid. The functions $\underline{e}_k(t)$, $\underline{h}_k(t)$ comprise not only the harmonic time evolution of the normal modes but also their expansion coefficients, represented by the amplitudes $\underline{e}_k(0)$, $\underline{h}_k(0)$

$$\underline{e}_k(t) = \underline{e}_k(0)\, \mathrm{e}^{\jmath \omega_k t}, \tag{3.3}$$

$$\underline{h}_k(t) = \underline{h}_k(0)\, \jmath \mathrm{e}^{\jmath \omega_k t}. \tag{3.4}$$

Knowing the fields $\underline{\mathbf{E}}(\mathbf{r}, t)$ and $\underline{\mathbf{H}}(\mathbf{r}, t)$, the *expansion functions* $\underline{e}_i(t)$, $\underline{h}_i(t)$ of each normal mode i can inversely be deduced on account of the orthogonality relations (2.55) and (2.56). By multiplying $\underline{\mathbf{E}}(\mathbf{r}, t)$ in (3.1) with the i-th stationary electric field $\mathbf{E}_i(\mathbf{r})$ and integrating the term over the complete resonator volume Ω_{res}

$$\iiint\limits_{\Omega_{\mathrm{res}}} \underline{\mathbf{E}}(\mathbf{r}, t) \cdot \mathbf{E}_i(\mathbf{r})\, \mathrm{d}V = \sum_{k=1}^{\infty} \underline{e}_k(t) \iiint\limits_{\Omega_{\mathrm{res}}} \mathbf{E}_k(\mathbf{r}) \cdot \mathbf{E}_i(\mathbf{r})\, \mathrm{d}V, \tag{3.5}$$

all sum terms except for the one with $i = k$ vanish according to (2.55), resulting in

$$\underline{e}_i(t) = \frac{\varepsilon}{2U_i} \iiint\limits_{\Omega_{\mathrm{res}}} \underline{\mathbf{E}}(\mathbf{r}, t) \cdot \mathbf{E}_i(\mathbf{r})\, \mathrm{d}V. \tag{3.6}$$

The magnetic expansion functions may likewise be determined from (3.2) and (2.56)

$$\underline{h}_i(t) = \frac{\mu}{2U_i} \iiint\limits_{\Omega_{\mathrm{res}}} \underline{\mathbf{H}}(\mathbf{r}, t) \cdot \mathbf{H}_i(\mathbf{r})\, \mathrm{d}V. \tag{3.7}$$

It also follows that knowing the complete fields $\underline{\mathbf{E}}(\mathbf{r}, 0)$ and $\underline{\mathbf{H}}(\mathbf{r}, 0)$ at $t = 0$ immediately yields the coefficients $\underline{e}_k(0)$ and $\underline{h}_k(0)$.

In the context of infinite series expansions, an important property considering the curl of the fields $\underline{\mathbf{E}}(\mathbf{r}, t)$ and $\underline{\mathbf{H}}(\mathbf{r}, t)$ has to be explained. At first sight, it might appear that $\boldsymbol{\nabla} \times \underline{\mathbf{E}}(\mathbf{r}, t)$ can directly be deduced from the series expansion (3.1). However, the curl of the infinite expansion is not equal to the infinite expansion of the curl, as shall be proven. Deriving $\boldsymbol{\nabla} \times \underline{\mathbf{E}}(\mathbf{r}, t)$ regularly from the complete magnetic field $\underline{\mathbf{H}}(\mathbf{r}, t)$ according to Faraday's law (2.7) and only then applying the series expansion (3.2) with the coefficients (3.7) to $\underline{\mathbf{H}}(\mathbf{r}, t)$ yields the expression

$$\boldsymbol{\nabla} \times \underline{\mathbf{E}}(\mathbf{r}, t) = -\mu \frac{\partial}{\partial t} \underline{\mathbf{H}}(\mathbf{r}, t)$$

$$\boldsymbol{\nabla} \times \underline{\mathbf{E}}(\mathbf{r}, t) = -\mu \frac{\partial}{\partial t} \sum_{k=1}^{\infty} \left(\mathbf{H}_k(\mathbf{r}) \frac{\mu}{2U_k} \iiint\limits_{\Omega_{\mathrm{res}}} \underline{\mathbf{H}}(\mathbf{r}, t) \cdot \mathbf{H}_k(\mathbf{r})\, \mathrm{d}V \right). \tag{3.8}$$

Here, the time derivative applies only to $\underline{\mathbf{H}}(\mathbf{r}, t)$ reintroducing $\boldsymbol{\nabla} \times \underline{\mathbf{E}}(\mathbf{r}, t)$

$$\boldsymbol{\nabla} \times \underline{\mathbf{E}}(\mathbf{r}, t) = \sum_{k=1}^{\infty} \left(\frac{\mu}{2U_k} \mathbf{H}_k(\mathbf{r}) \iiint\limits_{\Omega_{\mathrm{res}}} \left(\boldsymbol{\nabla} \times \underline{\mathbf{E}}(\mathbf{r}, t) \right) \cdot \mathbf{H}_k(\mathbf{r}) \, \mathrm{d}V \right). \tag{3.9}$$

So, the curl on the right-hand side of (3.9) still needs to be resolved. Starting with the following vector identity according to (A.7)

$$\boldsymbol{\nabla} \cdot \left(\underline{\mathbf{E}}(\mathbf{r}, t) \times \left(\boldsymbol{\nabla} \times \mathbf{E}_k(\mathbf{r}) \right) \right) = \left(\boldsymbol{\nabla} \times \mathbf{E}_k(\mathbf{r}) \right) \cdot \left(\boldsymbol{\nabla} \times \underline{\mathbf{E}}(\mathbf{r}, t) \right) - \underline{\mathbf{E}}(\mathbf{r}, t) \cdot \left(\boldsymbol{\nabla} \times \left(\boldsymbol{\nabla} \times \mathbf{E}_k(\mathbf{r}) \right) \right), \tag{3.10}$$

the second right-hand term is rewritten based on Gauss's law (2.50), the Helmholtz equation (2.39) and the vector identity (A.8) as

$$\boldsymbol{\nabla} \times \left(\boldsymbol{\nabla} \times \mathbf{E}_k(\mathbf{r}) \right) = \boldsymbol{\nabla} \cdot \underbrace{\left(\boldsymbol{\nabla} \cdot \mathbf{E}_k(\mathbf{r}) \right)}_{0} - \Delta \mathbf{E}_k(\mathbf{r})$$

$$\boldsymbol{\nabla} \times \left(\boldsymbol{\nabla} \times \mathbf{E}_k(\mathbf{r}) \right) = \omega_k^2 \mu \varepsilon \mathbf{E}_k(\mathbf{r}) . \tag{3.11}$$

Substituting (3.11) into (3.10) and integrating the terms over Ω_{res} yields

$$\iiint\limits_{\Omega_{\mathrm{res}}} \boldsymbol{\nabla} \cdot \left(\underline{\mathbf{E}}(\mathbf{r}, t) \times \left(\boldsymbol{\nabla} \times \mathbf{E}_k(\mathbf{r}) \right) \right) \mathrm{d}V =$$

$$\iiint\limits_{\Omega_{\mathrm{res}}} \left(\boldsymbol{\nabla} \times \underline{\mathbf{E}}(\mathbf{r}, t) \right) \cdot \left(\boldsymbol{\nabla} \times \mathbf{E}_k(\mathbf{r}) \right) \mathrm{d}V - \omega_k^2 \mu \varepsilon \underbrace{\iiint\limits_{\Omega_{\mathrm{res}}} \underline{\mathbf{E}}(\mathbf{r}, t) \cdot \mathbf{E}_k(\mathbf{r}) \, \mathrm{d}V}_{2U_k \underline{e}_k(t)} . \tag{3.12}$$

The expression then transforms into

$$\oiint\limits_{\partial\Omega_{\mathrm{res}}} \left(\underline{\mathbf{E}}(\mathbf{r}, t) \times \mathbf{H}_k(\mathbf{r}) \right) \cdot \mathrm{d}\mathbf{A} = \iiint\limits_{\Omega_{\mathrm{res}}} \left(\boldsymbol{\nabla} \times \underline{\mathbf{E}}(\mathbf{r}, t) \right) \cdot \mathbf{H}_k(\mathbf{r}) \, \mathrm{d}V - 2\omega_k U_k \underline{e}_k(t) \tag{3.13}$$

by applying the divergence theorem (A.3) to the volume integral on the left-hand side and Faraday's law (2.51) to the curl of the stationary electric field $\mathbf{E}_k(\mathbf{r})$. Substituting (3.13) into (3.9) finally provides the desired expression for the curl

$$\boldsymbol{\nabla} \times \underline{\mathbf{E}}(\mathbf{r}, t) = \sum_{k=1}^{\infty} \mu \mathbf{H}_k(\mathbf{r}) \left(\omega_k \underline{e}_k(t) + \frac{1}{2U_k} \oiint\limits_{\partial\Omega_{\mathrm{res}}} \left(\underline{\mathbf{E}}(\mathbf{r}, t) \times \mathbf{H}_k(\mathbf{r}) \right) \cdot \mathrm{d}\mathbf{A} \right). \tag{3.14}$$

Equation (3.14) demonstrates that the curl is not only composed by the sum of volume integrals resulting from the series expansion of $\underline{\mathbf{E}}(\mathbf{r}, t)$ but also by an additional sum of surface integrals related to the power flow through the resonator surface. An analogous expression can be found for the curl of the magnetic field

$$\boldsymbol{\nabla} \times \underline{\mathbf{H}}(\mathbf{r}, t) = \sum_{k=1}^{\infty} \varepsilon \mathbf{E}_k(\mathbf{r}) \left(\omega_k \underline{h}_k(t) + \frac{1}{2U_k} \oiint\limits_{\partial\Omega_{\mathrm{res}}} \left(\underline{\mathbf{H}}(\mathbf{r}, t) \times \mathbf{E}_k(\mathbf{r}) \right) \cdot \mathrm{d}\mathbf{A} \right) \tag{3.15}$$

based on the respective equations (2.8), (3.1), (3.6), (2.49), (2.40) and (2.52). By further equating (3.14) and (3.15) to the series expansions

$$\boldsymbol{\nabla} \times \underline{\mathbf{E}}(\mathbf{r}, t) = -\mu \frac{\partial}{\partial t} \sum_{k=1}^{\infty} \underline{h}_k(t) \, \mathbf{H}_k(\mathbf{r}) , \qquad (3.16)$$

$$\boldsymbol{\nabla} \times \underline{\mathbf{H}}(\mathbf{r}, t) = \quad \varepsilon \frac{\partial}{\partial t} \sum_{k=1}^{\infty} \underline{e}_k(t) \, \mathbf{E}_k(\mathbf{r}) , \qquad (3.17)$$

general differential equations for each expansion term of the series are obtained

$$\frac{\partial}{\partial t} \underline{h}_k(t) + \omega_k \underline{e}_k(t) = - \frac{1}{2U_k} \oiint_{\partial \Omega_{\mathrm{res}}} \big(\underline{\mathbf{E}}(\mathbf{r}, t) \times \mathbf{H}_k(\mathbf{r}) \big) \cdot \mathrm{d}\mathbf{A}, \qquad (3.18)$$

$$\frac{\partial}{\partial t} \underline{e}_k(t) - \omega_k \underline{h}_k(t) = \frac{1}{2U_k} \oiint_{\partial \Omega_{\mathrm{res}}} \big(\underline{\mathbf{H}}(\mathbf{r}, t) \times \mathbf{E}_k(\mathbf{r}) \big) \cdot \mathrm{d}\mathbf{A}. \qquad (3.19)$$

On condition that an EM field $\underline{\mathbf{E}}(\mathbf{r}, t)$, $\underline{\mathbf{H}}(\mathbf{r}, t)$ invariably fulfills the PEC or PMC boundary conditions along $\partial \Omega_{\mathrm{res}}$ both surface integrals vanish and the expansion coefficients $\underline{e}_k(t)$ and $\underline{h}_k(t)$ are decoupled providing a trivial solution for (3.18) – (3.19). However, in case the EM field does not fulfill these conditions, these two equations explain that there is a mutual interaction between each expansion coefficient of the electric field and the respective coefficient of the magnetic field, caused by the additional surface integrals. A physical interpretation of these Poynting integrals may be given. The term $(\underline{\mathbf{H}}(\mathbf{r}, t) \times \mathbf{E}_k(\mathbf{r})) \cdot \mathrm{d}\mathbf{A}$, rewritten as $(\mathbf{n} \times \underline{\mathbf{H}}(\mathbf{r}, t)) \cdot \mathbf{E}_k(\mathbf{r}) \, \mathrm{d}A$, describes a power flow that may arise from the discontinuity of the tangential magnetic field $\mathbf{n} \times \underline{\mathbf{H}}(\mathbf{r}, t)$ at the surface $\partial \Omega_{\mathrm{res}}$, i.e. the surface current $\mathbf{n} \times \underline{\mathbf{H}}(\mathbf{r}, t)$ may have non-zero values at the interior surface whereas it has to vanish at the exterior surface. Likewise, the term $(\underline{\mathbf{E}}(\mathbf{r}, t) \times \mathbf{H}_k(\mathbf{r})) \cdot \mathrm{d}\mathbf{A}$ involves a fictitious magnetic surface current caused by the discontinuity of the tangential electric field $\mathbf{n} \times \underline{\mathbf{E}}(\mathbf{r}, t)$ at $\partial \Omega_{\mathrm{res}}$, also entailing a power flow through the surface. Hence, if the tangential field components do not vanish on the surface $\partial \Omega_{\mathrm{res}}$ they create a coupling between the time evolution of electric and magnetic field. In this way the additional surface integrals allow to describe more general cases of electromagnetic fields, as will be demonstrated later. The two coupled first order ODEs (3.18) and (3.19) can also be transformed into two separate second order ODEs by analogy to the wave equations

$$\Big(\frac{\partial^2}{\partial t^2} + \omega_k^2 \Big) \underline{e}_k(t) = \frac{1}{2U_k} \bigg(\frac{\partial}{\partial t} \oiint_{\partial \Omega_{\mathrm{res}}} \big(\underline{\mathbf{H}}(\mathbf{r}, t) \times \mathbf{E}_k(\mathbf{r}) \big) \cdot \mathrm{d}\mathbf{A} - \omega_k \oiint_{\partial \Omega_{\mathrm{res}}} \big(\underline{\mathbf{E}}(\mathbf{r}, t) \times \mathbf{H}_k(\mathbf{r}) \big) \cdot \mathrm{d}\mathbf{A} \bigg),$$

$$(3.20)$$

$$\Big(\frac{\partial^2}{\partial t^2} + \omega_k^2 \Big) \underline{h}_k(t) = -\frac{1}{2U_k} \bigg(\frac{\partial}{\partial t} \oiint_{\partial \Omega_{\mathrm{res}}} \big(\underline{\mathbf{E}}(\mathbf{r}, t) \times \mathbf{H}_k(\mathbf{r}) \big) \cdot \mathrm{d}\mathbf{A} + \omega_k \oiint_{\partial \Omega_{\mathrm{res}}} \big(\underline{\mathbf{H}}(\mathbf{r}, t) \times \mathbf{E}_k(\mathbf{r}) \big) \cdot \mathrm{d}\mathbf{A} \bigg).$$

$$(3.21)$$

3.1.2 Unperturbed and Perturbed Resonator Eigenmodes

Some necessary fundamentals and definitions concerning the eigenmodes inside an unperturbed and a perturbed resonator are briefly explained in this part. Perturbed quantities are indicated by the additional tilde ($\sim$) above the actual quantity. For reasons of simplicity, quantities (e.g. eigenmodes) of the unperturbed resonator are also referred to as *unperturbed* (e.g. unperturbed eigenmodes) and quantities of the perturbed resonator as *perturbed* (e.g. perturbed eigenmodes).

The electromagnetic field $\underline{\mathbf{E}}_i(\mathbf{r}, t)$, $\underline{\mathbf{H}}_i(\mathbf{r}, t)$ of the i-th unperturbed mode is defined as

$$\underline{\mathbf{E}}_i(\mathbf{r}, t) = \mathrm{e}^{\jmath \omega_i t}\, \mathbf{E}_i(\mathbf{r}) \quad = \underline{e}_i^{\mathrm{t}}(t)\, \mathbf{E}_i(\mathbf{r})\,, \tag{3.22}$$

$$\underline{\mathbf{H}}_i(\mathbf{r}, t) = \jmath \mathrm{e}^{\jmath \omega_i t}\, \mathbf{H}_i(\mathbf{r}) = \underline{h}_i^{\mathrm{t}}(t)\, \mathbf{H}_i(\mathbf{r})\,, \tag{3.23}$$

i.e. all modes have the same phase and their time functions $\underline{e}_i^{\mathrm{t}}(t)$ and $\underline{h}_i^{\mathrm{t}}(t)$ are normalized to a magnitude of 1. The normalization of $\underline{e}_i^{\mathrm{t}}(t)$ and $\underline{h}_i^{\mathrm{t}}(t)$ is a basic requirement for the validity of the mode's energy definition according to (2.57) that will be used in the following sections. The unperturbed time functions $\underline{e}_i^{\mathrm{t}}(t)$ and $\underline{h}_i^{\mathrm{t}}(t)$ are not to be confused with the expansion functions $\underline{e}_i(t)$ and $\underline{h}_i(t)$. They have the same time dependences but the amplitudes of $\underline{e}_i(t)$ and $\underline{h}_i(t)$ are the coefficients $\underline{e}_i(0)$, $\underline{h}_i(0)$ of the series expansions, which can be different from 1. The EM field $\underline{\widetilde{\mathbf{E}}}_i(\mathbf{r}, t)$, $\underline{\widetilde{\mathbf{H}}}_i(\mathbf{r}, t)$ of the i-th perturbed mode can be written in an analogous manner as

$$\underline{\widetilde{\mathbf{E}}}_i(\mathbf{r}, t) = \mathrm{e}^{\jmath \widetilde{\omega}_i t}\, \widetilde{\mathbf{E}}_i(\mathbf{r}) \quad = \underline{\widetilde{e}}_i^{\mathrm{t}}(t)\, \widetilde{\mathbf{E}}_i(\mathbf{r})\,, \tag{3.24}$$

$$\underline{\widetilde{\mathbf{H}}}_i(\mathbf{r}, t) = \jmath \mathrm{e}^{\jmath \widetilde{\omega}_i t}\, \widetilde{\mathbf{H}}_i(\mathbf{r}) = \underline{\widetilde{h}}_i^{\mathrm{t}}(t)\, \widetilde{\mathbf{H}}_i(\mathbf{r})\,. \tag{3.25}$$

At this, $\widetilde{\omega}_i$ denotes the i-th *perturbed angular eigenfrequency*, $\widetilde{\mathbf{E}}_i(\mathbf{r})$ the i-th *perturbed stationary electric field* and $\widetilde{\mathbf{H}}_i(\mathbf{r})$ the i-th *perturbed stationary magnetic field*. Any EM field $\underline{\mathbf{E}}(\mathbf{r}, t)$, $\underline{\mathbf{H}}(\mathbf{r}, t)$ inside the unperturbed resonator may be expanded in terms of the unperturbed modes according to (3.20) and (3.21)

$$\frac{\partial}{\partial t}\underline{h}_k(t) + \omega_k \underline{e}_k(t) = -\frac{1}{2U_k} \oiint_S \left(\underline{\mathbf{E}}(\mathbf{r}, t) \times \mathbf{H}_k(\mathbf{r})\right) \cdot \mathrm{d}\mathbf{A}, \tag{3.26}$$

$$\frac{\partial}{\partial t}\underline{e}_k(t) - \omega_k \underline{h}_k(t) = \frac{1}{2U_k} \oiint_S \left(\underline{\mathbf{H}}(\mathbf{r}, t) \times \mathbf{E}_k(\mathbf{r})\right) \cdot \mathrm{d}\mathbf{A}. \tag{3.27}$$

Likewise, any field $\underline{\widetilde{\mathbf{E}}}(\mathbf{r}, t)$, $\underline{\widetilde{\mathbf{H}}}(\mathbf{r}, t)$ inside the perturbed resonator may be expanded in terms of the perturbed modes

$$\frac{\partial}{\partial t}\underline{\widetilde{h}}_k(t) + \widetilde{\omega}_k \underline{\widetilde{e}}_k(t) = -\frac{1}{2\widetilde{U}_k} \oiint_{\widetilde{S}} \left(\underline{\widetilde{\mathbf{E}}}(\mathbf{r}, t) \times \widetilde{\mathbf{H}}_k(\mathbf{r})\right) \cdot \mathrm{d}\mathbf{A}, \tag{3.28}$$

$$\frac{\partial}{\partial t}\underline{\widetilde{e}}_k(t) - \widetilde{\omega}_k \underline{\widetilde{h}}_k(t) = \frac{1}{2\widetilde{U}_k} \oiint_{\widetilde{S}} \left(\underline{\widetilde{\mathbf{H}}}(\mathbf{r}, t) \times \widetilde{\mathbf{E}}_k(\mathbf{r})\right) \cdot \mathrm{d}\mathbf{A}. \tag{3.29}$$

Figure 3.1 shows a simplified 2D illustration of the unperturbed and perturbed resonator geometry. The unperturbed geometry has a volume V that either may be bounded by

a surface S_{pec} with PEC boundary conditions or a surface S_{pmc} with PMC boundary conditions as plotted in Fig. 3.1(a). Thus, the stationary fields $\mathbf{E}_i(\mathbf{r})$, $\mathbf{H}_i(\mathbf{r})$ of the i-th unperturbed eigenmode fulfill the conditions

$$\mathbf{n} \times \mathbf{E}_i(\mathbf{r}) = \mathbf{0} \quad \text{and} \quad \mathbf{n} \cdot \mathbf{H}_i(\mathbf{r}) = 0 \quad \text{at } S_{\mathrm{pec}}, \tag{3.30}$$

$$\mathbf{n} \times \mathbf{H}_i(\mathbf{r}) = \mathbf{0} \quad \text{and} \quad \mathbf{n} \cdot \mathbf{E}_i(\mathbf{r}) = 0 \quad \text{at } S_{\mathrm{pmc}}. \tag{3.31}$$

Consistently, the perturbed geometry has a volume $\widetilde{V}$ bounded by the surfaces $\widetilde{S}_{\mathrm{pec}}$ and $\widetilde{S}_{\mathrm{pmc}}$ (see Fig. 3.1(b)). Here, the fields $\widetilde{\mathbf{E}}_i(\mathbf{r})$, $\widetilde{\mathbf{H}}_i(\mathbf{r})$ of the i-th perturbed eigenmode match

$$\mathbf{n} \times \widetilde{\mathbf{E}}_i(\mathbf{r}) = \mathbf{0} \quad \text{and} \quad \mathbf{n} \cdot \widetilde{\mathbf{H}}_i(\mathbf{r}) = 0 \quad \text{at } \widetilde{S}_{\mathrm{pec}}, \tag{3.32}$$

$$\mathbf{n} \times \widetilde{\mathbf{H}}_i(\mathbf{r}) = \mathbf{0} \quad \text{and} \quad \mathbf{n} \cdot \widetilde{\mathbf{E}}_i(\mathbf{r}) = 0 \quad \text{at } \widetilde{S}_{\mathrm{pmc}}. \tag{3.33}$$

The deformed part $\Delta\widetilde{S}$ of the perturbed surface $\widetilde{S}$ that has initially been the part ΔS of the unperturbed surface S can likewise be divided into a PEC part $\Delta\widetilde{S}_{\mathrm{pec}}$ and a PMC part $\Delta\widetilde{S}_{\mathrm{pmc}}$. In case the perturbations of PEC and PMC surfaces are clearly separated, as demonstrated in Fig. 3.1(c), the surfaces ΔS_{pec} and $\Delta\widetilde{S}_{\mathrm{pec}}$ enclose a deformed PEC volume ΔV_{pec} while the surfaces ΔS_{pmc} and $\Delta\widetilde{S}_{\mathrm{pmc}}$ enclose a deformed PMC volume ΔV_{pmc}. Generally, ΔV is the volume that is removed by the perturbation. The relations of the geometric parameters may be summarized as

$$S = S_{\mathrm{pec}} \cup S_{\mathrm{pmc}}, \tag{3.34}$$

$$\widetilde{S} = \widetilde{S}_{\mathrm{pec}} \cup \widetilde{S}_{\mathrm{pmc}}, \tag{3.35}$$

$$\Delta\widetilde{S} = \widetilde{S} \setminus S = (\widetilde{S}_{\mathrm{pec}} \setminus S_{\mathrm{pec}}) \cup (\widetilde{S}_{\mathrm{pmc}} \setminus S_{\mathrm{pmc}}), \tag{3.36}$$

$$\Delta S = S \setminus \widetilde{S} = (S_{\mathrm{pec}} \setminus \widetilde{S}_{\mathrm{pec}}) \cup (S_{\mathrm{pmc}} \setminus \widetilde{S}_{\mathrm{pmc}}), \tag{3.37}$$

$$\Delta V = V \setminus \widetilde{V}. \tag{3.38}$$
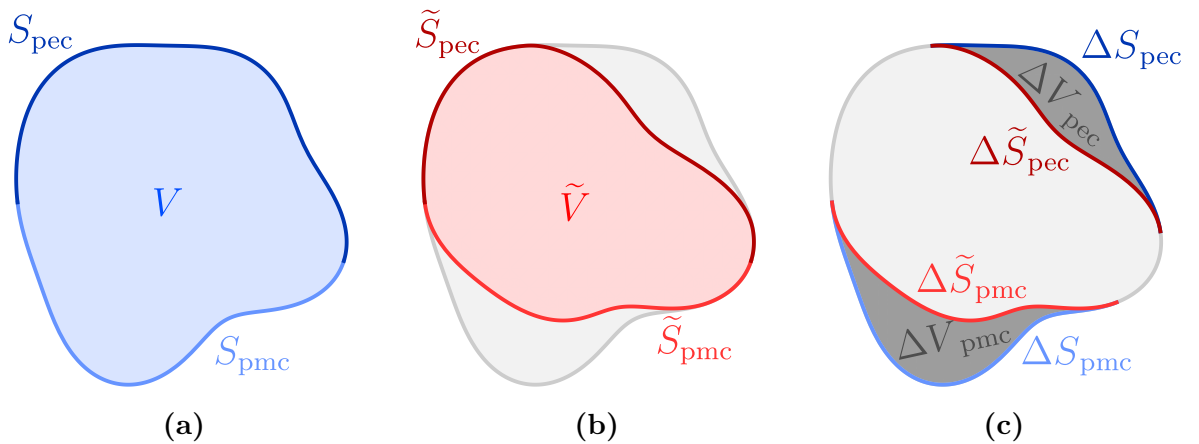
Figure 3.1: 2D scheme of the unperturbed and perturbed geometry of a resonator with PEC and PMC boundaries. (a) Unperturbed resonator shape with the volume V bounded by the surface S. (b) Perturbed resonator shape with the volume $\widetilde{V}$ bounded by the surface $\widetilde{S}$. (c) Volume ΔV removed by the perturbation and bounded by the deformed surface $\Delta\widetilde{S}$ and the corresponding original surface ΔS.

3.2 Slater's Cavity Perturbation Theorem

Slater's cavity perturbation theorem (ST) [28, Sec. III.7] provides a first order approximation of the perturbed frequencies inside a deformed perfect electric conductor. ST determines the perturbed frequency $\widetilde{\omega}_i$ of each perturbed mode i merely based on the corresponding unperturbed mode i, i.e. each perturbed mode i is processed detached from the rest of the unperturbed modes $k \neq i$. , This is done by applying the expansion in (3.28) and (3.29) to the EM field $\widetilde{\underline{\mathbf{E}}}_i(\mathbf{r}, t)$, $\widetilde{\underline{\mathbf{H}}}_i(\mathbf{r}, t)$ of the i-th perturbed mode instead of the arbitrary field $\widetilde{\underline{\mathbf{E}}}(\mathbf{r}, t)$, $\widetilde{\underline{\mathbf{H}}}(\mathbf{r}, t)$ and approximating the stationary field of the i-th perturbed expansion mode by the one of the i-th unperturbed mode. According to [28], this is permissible since the fields are considered as nearly equal over the surface. This yields the expression

$$(\frac{\partial^2}{\partial t^2} + \omega_i^2)\mu \iiint\limits_{\widetilde{V}} \widetilde{\underline{\mathbf{H}}}_i(\mathbf{r}, t) \cdot \mathbf{H}_i(\mathbf{r})\,\mathrm{d}V =$$

$$-\frac{\partial}{\partial t} \oiint\limits_{\widetilde{S}} \left(\widetilde{\underline{\mathbf{E}}}_i(\mathbf{r}, t) \times \mathbf{H}_i(\mathbf{r})\right) \cdot \mathrm{d}\mathbf{A} - \omega_i \oiint\limits_{\widetilde{S}} \left(\widetilde{\underline{\mathbf{H}}}_i(\mathbf{r}, t) \times \mathbf{E}_i(\mathbf{r})\right) \cdot \mathrm{d}\mathbf{A}. \tag{3.39}$$

Due to this approximation the fields are now coupled by their power flow through the perturbed surface. The time derivative on the left-hand side only applies to the time-depending perturbed magnetic field $\widetilde{\underline{\mathbf{H}}}_i(\mathbf{r}, t)$ that harmonically oscillates with the frequency $\widetilde{\omega}_i$. Hence, the second order time derivative can be substituted by $-\widetilde{\omega}_i^2$. The first term on the right-hand side of (3.39) vanishes since the perfect conductor has a purely PEC boundary and the perturbed electric field $\widetilde{\underline{\mathbf{E}}}_i(\mathbf{r}, t)$ is zero at $\widetilde{S}_{\mathrm{pec}}$ according to (3.32). Further, the second surface integral has to be evaluated only along the deformed surface part $\Delta\widetilde{S}_{\mathrm{pec}}$ due to the fact that the unperturbed electric field $\mathbf{E}_i(\mathbf{r})$ also vanishes at the surface $\widetilde{S}$ if $\widetilde{S}$ coincides with the unperturbed surface S (see (3.30)). Equation (3.39) then becomes

$$\left(\omega_i^2 - \widetilde{\omega}_i^2\right)\mu \iiint\limits_{\widetilde{V}} \widetilde{\underline{\mathbf{H}}}_i(\mathbf{r}, t) \cdot \mathbf{H}_i(\mathbf{r})\,\mathrm{d}V = -\omega_i \iint\limits_{\Delta\widetilde{S}_{\mathrm{pec}}} \left(\widetilde{\underline{\mathbf{H}}}_i(\mathbf{r}, t) \times \mathbf{E}_i(\mathbf{r})\right) \cdot \mathrm{d}\mathbf{A}. \tag{3.40}$$

The time dependence in (3.40) can completely be eliminated by applying (3.25). At the same time, the surface integral may be extended to ΔS_{pec} where $\mathbf{n} \times \mathbf{E}_i(\mathbf{r}) = \mathbf{0}$ holds, resulting again in a closed surface integral (see Fig. 3.1(c)). So, it can further be transformed into a volume integral by applying the divergence theorem (A.3). Here, the sign of the integral inverts because $\mathrm{d}\mathbf{A}$ is inward-oriented with respect to the closed surface $\Delta\widetilde{S}_{\mathrm{pec}} \cup \Delta S_{\mathrm{pec}}$ and (3.40) yields

$$\left(\omega_i^2 - \widetilde{\omega}_i^2\right)\mu \iiint\limits_{\widetilde{V}} \widetilde{\mathbf{H}}_i(\mathbf{r}) \cdot \mathbf{H}_i(\mathbf{r})\,\mathrm{d}V = -\omega_i \oiint\limits_{\Delta\widetilde{S}_{\mathrm{pec}} \cup \Delta S_{\mathrm{pec}}} \left(\widetilde{\mathbf{H}}_i(\mathbf{r}) \times \mathbf{E}_i(\mathbf{r})\right) \cdot \mathrm{d}\mathbf{A}$$

$$= \omega_i \iiint\limits_{\Delta V_{\mathrm{pec}}} \boldsymbol{\nabla} \cdot \left(\widetilde{\mathbf{H}}_i(\mathbf{r}) \times \mathbf{E}_i(\mathbf{r})\right)\mathrm{d}V. \tag{3.41}$$

At this point, two further approximations are applied as per [28]. Firstly, the perturbed field $\widetilde{\mathbf{H}}_i(\mathbf{r})$ is again replaced by the unperturbed field $\mathbf{H}_i(\mathbf{r})$. Secondly, the integral on the left is performed over the full unperturbed volume V instead of the perturbed volume $\widetilde{V}$. The approximations yield

$$\omega_i^2 - \widetilde{\omega}_i^2 \approx \frac{\omega_i \iiint\limits_{\Delta V_{\mathrm{pec}}} \boldsymbol{\nabla} \cdot \big(\mathbf{H}_i(\mathbf{r}) \times \mathbf{E}_i(\mathbf{r})\big)\mathrm{d}V}{\mu \iiint\limits_{V} \mathbf{H}_i(\mathbf{r}) \cdot \mathbf{H}_i(\mathbf{r})\,\mathrm{d}V}. \tag{3.42}$$

The volume integral in the denominator can directly be substituted by the energy of the unperturbed mode (2.57). The integration term in the numerator can be transformed into

$$\begin{aligned}\boldsymbol{\nabla} \cdot \big(\mathbf{H}_i(\mathbf{r}) \times \mathbf{E}_i(\mathbf{r})\big) &= \mathbf{E}_i(\mathbf{r}) \cdot \big(\boldsymbol{\nabla} \times \mathbf{H}_i(\mathbf{r})\big) - \mathbf{H}_i(\mathbf{r}) \cdot \big(\boldsymbol{\nabla} \times \mathbf{E}_i(\mathbf{r})\big) \\ &= \varepsilon\omega_i\big(\mathbf{E}_i(\mathbf{r}) \cdot \mathbf{E}_i(\mathbf{r})\big) - \mu\omega_i\big(\mathbf{H}_i(\mathbf{r}) \cdot \mathbf{H}_i(\mathbf{r})\big)\end{aligned} \tag{3.43}$$

by using the vector identity (A.7) and Maxwell's equations (2.51) and (2.52). Thus, equation (3.42) finally becomes *Slater's theorem*

$$\widetilde{\omega}_i^2 = \omega_i^2\left(1 + \frac{1}{2U_i} \iiint\limits_{\Delta V_{\mathrm{pec}}} \big(\mu\mathbf{H}_i(\mathbf{r}) \cdot \mathbf{H}_i(\mathbf{r}) - \varepsilon\mathbf{E}_i(\mathbf{r}) \cdot \mathbf{E}_i(\mathbf{r})\big)\mathrm{d}V\right). \tag{3.44}$$

Some sources [26], [77] present a simplified version of ST

$$\frac{\widetilde{\omega}_i - \omega_i}{\omega_i} = \frac{1}{4U_i} \iiint\limits_{\Delta V_{\mathrm{pec}}} \big(\mu\mathbf{H}_i(\mathbf{r}) \cdot \mathbf{H}_i(\mathbf{r}) - \varepsilon\mathbf{E}_i(\mathbf{r}) \cdot \mathbf{E}_i(\mathbf{r})\big)\mathrm{d}V \tag{3.45}$$

that directly yields the *angular frequency shift* $\Delta\omega_i$

$$\Delta\omega_i = \widetilde{\omega}_i - \omega_i. \tag{3.46}$$

Equation (3.45) is here denoted as the *first order approximation of Slater's theorem* since it is deduced from (3.44) by applying the first order approximation of the Taylor series of the square root [78, Sec. 7.3.5]

$$\sqrt{1 + x} \approx 1 + \frac{x}{2} \qquad \forall\,|x| \ll 1. \tag{3.47}$$

A direct derivation based on the curl functions of the i-th unperturbed and perturbed fields can be found in [26, Sec. 5.7.1] or [77, Sec. 4.39.2]. It should be pointed out that (3.45) represents a less accurate formula due to the additional approximation. ST determines the frequency $\widetilde{\omega}_i$ of a perturbed mode i exclusively from the respective unperturbed mode based on its frequency ω_i and the interaction of its stationary fields $\mathbf{E}_i(\mathbf{r})$, $\mathbf{H}_i(\mathbf{r})$ inside the deformed volume ΔV_{pec}. This approach involves only a low effort but also prevents the calculation of the perturbed fields, constituting the major disadvantage of Slater's theorem.

3.3 Generalization of Slater's Theorem

The fundamental idea of the *generalization of Slater's theorem* (GST) is to not merely derive a perturbed eigenmode from its corresponding unperturbed eigenmode but instead to expand it in terms of the complete set of known unperturbed modes. For this purpose, the coefficients of the linear series expansions are deduced from the energy-related mutual interactions of each unperturbed mode with every other unperturbed mode inside the deformed volume ΔV, as will be shown in the following.

Strictly speaking, the electromagnetic field inside a perturbed resonator can only be perfectly expanded in terms of the corresponding perturbed normal modes using (3.28) and (3.29). However, this requires the direct calculation of the perturbed modes, which shall be refrained from. Applying the standard approach of Slater's theorem to (3.28) and (3.29) and replacing the basis of unknown perturbed normal modes by the known set of unperturbed modes yields the coupling equations in form of

$$\frac{\partial}{\partial t}\underline{h}_k(t) + \omega_k \underline{e}_k(t) = -\frac{1}{2U_k} \oiint_{\widetilde{S}} \left(\widetilde{\underline{\mathbf{E}}}(\mathbf{r},t) \times \mathbf{H}_k(\mathbf{r}) \right) \cdot \mathrm{d}\mathbf{A}, \tag{3.48}$$

$$\frac{\partial}{\partial t}\underline{e}_k(t) - \omega_k \underline{h}_k(t) = \frac{1}{2U_k} \oiint_{\widetilde{S}} \left(\widetilde{\underline{\mathbf{H}}}(\mathbf{r},t) \times \mathbf{E}_k(\mathbf{r}) \right) \cdot \mathrm{d}\mathbf{A}. \tag{3.49}$$

These formulas are the basis of the generalization of ST as presented in [76], [79]. Consequently, each perturbed eigenmode is expressed as a sum of unperturbed modes

$$\widetilde{\underline{\mathbf{E}}}_i(\mathbf{r},t) = \sum_{k=1}^{\infty} \alpha_{ik} \underline{\mathbf{E}}_k(\mathbf{r},t) = \sum_{k=1}^{\infty} \underbrace{\alpha_{ik} \mathrm{e}^{\jmath\omega_k t}}_{\underline{e}_{ik}(t)} \mathbf{E}_k(\mathbf{r}), \tag{3.50}$$

$$\widetilde{\underline{\mathbf{H}}}_i(\mathbf{r},t) = \sum_{k=1}^{\infty} \beta_{ik} \underline{\mathbf{H}}_k(\mathbf{r},t) = \sum_{k=1}^{\infty} \underbrace{\beta_{ik} \jmath\mathrm{e}^{\jmath\omega_k t}}_{\underline{h}_{ik}(t)} \mathbf{H}_k(\mathbf{r}). \tag{3.51}$$

Here, α_{ik} and β_{ik} denote the *expansion coefficients for the i-th perturbed eigenmode based on the k-th unperturbed eigenmode.* So, the expansion functions $\underline{e}_{ik}(t)$ and $\underline{h}_{ik}(t)$ now have an additional index i indicating the perturbed mode. They can be rewritten as

$$\underline{e}_{ik}(t) = \frac{\varepsilon}{2U_k} \iiint_{\widetilde{V}} \widetilde{\underline{\mathbf{E}}}_i(\mathbf{r},t) \cdot \mathbf{E}_k(\mathbf{r}) \, \mathrm{d}V, \tag{3.52}$$

$$\underline{h}_{ik}(t) = \frac{\mu}{2U_k} \iiint_{\widetilde{V}} \widetilde{\underline{\mathbf{H}}}_i(\mathbf{r},t) \cdot \mathbf{H}_k(\mathbf{r}) \, \mathrm{d}V. \tag{3.53}$$

At this point, it must be emphasized that (3.52) and (3.53) are only valid if the perturbed volume $\widetilde{V}$ is completely enclosed by the unperturbed volume V. Only then the volume integrals can be extended from $\widetilde{V}$ to V without altering their result (since $\widetilde{\mathbf{E}}_i(\mathbf{r})$ and $\widetilde{\mathbf{H}}_i(\mathbf{r})$ are zero outside of $\widetilde{V}$), allowing to cancel all expansion terms except for the k-th one by applying the orthogonality relation of the unperturbed eigenmodes (as demonstrated in

(3.5) and (3.6)). If $\widetilde{V}$ exceeded the domain of V, the orthogonality would be violated and the expansion terms would not be separable. Hence, the initial geometry can exclusively be deformed inwardly. Besides, the unperturbed modes are not defined outside of V in most cases. Applying the additional perturbed mode index i to (3.48) and (3.49), the coupling equations become

$$\frac{\partial}{\partial t}\underline{h}_{ik}(t) + \omega_k \underline{e}_{ik}(t) = -\frac{1}{2U_k} \oiint\limits_{\widetilde{S}} \left(\widetilde{\underline{\mathbf{E}}}_i(\mathbf{r},t) \times \mathbf{H}_k(\mathbf{r}) \right) \cdot \mathrm{d}\mathbf{A}, \tag{3.54}$$

$$\frac{\partial}{\partial t}\underline{e}_{ik}(t) - \omega_k \underline{h}_{ik}(t) = \frac{1}{2U_k} \oiint\limits_{\widetilde{S}} \left(\widetilde{\underline{\mathbf{H}}}_i(\mathbf{r},t) \times \mathbf{E}_k(\mathbf{r}) \right) \cdot \mathrm{d}\mathbf{A}. \tag{3.55}$$

Since the unperturbed fields generally have non-zero values at the perturbed boundary $\widetilde{S}$, a simultaneous discontinuity of unperturbed and perturbed tangential fields may arise at $\widetilde{S}$, causing a linear coupling of the expansion coefficients in (3.54) and (3.55). Both closed surface integrals can be simplified. The integral in (3.54) is reduced to the perturbed PMC surface $\widetilde{S}_{\mathrm{pmc}}$ since the perturbed tangential electric field $\widetilde{\underline{\mathbf{E}}}_i(\mathbf{r},t)$ vanishes along the PEC surface $\widetilde{S}_{\mathrm{pec}}$ as per (3.32). Likewise, the integration in (3.55) is only done at the perturbed PEC surface $\widetilde{S}_{\mathrm{pec}}$ because $\mathbf{n} \times \widetilde{\mathbf{H}}_i(\mathbf{r},t) = \mathbf{0}$ along $\widetilde{S}_{\mathrm{pmc}}$ as per (3.33)

$$\frac{\partial}{\partial t}\underline{h}_{ik}(t) + \omega_k \underline{e}_{ik}(t) = -\frac{1}{2U_k} \iint\limits_{\widetilde{S}_{\mathrm{pmc}}} \left(\widetilde{\underline{\mathbf{E}}}_i(\mathbf{r},t) \times \mathbf{H}_k(\mathbf{r}) \right) \cdot \mathrm{d}\mathbf{A}, \tag{3.56}$$

$$\frac{\partial}{\partial t}\underline{e}_{ik}(t) - \omega_k \underline{h}_{ik}(t) = \frac{1}{2U_k} \iint\limits_{\widetilde{S}_{\mathrm{pec}}} \left(\widetilde{\underline{\mathbf{H}}}_i(\mathbf{r},t) \times \mathbf{E}_k(\mathbf{r}) \right) \cdot \mathrm{d}\mathbf{A}. \tag{3.57}$$

These simplifications are not only feasible but imperative. The closed surface integrals over $\widetilde{S}$ in (3.48) and (3.49) must not be directly transformed into a volume integral since this leaves the boundary conditions of the perturbed fields undefined. Only by implying explicit boundary conditions and thereby reducing the two integrals to either PMC or PEC surfaces reasonable results will be obtained.

Considering now the case that the perturbations of PEC and PMC boundaries are clearly separated as in Fig. 3.1(c), the surface integrals can be further transformed. The integral in (3.56) is restricted to the deformed part $\Delta\widetilde{S}_{\mathrm{pmc}}$ of $\widetilde{S}_{\mathrm{pmc}}$ since the tangential $\mathbf{H}_k(\mathbf{r})$ vanishes where $\widetilde{S}_{\mathrm{pmc}}$ coincides with the unperturbed surface S_{pmc} due to (3.31). Likewise, the integral in (3.57) reduces to the deformed surface $\Delta\widetilde{S}_{\mathrm{pec}}$ according to (3.30)

$$\frac{\partial}{\partial t}\underline{h}_{ik}(t) + \omega_k \underline{e}_{ik}(t) = -\frac{1}{2U_k} \iint\limits_{\Delta\widetilde{S}_{\mathrm{pmc}}} \left(\widetilde{\underline{\mathbf{E}}}_i(\mathbf{r},t) \times \mathbf{H}_k(\mathbf{r}) \right) \cdot \mathrm{d}\mathbf{A}, \tag{3.58}$$

$$\frac{\partial}{\partial t}\underline{e}_{ik}(t) - \omega_k \underline{h}_{ik}(t) = \frac{1}{2U_k} \iint\limits_{\Delta\widetilde{S}_{\mathrm{pec}}} \left(\widetilde{\underline{\mathbf{H}}}_i(\mathbf{r},t) \times \mathbf{E}_k(\mathbf{r}) \right) \cdot \mathrm{d}\mathbf{A}. \tag{3.59}$$

At this point, an important fact arising from the discontinuous nature of the fields at the boundaries has to be explained. Due to their discontinuity, the expanded fields $\widetilde{\underline{\mathbf{E}}}_i(\mathbf{r},t)$

and $\widetilde{\underline{\mathbf{H}}}_i(\mathbf{r}, t)$ are subject to a form of *Gibbs phenomenon* [49] at the deformed parts of the boundary. While the fields at the interior surface may take non-zero values they have to be zero at the exterior surface. However, the normal modes used for the expansion only allow for continuous amplitude changes inside V. As a consequence, all non-zero field components are forced to only half their actual value at a deformed surface, reflecting the mean value of the component at either side of $\widetilde{S}$. Therefore, the surface currents $\mathbf{n} \times \widetilde{\underline{\mathbf{H}}}_i(\mathbf{r}, t)$ and $\mathbf{n} \times \widetilde{\underline{\mathbf{E}}}_i(\mathbf{r}, t)$ in (3.58) and (3.59) have to be substituted by $2(\mathbf{n} \times \widetilde{\underline{\mathbf{H}}}_i(\mathbf{r}, t))$ and $2(\mathbf{n} \times \widetilde{\underline{\mathbf{E}}}_i(\mathbf{r}, t))$, resulting in

$$\frac{\partial}{\partial t}\underline{h}_{ik}(t) + \omega_k \underline{e}_{ik}(t) = -\frac{1}{U_k}\iint\limits_{\Delta \widetilde{S}_{\mathrm{pmc}}} \left(\widetilde{\underline{\mathbf{E}}}_i(\mathbf{r}, t) \times \mathbf{H}_k(\mathbf{r})\right) \cdot \mathrm{d}\mathbf{A}, \tag{3.60}$$

$$\frac{\partial}{\partial t}\underline{e}_{ik}(t) - \omega_k \underline{h}_{ik}(t) = \frac{1}{U_k}\iint\limits_{\Delta \widetilde{S}_{\mathrm{pec}}} \left(\widetilde{\underline{\mathbf{H}}}_i(\mathbf{r}, t) \times \mathbf{E}_k(\mathbf{r})\right) \cdot \mathrm{d}\mathbf{A}. \tag{3.61}$$

The correctness of the results in Chapter 5 and 6 invariably prove the validity of this modification. Figure 5.6(b), for instance, demonstrates the arising Gibbs phenomenon. The additional prefactor of 2 is also established in [79]. However, it is not mentioned in [76]. Again, it should be pointed out that this adjustment is only valid considering a deformed surface $\Delta \widetilde{S}$. At the unperturbed boundary, the fields $\underline{\mathbf{E}}(\mathbf{r}, t)$ and $\underline{\mathbf{H}}(\mathbf{r}, t)$ are not affected and the general equations (3.26) – (3.29) remain valid. Next, the surface integrals are in turn extended to the surfaces ΔS_{pmc} or ΔS_{pec}, respectively. This is permissible since the extra terms have a contribution of zero according to (3.31) or (3.30). The resulting closed surface integrals, with an inward-oriented surface vector $\mathbf{n}$, can again be transformed into volume integrals by applying (A.3), as Fig. 3.1(c) illustrates. Equations (3.60) and (3.61) then become

$$\frac{\partial}{\partial t}\underline{h}_{ik}(t) + \omega_k \underline{e}_{ik}(t) = -\frac{1}{U_k}\oiint\limits_{\Delta \widetilde{S}_{\mathrm{pmc}} \cup \Delta S_{\mathrm{pmc}}} \left(\widetilde{\underline{\mathbf{E}}}_i(\mathbf{r}, t) \times \mathbf{H}_k(\mathbf{r})\right) \cdot \mathrm{d}\mathbf{A}$$

$$= \frac{1}{U_k}\iiint\limits_{\Delta V_{\mathrm{pmc}}} \boldsymbol{\nabla} \cdot \left(\widetilde{\underline{\mathbf{E}}}_i(\mathbf{r}, t) \times \mathbf{H}_k(\mathbf{r})\right)\mathrm{d}V, \tag{3.62}$$

$$\frac{\partial}{\partial t}\underline{e}_{ik}(t) - \omega_k \underline{h}_{ik}(t) = \frac{1}{U_k}\oiint\limits_{\Delta \widetilde{S}_{\mathrm{pec}} \cup \Delta S_{\mathrm{pec}}} \left(\widetilde{\underline{\mathbf{H}}}_i(\mathbf{r}, t) \times \mathbf{E}_k(\mathbf{r})\right) \cdot \mathrm{d}\mathbf{A}$$

$$= -\frac{1}{U_k}\iiint\limits_{\Delta V_{\mathrm{pec}}} \boldsymbol{\nabla} \cdot \left(\widetilde{\underline{\mathbf{H}}}_i(\mathbf{r}, t) \times \mathbf{E}_k(\mathbf{r})\right)\mathrm{d}V. \tag{3.63}$$

The perturbed fields in both integrals are now eliminated by applying the expansions (3.50) or (3.51) as well as the vector cross product of the divergence as per (A.7). The first volume integral in (3.62) transforms into

$$\iiint\limits_{\Delta V_{\mathrm{pmc}}} \boldsymbol{\nabla} \cdot \left(\widetilde{\underline{\mathbf{E}}}_i(\mathbf{r}, t) \times \mathbf{H}_k(\mathbf{r})\right)\mathrm{d}V = \sum_{j=1}^{\infty} \underline{e}_{ij}(t)\iiint\limits_{\Delta V_{\mathrm{pmc}}} \boldsymbol{\nabla} \cdot \left(\mathbf{E}_j(\mathbf{r}) \times \mathbf{H}_k(\mathbf{r})\right)\mathrm{d}V \tag{3.64}$$

with

$$\nabla \cdot \big(\mathbf{E}_j(\mathbf{r}) \times \mathbf{H}_k(\mathbf{r})\big) = \mathbf{H}_k(\mathbf{r}) \cdot \big(\nabla \times \mathbf{E}_j(\mathbf{r})\big) - \mathbf{E}_j(\mathbf{r}) \cdot \big(\nabla \times \mathbf{H}_k(\mathbf{r})\big)$$
$$= \omega_j \mu \big(\mathbf{H}_k(\mathbf{r}) \cdot \mathbf{H}_j(\mathbf{r})\big) - \omega_k \varepsilon \big(\mathbf{E}_k(\mathbf{r}) \cdot \mathbf{E}_j(\mathbf{r})\big). \tag{3.65}$$

The second integral in (3.63) becomes

$$\iiint\limits_{\Delta V_{\text{pec}}} \nabla \cdot \big(\widetilde{\mathbf{H}}_i(\mathbf{r},t) \times \mathbf{E}_k(\mathbf{r})\big) \mathrm{d}V = \sum_{j=1}^{\infty} \underline{h}_{ij}(t) \iiint\limits_{\Delta V_{\text{pec}}} \nabla \cdot \big(\mathbf{H}_j(\mathbf{r}) \times \mathbf{E}_k(\mathbf{r})\big) \mathrm{d}V \tag{3.66}$$

with

$$\nabla \cdot \big(\mathbf{H}_j(\mathbf{r}) \times \mathbf{E}_k(\mathbf{r})\big) = \mathbf{E}_k(\mathbf{r}) \cdot \big(\nabla \times \mathbf{H}_j(\mathbf{r})\big) - \mathbf{H}_j(\mathbf{r}) \cdot \big(\nabla \times \mathbf{E}_k(\mathbf{r})\big)$$
$$= \omega_j \varepsilon \big(\mathbf{E}_k(\mathbf{r}) \cdot \mathbf{E}_j(\mathbf{r})\big) - \omega_k \mu \big(\mathbf{H}_k(\mathbf{r}) \cdot \mathbf{H}_j(\mathbf{r})\big). \tag{3.67}$$

Substituting the expressions (3.64) and (3.65) into (3.62) as well as (3.66) and (3.67) into (3.63) yields the two ODEs

$$\frac{\partial}{\partial t}\underline{h}_{ik}(t) + \omega_k \underline{e}_{ik}(t) = \frac{1}{U_k} \sum_{j=1}^{\infty} \underline{e}_{ij}(t) \underbrace{\iiint\limits_{\Delta V_{\text{pmc}}} \Big(\omega_j \mu \mathbf{H}_k(\mathbf{r}) \cdot \mathbf{H}_j(\mathbf{r}) - \omega_k \varepsilon \mathbf{E}_k(\mathbf{r}) \cdot \mathbf{E}_j(\mathbf{r})\Big)\mathrm{d}V}_{q_{kj}},$$

$$\tag{3.68}$$

$$\frac{\partial}{\partial t}\underline{e}_{ik}(t) - \omega_k \underline{h}_{ik}(t) = \frac{1}{U_k} \sum_{j=1}^{\infty} \underline{h}_{ij}(t) \underbrace{\iiint\limits_{\Delta V_{\text{pec}}} \Big(\omega_k \mu \mathbf{H}_k(\mathbf{r}) \cdot \mathbf{H}_j(\mathbf{r}) - \omega_j \varepsilon \mathbf{E}_k(\mathbf{r}) \cdot \mathbf{E}_j(\mathbf{r})\Big)\mathrm{d}V}_{s_{kj}}$$

$$\tag{3.69}$$

that describe the coupling of the time coefficients exclusively based on the unperturbed eigenmodes by the *PMC interaction terms* q_{kj} and the *PEC interaction terms* s_{kj}. Then, the electric and magnetic coefficients are decoupled to gain independent series for the perturbed electric and magnetic field. For this purpose, the ω_k terms on the left-hand side of the equations are included in the sums on the right side by applying the Kronecker delta δ_{jk}

$$\frac{\partial}{\partial t}\underline{h}_{ik}(t) = \sum_{j=1}^{\infty} \Big(-\omega_k \delta_{jk} + \frac{q_{kj}}{U_k}\Big)\underline{e}_{ij}(t), \tag{3.70}$$

$$\frac{\partial}{\partial t}\underline{e}_{ik}(t) = \sum_{j=1}^{\infty} \Big(\omega_k \delta_{jk} + \frac{s_{kj}}{U_k}\Big)\underline{h}_{ij}(t). \tag{3.71}$$

By differentiating (3.71) with respect to time and then inserting (3.70), the equation for

determining the $\underline{e}_{ik}(t)$ is further rearranged into

$$
\begin{aligned}
\frac{\partial^2}{\partial t^2}\underline{e}_{ik}(t) &= \sum_{l=1}^{\infty}\left(\omega_k\delta_{lk} + \frac{s_{kl}}{U_k}\right)\frac{\partial}{\partial t}\underline{h}_{il}(t) \\
&= \sum_{l=1}^{\infty}\left(\left(\omega_k\delta_{lk} + \frac{s_{kl}}{U_k}\right)\sum_{j=1}^{\infty}\left(-\omega_l\delta_{jl} + \frac{q_{lj}}{U_l}\right)\underline{e}_{ij}(t)\right) \\
&= \sum_{l=1}^{\infty}\left(-\omega_l\omega_k\delta_{lk} - \omega_l\frac{s_{kl}}{U_k}\right)\underline{e}_{il}(t) + \sum_{j=1}^{\infty}\left(\omega_k\frac{q_{kj}}{U_k} + \sum_{l=1}^{\infty}\frac{s_{kl}q_{lj}}{U_kU_l}\right)\underline{e}_{ij}(t) \\
&= \sum_{j=1}^{\infty}\left(-\omega_k^2\delta_{kj} - \omega_j\frac{s_{kj}}{U_k} + \omega_k\frac{q_{kj}}{U_k} + \sum_{l=1}^{\infty}\frac{s_{kl}q_{lj}}{U_kU_l}\right)\underline{e}_{ij}(t).
\end{aligned}
\tag{3.72}
$$

In an analogous manner, the equation for $\underline{h}_{ik}(t)$ is derived by taking the time derivative of (3.70) and then inserting (3.71)

$$
\begin{aligned}
\frac{\partial^2}{\partial t^2}\underline{h}_{ik}(t) &= \sum_{l=1}^{\infty}\left(-\omega_k\delta_{lk} + \frac{q_{kl}}{U_k}\right)\frac{\partial}{\partial t}\underline{e}_{il}(t) \\
&= \sum_{l=1}^{\infty}\left(\left(-\omega_k\delta_{lk} + \frac{q_{kl}}{U_k}\right)\sum_{j=1}^{\infty}\left(\omega_l\delta_{jl} + \frac{s_{lj}}{U_l}\right)\underline{h}_{ij}(t)\right) \\
&= \sum_{l=1}^{\infty}\left(-\omega_l\omega_k\delta_{lk} + \omega_l\frac{q_{kl}}{U_k}\right)\underline{h}_{il}(t) + \sum_{j=1}^{\infty}\left(-\omega_k\frac{s_{kj}}{U_k} + \sum_{l=1}^{\infty}\frac{q_{kl}s_{lj}}{U_kU_l}\right)\underline{h}_{ij}(t) \\
&= \sum_{j=1}^{\infty}\left(-\omega_k^2\delta_{kj} + \omega_j\frac{q_{kj}}{U_k} - \omega_k\frac{s_{kj}}{U_k} + \sum_{l=1}^{\infty}\frac{q_{kl}s_{lj}}{U_kU_l}\right)\underline{h}_{ij}(t).
\end{aligned}
\tag{3.73}
$$

Equations (3.72) and (3.73) still contain unresolved time derivatives of the expansion functions. However, they can straightly be transformed into the perturbed frequencies $\widetilde{\omega}_i$. For example, using the definition (3.52) of $\underline{e}_{ik}(t)$ it is obvious that $\frac{\partial^2}{\partial t^2}$ only applies to $\widetilde{\mathbf{E}}_i(\mathbf{r},t)$ and hence may be substituted by $-\widetilde{\omega}_i^2$ according to (3.24)

$$
\frac{\partial^2}{\partial t^2}\underline{e}_{ik}(t) = \frac{\varepsilon}{2U_k}\iiint_{\widetilde{V}}\left(\underbrace{\left(\frac{\partial^2}{\partial t^2}\widetilde{\mathbf{E}}_i(\mathbf{r},t)\right)}_{-\widetilde{\omega}_i^2\widetilde{\mathbf{E}}_i(\mathbf{r},t)}\cdot\mathbf{E}_k(\mathbf{r})\right)\mathrm{d}V
$$

$$
\frac{\partial^2}{\partial t^2}\underline{e}_{ik}(t) = -\widetilde{\omega}_i^2\underline{e}_{ik}(t).
\tag{3.74}
$$

The same applies to $\underline{h}_{ik}(t)$. Equations (3.72) and (3.73) then finally become

$$
\widetilde{\omega}_i^2\underline{e}_{ik}(t) = \sum_{j=1}^{\infty}\underbrace{\left(\omega_k^2\delta_{kj} + \omega_j\frac{s_{kj}}{U_k} - \omega_k\frac{q_{kj}}{U_k} - \sum_{l=1}^{\infty}\frac{s_{kl}q_{lj}}{U_kU_l}\right)}_{a_{kj}}\underline{e}_{ij}(t),
\tag{3.75}
$$

$$
\widetilde{\omega}_i^2\underline{h}_{ik}(t) = \sum_{j=1}^{\infty}\underbrace{\left(\omega_k^2\delta_{kj} - \omega_j\frac{q_{kj}}{U_k} + \omega_k\frac{s_{kj}}{U_k} - \sum_{l=1}^{\infty}\frac{q_{kl}s_{lj}}{U_kU_l}\right)}_{b_{kj}}\underline{h}_{ij}(t),
\tag{3.76}
$$

describing the coupling of the expansion coefficients for the electric and magnetic field of a perturbed mode i independently of one another by the *electric coupling terms* a_{kj} and the *magnetic coupling terms* b_{kj}. The first sum term in (3.75) and (3.76) represents the squared unperturbed frequency that occurs solely once in both equations. The other sum terms describe the interactions (IAs) of the unperturbed modes by the ratio of their electric and magnetic energy inside the deformed volume ΔV. It is apparent that a simultaneous deformation of PMC and PEC boundaries not only involves a simple sum of the PMC and PEC IA terms q_{kj}, s_{kj} but also an additional coupling sum comprising products of both IA terms. Formulating the interactions of each unperturbed mode k with every other unperturbed mode j describes the complete coupling by two systems of equations that can be written in matrix representation as

$$\widetilde{\omega}_i^2 \begin{pmatrix} \underline{e}_{i,1}(t) \\ \underline{e}_{i,2}(t) \\ \vdots \end{pmatrix} = \underbrace{\begin{pmatrix} a_{1,1} & a_{1,2} & \cdots \\ a_{2,1} & a_{2,2} & \cdots \\ \vdots & \vdots & \ddots \end{pmatrix}}_{\mathbf{A}} \cdot \begin{pmatrix} \underline{e}_{i,1}(t) \\ \underline{e}_{i,2}(t) \\ \vdots \end{pmatrix}, \tag{3.77}$$

$$\widetilde{\omega}_i^2 \begin{pmatrix} \underline{h}_{i,1}(t) \\ \underline{h}_{i,2}(t) \\ \vdots \end{pmatrix} = \underbrace{\begin{pmatrix} b_{1,1} & b_{1,2} & \cdots \\ b_{2,1} & b_{2,2} & \cdots \\ \vdots & \vdots & \ddots \end{pmatrix}}_{\mathbf{B}} \cdot \begin{pmatrix} \underline{h}_{i,1}(t) \\ \underline{h}_{i,2}(t) \\ \vdots \end{pmatrix}. \tag{3.78}$$

By applying further the definitions of the expansion functions made in (3.50) and (3.51) and considering the initial condition $t = 0$, the time functions of the unperturbed modes are eliminated, leaving only the expansion coefficients α_{ik} and β_{ik}

$$\widetilde{\omega}_i^2 \begin{pmatrix} \alpha_{i,1} \\ \alpha_{i,2} \\ \vdots \end{pmatrix} = \mathbf{A} \cdot \begin{pmatrix} \alpha_{i,1} \\ \alpha_{i,2} \\ \vdots \end{pmatrix}, \tag{3.79}$$

$$\widetilde{\omega}_i^2 \begin{pmatrix} \beta_{i,1} \\ \beta_{i,2} \\ \vdots \end{pmatrix} = \mathbf{B} \cdot \begin{pmatrix} \beta_{i,1} \\ \beta_{i,2} \\ \vdots \end{pmatrix}. \tag{3.80}$$

Equations (3.79) and (3.80) describe eigenvalue problems. Both matrices $\mathbf{A}$ and $\mathbf{B}$ are non-symmetric. The i-th eigenvalue of the *electric coupling matrix* $\mathbf{A}$ specifies the squared frequency $\widetilde{\omega}_i^2$ of the i-th perturbed eigenmode while the corresponding eigenvector $\boldsymbol{\alpha}_i$ provides the expansion coefficients of its stationary electric field $\widetilde{\mathbf{E}}_i(\mathbf{r})$. The *magnetic coupling matrix* $\mathbf{B}$ gives identical eigenvalues $\widetilde{\omega}_i^2$ whereas its eigenvectors $\boldsymbol{\beta}_i$ provide the expansion coefficients of the perturbed stationary magnetic fields $\widetilde{\mathbf{H}}_i(\mathbf{r})$. In practice, the expansion is naturally restricted to a finite *number of unperturbed eigenmodes* N_{modes}

$$\widetilde{\mathbf{E}}_i(\mathbf{r}) = \sum_{k=1}^{N_{\mathrm{modes}}} \alpha_{ik} \mathbf{E}_k(\mathbf{r}), \tag{3.81}$$

$$\widetilde{\mathbf{H}}_i(\mathbf{r}) = \sum_{k=1}^{N_{\mathrm{modes}}} \beta_{ik} \mathbf{H}_k(\mathbf{r}), \tag{3.82}$$

reducing $\mathbf{A}$ and $\mathbf{B}$ to square $N_\text{modes} \times N_\text{modes}$ matrices. By analyzing the complete mutual coupling of a set of N_modes unperturbed modes, GST yields an equal number of perturbed modes. However, it must be considered that reasonable results can only be obtained for those perturbed modes for which the unperturbed modes have a sufficiently high order. Thus, the actual *number of perturbed eigenmodes* $\widetilde{N}_\text{modes}$ will be smaller than N_modes. In this context, it must also be taken into account that the upper limit of the unperturbed mode order determines a lower limit of the *perturbation extent* $\Delta\xi$ (unit: m), which defines the minimal 1D dimension of the perturbation. This means, that the highest expansion mode with the index i_max must have a wavelength λ_min smaller than or at most equal to the size of the perturbation [i]

$$\lambda_\text{min} = \lambda_{i_\text{max}} < \Delta\xi. \tag{3.83}$$

The coupling equations (3.79) and (3.80) may also be expressed by use of the temporal frequencies f_k. By dividing both equations by a factor of 2π, all ω_k transform into f_k and the eigenvalues of $\mathbf{A}$ and $\mathbf{B}$ become the squared perturbed frequencies $\widetilde{f}_i^2$. Each modification of the unperturbed resonator geometry into another perturbed geometry involves a different deformed volume ΔV and thereby different coupling matrices $\mathbf{A}$ and $\mathbf{B}$, yielding the corresponding set of perturbed eigenmodes. Principally, an unlimited number of modified resonators can be analyzed with GST, based on one unperturbed resonator geometry on condition that the perturbations exclusively inwardly deform the unperturbed resonator. If a perturbation only affects the PEC boundary of a resonator and $\widetilde{S}_\text{pmc}$ equals S_pmc, all volume integrals q_{kj} vanish and the electric and magnetic coupling terms simplify to

$$a_{kj}^\text{pec} = \omega_k^2 \delta_{kj} + \omega_j \frac{s_{kj}}{U_k}, \tag{3.84}$$

$$b_{kj}^\text{pec} = \omega_k^2 \delta_{kj} + \omega_k \frac{s_{kj}}{U_k}. \tag{3.85}$$

Analogously, the coupling terms reduce to

$$a_{kj}^\text{pmc} = \omega_k^2 \delta_{kj} - \omega_k \frac{q_{kj}}{U_k}, \tag{3.86}$$

$$b_{kj}^\text{pmc} = \omega_k^2 \delta_{kj} - \omega_j \frac{q_{kj}}{U_k} \tag{3.87}$$

if a perturbation is exclusively applied to a PMC boundary. So, in both cases each matrix entry a_{kj} or b_{kj} is merely related to a single PEC or PMC interaction term.

In the following, more general cases of perturbations are considered that do not satisfy the previously applied assumption of clearly separated PEC and PMC surface perturbations. Such cases might be relevant, for instance, if a cavity is treated as a resonator with PEC walls and PMC port faces, as shown in Fig. 3.2. Firstly, a perturbation is examined where the PEC surface is deformed while the PMC surface is shortened or partially removed. This case is demonstrated in Fig. 3.2(a) by a reduction of the cell radius.
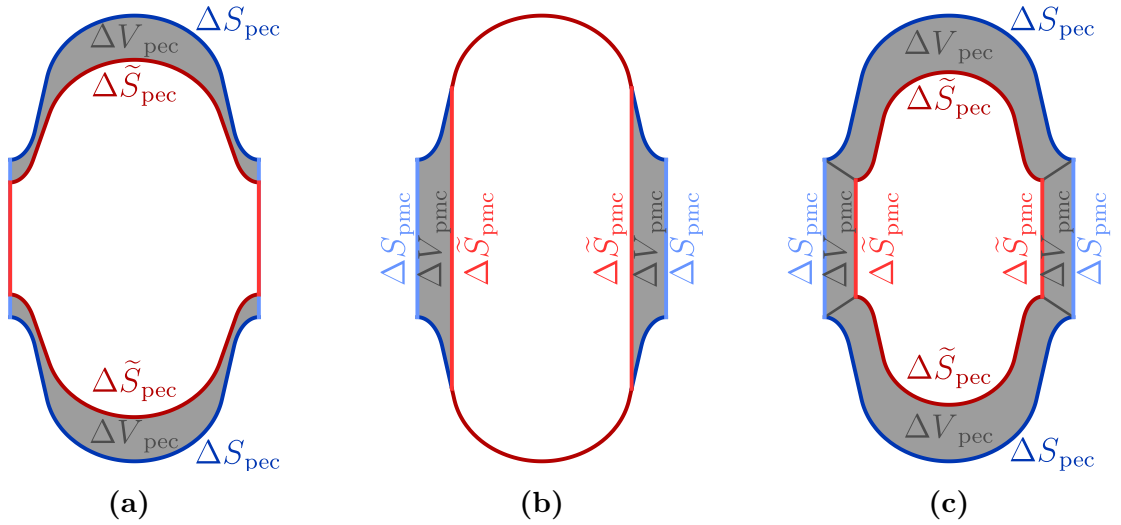
---

[i]The (fictitious) perturbation extent $\Delta\xi$ and wavelength λ_min rather qualitatively describe the required expansion modes since the distribution of the local field extrema may considerably vary in different spatial directions and the perturbation is often irregularly shaped. Nevertheless, equation (3.83) provides an appropriate approximation if the value for $\Delta\xi$ is properly specified.

Regarding the stated conditions, the equations (3.60) and (3.61) with the two surface integrals over $\Delta \widetilde{S}_{\mathrm{pmc}}$ and $\Delta \widetilde{S}_{\mathrm{pec}}$ are still valid. The integral over $\Delta \widetilde{S}_{\mathrm{pmc}}$ in (3.60) vanishes since the perturbed PMC surface $\widetilde{S}_{\mathrm{pmc}}$ always coincides with S_{pmc}, as Fig. 3.3(a) shows by a simplified illustration. Yet, the integral over $\Delta \widetilde{S}_{\mathrm{pec}}$ cannot be transformed into a closed surface integral as it is the case for (3.63) since this would require to also include the unperturbed surface ΔS_{pmc} into the integration (see Fig. 3.3(b)). This, however, is excluded since the tangential component of $\mathbf{E}_k(\mathbf{r})$ does not vanish along ΔS_{pmc} and the closed integral would introduce an additional non-zero term

$$\iint\limits_{\Delta \widetilde{S}_{\mathrm{pec}}} \left(\underline{\widetilde{\mathbf{H}}}_i(\mathbf{r}, t) \times \mathbf{E}_k(\mathbf{r}) \right) \cdot \mathrm{d}\mathbf{A} \neq \oiint\limits_{\Delta \widetilde{S}_{\mathrm{pec}} \cup \Delta S_{\mathrm{pec}} \cup \Delta S_{\mathrm{pmc}}} \left(\underline{\widetilde{\mathbf{H}}}_i(\mathbf{r}, t) \times \mathbf{E}_k(\mathbf{r}) \right) \cdot \mathrm{d}\mathbf{A}. \tag{3.88}$$

(a)   **(b)**   **(c)**

Figure 3.2: Different types of perturbations exemplarily applied to an elliptical resonator with a PEC wall and PMC port faces: (a) Deformation of PEC boundary. (b) Deformation of PMC boundary. (c) Simultaneous deformation of PEC and PMC boundary.

**(a)**   **(b)**   **(c)**
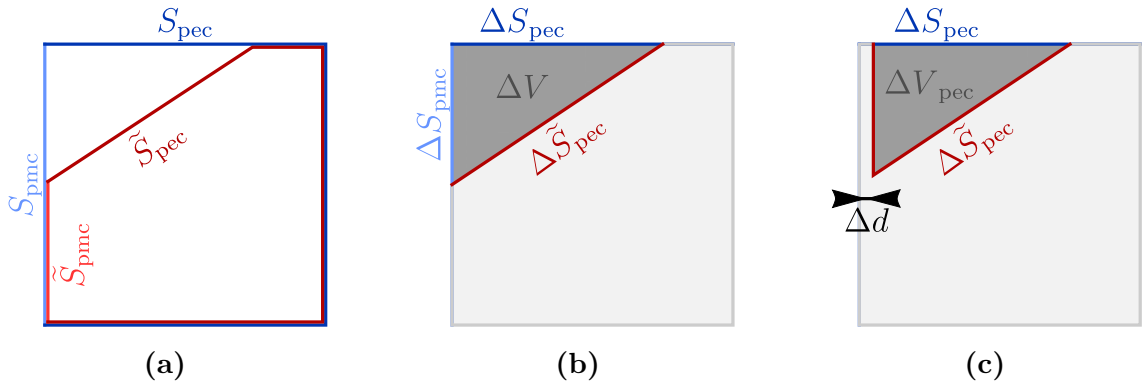
Figure 3.3: Example of a perturbation that deforms the PEC boundary and shortens the PMC boundary: (a) Unperturbed and perturbed surfaces. (b) Removed volume ΔV bounded by the deformed surface $\Delta \widetilde{S}_{\mathrm{pec}}$ and the original surfaces ΔS_{pec}, ΔS_{pmc}. (c) Approximation of ΔV by a volume ΔV_{pec} exclusively bounded by the PEC surfaces $\Delta \widetilde{S}_{\mathrm{pec}}$ and ΔS_{pec} with an infinitely small distance Δd to the actual boundary ΔS_{pmc}.

So, the surface integral may not be converted into the necessary volume integral using the standard approach. Since the PMC surface ΔS_{pmc} cannot be removed directly, it is now assumed that ΔS_{pmc} instead is approached by the perturbed PEC surface $\Delta \widetilde{S}_{\mathrm{pec}}$, as demonstrated in Fig. 3.3(c). By doing so, the volume ΔV is completely bounded by PEC surfaces so that (3.63) and all following equations are valid again. The resulting approximated resonator differs from the actual perturbed resonator by an additional small volume with the thickness Δd that is connected to the actual resonator merely by a short joint with the same thickness Δd. The eigenmodes inside the approximated resonator will only differ noticeably from the ones inside the actual resonator if their wavelength is shorter or at least equal to Δd. By making Δd infinitely small and practically superposing the unperturbed surface ΔS_{pmc} by a perturbed PEC surface $\Delta \widetilde{S}_{\mathrm{pec}}$, the differences become negligible for any finite set of eigenmodes. Consequently, the perturbed eigenmodes can be computed in a very good approximation even in case a part of the unperturbed PMC surface is removed. Self-evidently, the same applies to a deformed PMC surface and a removed PEC surface, as shown in Fig. 3.2(b). A length perturbation of a cylindrical resonator with PEC walls and PMC port faces may serve as a vivid example for the validity of this approach. The IA terms of this clearly one-dimensional perturbation are only determined by the longitudinal dependences of the unperturbed modes and thus have to be independent of the boundary type of the resonator wall.

Secondly, perturbations with truly mixed boundary conditions are regarded. Such a case might occur if a resonator is scaled down, as shown in Fig. 3.2(c). Here, both boundary types are deformed involving a joint volume ΔV. Therefore, neither of the two surface integrals in (3.60) and (3.61) can be extended to a closed surface. Figure 3.4(a) illustrates the underlying geometric relations. Following the previously examined case (see

(a)   **(b)**   **(c)**
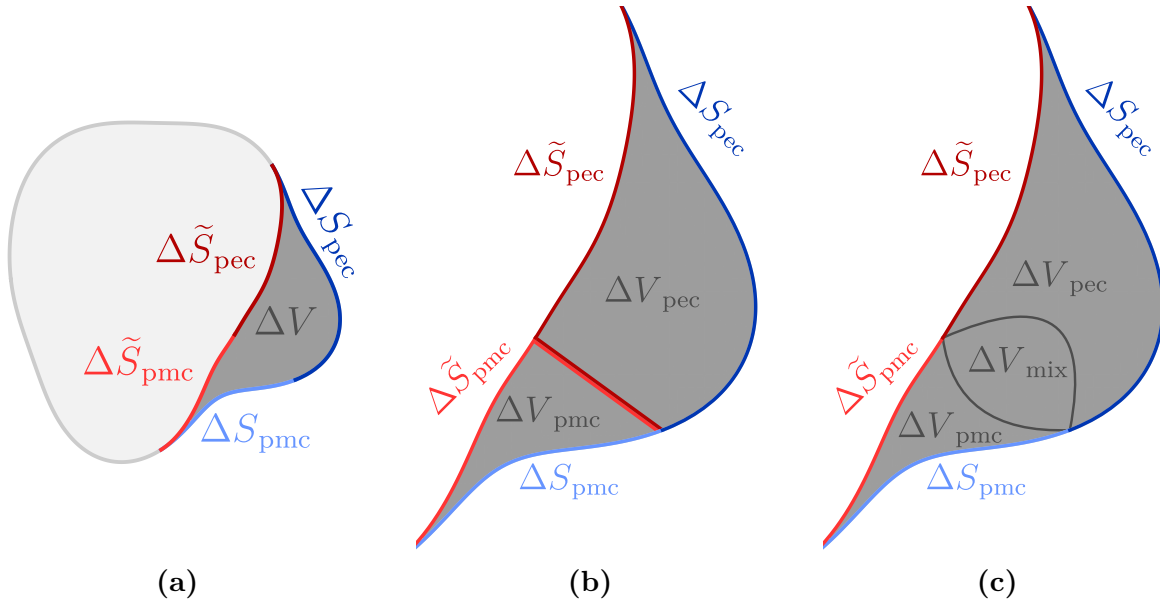
Figure 3.4: 2D scheme of a simultaneous PEC and PMC perturbation: (a) Removed volume ΔV bounded by both PEC and PMC surfaces. (b) Attempt to separate ΔV into distinct PEC and PMC volumes ΔV_{pec}, ΔV_{pmc}. (c) Arbitrarily definable interface between ΔV_{pec} and ΔV_{pmc} that creates a freely assignable volume ΔV_{mix}.

Fig. 3.3(c)), the obvious assumption is to divide the perturbation into two separate PEC and PMC perturbations with an infinitely small distance, as shown in Fig. 3.4(b). Here, the interface between the volumes ΔV_{pec} and ΔV_{pmc} has different boundary conditions on either side. However, while the edges of the interface are clearly defined by the transitions from $\widetilde{S}_{\text{pec}}$ to $\widetilde{S}_{\text{pmc}}$ and from S_{pec} to S_{pmc}, the interface may be arbitrarily shaped in-between. This entails that a volume ΔV_{mix} between two possible interfaces, as illustrated in Fig. 3.4(c), can be assigned to the volume ΔV_{pec} as well as to the volume ΔV_{pmc}. But this would not only cause different volume integrals s_{kj} and q_{kj} but also different electric and magnetic coupling matrices $\mathbf{A}$ and $\mathbf{B}$, as can be easily understood from (3.75) and (3.76). It follows that the approach is invalid for such a case. A possible explanation is that, in contrast to the previous case where a former unperturbed boundary is superposed with a new perturbed boundary at the outer edge of ΔV, here, an artificial boundary is created within the volume ΔV. As a consequence, perturbations that deform both PEC and PMC surfaces at the transition between the two boundary types cannot be covered by GST and the eigenmodes of a perturbed resonator, as shown in Fig. 3.2(c), cannot be computed.

Resonators with a finite conductivity causing intrinsic wall losses cannot be treated directly. The non-orthogonality of their eigenmodes and the simultaneous occurrence of non-zero tangential electric and magnetic fields at the surface $\widetilde{S}$ prevent a derivation as from (3.56) on. A derivation based on a generalized orthogonality could not be found. However, for good conductors, which is the case for both SC and NC cavities, energy loss effects and even the non-orthogonal modes can be determined a posteriori by perturbation techniques as described in Subsection 2.4.2.

As a last point, the calculation of the resulting energy of the perturbed modes is briefly discussed since it is frequently required for the resonator characteristics. In analogy to (2.55) the *energy of the i-th perturbed eigenmode* $\widetilde{U}_i$ is defined by its stationary electric field

$$\widetilde{U}_i = \frac{\varepsilon}{2} \iiint\limits_{\widetilde{V}} \widetilde{\mathbf{E}}_i(\mathbf{r}) \cdot \widetilde{\mathbf{E}}_i(\mathbf{r}) \, \mathrm{d}V. \tag{3.89}$$

To avoid the additional expense of analyzing the field inside the complete perturbed volume $\widetilde{V}$, the integration is reduced to the deformed volume ΔV by applying the series expansion (3.81) and the orthogonality relation (2.55) of the unperturbed modes

$$
\begin{aligned}
\widetilde{U}_i &= \sum_{k=1}^{N_{\text{modes}}} \sum_{j=1}^{N_{\text{modes}}} \left(\alpha_{ij}\alpha_{ik} \frac{\varepsilon}{2} \iiint\limits_{\widetilde{V}} \mathbf{E}_k(\mathbf{r}) \cdot \mathbf{E}_j(\mathbf{r}) \, \mathrm{d}V \right) \\
&= \sum_{k=1}^{N_{\text{modes}}} \sum_{j=1}^{N_{\text{modes}}} \alpha_{ij}\alpha_{ik} \frac{\varepsilon}{2} \left(\iiint\limits_{V} \mathbf{E}_k(\mathbf{r}) \cdot \mathbf{E}_j(\mathbf{r}) \, \mathrm{d}V - \iiint\limits_{\Delta V} \mathbf{E}_k(\mathbf{r}) \cdot \mathbf{E}_j(\mathbf{r}) \, \mathrm{d}V \right) \\
&= \sum_{k=1}^{N_{\text{modes}}} \left(\alpha_{ik}^2 U_k - \sum_{j=1}^{N_{\text{modes}}} \alpha_{ij}\alpha_{ik} \left(\underbrace{\frac{\varepsilon}{2} \iiint\limits_{\Delta V_{\text{pmc}}} \mathbf{E}_k(\mathbf{r}) \cdot \mathbf{E}_j(\mathbf{r}) \, \mathrm{d}V}_{q_{e_{kj}}} + \underbrace{\frac{\varepsilon}{2} \iiint\limits_{\Delta V_{\text{pec}}} \mathbf{E}_k(\mathbf{r}) \cdot \mathbf{E}_j(\mathbf{r}) \, \mathrm{d}V}_{s_{e_{kj}}} \right) \right).
\end{aligned}
$$

$$\tag{3.90}$$

The resulting formula expresses the perturbed energy only in terms of already known quantities. For instance, the volume integrals $q_{e_{kj}}$ and $s_{e_{kj}}$ represent the electric energy part in the IA terms q_{kj} and s_{kj} (without the prefactor of 2). Likewise, the energy can be determined from the stationary magnetic field based on (3.82) and (2.56)

$$
\widetilde{U}_i = \sum_{k=1}^{N_{\text{modes}}} \left(\beta_{ik}^2 U_k - \sum_{j=1}^{N_{\text{modes}}} \beta_{ij}\beta_{ik} \left(\underbrace{\frac{\mu}{2} \iiint\limits_{\Delta V_{\text{pmc}}} \mathbf{H}_k(\mathbf{r}) \cdot \mathbf{H}_j(\mathbf{r})\, \mathrm{d}V}_{q_{h_{kj}}} + \underbrace{\frac{\mu}{2} \iiint\limits_{\Delta V_{\text{pec}}} \mathbf{H}_k(\mathbf{r}) \cdot \mathbf{H}_j(\mathbf{r})\, \mathrm{d}V}_{s_{h_{kj}}} \right) \right).
$$

(3.91)

On condition that the energy U_k of all unperturbed modes is normalized to $1\,\mathrm{J}$ and the expansion coefficients are normalized to an absolute value of $\|\boldsymbol{\alpha}_i\| = 1$ and $\|\boldsymbol{\beta}_i\| = 1$ the equations (3.90) and (3.91) simplify to

$$
\widetilde{U}_i = 1\,\mathrm{J} - \sum_{k=1}^{N_{\text{modes}}} \sum_{j=1}^{N_{\text{modes}}} \alpha_{ij}\alpha_{ik} \left(q_{e_{kj}} + s_{e_{kj}} \right),
$$

(3.92)

$$
\widetilde{U}_i = 1\,\mathrm{J} - \sum_{k=1}^{N_{\text{modes}}} \sum_{j=1}^{N_{\text{modes}}} \beta_{ij}\beta_{ik} \left(q_{h_{kj}} + s_{h_{kj}} \right).
$$

(3.93)

3.4 Expansion of a Reduced Eigenmode Set

Considering a deformation that diminishes the volume of the unperturbed resonator, it is evident that a set of N_{modes} unperturbed eigenmodes only allows for expanding a reduced number of perturbed eigenmodes $\widetilde{N}_{\text{modes}} < N_{\text{modes}}$. Depending on the perturbation extent $\Delta\xi$, the wavelength of all modes diminishes. Thus, exceeding a certain mode order, denoted as the *deficient mode order* i_{defi}, the perturbed wavelength $\widetilde{\lambda}_i$ is shorter than the wavelength λ_{min} of the highest unperturbed mode

$$
\widetilde{\lambda}_{i_{\text{defi}}} < \lambda_{\text{min}}.
$$

(3.94)

These deficient perturbed modes with $i \geq i_{\text{defi}}$ cannot in the least be adequately expanded. The just described generalization of Slater's theorem, however, always provides N_{modes} perturbed modes. This is the major drawback of GST since it forces the method to compensate the excess number of perturbed modes. The compensatory mechanism will be discussed in detail in Subsection 5.1.3. In the following, an alternative perturbative method is introduced that was developed particularly to a priori reduce the number of perturbed modes and thereby evade the generation of deficient modes. The method is therefore denoted as *expansion of a reduced eigenmode set* (ERES) and was published in [80]. ERES also bases on the ansatz to expand the stationary electromagnetic field of each

perturbed mode i in terms of a known set of unperturbed modes

$$\widetilde{\mathbf{E}}_i(\mathbf{r}) = \sum_{k=1}^{N_{\text{modes}}} \alpha_{ik}\mathbf{E}_k(\mathbf{r}), \tag{3.95}$$

$$\widetilde{\mathbf{H}}_i(\mathbf{r}) = \sum_{k=1}^{N_{\text{modes}}} \beta_{ik}\mathbf{H}_k(\mathbf{r}). \tag{3.96}$$

In contrast to GST, ERES additionally requires that the energy of all unperturbed modes is invariably normalized to a value of $1\,\text{J}$, as will be explained in the following. The normalization is achieved by dividing the field $\check{\mathbf{E}}_i(\mathbf{r})$, $\check{\mathbf{H}}_i(\mathbf{r})$ of a mode with any particular energy $\check{U}_i$ by the root of its energy

$$\mathbf{E}_i(\mathbf{r}) = \frac{\check{\mathbf{E}}_i(\mathbf{r})}{\sqrt{\check{U}_i}}, \tag{3.97}$$

$$\mathbf{H}_i(\mathbf{r}) = \frac{\check{\mathbf{H}}_i(\mathbf{r})}{\sqrt{\check{U}_i}}. \tag{3.98}$$

Starting with the electric field, the series (3.95) is first applied to the orthogonality relation of the perturbed modes

$$\delta_{ik} = \frac{\varepsilon}{2\widetilde{U}_i} \iiint\limits_{\widetilde{V}} \widetilde{\mathbf{E}}_i(\mathbf{r}) \cdot \widetilde{\mathbf{E}}_k(\mathbf{r})\,\mathrm{d}V$$

$$= \frac{1}{\widetilde{U}_i} \sum_{j=1}^{N_{\text{modes}}} \sum_{l=1}^{N_{\text{modes}}} \alpha_{ij}\alpha_{kl}\frac{\varepsilon}{2} \iiint\limits_{\widetilde{V}} \mathbf{E}_j(\mathbf{r}) \cdot \mathbf{E}_l(\mathbf{r})\,\mathrm{d}V. \tag{3.99}$$

It is now assumed that each perturbed mode also has an energy $\widetilde{U}_i$ of $1\,\text{J}$. This is permissible since the expansion coefficients $\boldsymbol{\alpha}_i$ of a perturbed mode can always be multiplied by a constant factor to adjust the mode's amplitude. Equation (3.99) then becomes

$$\delta_{ik} = \sum_{j=1}^{N_{\text{modes}}} \sum_{l=1}^{N_{\text{modes}}} \alpha_{ij}\alpha_{kl} \underbrace{\frac{\varepsilon}{2\,\text{J}} \iiint\limits_{\widetilde{V}} \mathbf{E}_j(\mathbf{r}) \cdot \mathbf{E}_l(\mathbf{r})\,\mathrm{d}V}_{g_{e_{jl}}}. \tag{3.100}$$

Here, $g_{e_{jl}}$ denotes the *electric interaction term of the j-th and l-th unperturbed mode* inside the complete perturbed volume. The volume integral can again be reduced to the deformed volume ΔV by applying the orthogonality relation (2.55) and energy normalization (3.97) of the unperturbed modes

$$g_{e_{jl}} = \frac{\varepsilon}{2\,\text{J}} \iiint\limits_{V} \mathbf{E}_j(\mathbf{r}) \cdot \mathbf{E}_l(\mathbf{r})\,\mathrm{d}V - \frac{\varepsilon}{2\,\text{J}} \iiint\limits_{\Delta V} \mathbf{E}_j(\mathbf{r}) \cdot \mathbf{E}_l(\mathbf{r})\,\mathrm{d}V$$

$$= \delta_{jl} - \frac{\varepsilon}{2\,\text{J}} \iiint\limits_{\Delta V} \mathbf{E}_j(\mathbf{r}) \cdot \mathbf{E}_l(\mathbf{r})\,\mathrm{d}V. \tag{3.101}$$

Considering the cases of a purely PEC or purely PMC bounded resonator, the IA terms can be expressed by the same volume integrals as for GST

$$g_{e_{jl}}^{\text{pec}} = \delta_{jl} - s_{e_{jl}}, \tag{3.102}$$
$$g_{e_{jl}}^{\text{pmc}} = \delta_{jl} - q_{e_{jl}}. \tag{3.103}$$

So, both methods found on the same basic integrals. Formulating the interactions of all modes for PEC or PMC boundaries yields the matrix representation of (3.100)

$$\mathbf{I} = \boldsymbol{\mathcal{A}} \cdot \mathbf{G}_e \cdot \boldsymbol{\mathcal{A}}^T, \tag{3.104}$$

with the *electric expansion matrix* $\boldsymbol{\mathcal{A}}$, the symmetric *electric interaction matrix* $\mathbf{G}_e$ and the *identity matrix* $\mathbf{I}$. Both $\boldsymbol{\mathcal{A}}$ and $\mathbf{G}_e$ are $N_{\text{modes}} \times N_{\text{modes}}$ matrices. Examining the eigensystem of $\mathbf{G}_e$ for one of the cases (3.102) or (3.103) reveals that the majority of the eigenvalues ψ_{e_k} is equal to 1 while the rest of them are positive values in the range $0 \leq \psi_{e_k} < 1$. Please note that this applies only if all unperturbed mode energies are normalized to 1 J according to (3.97). The eigenvectors $\mathbf{v}_{e_k}$ of $\mathbf{G}_e$ form an orthogonal matrix $\mathbf{V}_e$ for which holds

$$\mathbf{V}_e^{-1} = \mathbf{V}_e^T. \tag{3.105}$$

Using the definition that each row of $\mathbf{V}_e$ contains one eigenvector $\mathbf{v}_{e_k}$, the eigenvalue problem of $\mathbf{G}_e$ then is written as

$$\mathbf{G}_e \cdot \mathbf{V}_e^T = \mathbf{V}_e^T \cdot \mathbf{D}_{\psi_e} \tag{3.106}$$
$$\mathbf{D}_{\psi_e} = \mathbf{V}_e \cdot \mathbf{G}_e \cdot \mathbf{V}_e^T. \tag{3.107}$$

Since the eigenvalue matrix $\mathbf{D}_{\psi_e}$ is almost identical to the identity matrix $\mathbf{I}$, (3.107) may be approximated by

$$\mathbf{I} \approx \mathbf{V}_e \cdot \mathbf{G}_e \cdot \mathbf{V}_e^T. \tag{3.108}$$

Comparing (3.108) to (3.104) demonstrates that $\mathbf{V}_e$ thus approximately satisfies the requirements for the expansion coefficient matrix $\boldsymbol{\mathcal{A}}$. For a completely correct solution of the expansion coefficients, however, it is requisite that (3.104) is fulfilled for every row. Therefore, the eigensystem of $\mathbf{G}_e$ is truncated by removing all eigenvalues smaller than 1. The eigenvalue matrix $\mathbf{D}_{\psi_e}$ is thereby limited to a $\widehat{N}_{\text{modes}} \times \widehat{N}_{\text{modes}}$ *truncated eigenvalue matrix* $\widehat{\mathbf{D}}_{\psi_e}$ that is truly identical to $\mathbf{I}$ while the matrix $\mathbf{V}_e$ is reduced to a $\widehat{N}_{\text{modes}} \times N_{\text{modes}}$ *truncated eigenvector matrix* $\widehat{\mathbf{V}}_e$ containing only the corresponding $\widehat{N}_{\text{modes}}$ eigenvectors. So, the number of eigenvalues $\psi_{e_k} = 1$ defines the *reduced number of perturbed modes* $\widehat{N}_{\text{modes}}$. Figure 3.5 illustrates the matrix truncations that transform the eigensystem equation (3.107) into

$$\mathbf{I} = \widehat{\mathbf{V}}_e \cdot \mathbf{G}_e \cdot \widehat{\mathbf{V}}_e^T, \tag{3.109}$$

where $\widehat{\mathbf{V}}_e$ completely satisfies the requirements for $\boldsymbol{\mathcal{A}}$ in (3.104). However, $\widehat{\mathbf{V}}_e$ does not necessarily yield the desired expansion coefficients α_{ik} of the electric fields. Multiplying

|(a)|(b)|(c)|(d)|
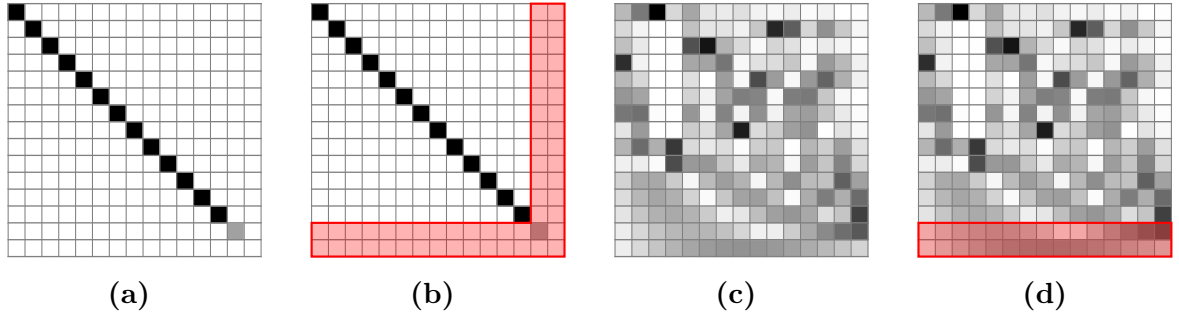
Figure 3.5: Absolute values (white: 0, black: 1) of the eigensystem matrices of $\mathbf{G}_e$: (a) Full eigenvalue matrix $\mathbf{D}_{\psi_e}$. (b) Truncated eigenvalue matrix $\widehat{\mathbf{D}}_{\psi_e}$. (c) Full eigenvector matrix $\mathbf{V}_e$. (d) Truncated eigenvector matrix $\widehat{\mathbf{V}}_e$. The red framed entries are removed to obtain $\widehat{\mathbf{V}}_e$ and $\widehat{\mathbf{D}}_{\psi_e}$.

(3.109) by an arbitrary orthogonal matrix $\mathbf{W}_e$ according to a similarity transformation [81, Ch. 1]

$$\mathbf{I} = \mathbf{W}_e{}^T \cdot \widehat{\mathbf{V}}_e \cdot \mathbf{G}_e \cdot \widehat{\mathbf{V}}_e{}^T \cdot \mathbf{W}_e, \tag{3.110}$$

elucidates that a multitude of solutions for $\boldsymbol{\mathcal{A}}$ exists

$$\boldsymbol{\mathcal{A}} = \mathbf{W}_e{}^T \cdot \widehat{\mathbf{V}}_e. \tag{3.111}$$

Although each eigenvector $\widehat{\mathbf{v}}_{e_i}$ provides a vector field that satisfies the orthogonality (3.99) and thereby the boundary conditions of the electric field of a perturbed eigenmode, it does not guarantee that the field also satisfies Maxwell's equations. To get a unique and particularly the intended solution for $\boldsymbol{\mathcal{A}}$ the additional condition of a steady-state time-harmonic EM field is introduced by the Helmholtz equation (2.53), which has to be valid for every unperturbed and perturbed mode

$$\Delta\mathbf{E}_i(\mathbf{r}) + \omega_i^2 \mu\varepsilon\mathbf{E}_i(\mathbf{r}) = \mathbf{0}, \tag{3.112}$$

$$\Delta\widetilde{\mathbf{E}}_i(\mathbf{r}) + \widetilde{\omega}_i^2 \mu\varepsilon\widetilde{\mathbf{E}}_i(\mathbf{r}) = \mathbf{0}. \tag{3.113}$$

The perturbed field $\widetilde{\mathbf{E}}_i(\mathbf{r})$ is eliminated from (3.113) by applying again the series (3.95) and substituting the Laplacian operator in each sum term according to (3.112)

$$\widetilde{\omega}_i^2 \mu\varepsilon\widetilde{\mathbf{E}}_i(\mathbf{r}) = -\Delta\widetilde{\mathbf{E}}_i(\mathbf{r})$$

$$\widetilde{\omega}_i^2 \mu\varepsilon \sum_{k=1}^{N_{\mathrm{modes}}} \alpha_{ik}\mathbf{E}_k(\mathbf{r}) = -\sum_{k=1}^{N_{\mathrm{modes}}} \alpha_{ik}\big(\Delta\mathbf{E}_k(\mathbf{r})\big)$$

$$\widetilde{\omega}_i^2 \sum_{k=1}^{N_{\mathrm{modes}}} \alpha_{ik}\mathbf{E}_k(\mathbf{r}) = \sum_{k=1}^{N_{\mathrm{modes}}} \alpha_{ik}\omega_k^2\,\mathbf{E}_k(\mathbf{r}). \tag{3.114}$$

The resulting equation contains the unperturbed and perturbed frequencies which have not been involved so far. Its matrix formulation

$$\mathbf{D}_{\widetilde{\omega}}^2 \cdot \boldsymbol{\mathcal{A}} \cdot \begin{pmatrix} \mathbf{E}_1(\mathbf{r}) \\ \vdots \\ \mathbf{E}_{N_{\mathrm{modes}}}(\mathbf{r}) \end{pmatrix} = \boldsymbol{\mathcal{A}} \cdot \mathbf{D}_{\omega}^2 \cdot \begin{pmatrix} \mathbf{E}_1(\mathbf{r}) \\ \vdots \\ \mathbf{E}_{N_{\mathrm{modes}}}(\mathbf{r}) \end{pmatrix}, \tag{3.115}$$

with the *unperturbed eigenfrequency matrix* $\mathbf{D}_\omega$ and the *perturbed eigenfrequency matrix* $\mathbf{D}_{\widetilde{\omega}}$ has to be valid at every position $\mathbf{r}$ within V. Thus, the unperturbed fields $\mathbf{E}_i(\mathbf{r})$ can also be eliminated, resulting in the expression

$$\mathbf{D}_{\widetilde{\omega}}^2 \cdot \boldsymbol{\mathcal{A}} = \boldsymbol{\mathcal{A}} \cdot \mathbf{D}_\omega^2, \tag{3.116}$$

that describes the Helmholtz equation in terms of the expansion coefficients. Substituting the coefficient matrix $\boldsymbol{\mathcal{A}}$ now by the expression (3.111) and right-multiplying, both sides of (3.116) with $\widehat{\mathbf{V}}_e^{\,T}$ yields

$$\mathbf{D}_{\widetilde{\omega}}^2 \cdot \mathbf{W}_e^{\,T} \cdot \widehat{\mathbf{V}}_e = \mathbf{W}_e^{\,T} \cdot \widehat{\mathbf{V}}_e \cdot \mathbf{D}_\omega^2$$
$$\mathbf{D}_{\widetilde{\omega}}^2 \cdot \mathbf{W}_e^{\,T} = \mathbf{W}_e^{\,T} \cdot \left(\widehat{\mathbf{V}}_e \cdot \mathbf{D}_\omega^2 \cdot \widehat{\mathbf{V}}_e^{\,T} \right), \tag{3.117}$$

due to the orthogonality (3.105) of $\widehat{\mathbf{V}}_e$. Further transposing both sides of (3.117) finally results in another eigenvalue problem

$$\mathbf{W}_e \cdot \mathbf{D}_{\widetilde{\omega}}^2 = \underbrace{\left(\widehat{\mathbf{V}}_e \cdot \mathbf{D}_\omega^2 \cdot \widehat{\mathbf{V}}_e^{\,T} \right)}_{\mathbf{Z}_e} \cdot \mathbf{W}_e. \tag{3.118}$$

The $\widehat{N}_{\mathrm{modes}} \times \widehat{N}_{\mathrm{modes}}$ matrix $\mathbf{Z}_e$ is composed of the unperturbed frequencies and the previously determined eigenvectors of the electric interaction matrix $\mathbf{G}_e$. The square root of its eigenvalues directly provides the perturbed frequencies $\widetilde{\omega}_i$ while its eigenvector matrix $\mathbf{W}_e$ forms the required additional orthogonal matrix for determining the $\widehat{N}_{\mathrm{modes}}$ electric expansion coefficients $\boldsymbol{\alpha}_i$ according to (3.111).

The stationary magnetic fields can be determined in an analogous manner based on the $\widehat{N}_{\mathrm{modes}} \times N_{\mathrm{modes}}$ *magnetic expansion matrix* $\boldsymbol{\mathcal{B}}$

$$\boldsymbol{\mathcal{B}} = \mathbf{W}_h^{\,T} \cdot \widehat{\mathbf{V}}_h. \tag{3.119}$$

The $\widehat{N}_{\mathrm{modes}} \times N_{\mathrm{modes}}$ *truncated eigenvector matrix* $\widehat{\mathbf{V}}_h$ of the symmetric *magnetic interaction matrix* $\mathbf{G}_h$ with

$$\mathbf{I} = \widehat{\mathbf{V}}_h \cdot \mathbf{G}_h \cdot \widehat{\mathbf{V}}_h^{\,T}, \tag{3.120}$$

provides the first matrix necessary for (3.119). At this, the *magnetic interaction term of the j-th and l-th normalized unperturbed mode* $g_{h_{jl}}$ is defined as

$$g_{h_{jl}} = \frac{\mu}{2\,\mathrm{J}} \iiint\limits_{\widetilde{V}} \left(\mathbf{H}_j(\mathbf{r}) \cdot \mathbf{H}_l(\mathbf{r}) \right) \mathrm{d}V. \tag{3.121}$$

Derived from the Helmholtz equation for the magnetic field (2.54)

$$\mathbf{W}_h \cdot \mathbf{D}_{\widetilde{\omega}}^2 = \underbrace{\left(\widehat{\mathbf{V}}_h \cdot \mathbf{D}_\omega^2 \cdot \widehat{\mathbf{V}}_h^{\,T} \right)}_{\mathbf{Z}_h} \cdot \mathbf{W}_h, \tag{3.122}$$

the second required matrix is formed by the eigenvector matrix $\mathbf{W}_h$ of the $\widehat{N}_{\mathrm{modes}} \times \widehat{N}_{\mathrm{modes}}$ matrix $\mathbf{Z}_h$. The eigenvalue matrix $\mathbf{D}_{\widetilde{\omega}}^2$ of $\mathbf{Z}_h$ again provides perturbed frequencies $\widetilde{\omega}_i$.

As initially mentioned, ERES inherently reduces the number $\widehat{N}_{\mathrm{modes}}$ of computed perturbed modes to the actually computable number $\widetilde{N}_{\mathrm{modes}}$. Consequently, $\widehat{N}_{\mathrm{modes}}$ decreases with increasing perturbation extent $\Delta\xi$. The exact number $\widehat{N}_{\mathrm{modes}}$ is defined by

$$|1 - \psi_{e_k}| < \epsilon_{\mathrm{EV}}. \tag{3.123}$$

Here, the *eigenvalue truncation accuracy* ϵ_{EV} determines the threshold value for the removal of deficient perturbed modes from the eigensystem of the interaction matrices $\mathbf{G}_e$ or $\mathbf{G}_h$ and thus regulates the reduced number $\widehat{N}_{\mathrm{modes}}$ of perturbed modes. The energy of the ERES-based perturbed modes can be determined according to (3.92) and (3.93) in the same way as for GST.

Chapter 4

Implementation of Perturbative Methods

This chapter briefly explains the main aspects of the implementation of the perturbative methods (PMs), significant for a correct and precise execution. In addition to it, the most relevant procedures for an enhancement of accuracy or efficiency are described. Some aspects were already published in [82], [83], [84]. Figure 4.1 and 4.2 illustrate the basic execution steps and the related quantities of the generalization of Slater's theorem and
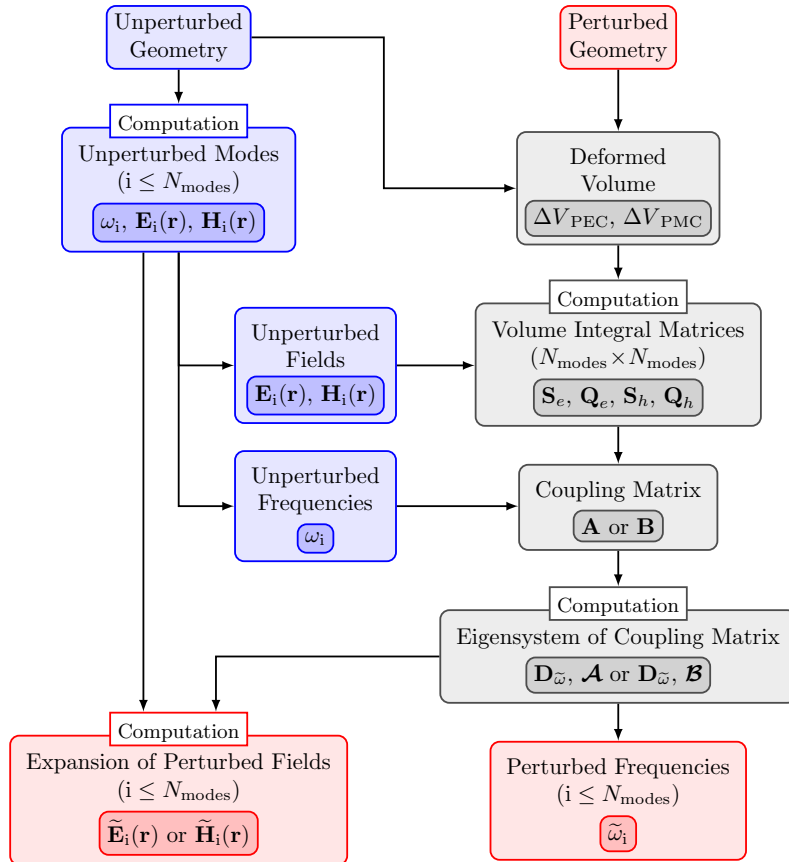
Figure 4.1: Basic execution steps of GST.

the expansion of a reduced eigenmode set. There, unperturbed initial quantities are high-lighted in blue, perturbed target quantities in red and method specific procedures in gray. The implementationally most significant steps are the computation of the unperturbed eigenmodes, the computation of the volume integrals describing the interactions of the unperturbed modes, the solution of the involved eigenvalue problems and the expansion of the perturbed fields. The execution of both PMs, the control of further required applications and the data management was implemented in *Wolfram Mathematica* [85], a commercial symbolic mathematical computation program. Besides a comprehensive range of mathematical function libraries, it also provides several further features including im- and export of a multitude of data formats, basic file system operations, parallel computing and communication with other applications.
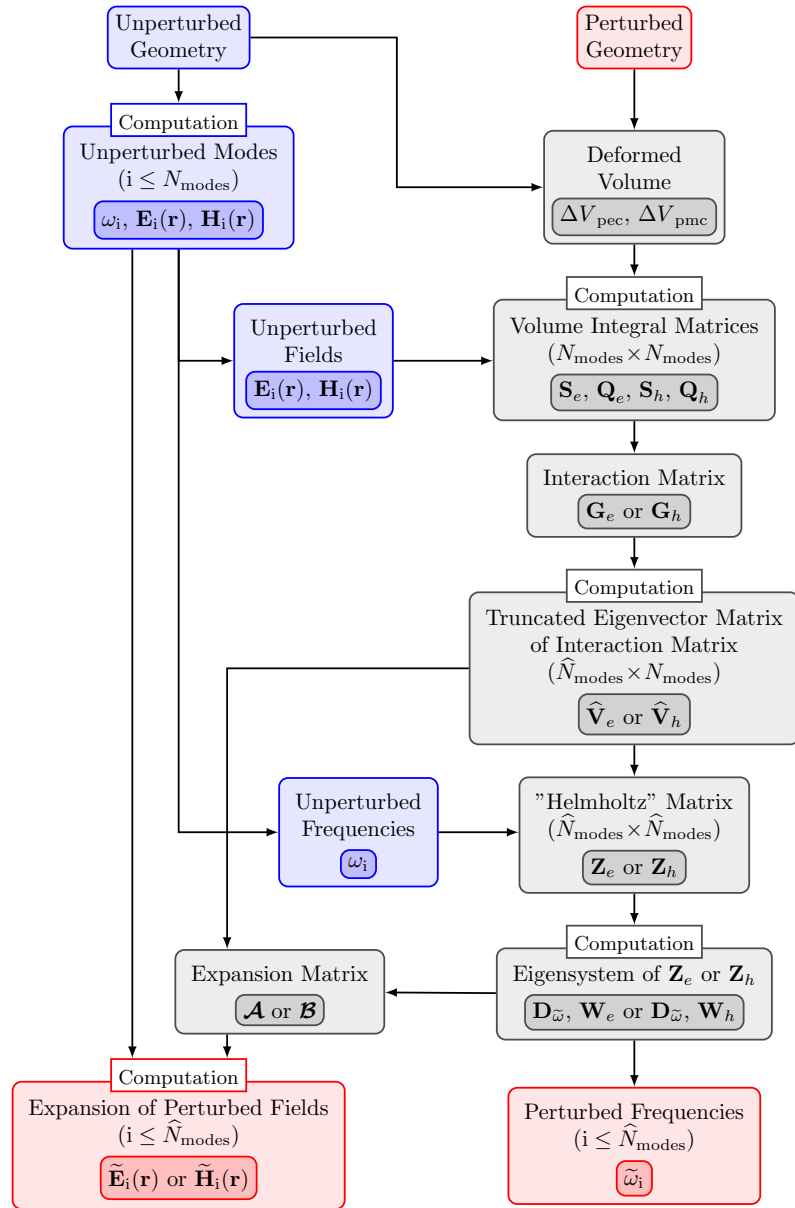
Figure 4.2: Basic execution steps of ERES.

4.1 Calculation of Unperturbed Eigenmodes

An accurate determination of the unperturbed eigenmodes is essential for the PM results since they form the basis of all calculations. The precision of the EM fields is not only relevant for the accuracy of the series expansions of perturbed fields but particularly for the accuracy of the interaction terms which are the key elements of the PMs.

4.1.1 Analytical Calculation of Unperturbed Eigenmodes

The unperturbed and perturbed eigenmodes of rectangular and cylindrical resonator geometries constitute a simple boundary value problem and can analytically be determined as described in Subsection 2.2.2. The corresponding rectangular and cylindrical harmonics, listed in Appendix B, were calculated with Mathematica. At this, the accuracy is set by the machine working precision of the hardware. The used machine precision is about 10^{-16} (single precision of 64 bit CPU) [86, Ch. 1]. Since ERES requires unperturbed modes with an energy of 1 J, the amplitudes of all modes are accordingly normalized.

4.1.2 Numerical Computation of Unperturbed Eigenmodes

In case of a realistic, complex resonator shape the unperturbed eigenmodes cannot be calculated analytically and a numerical computation algorithm is required. For this thesis, the 3D eigenmode solver of *CST Microwave Studio®* (CST MWS) [87] was used. The commercial CST Studio Suite offers a wide range of EM simulation software including static, time or frequency domain solvers and further features like a macro language for script-based execution and a multitude of post processing procedures for the evaluation of the EM fields. CST MWS was further utilized for comparative computations of the eigenmodes of investigated perturbed resonators that serve as reference for the PMs.

Besides the unperturbed frequencies ω_k, the volume integrals $s_{e_{kj}}$, $q_{e_{kj}}$, $q_{e_{kj}}$ and $q_{h_{kj}}$ of the unperturbed electric and magnetic fields over the deformed volume ΔV are the essential base for both GST and ERES (see Fig. 4.1 and 4.2). Since the deformed volume is to a great extent located in direct vicinity to the boundaries of the unperturbed resonator, it is of major importance to accurately compute the fields especially in the boundary region. In addition to an appropriate mesh density, hence, a precise discretization of the boundary is significant. Since the geometry error, a discrepancy between discretized and actual boundary, may lead to an incorrect transition of the fields to zero, an insufficient discretization can seriously distort the volume integrals. CST MWS provides two finite integration technique (FIT) solvers and a finite element method (FEM) solver. A hexahedral dual grid, as used for the FIT-based algorithms (iterative advanced Krylov subspace (AKS) or Jacobi-Davidson (JD) algorithm), is not sufficient for such kind of computations. Despite the use of partially filled mesh cells (perfect boundary approximation, PBA) in order to reduce the geometry error, the boundary fields of structures with a curved shape are strongly affected by the inappropriate hexahedral discretization, as Fig. 4.3 shows. The figure demonstrates that FEM combined with a tetrahedral mesh and the use of curved elements proved to reproduce the boundary much more precisely than a hexahedral mesh with the same mesh resolution. Therefore, all eigenmodes were
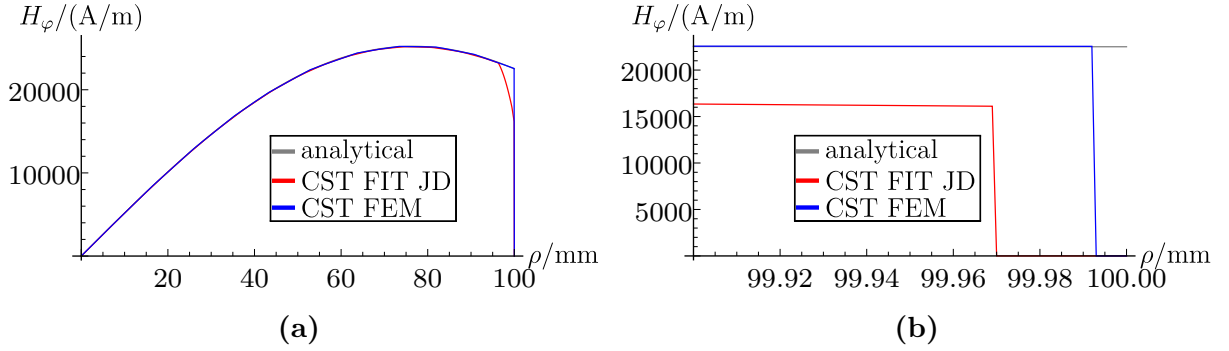
Figure 4.3: Effect of the geometry error for a cylindrical resonator ($R = 100\,\mathrm{mm}$) computed in CST MWS demonstrated by the $\mathrm{TM}_{0,1,0}$ magnetic field H_φ along the radial coordinate direction ρ (at $\varphi = \pi/9$) based on FIT with hexahedral mesh and FEM with tetrahedral mesh ($N_{\mathrm{step}\lambda} \approx 25$): (a) The FIT-based field noticeably deviates in the boundary region whereas the FEM-based field coincides very well. (b) The FEM-based field also has a distinctly smaller defective boundary region ($7.5\,\mu\mathrm{m}$) than the FIT field ($29.5\,\mu\mathrm{m}$).

exclusively computed based on a tetrahedral mesh and the FEM solver with basis functions of second or third order. Since a relatively large number of unperturbed modes over a wide frequency range is required for the PMs, the numerical eigenmode computation is realized by an automated script that iteratively computes sets of modes over consecutive frequency intervals. Each frequency interval constitutes an independent simulation which is executed with a fixed initial *number of steps per wavelength* $N_{\mathrm{step}\lambda}$, defined by the lowest frequency within the interval. Subsequently, an adaptive mesh refinement is performed whose termination criterion is determined by the desired relative frequency accuracy. However, the available RAM memory poses an upper limit for the *number of mesh cells* N_{mc}. Since the required number of mesh cells increases by the third power of a mode's frequency and the number of steps per wavelength $N_{\mathrm{step}\lambda}$

$$N_{\mathrm{mc}} \propto \left(N_{\mathrm{step}\lambda}\, \omega_i\right)^3, \tag{4.1}$$

the number of steps $N_{\mathrm{step}\lambda}$ has to be reduced when exceeding a certain frequency value. Thus, the desired accuracy cannot be achieved beyond this value and the accuracy increasingly reduces for modes of higher order. The restriction is exemplarily shown for a set of $\mathrm{TM}_{2,n,2}$ modes of a cylindrical resonator in Fig. 4.4. This forces a tradeoff between the number N_{modes} of computed unperturbed modes and their accuracy. A small number N_{modes} restrains the minimal wavelength λ_{min} for the expansion of the perturbed fields while imprecise unperturbed fields result in incorrect interaction terms that likewise distort the PM results. Consequently, the lower accuracy limit must be carefully chosen and verified. CST MWS offers a multitude of further simulation parameters concerning special mesh properties, mesh refinement or solver accuracy that are described in detail in [88]. The fields computed with CST MWS are exported in form of discrete field points for further processing in Mathematica. The CST result reader DLL interface disadvantageously does not support a field export for tetrahedral meshes. Thus, a further script for the automated, correctly ordered export of all modes from the consecutive frequency interval simulations had to be developed. CST MWS automatically normalizes the computed modes to an energy of $1\,\mathrm{J}$. So the modes can directly be utilized for GST and ERES.
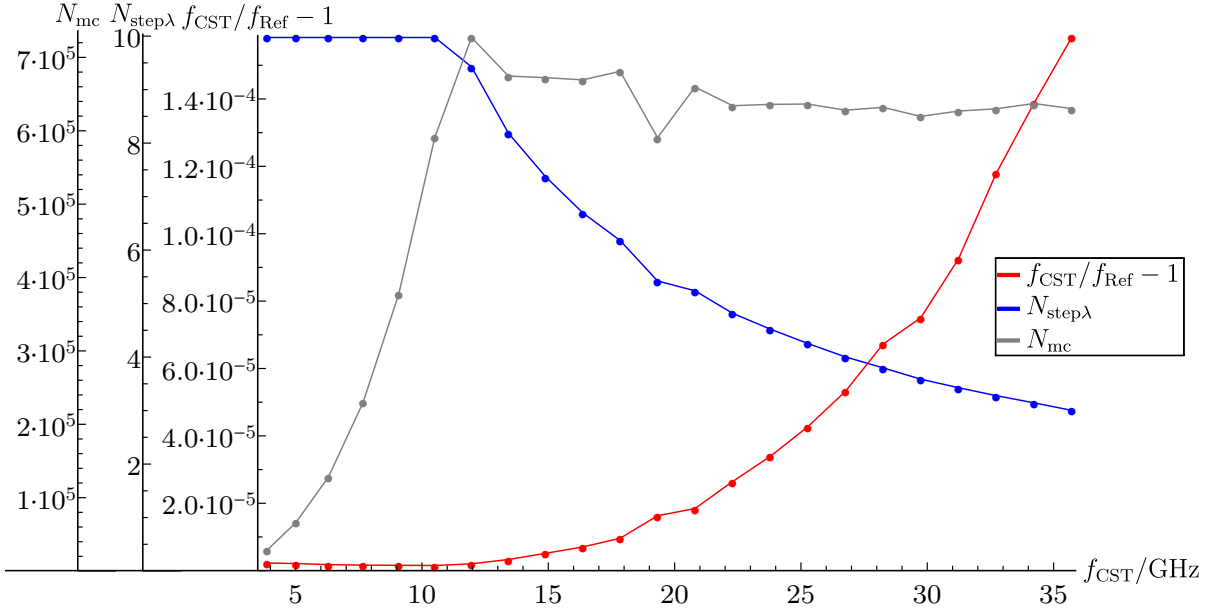
Figure 4.4: Parameters of a CST MWS eigenmode computation of $TM_{2,n,2}$ modes ($1 \leq n \leq 23$) of a cylindrical resonator depending on the frequency f_{CST}: Steps per wavelength $N_{\text{step}\lambda}$, number of used mesh cells N_{mc} and resulting relative frequency error.

4.2 Calculation of Interaction Terms

Like the unperturbed eigenmodes, the interaction terms of both PMs can be computed analytically and numerically. However, the computation type of the unperturbed modes does not necessarily define the type of the IA terms. The IA matrices $\mathbf{Q}$, $\mathbf{S}$ of GST as well as the IA matrices $\mathbf{G}_e$, $\mathbf{G}_h$ of ERES can directly be deduced from the volume integral matrices $\mathbf{Q}_e$, $\mathbf{S}_e$, $\mathbf{Q}_h$, $\mathbf{S}_h$ of the EM fields and the frequency matrix $\mathbf{D}_\omega$. Hence, once the volume integral matrices are determined, the final IA matrices can easily be calculated by simple mathematical operations. All volume integral matrices are symmetric. Thus, only $(N_{\text{modes}}+1)N_{\text{modes}}/2$ integrals, about half the number of IA terms, need to be determined from the EM fields.

4.2.1 Analytical Calculation of Volume Integral Matrices

In case the EM fields are described by continuous functions, the electric and magnetic volume integrals can be analytically calculated according to

$$q_{e_{kj}} = \frac{\varepsilon}{2} \iiint\limits_{\Delta V_{\text{pmc}}} \mathbf{E}_k(\mathbf{r}) \cdot \mathbf{E}_j(\mathbf{r}) \, \mathrm{d}V, \tag{4.2}$$

$$s_{e_{kj}} = \frac{\varepsilon}{2} \iiint\limits_{\Delta V_{\text{pec}}} \mathbf{E}_k(\mathbf{r}) \cdot \mathbf{E}_j(\mathbf{r}) \, \mathrm{d}V, \tag{4.3}$$

$$q_{h_{kj}} = \frac{\mu}{2} \iiint\limits_{\Delta V_{\text{pmc}}} \mathbf{H}_k(\mathbf{r}) \cdot \mathbf{H}_j(\mathbf{r}) \, \mathrm{d}V, \tag{4.4}$$

$$s_{h_{kj}} = \frac{\mu}{2} \iiint\limits_{\Delta V_{\text{pec}}} \mathbf{H}_k(\mathbf{r}) \cdot \mathbf{H}_j(\mathbf{r}) \, \mathrm{d}V. \tag{4.5}$$

This is invariably feasible for analytically calculated eigenmodes but also for numerically computed ones since the discrete fields may be interpolated to create continuous functions. However, the analytical integration based on interpolation functions for the numerical modes turned out to be very expensive because accurate results can only be achieved by a 3D interpolation of higher degree. Thus, in practice the analytical integration is restricted to analytical eigenmodes.

4.2.2 Numerical Computation of the IA Volume Integrals

An alternative approach for the integration of numerical eigenmodes is a simple numerical integration [89] based on discrete volume elements. Here, each continuous integration is substituted by a sum of discrete field and volume values

$$\iiint\limits_{\Delta V} \mathbf{E}_k(\mathbf{r}) \cdot \mathbf{E}_j(\mathbf{r}) \, \mathrm{d}V \approx \sum_{\nu=1}^{N_{\text{elem}}} \mathbf{E}_k(\mathbf{r}_\nu) \cdot \mathbf{E}_j(\mathbf{r}_\nu) \, V_{\text{elem}_\nu}, \tag{4.6}$$

$$\iiint\limits_{\Delta V} \mathbf{H}_k(\mathbf{r}) \cdot \mathbf{H}_j(\mathbf{r}) \, \mathrm{d}V \approx \sum_{\nu=1}^{N_{\text{elem}}} \mathbf{H}_k(\mathbf{r}_\nu) \cdot \mathbf{H}_j(\mathbf{r}_\nu) \, V_{\text{elem}_\nu}, \tag{4.7}$$

where N_{elem} is the *number of volume elements*. The vector $\mathbf{r}_\nu$ defines the *center of the ν-th volume element* with the volume V_{elem_ν} inside the volume ΔV. At this, ΔV is representative for the volumes ΔV_{pmc} or ΔV_{pec}. Figure 4.5(a) illustrates the commonly used partitioning into cubic elements with a *step size* Δz, also known as *voxels*. Expectedly, the majority of realistic perturbations involve an elongated deformed volume ΔV with a large aspect ratio rather than a volume with equal dimensions in all directions. For instance, a radial deformation has a small radial but a large longitudinal dimension. This results in a relatively high amount of elements intersecting with the boundaries of ΔV. Consequently, a standard voxel partitioning is neither suitable for an adequate discretization of ΔV nor for an accurate sampling of the EM fields due the most likely occurrence of incorrect zero field values. Therefore, an improved partitioning algorithm was developed. It bases on the idea to determine the volume and center of elements that exceed the boundary of ΔV accordingly to the center of mass of a solid [90, Sec. 1.19]

$$V_{\text{elem}_\nu} = \iiint\limits_{V_{\text{elem}_\nu}} \mathrm{d}V, \tag{4.8}$$

$$\mathbf{r}_\nu = \frac{1}{V_{\text{elem}_\nu}} \iiint\limits_{V_{\text{elem}_\nu}} \mathbf{r} \, \mathrm{d}V. \tag{4.9}$$
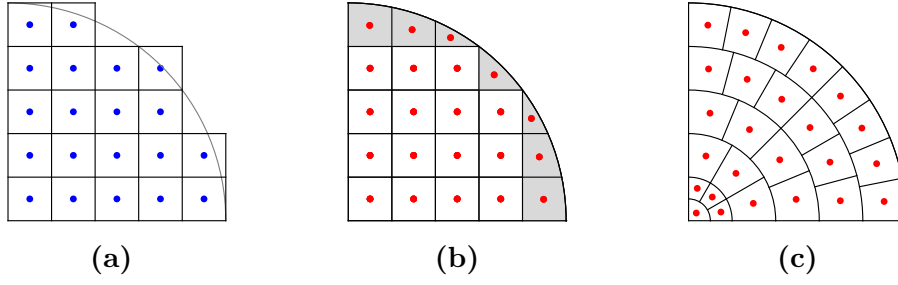
Figure 4.5: 2D scheme of the volume element types for the discretization of a solid: (a) Standard voxel elements. (b) Analytical voxel elements. The center and volume of the boundary elements highlighted in gray are analytically calculated. (c) Analytical cylindrical ring elements with finer discretized inner cylinder.

Figure 4.6: Combination of an adversely small volume element with an adjacent element of regular size: (a) Original separate elements. (b) Combined elements highlighted in gray.

For this, the domain V_{elem_ν} of an element is determined by intersecting the domain of respective *basic volume element* V_{elemStd_ν} and the domain ΔV

$$V_{\mathrm{elem}_\nu} = V_{\mathrm{elemStd}_\nu} \cap \Delta V. \tag{4.10}$$

Since the shapes of the unperturbed and perturbed resonator are usually described by piecewise continuous functions, both the volume and the center of these volume elements can be calculated analytically. Therefore, they are denoted as *analytical volume elements* in the following. Figure 4.5(b) shows an example of a solid discretized with analytical voxel elements. In addition to the voxel, a second basic element type, the *cylindrical ring element*, was implemented specially for rotationally symmetric structures. A basic cylindrical ring element is defined by a fixed *polar radial step size* $\Delta\rho$ that is equal to the *longitudinal step size* Δz and a radius-dependent *azimuthal step size* $\Delta\varphi$ that is about $\Delta\rho/\rho_\nu$. The distribution of these elements more adequately matches the EM field patterns in rotationally symmetric structures, as illustrated in Fig. 4.5(c), and they can likewise easily be calculated. Analytical boundary volume elements allow not only for a correct calculation of their volume but more importantly also guarantee that their center is invariably inside ΔV. In this way the occurrence of incorrect zero field values is greatly reduced and the accuracy of the discrete volume integrals $\mathbf{Q}_e$, $\mathbf{S}_e$, $\mathbf{Q}_h$ and $\mathbf{S}_h$ is significantly improved. The partitioning algorithm further has the feature to combine unnecessarily small boundary elements with adjacent, well dimensioned elements, as demonstrated in Fig. 4.6. Such small elements arising from an adverse intersection of the basic element with the boundary of ΔV not only needlessly increase the element number N_{elem} but often also entails incorrect sampling field values of zero. Each adverse element is detected by a limited *minimal volume size* $V_{\mathrm{elem}_{\min}}$ and is combined with an adjacent element by calculating their joint center and summing up their volumes. Table C.1 in Appendix C.2 demonstrates the

achievable reduction of elements for an elliptical cell. Moreover, the algorithm supports the reduction of 3D cylindrical volume elements to discrete 2D area elements in case of a rotationally symmetric volume ΔV in order to reduce the computational time. At this, the intersection determination (4.10) is only performed for the 2D areas and the 3D volume elements are calculated by shifting the azimuthal coordinate of their centers and multiply their volumes by the respective azimuthal step size $\Delta\varphi$.

For complex perturbations like a dent in the resonator wall, the calculation of analytical volume elements can become computationally more expensive. In such cases it is often more suitable to use a simpler partitioning method. For this reason, another algorithm based on tetrahedra was implemented since the center and volume of the tetrahedral elements can be easily calculated. Mathematica provides a package for *TetGen*, a tetrahedral mesh generator and a 3D Delaunay triangulator [91] that allows to mesh any 3D polyhedral domain. To mesh the volume ΔV, TetGen requires the surface vertices and facets of the domain of ΔV. For this, the unperturbed and perturbed surfaces ΔS, $\Delta\widetilde{S}$ that bound ΔV are discretized based on their analytical shape functions, as shown in Fig. 4.7(a) and 4.7(b). Both surfaces are connected by a number of identical connection points (see red points in Fig. 4.7(c)) that close the surface. At this, dispensable outer connection points

(a)

(b)

(c)

(d)
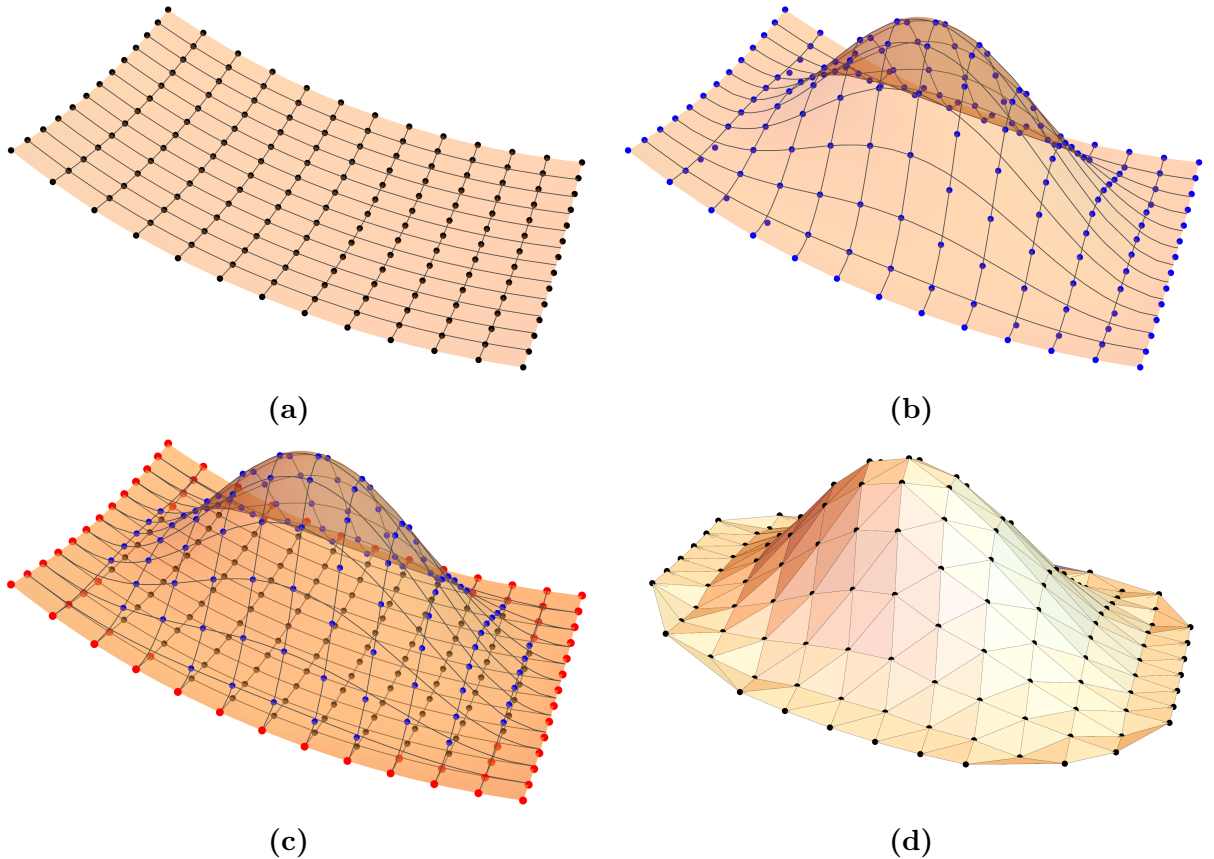
Figure 4.7: Discrete surface points of deformed volume ΔV: (a) Discrete points of unperturbed surface part ΔS. (b) Discrete points of perturbed surface part $\Delta\widetilde{S}$. (c) Discrete points of closed surface of ΔV. The connection points of ΔS and $\Delta\widetilde{S}$ with identical coordinates are displayed in red. (d) Vertices and facets of adjusted closed surface mesh.

(a) **(b)**
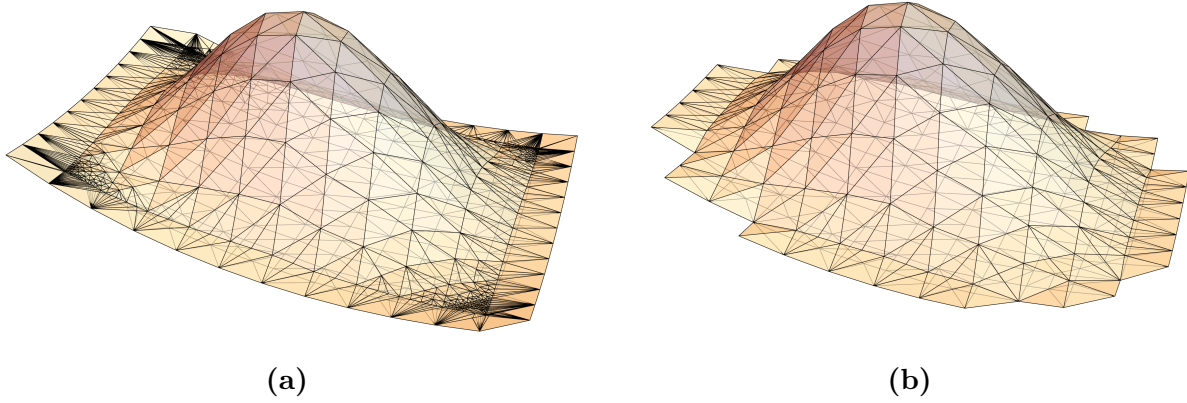
Figure 4.8: Surface mesh after tetrahedralization of discretized volume ΔV: (a) Original discretized surface. (b) Adjusted discretized surface with equalization of adversely close surface points.

that will not necessarily form a vertex of a tetrahedron are deleted to create a smooth surface mesh. If two points of the unperturbed and perturbed surface are too close to each other, this can entail the generation of a huge number of extremely small tetrahedra, as Fig. 4.8(a) demonstrates. To avoid this effect affected perturbed surface points are detected on the basis of a minimal point distance and are set equal to the corresponding unperturbed surface point. In this way, the connection points are additionally adjusted before creating the surface mesh by a 2D Delaunay triangulation of the surface points. The vertices and facets of the resulting surface mesh are displayed in Fig. 4.7(d). Based on the adjusted surface mesh the volume is partitioned with an adequate number of well dimensioned tetrahedra shown in Fig. 4.8(b). By defining a sufficiently small step size for the surface discretization but setting a higher maximal tetrahedron volume, a fine surface mesh can be generated without unnecessarily increasing the number N_{elem} of elements.

Independently of the type of a volume element, the dimensions of the elements have to be suitably small to discretize the wavelength λ_{min} of the highest unperturbed mode. Figure 4.9 illustrates this for a set of $TM_{1,n,2}$ modes in a cylindrical resonator subject to radial perturbations $\Delta R/R$. It shows the maximal absolute error of the discrete volume integrals within two different frequency ranges. An adequate accuracy can already be achieved with a step size $\Delta\rho$ of about $\lambda_{\text{min}}/3.5$. For larger values of $\Delta\rho$, the error significantly increases. Thus, the largest dimension of an element is specified to be at least four times smaller than the minimal wavelength λ_{min} that shall be calculated. Furthermore, the element size also has be adjusted to the size of the deformed volume ΔV. The smaller ΔV is, the smaller principally are the absolute values of the $q_{e_{kj}}$, $s_{e_{kj}}$, $q_{h_{kj}}$ and $s_{h_{kj}}$. This means that although the absolute error of the discrete integrals does not depend on the perturbation extent (see Fig. 4.9) the relative error does. Thus, smaller perturbations require a higher accuracy for the discrete volume integrals (4.6)–(4.7) than larger perturbations to yield PM results with the same precision. Figure 4.10 clearly demonstrates this. In general, the volume integrals can have values within a range of ± 1 J due to the energy normalization. A rough estimation of the value range and consequently also of the necessary accuracy is given by the ratio of the deformed volume ΔV to the complete unperturbed volume V. Hence, the λ_{min}-related step size needs to be decreased approxi-
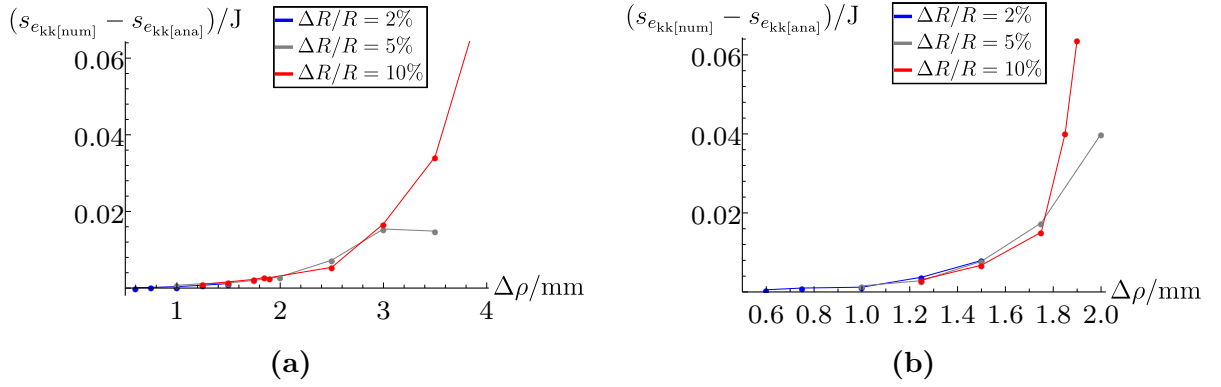
Figure 4.9: Maximal absolute error of discrete electric volume integrals $s_{e_{kk}}$ for $TM_{1,n,2}$ modes depending on the step size $\Delta\rho$ (cylindrical ring elements): (a) Error up to $37.97\,\mathrm{GHz}$ ($\lambda_{\min} = 7.90\,\mathrm{mm}$). (b) Error up to $75.38\,\mathrm{GHz}$ ($\lambda_{\min} = 3.98\,\mathrm{mm}$).
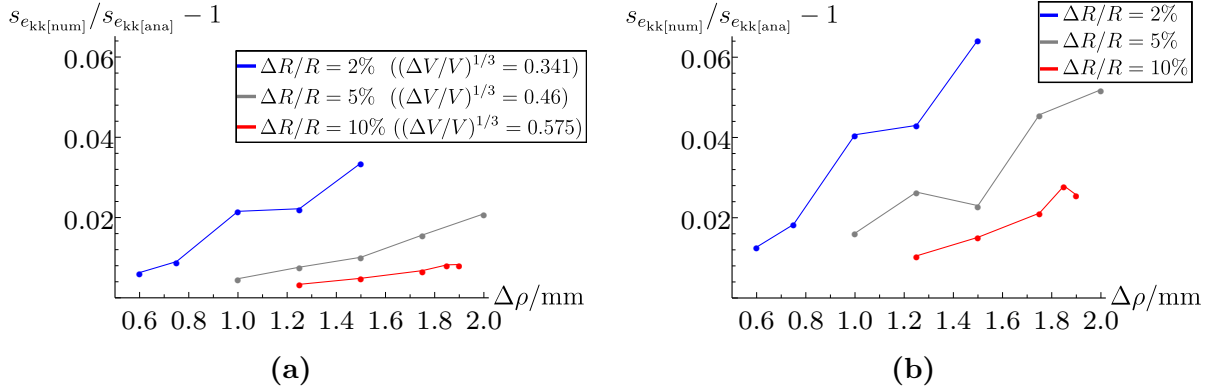
Figure 4.10: Relative error of discrete electric volume integrals $s_{e_{kk}}$ for $TM_{1,n,2}$ modes depending on the step size $\Delta\rho$ up to $37.97\,\mathrm{GHz}$ ($\lambda_{\min} = 7.90\,\mathrm{mm}$): (a) Mean error. (b) Maximal error.

mately by a factor $\sqrt[3]{\Delta V/V}$. The minimal value of the integrals $q_{e_{kk}}$, $s_{e_{kk}}$, $q_{h_{kk}}$ and $s_{h_{kk}}$, referring to the energy amount of the k-th mode contained in ΔV, provides a more exact reference value for the necessary refinement of the step size $\Delta\rho$ or Δz. The sufficiency of the step size can easily be validated by analyzing the convergence of these integral values of a small number of the highest unperturbed modes.

As a last point, a discretization algorithm dedicated to rotationally symmetric unperturbed structures is explained. For such structures, it is only necessary to determine the discrete field values in the 2D plane of the longitudinal section. The sinusoidal azimuthal dependence of the fields is directly factored in during the 3D summation (4.6)–(4.7) in consideration of their polarization. The discretization is therefore denoted as *semi-analytical*. It allows to greatly reduce the amount of processed discrete field data and at the same time to increase the discretization step size. In case the perturbation is also rotationally symmetric the 3D integrals can further be simplified to discrete 2D surface integrals multiplied by a factor of π, reducing the computational effort even more.

4.3 Calculation of Perturbed Eigenmodes

After the calculation of the IA matrices, the arithmetic operations of the respective PM, mostly matrix operations, have to be performed. These finally yield the perturbed frequencies and the series expansion coefficients of the perturbed fields. The operations are identical for analytical and numerical IA terms and are executed with machine working precision. For the expansion of the perturbed fields and a couple of cavity characteristics additional post processing steps were implemented.

4.3.1 Solving of the Eigenvalue Problem

Both perturbative methods require the numerical solution of eigenvalue problems. Mathematica provides different solution methods as described in [92]. For the dense PM matrices, direct solver algorithms based on the package LAPACK [93] are used that transform symmetric matrices into a tridiagonal form [81, Ch. 4] and non-symmetric matrices into a Hessenberg form [81, Ch. 6] before determining the eigensystem. GST only involves the determination of the eigensystems of the two coupling matrices $\mathbf{A}$ and $\mathbf{B}$. Each matrix is non-symmetric and its *condition number* κ (Euclidean norm) is given by the ratio of its maximal and minimal *singular value* σ_i [81, Sec. 4.4]. The condition number defines the sensitivity of the perturbed quantities to the inaccuracy of the entries of $\mathbf{A}$ and $\mathbf{B}$. In the special case of the matrices $\mathbf{A}$ and $\mathbf{B}$, their singular values σ_i are only slightly different from their eigenvalues which are equal to the squares of the perturbed frequencies $\widetilde{f}_i$. Thus, their *condition number* is approximately given by

$$\kappa_{\mathbf{A}} = \kappa_{\mathbf{B}} = \frac{\sigma_{\max}}{\sigma_{\min}} \approx \frac{\left|\widetilde{f}^2_{\max}\right|}{\left|\widetilde{f}^2_{\min}\right|}. \tag{4.11}$$

Depending on the investigated frequency range, $\kappa_{\mathbf{A}}$ and $\kappa_{\mathbf{B}}$ typically lie in a range of 10^2 up to 10^3. However, $\mathbf{A}$ and $\mathbf{B}$ can easily be preconditioned by a *shift-and-invert* transformation [93] that temporarily shifts the eigenvalues without changing the eigenvectors. By defining the eigenvalue shift as the squared maximal unperturbed frequency $f^2_{\max}$, they are transformed into well-conditioned matrices with a condition number of about one. ERES necessitates to compute the eigensystems of the symmetric volume integral matrices $\mathbf{Q}_e$, $\mathbf{S}_e$, $\mathbf{Q}_h$ or $\mathbf{S}_h$ first. Their eigenvalues lie in the range between zero and one. Thus, these matrices can likewise easily be transformed into well-conditioned matrices by an eigenvalue shift of at least one. The same applies to the final symmetric ERES matrices $\mathbf{Z}_e$ and $\mathbf{Z}_h$ whose singular values are exactly the squared perturbed frequencies. Since all eigenvalue problems merely involve small matrices with a couple of hundred elements, the solution requires only a nominal computational effort.

4.3.2 Calculation of Perturbed Fields and Cavity Characteristics

For the evaluation of the perturbed stationary fields or the desired cavity characteristics, a certain amount of unperturbed fields inside the perturbed volume $\widetilde{V}$, or inside a part of

$\widetilde{V}$, needs to be determined to conduct the series expansion. For analytical unperturbed fields, this can be done without effort. In case of numerically computed modes, the respective discrete field data is imported into Mathematica involving an additional expense. Furthermore, post processing routines according to the definitions given in 2.4 were implemented for the calculation of the accelerating voltage V_{acc}, the peak surface fields $E_{\mathrm{peak,sf}}$ and $H_{\mathrm{peak,sf}}$, the longitudinal and transverse shunt impedances over the intrinsic quality factor $R_{\parallel}/Q_0$, $R_{\perp}/Q_0$, as well as for the field flatness η_{ff}.

4.4 Reduction of Computational Effort

In the following, the most essential ancillary routines for improving the effectiveness and efficiency of the PMs are described.

4.4.1 Choice and Segmentation of Unperturbed Geometry

A suitable choice of the initial unperturbed geometry is crucial for an effective application of PMs in the context of parameter studies. Due to the fact that the unperturbed shape can exclusively be deformed inwardly and has to be defined as the very first step, it must be chosen most flexible but at the same time as conformable as possible to the intended perturbed shapes. This is a difficult task especially for the optimization of multicell cavities since the potential geometric changes are difficult to gauge. For sensitivity analyses, it is additionally necessary to likewise de- and increase the geometry. It is therefore often expedient to make the unperturbed geometry generally larger to guarantee that it encloses all potential perturbed geometries. Furthermore, the shape should be defined as symmetric as possible. This not only reduces the expense for computing the unperturbed modes but particularly allows to extend the computable frequency range which is of major importance for the accuracy of the PMs, as will emphatically be demonstrated in Subsection 6.3.2. Besides, asymmetric perturbations are equally feasible based on a symmetric unperturbed shape. It also should carefully be considered which parts of a cavity structure are reasonable to include. For instance, the longitudinal shifting of a HOM coupler, in order to find the optimal coupler position, cannot be sensibly realized since this would require a completely different initial coupler volume. Such structure elements should be attached after a first PM optimization of the pure multicell cavity.

Parameter studies involving the variation of multiple geometric parameters often implicate a large number of investigated geometries. Calculating each volume integral matrix $\mathbf{Q}_e$, $\mathbf{S}_e$, $\mathbf{Q}_h$ or $\mathbf{S}_h$ individually for every case may entail a great expense merely because of the high number of geometries. However, in many cases the individual volumes ΔV involve identical sub-volumes and thus identical sub-integrals that can repetitively be used. By dividing the complete geometry into appropriate segments, as exemplarily shown for a three-cell resonator in Fig. 4.11(a), ΔV can be partitioned into *sub-volumes* ΔV_{ν}

$$\Delta V = \sum_{\nu=1}^{N_{\mathrm{segm}}} \Delta V_{\nu}. \tag{4.12}$$
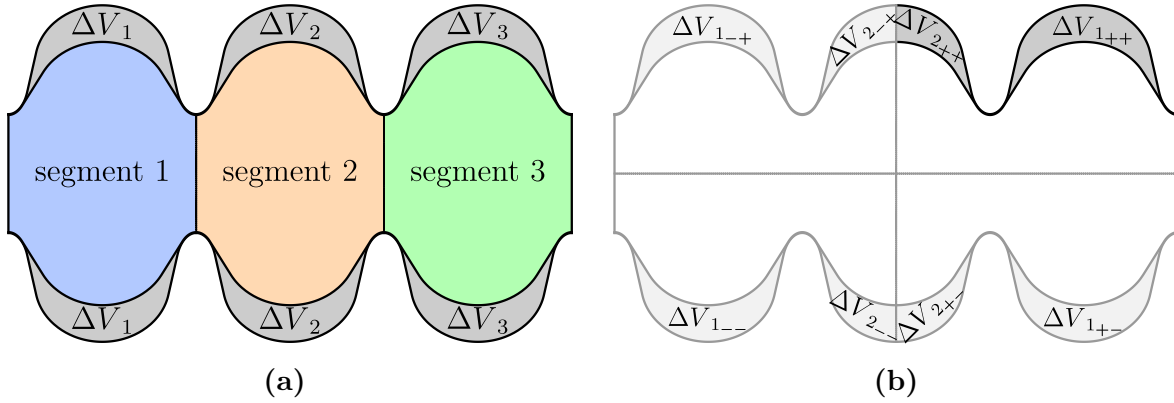
Figure 4.11: Segmentation of a three-cell resonator for the determination of the IA terms: (a) Segmentation into three segments with separate volumes ΔV_1, ΔV_2, ΔV_3. (b) Application of symmetry conditions: Only the IA terms inside $\Delta V_{1_{++}}$ and $\Delta V_{2_{++}}$ are computed from EM field data. All other terms are determined by mirroring these IA terms.

The sub-volume integral matrices of each segment ν are processed separately and a complete integral matrix is formed by the combination of the respective N_{segm} sub-matrices. Thereby, each segment can be varied independently of the others and the effort can be significantly reduced, especially for complex structures and extensive studies. If the unperturbed geometry possesses symmetries, the determination of the volume integrals is further optimized by reducing the amount of field data that has to be processed. Exclusively the integrals on one side of a symmetry plane, here denoted as the positive coordinate range (+), are computed based on the exported EM fields. The quantity of the integrals on the opposite side, in the negative coordinate range (-), are directly deduced from the ones in the positive range according to the applied symmetry conditions, as Fig. 4.11(b) illustrates. For this *mirroring* routine, each integral $q_{e_{kj[\nu]}}$, $s_{e_{kj[\nu]}}$, $q_{h_{kj[\nu]}}$ or $s_{h_{kj[\nu]}}$ only needs to be multiplied with a factor of $+1$ or -1, depending on the relation of the symmetry conditions of the respective k-th and j-th mode. By varying for instance the equator radius of each cell of a N_{cell}-resonator by N_{varEq} different radius values, the eigenmodes of $(N_{\text{varEq}} + 1)^{N_{\text{cell}}} - 1$ geometries can be determined based on just $N_{\text{varEq}} \cdot N_{\text{cell}}$ sets of sub-volume integrals for which only one eighth is determined from exported field data.

4.4.2 Separation of Eigenmodes into Sets of Interacting Modes

In principle, all unperturbed modes of a resonator may be used for the series expansion of a perturbed mode. However, depending on the symmetries of the resonator shape and the symmetries of the applied perturbation not all modes contribute to the expansion. For example, in case that both the unperturbed and perturbed geometry are rotationally symmetric a perturbed mode has to be expanded only in terms of modes with the same azimuthal index m since the φ-dependences of the fields are not affected. Thus, solely monopole modes ($m = 0$), dipole modes ($m = 1$) and so forth mutually interact inside the deformed volume ΔV. In general, the volume integrals $s_{e_{ik}}$, $q_{e_{ik}}$, $s_{h_{ik}}$, $q_{h_{ik}}$ of the EM fields or the resulting IA terms s_{ik}, q_{ik} of two non-interacting modes i and k are zero, i.e. their mutual expansion coefficients α_{ik}, β_{ik} or α_{ki}, β_{ki} vanish. Therefore, each set of
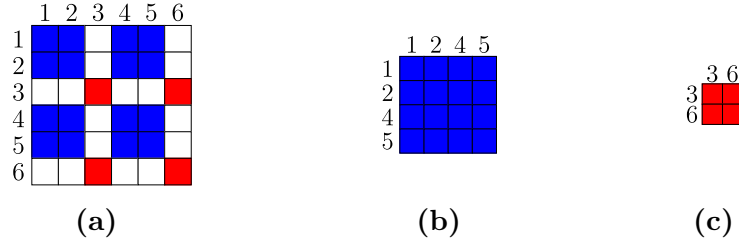
Figure 4.12: Example of an interaction term matrix for a set of six modes: Colored elements indicate actual IA terms unequal to zero while white elements identify non-interacting modes with a zero IA term. (a) Sparse matrix including all modes. (b) Dense matrix of first subset of the modes 1, 2, 4, 5. (c) Dense matrix of second subset of the modes 3, 6.

interacting modes may be processed separately. Instead of one huge set of N_{modes} modes that involves $N_{\mathrm{modes}} \times N_{\mathrm{modes}}$ matrices smaller subsets of N_{ia_ν} modes, each involving only $N_{\mathrm{ia}_\nu} \times N_{\mathrm{ia}_\nu}$ matrices, have to be handled, as illustrated in Fig. 4.12. Depending on the size of the subsets, both the computational effort for determining the IA matrices, performing the PM matrix operations and expanding the perturbed fields, as well as the required data storage may significantly be reduced. To generate the subsets of interacting modes for numerical eigenmodes computed with CST MWS, a mode recognition algorithm for categorizing the modes according to their azimuthal type and their radial and longitudinal dependences was developed [70]. In addition, the regularities of the fields according to their Cartesian symmetries can directly be deduced from the symmetry plane settings in CST MWS.

Chapter 5

Proof of Principle

This chapter presents a validation of the introduced perturbative methods regarding: application range, achievable accuracy and involved computational effort. The validation is performed by means of simple resonator structures subject to simple shapes of perturbations. This allows for an analytical solution of unperturbed and perturbed eigenmodes alike, minimizing the influence of numerical errors. The same applies to the computation of the volume integrals $\mathbf{S}_e$, $\mathbf{Q}_e$, $\mathbf{S}_h$ and $\mathbf{Q}_h$ and thus to the entire implementation of the perturbative methods.

Please note that for reasons of simplicity, physical quantities (primarily the eigenfrequencies and stationary fields) may be named in a shortened notation in this chapter and the following one. For instance, the perturbed stationary electric and magnetic field $\widetilde{\mathbf{E}}(\mathbf{r})$ and $\widetilde{\mathbf{H}}(\mathbf{r})$ are referred to without spatial dependence or overscript symbol $\sim$ as $\mathbf{E}$ and $\mathbf{H}$. In cases where both, unperturbed and perturbed quantities are presented, this is indicated in the text, the figure labels or the figures themselves. For an easier evaluation of the stationary EM fields, the 3D field vectors in the shown figures are normalized to a maximal magnitude of $\|\mathbf{E}_{\max}(\mathbf{r})\| = E_{\max} = 1\,\mathrm{V/m}$ and $\|\mathbf{H}_{\max}(\mathbf{r})\| = H_{\max} = 1\,\mathrm{A/m}$, respectively. So, each field component (in cylindrical coordinates: E_ρ, E_φ, E_z, H_ρ, H_φ and H_z) may vary in a range of ± 1 at most. This allows to use the absolute error representative for the relative error, evading the interfering high sensitivity of the relative error to zero crossings. It must be pointed out, that since electric and magnetic fields are normalized separately, the ratio of their amplitudes in the figures does not satisfy the true physical relation.

5.1 Generalization of Slater's Theorem

This section expounds the accuracy and convergence behavior of the Generalization of Slater's theorem (GST) by evaluating the frequencies and stationary EM fields of the perturbed eigenmodes for different examples of cylindrical and coaxial resonators as well as for perturbations of different kind and extent. Further, the section explains specific characteristics of GST, shows a brief comparison to Slater's cavity perturbation theorem and outlines the required quantity of unperturbed eigenmodes and the computation time involved for the execution of the method. A part of the information was published in [94].

5.1.1 Cylindrical Resonator

A cylindrical resonator represents a simple boundary value problem. Hence, in addition to the transverse mode type (TM or TE) its eigenmodes may be differentiated by an *azimuthal index m* (coordinate φ), a *polar radial index n* (coordinate ρ) and a *longitudinal index p* (coordinate z). The cylindrical harmonics of $\text{TM}_{m,n,p}$ and $\text{TE}_{m,n,p}$ are listed in Appendix B.2. Exemplarily, a cylindrical resonator with PEC boundaries, a length L of 100 mm and a radius R of 100 mm is subject to different topologically one-dimensional perturbations, shown in Fig. 5.1 (radial variation of $\Delta R = R - \widetilde{R}$ or longitudinal variation of $\Delta L = L - \widetilde{L}$), and topologically two-dimensional (simultaneously variation of ΔL and ΔR) perturbations. Due to these simple 1D and 2D perturbations, only specific sets of unperturbed modes interact inside the perturbed volume ΔV. As Table 5.1 displays, there are no interdependences between TM and TE modes and exclusively the mode indices corresponding to the type of perturbation need to be varied. So, each set of interacting modes may be processed separately by the PMs as outlined in Subsection 4.4.2.

The GST-based perturbed frequencies f_{GST} uniformly converge towards the correct solutions f_{Ref}, as Fig. 5.2(a) demonstrates for different $\text{TM}_{0,n,0}$ modes subject to a radial perturbation. The error exponentially decreases to very low values by using only the first few unperturbed modes N_{modes}, as particularly evident for the fundamental mode $\text{TM}_{0,1,0}$ at 1.21 GHz. Figure 5.3 further depicts that the frequency error has a linear convergence rate with respect to the frequency of the highest used unperturbed mode.
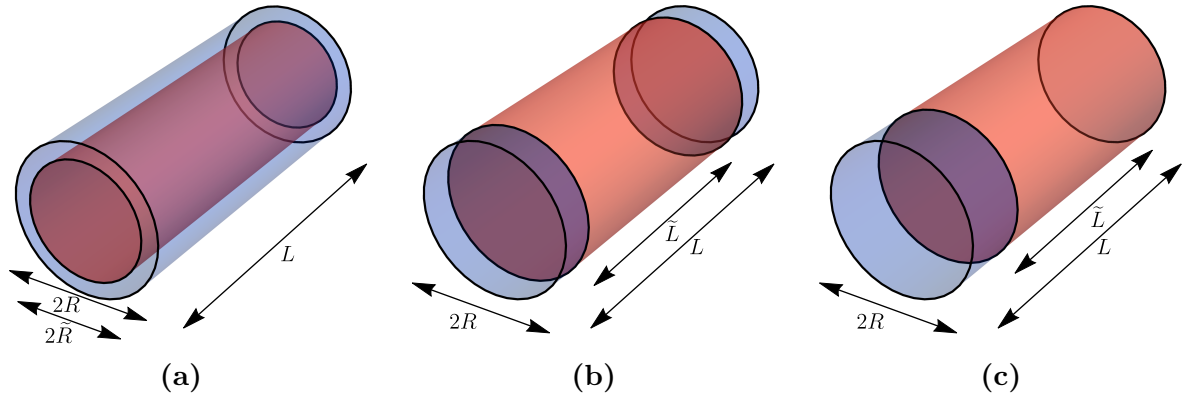
Figure 5.1: Unperturbed (blue) and perturbed (red) cylindrical resonator: (a) Radial perturbation. (b) Symmetric longitudinal perturbation. (c) Asymmetric longitudinal perturbation.

Table 5.1: Subsets of interacting eigenmodes in a cylindrical resonator subject to 1D and 2D perturbations.

Mode specification	Perturbation of			
	R	L (asym.)	L (sym.)	R & L (sym.)
Transverse type (TM/TE)	const.	const.	const.	const.
Azimuthal index m	const.	const.	const.	const.
Polar radial index n	variable	const.	const.	variable
Longitudinal index p	const.	variable	var.: odd/even	var.: odd/even

It can also be seen, that for different mode orders n, the error oscillates with the same period but (minor) differences in amplitude. In contrast, the perturbation extent $\Delta\xi$ does not affect the error amplitude but changes its oscillation period. The extent $\Delta\xi$ determines the unperturbed wavelength λ_{min} that is at least required for an adequate expansion (see (3.83)). An important consequence is that smaller perturbations require a higher number N_{modes} of unperturbed modes for reaching a converging state, as Fig. 5.2(b) clearly illustrates for the $TM_{0,1,0}$ mode. In this context, *converging state* means that the GST frequency of a perturbed mode crosses the correct frequency value for the first time and starts to oscillate around the correct value. Figure 5.2 further depicts that the GST frequencies oscillate approximately symmetrically around it. This entails another essential

(a)

(b)
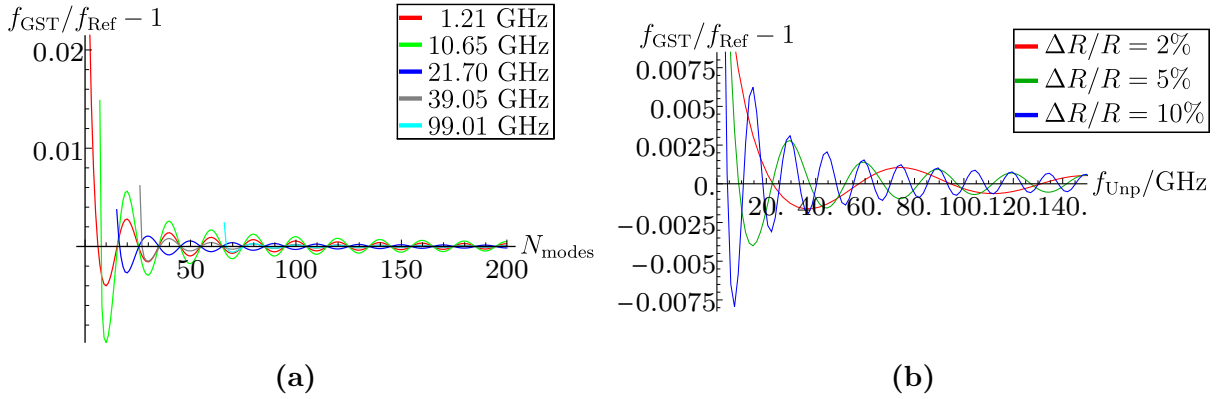
Figure 5.2: Relative frequency error for $TM_{0,n,0}$ modes subject to radial perturbations: (a) Error depending on the number N_{modes} of unperturbed modes for different mode orders ($n = 1, 7, 14, 25, 63$) with $\Delta R/R = 5\%$. (b) Error of the $TM_{0,1,0}$ mode depending on the unperturbed frequency for different perturbations $\Delta R/R$.
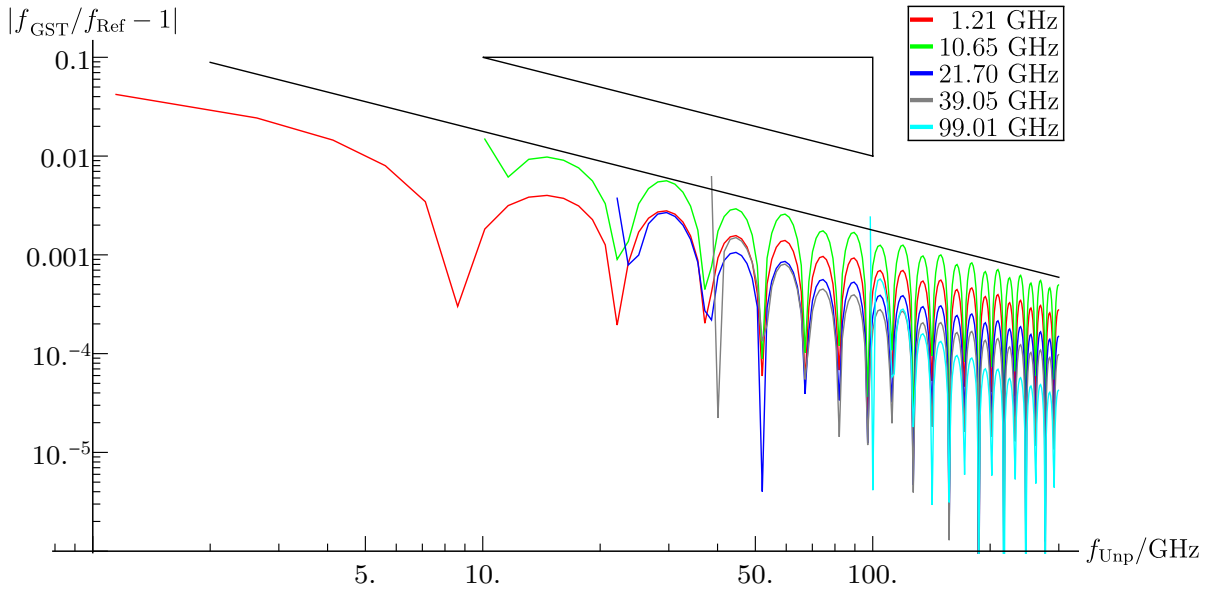
Figure 5.3: Relative frequency error of $TM_{0,n,0}$ modes ($n = 1, 7, 14, 25, 63$) depending on the frequency of the highest unperturbed mode for a radial perturbation of $\Delta R/R = 5\%$. The black line depicts a linear rate of convergence.

conclusion: On condition that the GST frequency of a certain perturbed mode has an ascertainable oscillating behavior (depending on N_{modes}), the optimal GST result for this mode is provided by that number N_{modes} that yields the frequency closest to the average GST frequency. Consequently, the accuracy can potentially be improved by examining the convergence behavior and specifying the respective number N_{modes}. For instance, for the 5 % radial perturbation a N_{modes} of 45 or 55 is optimal (see Fig. 5.2(a)).

For a constant number N_{modes}, each perturbed mode is expanded in terms of the same unperturbed modes. With increasing perturbed mode order (or frequency), less of these modes have a shorter wavelength than the perturbed mode. As a consequence, less modes with a significant contribution to the series expansion exist, in the following denoted as *dominating expansion modes*, since primarily modes with the same or a shorter wavelength involve large expansion coefficients and thereby contribute to the expansion. A comparison of the *GST-based frequency shift* Δf_{GST} between the unperturbed and perturbed frequencies with the *reference frequency shift* Δf_{Ref} in Fig. 5.4 emphasizes this. All of the modes provide a shift ratio $\Delta f_{\mathrm{GST}}/\Delta f_{\mathrm{Ref}}$ smaller than the intended ratio of 1. As expected, the ratio increasingly deviates with rising frequency. Especially the last six modes show significant discrepancies due to the small number of dominating expansion modes. Thus, due to their diminished accuracy, the PM results for the modes of highest order should always be deliberately used. In addition, the 10th, 29th and 48th mode display abruptly increased deviations. This phenomenon, contrary to expectation, will be explained in detail in Subsection 5.1.3. Excluding the 10th, 29th and 48th mode, the majority of the modes fits the true solution very well despite the small number N_{modes} of just 54 modes. The ratio $\Delta f_{\mathrm{GST}}/\Delta f_{\mathrm{Ref}}$ deviates only $4.58 \cdot 10^{-3}$ at minimum and $3.58 \cdot 10^{-2}$ on average from 1. The frequency shift Δf is a well suited criterion for evaluating the accuracy of the underlying PM since it exactly displays if the changes caused by a perturbation can be reproduced. However, modes with a low sensitivity to a certain kind of perturbation may have a relatively high error for Δf since the frequency only slightly changes. But precisely because of the small shift its error is of minor relevance. In contrast to the frequency shift, the relative frequency error $f_{\mathrm{GST}}/f_{\mathrm{Ref}} - 1$ states if the perturbed frequency itself is correct. Thus, the relative frequency error is a rather practically relevant criterion. Figure 5.5 shows that both absolute and relative frequency error are approximately equally distributed around the intended value of zero. Except for the abruptly increased deviations for the 10th, 29th and 48th mode, the absolute error is relatively constant and
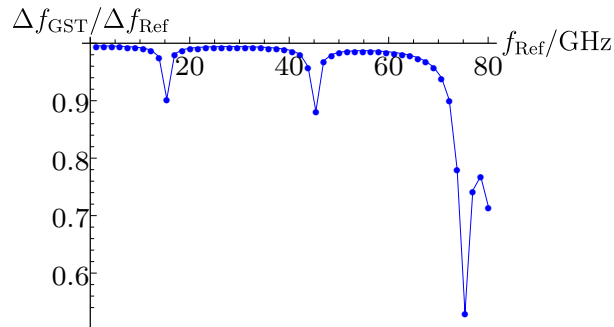

Figure 5.4: Ratio of GST-based and reference frequency shift of $\mathrm{TM}_{0,n,0}$ modes depending on perturbed frequency for $N_{\mathrm{modes}} = 54$ and $\Delta R/R = 5\,\%$.
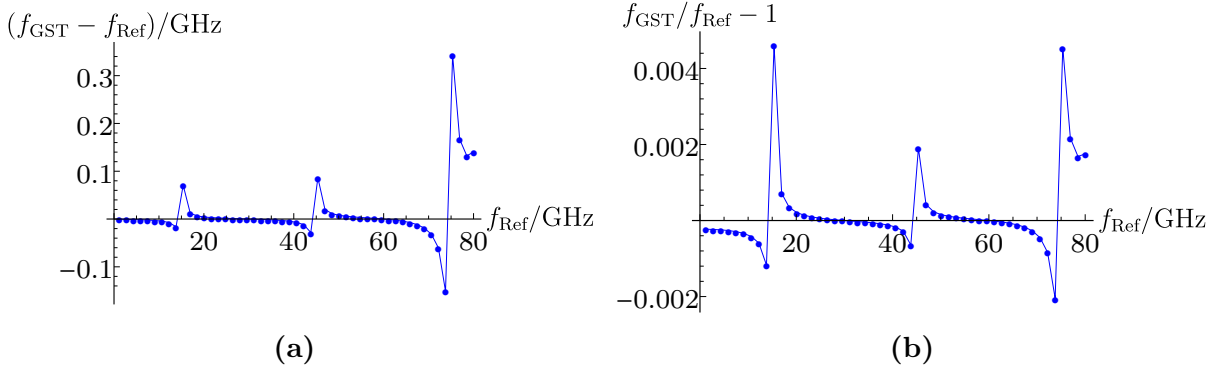
Figure 5.5: Perturbed frequencies of $TM_{0,n,0}$ modes depending on perturbed frequency for $N_{\mathrm{modes}} = 54$ and $\Delta R/R = 5\%$: (a) Absolute error. (b) Relative error.

noticeably increases again only for the last six modes (see Fig. 5.5(a)). The relative error, in contrast, is also increased for the first ten modes (see Fig. 5.5(b)) since their frequencies are comparatively lower. The absolute value of the relative error $|f_{\mathrm{GST}}/f_{\mathrm{Ref}} - 1|$ does not exceed $4.61 \cdot 10^{-3}$ and is $5.62 \cdot 10^{-4}$ on average.

One of the essential advantages of GST is that the method also provides the stationary fields of the perturbed modes. Starting with lower order modes, Fig. 5.6 plots the GST-based EM field, its absolute error and the analytical reference field of the fundamental mode $TM_{0,1,0}$ for a relative radial perturbation $\Delta R/R$ of 5%. As mentioned at the beginning of this chapter, the fields are normalized to a maximal magnitude of $E_{\mathrm{max}} = 1\,\mathrm{V/m}$ and $H_{\mathrm{max}} = 1\,\mathrm{A/m}$ to facilitate the evaluation of the absolute error. As obvious from Fig. 5.6(a), the GST-based electric field E_z coincides very well with the reference field. Its mean absolute error amounts to $1.56 \cdot 10^{-4}$ V/m. Solely close to the perturbed boundary the error increases to $2.60 \cdot 10^{-3}$ V/m. In contrast, the magnetic field H_φ shows distinct deviations, oscillating around the correct field curve (see Fig. 5.6(b)). This oscillating behavior, known as Gibbs phenomenon [49], arises from the non-zero value of H_φ at the interior PEC boundary $\rho = \widetilde{R}$: The unperturbed fields generally have non-zero values at both sides of a perturbed boundary $\Delta \widetilde{S}$ since $\Delta \widetilde{S}$ lies inside the unperturbed volume. But they must reproduce an abrupt transition from a non-zero value to zero in case the boundary condition implies a non-zero perturbed field component. Thus, affected components are reduced to half of their actual value at the perturbed boundary $\Delta \widetilde{S}$, as was explained in detail in Section 3.3. E_z is not affected since it is zero at the radial PEC boundary. The effect reduces the higher the mode order n becomes, as Fig. 5.7(b) demonstrates for the $TM_{0,7,0}$ mode. Here, the deviations due to oscillations are smaller and primarily occur in close proximity of the boundary. A simple spatial low pass filter can be used to remove the Gibbs phenomenon by smoothing the fields. Since the frequency of a perturbed mode and hence its wave number k are known, the 3D wave number k can be used as a good approximation for the 1D wave numbers (in cylindrical coordinates: k_ρ, k_φ and k_z) for adjusting the cutoff wavelength of the low pass filter. So, the undesired GST-induced oscillations can be smoothed without distorting the actual field pattern. Furthermore, H_φ may be replaced by twice its value at $\rho = \widetilde{R}$ to obtain its correct boundary value. By doubling the boundary field value and interpolating the field values in direct vicinity, additionally, a premature reduction towards zero may be avoided. Figure 5.8 displays the
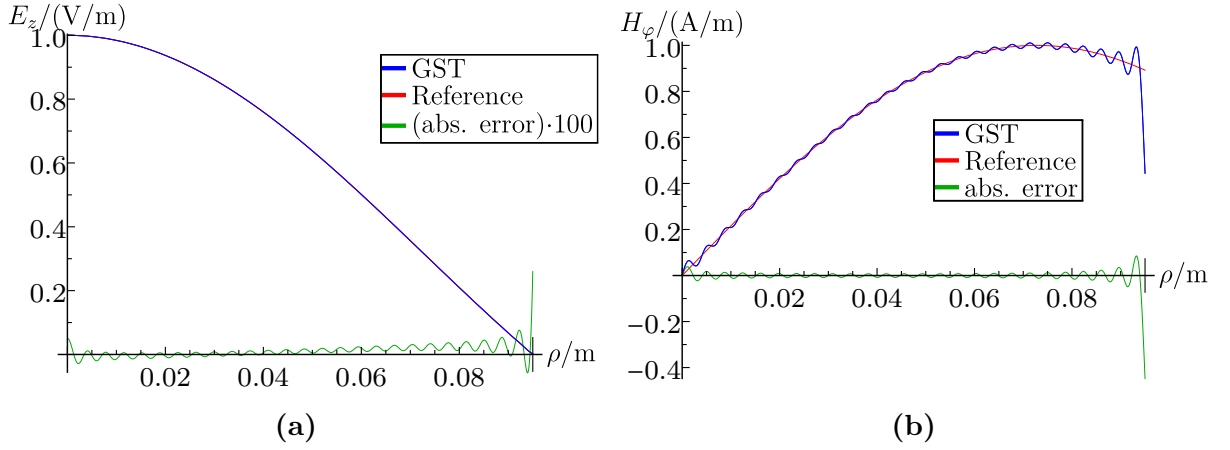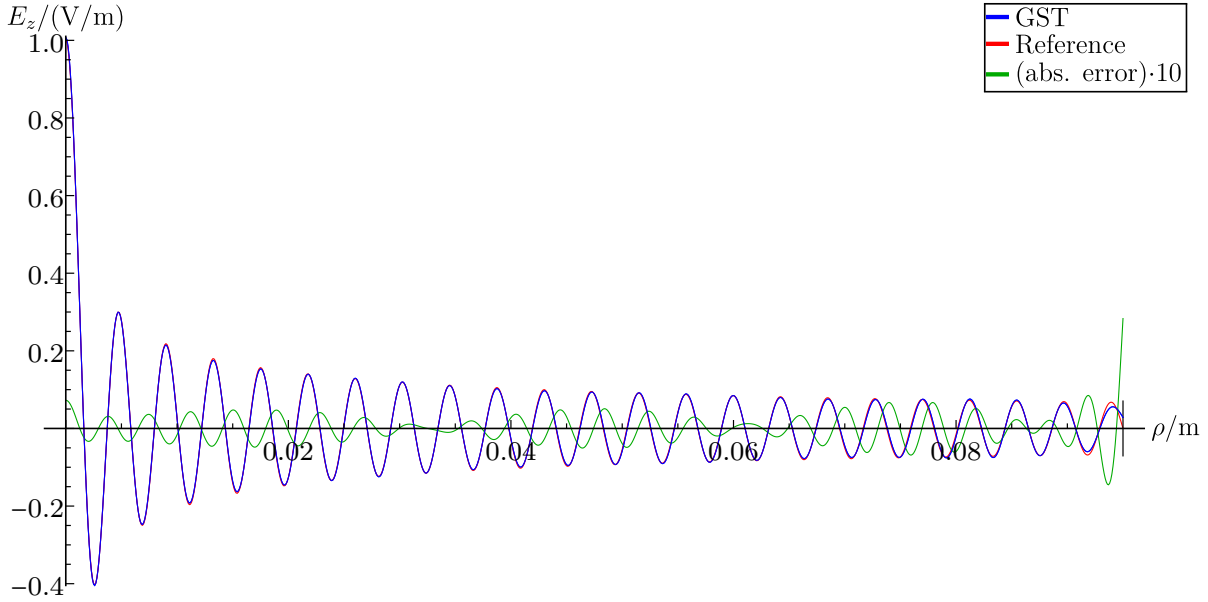
Figure 5.6: Perturbed EM field of the $TM_{0,1,0}$ mode along the perturbed coordinate direction ρ for $\Delta R/R = 5\%$ and $N_{\text{modes}} = 54$: The field components E_φ, E_ρ, H_ρ and H_z are zero and therefore not displayed.
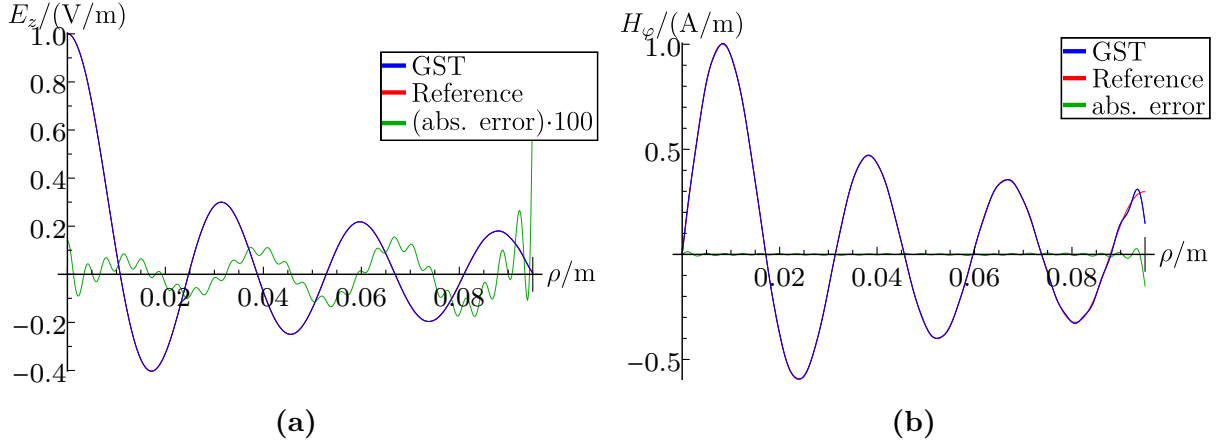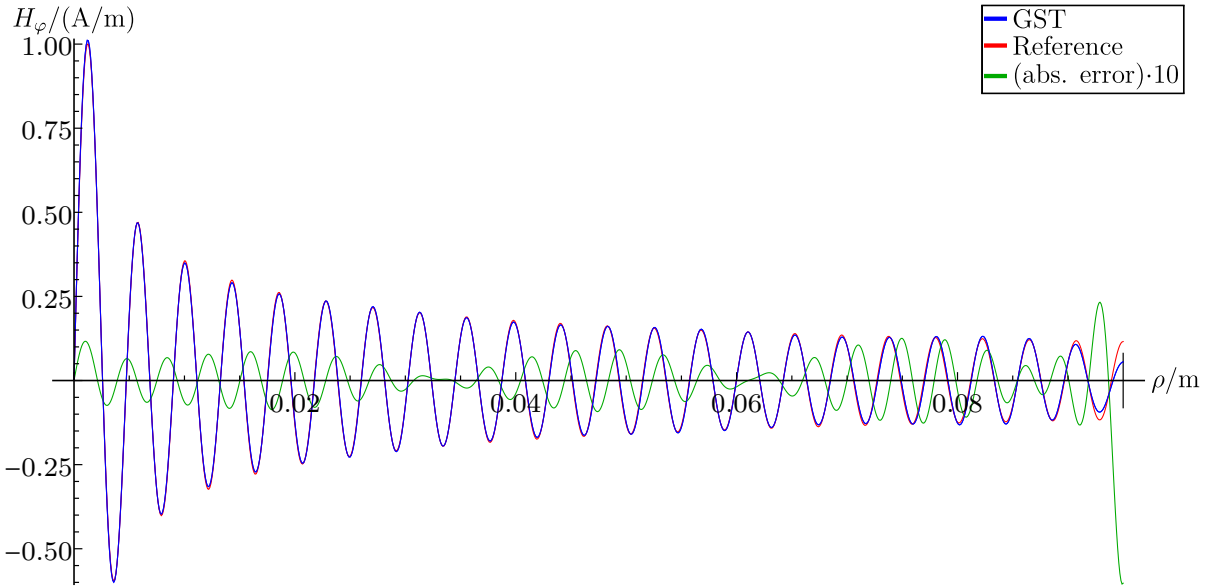

Figure 5.7: Perturbed EM field of the $TM_{0,7,0}$ mode along the perturbed coordinate direction ρ for $\Delta R/R = 5\%$ and $N_{\text{modes}} = 54$: The field components E_φ, E_ρ, H_ρ and H_z are zero and therefore not displayed.
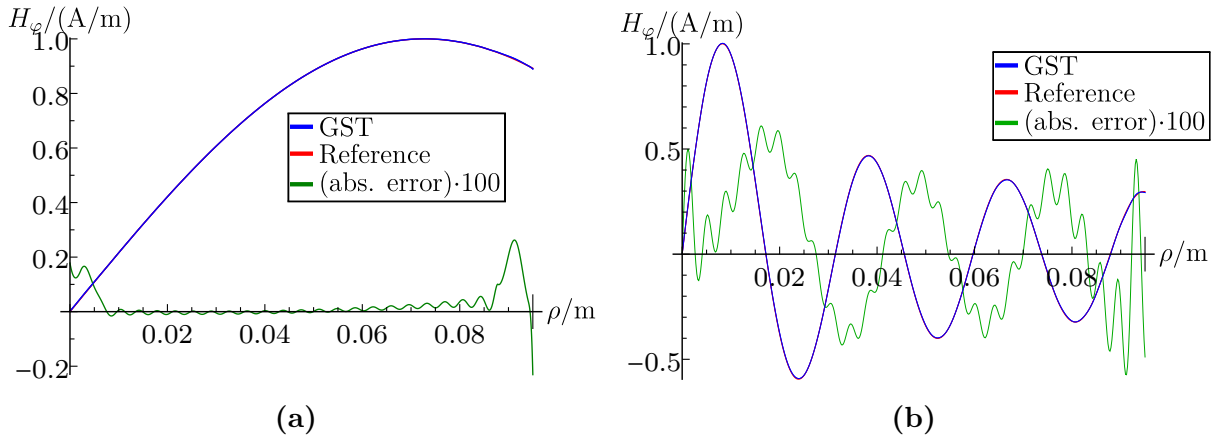
Figure 5.8: Low pass filter smoothed magnetic field H_φ: (a) $TM_{0,1,0}$ mode. (b) $TM_{0,7,0}$ mode.

(a)

(b)

Figure 5.9: Perturbed EM field (unfiltered) of the $TM_{0,45,0}$ mode along the perturbed coordinate direction ρ for $\Delta R/R = 5\%$ and $N_{\mathrm{modes}} = 54$: The field components E_φ, E_ρ, H_ρ and H_z are zero and therefore not displayed.

accordingly smoothed magnetic fields of the $TM_{0,1,0}$ and $TM_{0,7,0}$ mode. The smoothed field H_φ of the $TM_{0,1,0}$ mode has a similar accuracy as E_z except for a minor residue of Gibbs phenomenon close to the boundary where the error rises to $2.65 \cdot 10^{-3}$ V/m. The residue is accounted for by the low mode frequency. Nevertheless, by smoothing H_φ its mean absolute error can be reduced to $4.81 \cdot 10^{-4}$ A/m. The error of the smoothed H_φ field of the $TM_{0,7,0}$ is relatively equally distributed along ρ and on average only slightly higher (by a factor of 2) than the error of the unfiltered electric field. In accordance to the trend of the frequency error, the field deviations increase with rising mode order n. Exemplarily, Fig. 5.9 shows the field of the $TM_{0,45,0}$ mode, for which the frequency shift error begins distinctly to increase (see Fig. 5.4). As a consequence, the absolute error of electric and magnetic field of the $TM_{0,45,0}$ mode is round about one order of magnitude higher than the one of the $TM_{0,1,0}$ mode. The mean absolute errors are $2.71 \cdot 10^{-3}$ V/m (E_z) and $5.26 \cdot 10^{-3}$ A/m (H_φ) while the maximal errors are $2.83 \cdot 10^{-2}$ V/m (E_z) and $6.05 \cdot 10^{-2}$ A/m (H_φ). Nevertheless, despite the high mode order, the GST-based field still matches the reference field to a large extent and marked deviations are solely detectable in close vicinity of the boundary. Figure 5.10 displays the electric field E_z of the $TM_{0,1,0}$ and $TM_{0,7,0}$ mode for an enlarged radial perturbation of $\Delta R/R = 10\%$ to demonstrate the influence of the perturbation extent on the accuracy. A comparison of Fig. 5.10(a) with Fig. 5.6(a) and Fig. 5.10(b) with Fig. 5.7(a) illustrates that the field error only slightly changes if $\Delta R/R$ is doubled and N_{modes} is kept constant. Thus, the perturbation extent just marginally affects the accuracy of the results, however, only provided that N_{modes} is sufficiently high, which means that the series expansion reached a converging state (see Fig. 5.2(b)). Minor differences in the accuracy may arise from the different oscillating behavior, as Fig. 5.2(b) also shows. Appendix C.1 contains further GST results concerning the accuracy of frequencies and stationary fields for $TE_{0,1,p}$ monopole and $TE_{1,1,p}$ dipole modes subject to longitudinal perturbations. In principle, the perturbed quantities for longitudinal perturbations can be determined with a similar accuracy as the just presented radial perturbations.
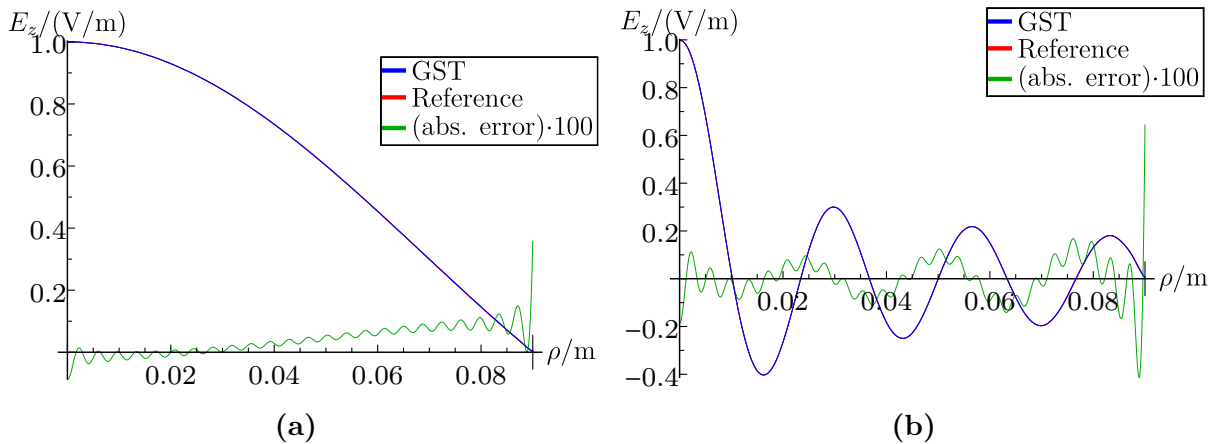
Figure 5.10: Perturbed electric field E_z of $TM_{0,n,0}$ modes along the perturbed coordinate direction ρ for $\Delta R/R = 10\%$ and $N_{\mathrm{modes}} = 54$ (a) $TM_{0,1,0}$ mode. (b) $TM_{0,7,0}$ mode.

In contrast to the one-dimensional perturbations, the number of interacting unperturbed modes increases if a two-dimensional perturbation is applied since not only one but two mode indices are variable, as previously listed in Table 5.1. As a consequence, the frequencies of the unperturbed modes increase considerably slower, as Fig. 5.11 illustrates. The frequency of the 200th unperturbed $TE_{0,n,p}$ mode for a simultaneous radial and longitudinal perturbation is about 17 times smaller than the frequency of the 200th unperturbed $TE_{0,1,p}$ mode for a longitudinal perturbation. This narrowed spacing between neighboring frequencies reduces the speed of convergence depending on the number of modes since the wave numbers of the modes used for the series expansion also increase slower. For instance, $TE_{0,39,3}$ and $TE_{0,5,39}$ are the modes with the highest radial and longitudinal index, respectively, within the first 600 $TE_{0,n,p}$ modes. Thus, GST requires a higher number of modes N_{modes} to reach the same accuracy as for 1D perturbations. The slower convergence of a 2D perturbation is clearly evident from Fig. 5.12. Up to 90 modes are needed for a first crossing of the correct frequency for a simultaneous radial and longitudinal perturbation of $\Delta R/R = 5\,\%$ and $\Delta L/L = 5\,\%$. It also becomes apparent that the frequencies no longer steadily oscillate but show step-like changes. This arises from the fact, that the indices n and p of the dominating modes, providing a higher weight in series expansion, are similar to the ones of the perturbed mode. Thus, the frequency error only significantly changes if such a mode is added to the expansion. By using 96 unperturbed modes, a number just sufficient for a converging state, the first 50 perturbed frequencies can be computed with a mean relative error (MRE) $|f_{\mathrm{GST}}/f_{\mathrm{Ref}} - 1|$ of $2.94 \cdot 10^{-3}$. Compared to 1D perturbations this is an increase of error but still an adequately high accuracy. Increasing N_{modes} to 450 reduces the relative error to only $1.31 \cdot 10^{-3}$ on average and $5.56 \cdot 10^{-3}$ at maximum, as Fig. 5.13 displays for the first 100 $TE_{0,n,p}$ modes. Consequently, the same accuracy as for 1D perturbations can be obtained at the expense of a higher N_{modes}. Figure 5.13 also shows that the frequencies are rather randomly distributed around the correct solution. The figures 5.14 – 5.17 on the following pages present the (partially smoothed) stationary EM fields of the perturbed $TE_{0,1,1}$, $TE_{0,6,1}$, $TE_{0,1,9}$ and $TE_{0,10,9}$ mode. The selection includes the lowest order mode and modes for which one or both mode indices n and p have comparatively high values. Each field component is
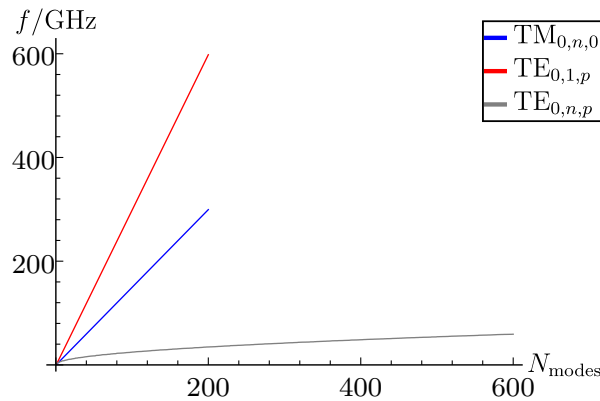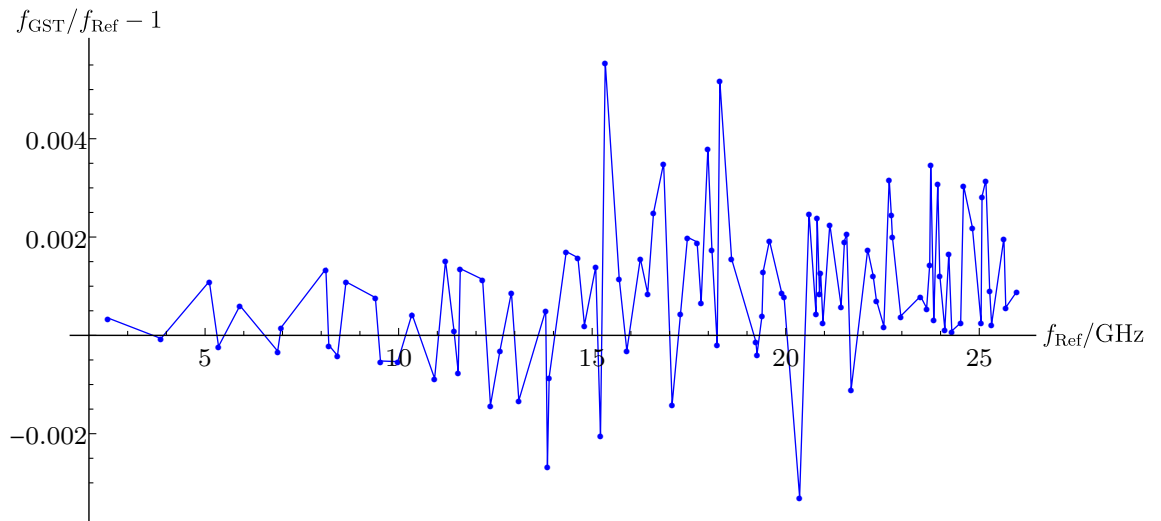

Figure 5.11: Unperturbed frequencies depending on the number N_{modes} of unperturbed modes for different sets of IA modes i.e. for different types of perturbations: $TM_{0,n,0}$ modes for a radial perturbation (blue curve), $TE_{0,1,p}$ (p: odd) modes for a longitudinal perturbation (red curve) and $TE_{0,n,p}$ (p: odd) modes for a 2D perturbation (gray curve).
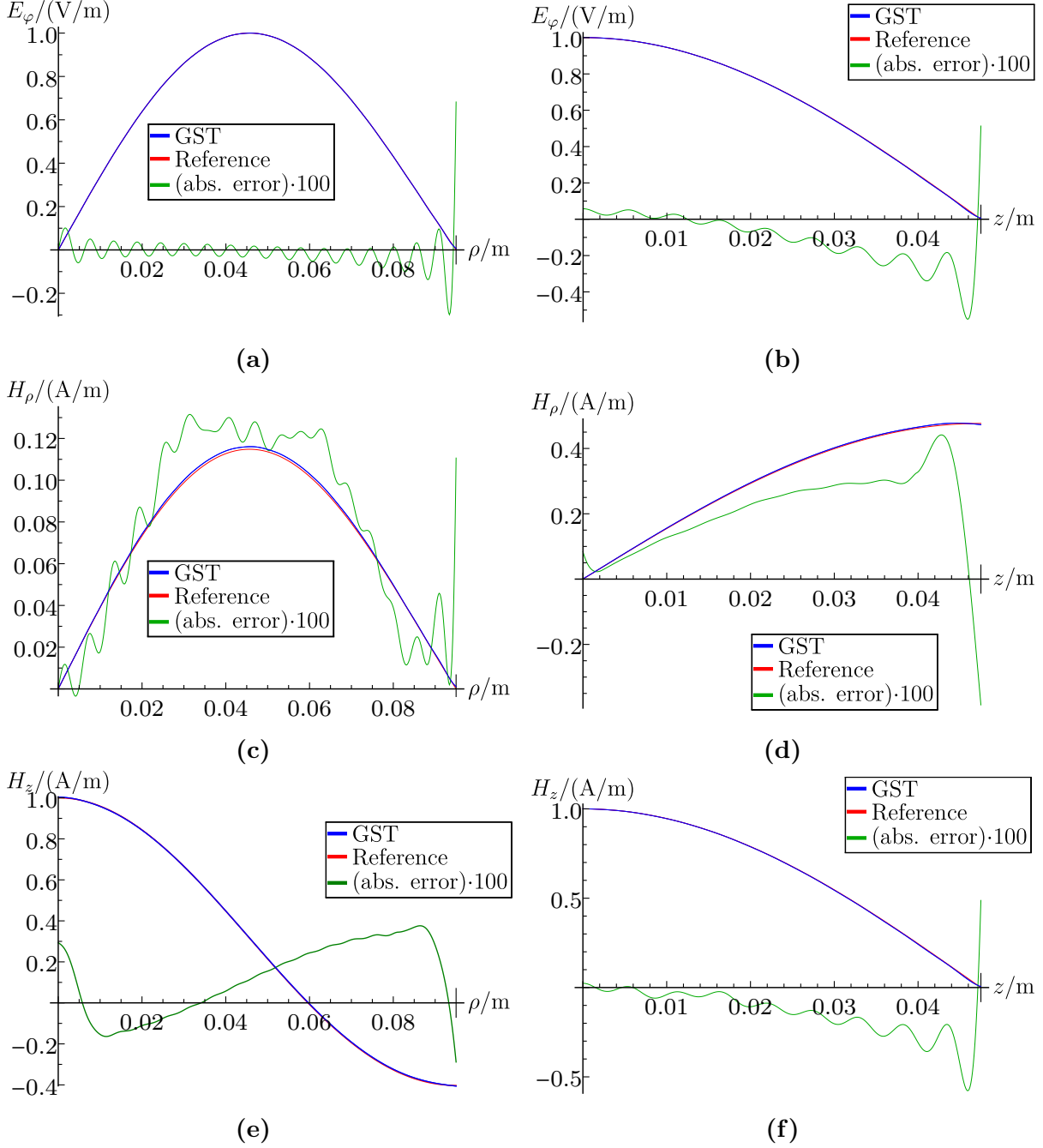
plotted along both perturbed coordinate directions. Almost all figures show a very good agreement between GST-based and reference fields with an accuracy similar to that of the 1D perturbations. Only in Fig. 5.14(c) and 5.15(c), it appears that H_ρ noticeably deviates from the reference field. (The same applies to H_z in Fig. 5.17(f).) However, there H_ρ has a distinctly lower magnitude than the corresponding H_z (see Fig. 5.14(e) and 5.15(e)). Therefore, it may be inferred that the deviations are only seemingly increased due to the generally smaller field values. The consistent absolute error substantiates this. Thus, GST allows for a very accurate computation of perturbed eigenmodes provided that the number of unperturbed modes is sufficient.
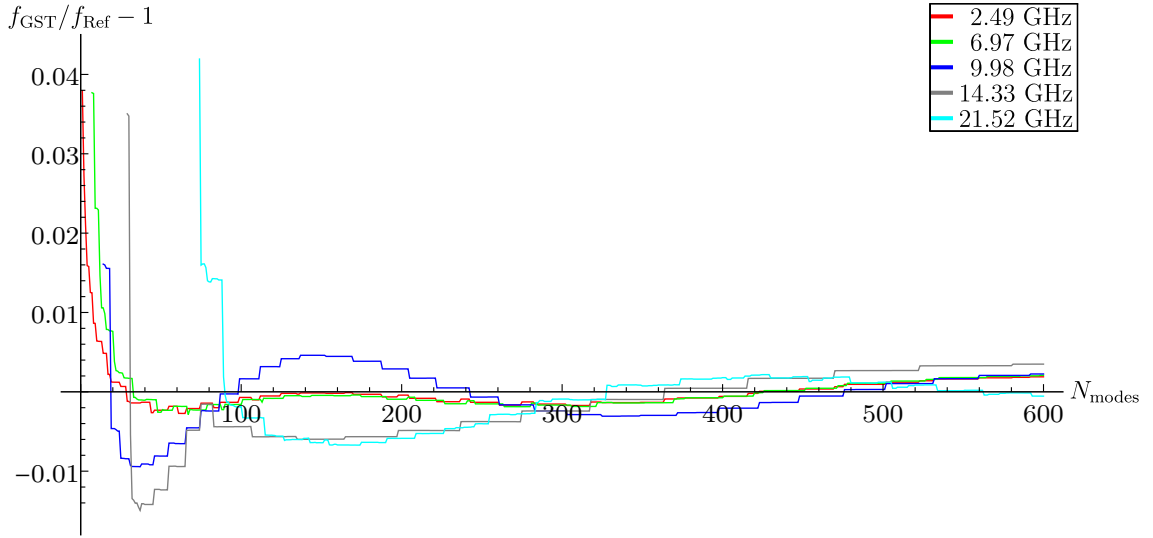

Figure 5.12: Relative frequency error depending on the number N_{modes} of unperturbed modes for $\text{TE}_{0,n,p}$ (p: odd) modes subject to a two-dimensional perturbation of $\Delta R/R = 5\,\%$ and $\Delta L/L = 5\,\%$: $\text{TE}_{0,1,1}$ (2.49 GHz), $\text{TE}_{0,3,3}$ (6.97 GHz), $\text{TE}_{0,6,1}$ (9.98 GHz), $\text{TE}_{0,1,9}$ (14.33 GHz) and $\text{TE}_{0,10,9}$ (21.52 GHz).


Figure 5.13: Relative frequency error depending on the perturbed frequency for the first 100 $\text{TE}_{0,n,p}$ (p: odd) modes subject to a two-dimensional perturbation of $\Delta R/R = 5\,\%$ and $\Delta L/L = 5\,\%$ for $N_{\text{modes}} = 450$.
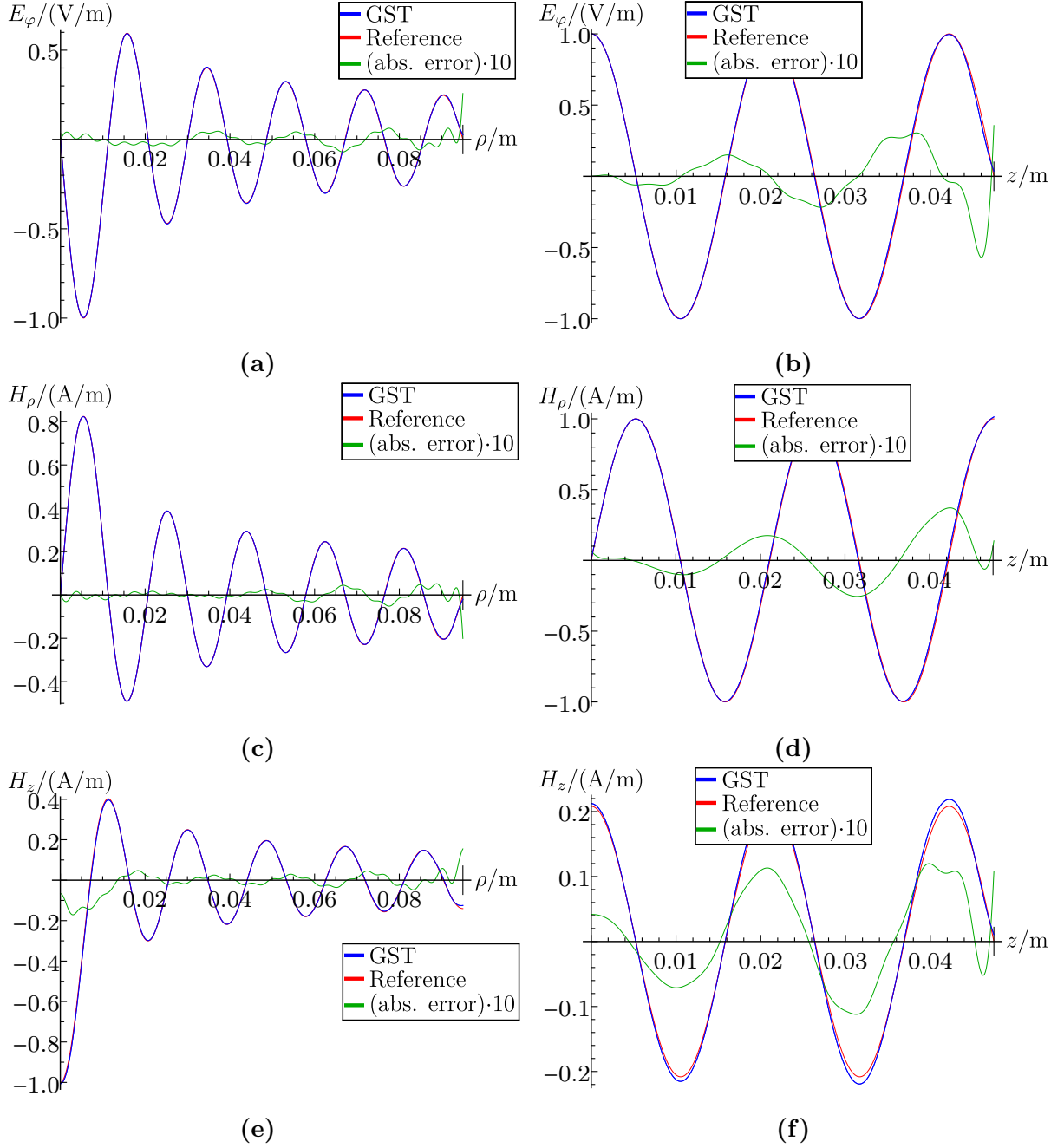
Figure 5.14: Perturbed EM field of the $TE_{0,1,1}$ mode along both perturbed coordinate directions ρ and z for $\Delta R/R = 5\,\%$, $\Delta L/L = 5\,\%$ and $N_{\text{modes}} = 480$: The field components E_ρ, E_z and H_φ are zero and therefore not displayed.
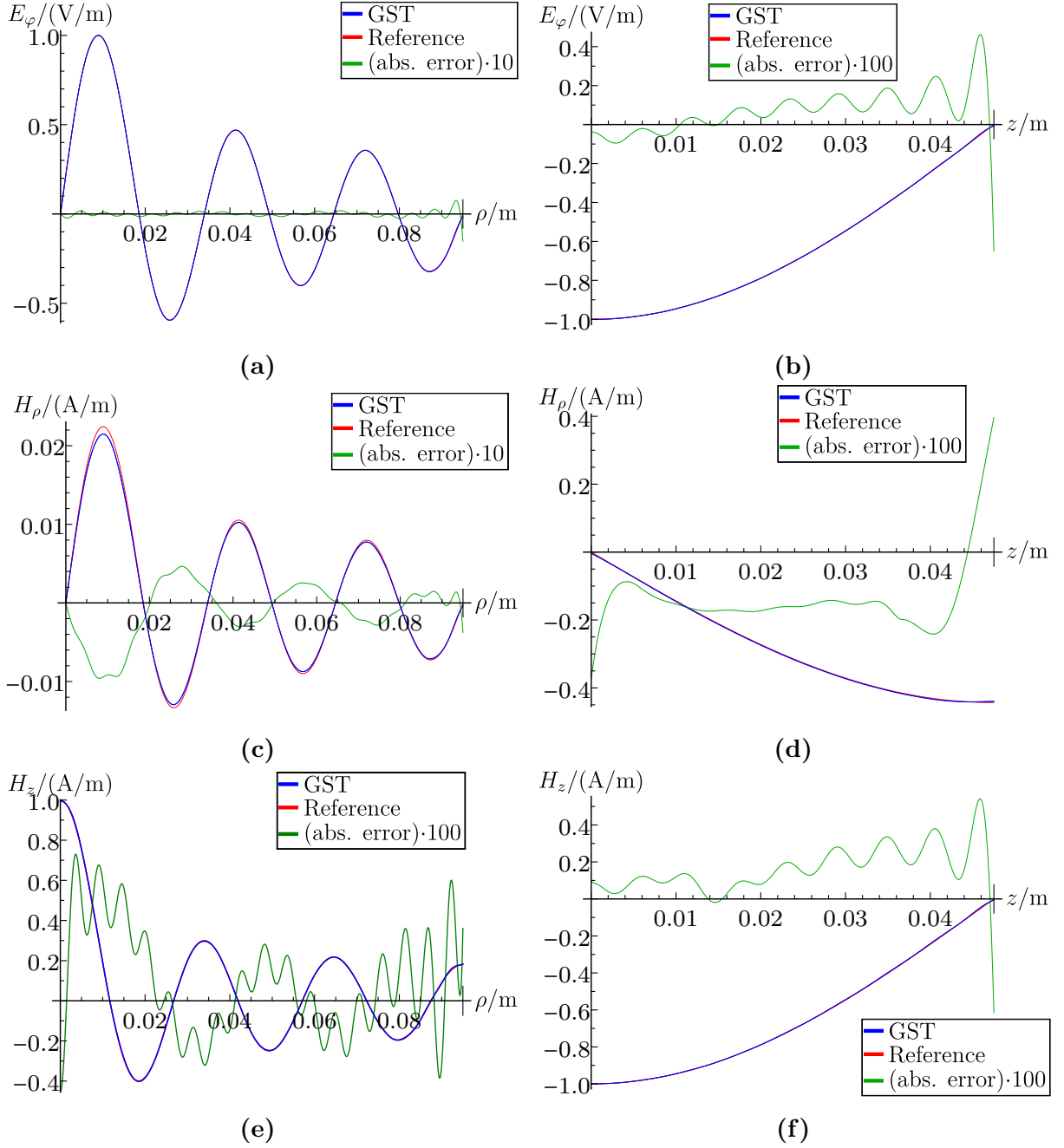
Figure 5.15: Perturbed EM field of the $TE_{0,6,1}$ mode along both perturbed coordinate directions ρ and z for $\Delta R/R = 5\,\%$, $\Delta L/L = 5\,\%$ and $N_{\mathrm{modes}} = 480$: The field components E_ρ, E_z and H_φ are zero and therefore not displayed.
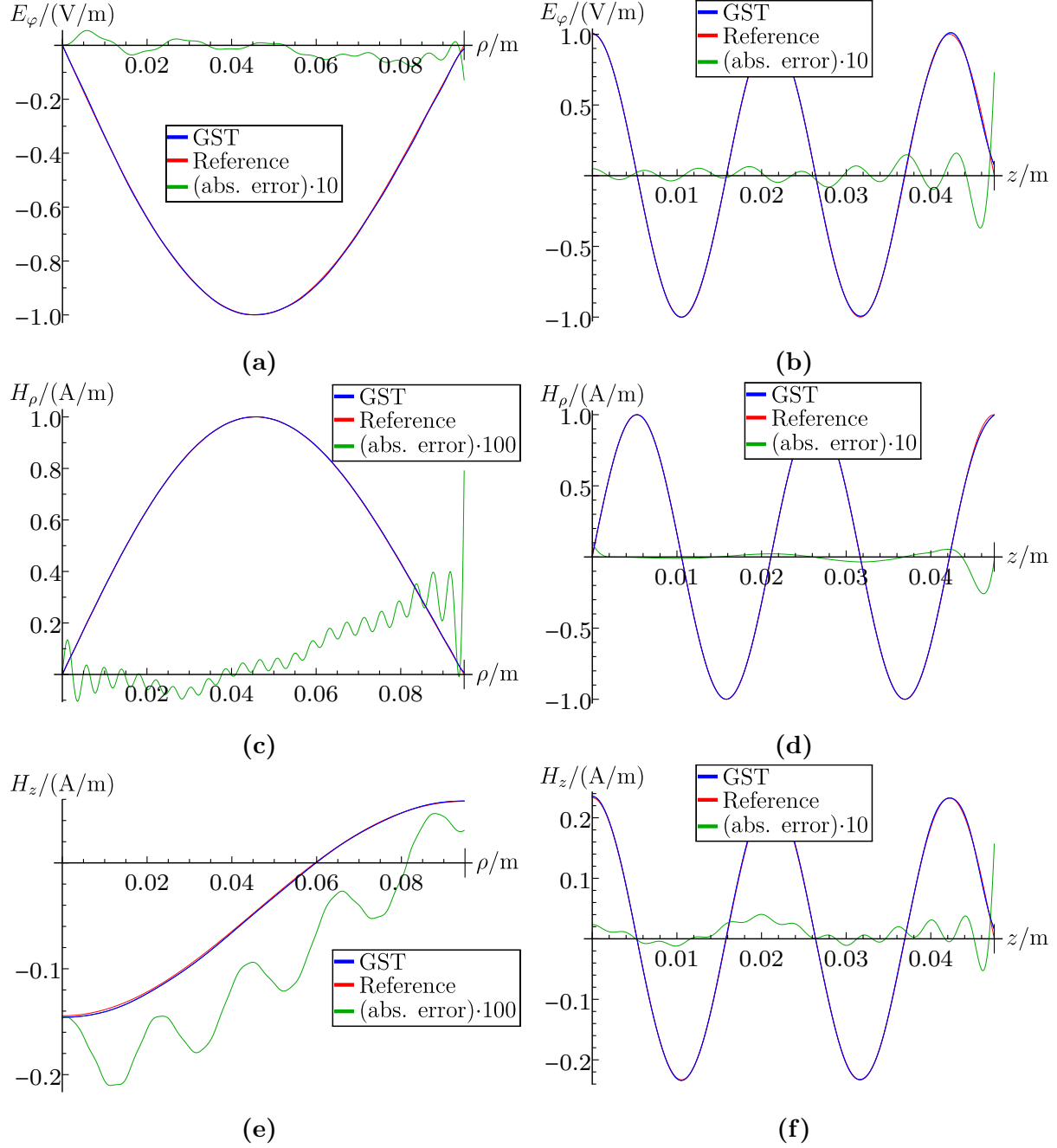
Figure 5.16: Perturbed EM field of the $TE_{0,1,9}$ mode along both perturbed coordinate directions ρ and z for $\Delta R/R = 5\%$, $\Delta L/L = 5\%$ and $N_{\text{modes}} = 370$: The field components E_ρ, E_z and H_φ are zero and therefore not displayed.

Figure 5.17: Perturbed EM field of the $TE_{0,10,9}$ mode along both perturbed coordinate directions ρ and z for $\Delta R/R = 5\,\%$, $\Delta L/L = 5\,\%$ and $N_{\mathrm{modes}} = 510$: The field components E_ρ, E_z and H_φ are zero and therefore not displayed.

5.1.2 Coaxial Resonator

While the previous subsection presented examples for deformations of an existing boundary this subsection demonstrates that GST also allows to create additional boundaries by removing a volume from the interior of a cavity. As a minimal example serves a coaxial resonator derived from a cylindrical cavity, as shown in Fig. 5.18. For this purpose, the volume ΔV is defined as a cylinder with the length L and the radius R_{in} that is equal to the inner radius of the coaxial resonator. Since this presents a purely radial perturbation, only modes with the same azimuthal and longitudinal indices m, p and a different radial index n interacts for GST (see Table 5.1). Exemplarily, coaxial $TM_{0,n,0}$ modes based on the set of cylindrical $TM_{0,n,0}$ modes are presented.
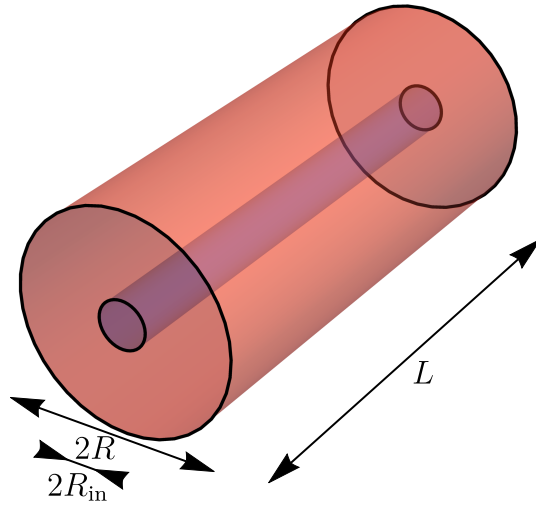

Figure 5.18: Coaxial resonator with an outer radius R and an inner radius R_{in} (perturbed resonator, red) based on a cylindrical resonator with a radius R.
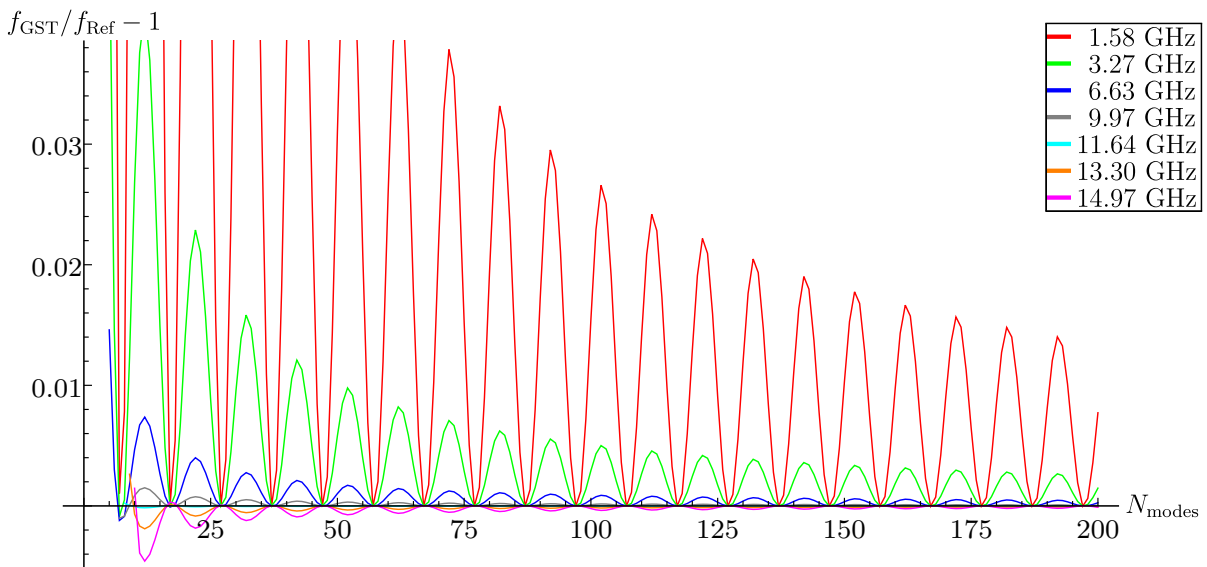

Figure 5.19: Relative frequency error depending on the number N_{modes} of unperturbed modes for $TM_{0,n,0}$ modes ($n = 1, 2, 4, 6, 7, 8, 9$) of a coaxial resonator with $R_{in} = \frac{1}{10}R$.

The GST-based frequencies f_{GST} converge towards the correct solution. However, in contrast to a perturbation of an existing boundary (see Fig. 5.2(b)), the correct frequency is always approached from one direction, i.e. the GST frequency of a certain mode is almost exclusively greater equal (or less equal) than the correct one, as Fig. 5.19 demonstrates for a selection of modes. As a consequence, for each perturbed mode, the corresponding minimal (or maximal) GST frequency (depending on N_{modes}) represents the best possible result instead of the corresponding average GST frequency. Figure 5.20 illustrates this by the relative frequency error of the first ten $\text{TM}_{0,n,0}$ modes. Here, it is apparent, that the optimal (minimal or maximal) GST frequencies ($N_{\text{modes}} = 57$) in the range of 48 to 57 unperturbed modes are far more accurate than a set of rather average GST frequencies ($N_{\text{modes}} = 55$). Further, it can be seen from Fig. 5.19 and 5.20 that the $\text{TM}_{0,1,0}$ mode has a comparatively high error in contrast to $\text{TM}_{0,n,0}$ modes of higher order. Regarding the specific convergence behavior, the EM fields can accurately be computed, as Fig. 5.21 shows for the $\text{TM}_{0,1,0}$ and $\text{TM}_{0,4,0}$ mode. Solely close to the inner radial boundary, the magnetic field H_φ noticeably deviates from the reference field due to the Gibbs phenomenon (see Subsection 5.1.1). The mean absolute error of the electric field is $2.16 \cdot 10^{-4}$ V/m for $\text{TM}_{0,1,0}$ and $4.32 \cdot 10^{-4}$ V/m for $\text{TM}_{0,4,0}$. The maximal errors are $1.52 \cdot 10^{-2}$ V/m and $3.61 \cdot 10^{-2}$ V/m, respectively. Expectedly, the electric fields of the $\text{TM}_{0,1,0}$ and $\text{TM}_{0,4,0}$ mode based on $N_{\text{modes}} = 55$ show increased deviations, as depicted in Fig. 5.22. Their mean absolute error rises to $3.15 \cdot 10^{-2}$ V/m and $2.42 \cdot 10^{-3}$ V/m, respectively. Thus, a wrongly chosen N_{modes} primarily affects the $\text{TM}_{0,1,0}$ mode due to its generally lower accuracy. Though the higher $\text{TM}_{0,n,0}$ modes are also impaired, their fields still coincide very well with the reference fields. It should be pointed out that, even without knowing the correct perturbed modes, the progression of a certain GST frequency depending on N_{modes} indicates if it converges symmetrically or from one direction towards the solution, provided that a sufficient number of modes N_{modes} is used. Figure 5.23 illustrates this for the GST frequency of the $\text{TM}_{0,1,0}$ mode. Consequently, the convergence behavior should always be considered for choosing the best N_{modes}.

As introduced in Subsection 2.2.2, the creation of two separate boundaries results in the existence of additional TEM_p modes with a wave number k equal to the longitudinal wave number $k = k_z$ since the transverse wave number k_T is zero. Hence, the TEM_0 mode

(a)   (b)
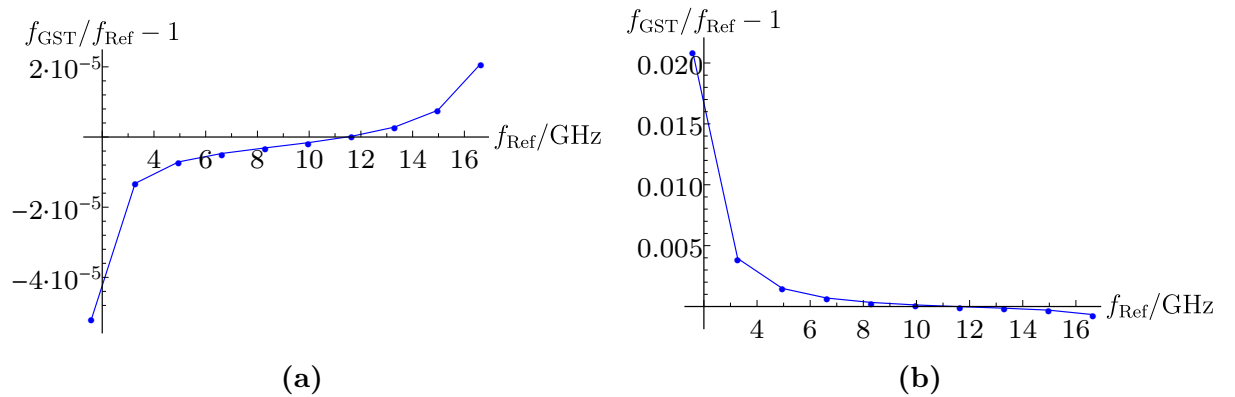
Figure 5.20: Relative frequency error of the first ten $\text{TM}_{0,n,0}$ modes depending on perturbed frequency for a coaxial resonator with $R_{\text{in}} = \frac{1}{10}R$: (a) Optimal GST frequencies resulting from $N_{\text{modes}} = 57$. (b) Average GST frequencies resulting from $N_{\text{modes}} = 55$.
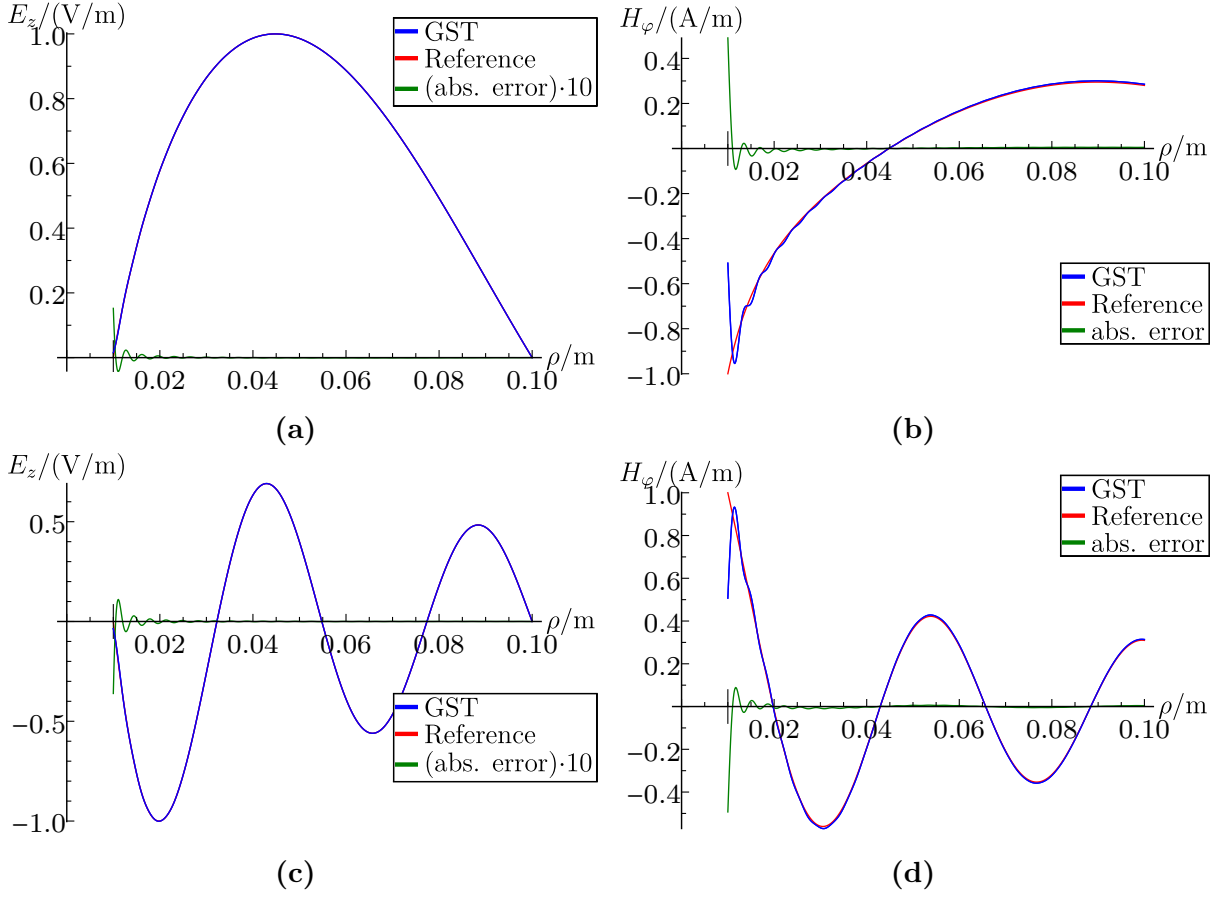
Figure 5.21: Optimal perturbed EM field (unfiltered) of $TM_{0,n,0}$ modes along the perturbed coordinate direction ρ for a coaxial resonator with $R_{in} = \frac{1}{10}R$ and $N_{modes} = 57$: (a) – (b): $TM_{0,1,0}$ mode. (c) – (d): $TM_{0,4,0}$ mode. The field components E_φ, E_ρ, H_ρ and H_z are zero and therefore not displayed.
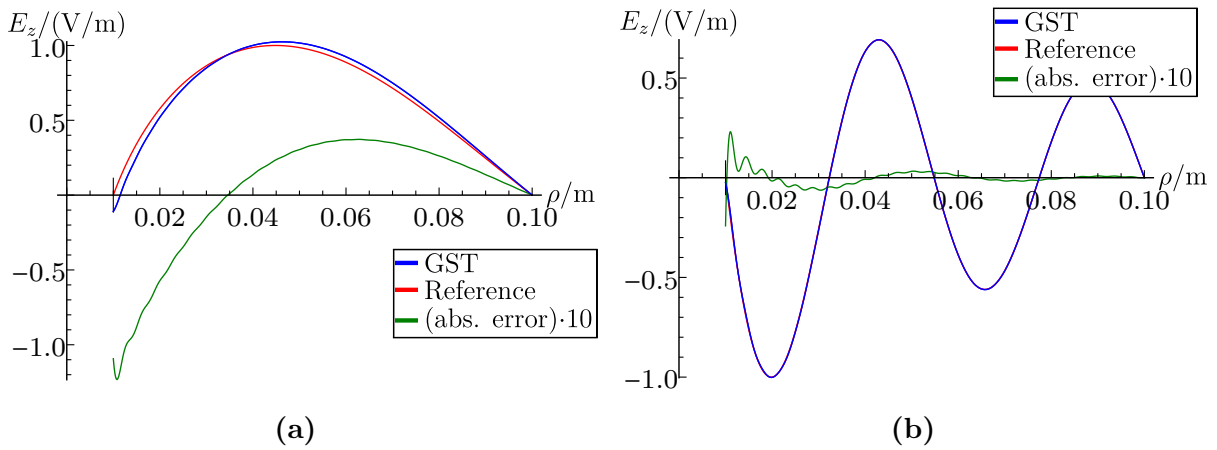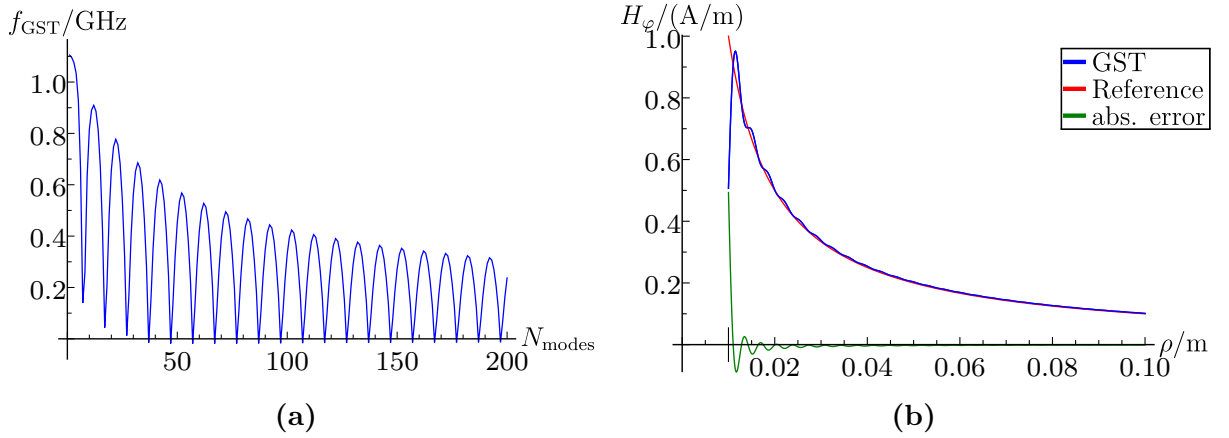

Figure 5.22: Perturbed electric field of $TM_{0,n,0}$ modes along the perturbed coordinate direction ρ for a coaxial resonator with $R_{in} = \frac{1}{10}R$ for a non-optimal N_{modes} of 55: (a): $TM_{0,1,0}$ mode. (b): $TM_{0,4,0}$ mode.
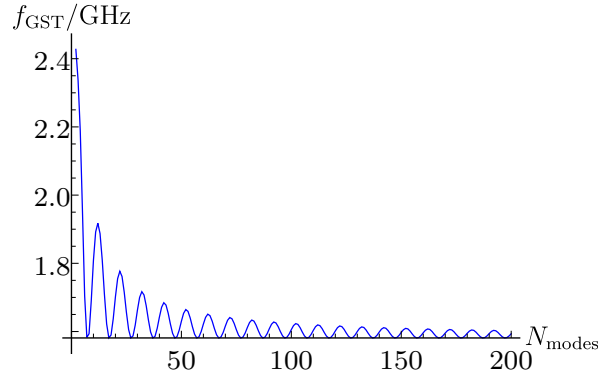
Figure 5.23: Perturbed frequency of the $TM_{0,1,0}$ mode depending on the number N_{modes} of unperturbed modes for a coaxial resonator with $R_{\text{in}} = \frac{1}{10}R$


Figure 5.24: Perturbed TEM_0 mode of a coaxial resonator with $R_{\text{in}} = \frac{1}{10}R$: (a) Frequency depending on the number N_{modes} of unperturbed modes. (b) Magnetic field H_φ for $N_{\text{modes}} = 57$.

has an eigenfrequency of zero. Strictly speaking, the TEM_0 can only exist inside a waveguide, implying that the inner and outer radius boundary are not connected. Nevertheless, GST yields a result for the TEM_0 mode based on the set of cylindrical $TM_{0,n,0}$ modes. Figure 5.24(a) shows the frequency error of the respective GST frequency. At first sight, the frequency seems to have abrupt changes. This arises from the fact that the GST frequencies f_{GST} are exclusively defined as (physically sensible) positive values. However, since f_{GST} may also be defined as a negative value, the TEM_0 frequency actually oscillates symmetrically around the correct value of zero. The corresponding magnetic field can be correctly reproduced, as Fig. 5.24(b) shows. In contrast, the purely radial electric field E_ρ of the TEM_0 mode can not be computed by GST since the unperturbed cylindrical $TM_{0,n,0}$ modes have no radial electric field component E_ρ (see Appendix B.2.1). So the set of unperturbed modes inherently inhibits to do so. The TEM_0 mode can likewise not be determined from a set of $TE_{0,n,0}$ modes since no $TE_{m,n,0}$ modes exist. Therefore, the electric field $\mathbf{E}$ inevitably has to be determined from the curl of $\mathbf{H}$ based on Maxwell's equations. However, this involves a certain effort.

5.1.3 Specific Characteristics of GST

Some of the specific characteristics of GST were already discussed in [94] [i]. A direct comparison of GST with the simple perturbation approach of Slater's theorem (ST) shows the significantly higher accuracy of GST. For both ST and the first order approximation of ST, the relative frequency error of the fundamental mode is already one order of magnitude higher than the one of GST, as Fig. 5.25 illustrates for a radial perturbation of $\Delta R/R = 5\,\%$. The ST-based frequency error also increases rapidly with rising frequency until it reaches a value that is equal to the relative extent of the perturbation ($5\,\%$) and continues oscillating around this value. A relative error equal to the relative extent of perturbation is absolutely inadequate and indicates the failure of ST for modes beyond a certain mode order. Hence, for a $5\,\%$ perturbation, only the frequency shift of the first
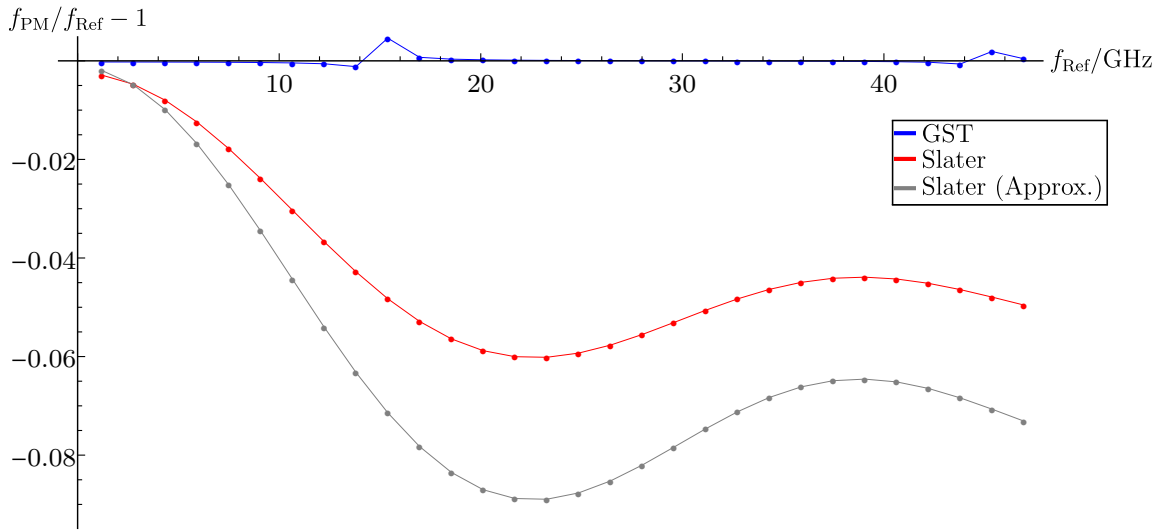
Figure 5.25: Comparison of GST to Slater's theorem: Relative frequency error of $TM_{0,n,0}$ modes depending on perturbed frequency for $\Delta R/R = 5\,\%$ based on GST with $N_{\text{modes}} = 54$ (blue), Slater's theorem (red) and first order approximation of ST (gray).
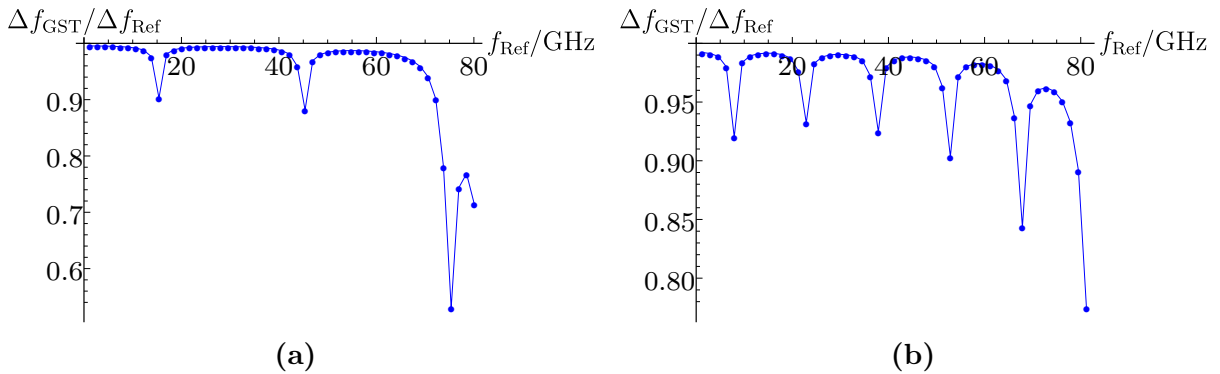
Figure 5.26: Ratio of GST-based and reference frequency shift of $TM_{0,n,0}$ modes depending on the perturbed frequency for $N_{\text{modes}} = 54$: (a) 51 modes for $\Delta R/R = 5\,\%$. (b) 49 modes for $\Delta R/R = 10\,\%$.

---

[i]Some of the conclusions in [94] proved to be partially incomplete and therefore do not match the completed information in this subsection.

nine perturbed modes can be computed with ST at all. A restriction to even less modes is, however, advisable because of the high error. The accuracy of the first order approximation of ST is even worse and therefore must be used on no account. It is also apparent from Fig. 5.25 that the perturbed mode for which the ST-based frequency error reaches a value of 5 % and starts oscillating is exactly the same mode for that the GST-based frequencies display a first abrupt error increase. In addition, Fig. 5.26 clarifies that the occurrence of these abrupt deviations is directly related to the perturbation extent. There, it is obvious that a perturbation of 10 % creates twice as many modes with such an anomaly as a 5 % perturbation. In case of 1D perturbations, a definite regularity for the affected modes can be found, set by the *irregular GST mode index* i_{GSTirr}

$$i_{\mathrm{GSTirr}} = \left\lceil \frac{\xi}{2\Delta\xi} + \frac{\xi}{\Delta\xi} i_{\mathbb{N}} \right\rceil . \tag{5.1}$$

Here, $\Delta\xi/\xi$ is representative for the relative extent of the 1D perturbation (e.g. $\Delta R/R$ or $\Delta L/L$) and $i_{\mathbb{N}} \in \mathbb{N}_0 = \{0, 1, 2, ...\}$. A closer examination of the magnitudes of the expansion coefficients $\boldsymbol{\alpha}_i$ or $\boldsymbol{\beta}_i$ allows to gain a better understanding of the phenomenon. At this, the focus is on the *prime dominant expansion mode* or dominant expansion mode for short. The i-th dominant expansion mode is the unperturbed mode whose expansion coefficients $\alpha_{i_{\mathrm{dom}}}$ and $\beta_{i_{\mathrm{dom}}}$ have the highest absolute values for a perturbed mode i

$$\alpha_{i_{\mathrm{dom}}} = \max_{k=1}^{N_{\mathrm{modes}}} |\alpha_{ik}|, \tag{5.2}$$

$$\beta_{i_{\mathrm{dom}}} = \max_{k=1}^{N_{\mathrm{modes}}} |\beta_{ik}| \tag{5.3}$$

and thereby have the highest contribution to the series expansion. Figure 5.27 shows a comparison of the frequencies of the unperturbed modes, the perturbed modes and the
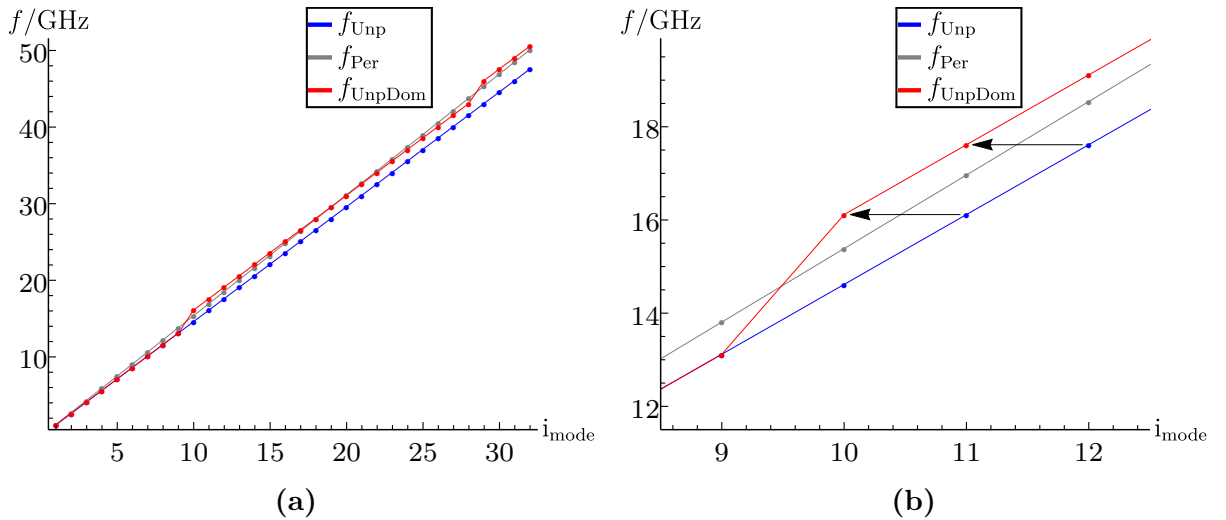
Figure 5.27: Frequencies of $\mathrm{TM}_{0,n,0}$ modes depending on the mode index i_{mode} for $\Delta R/R = 5\,\%$: (a) For each perturbed mode (gray curve) the equivalent unperturbed mode (blue curve) and the corresponding prime dominant unperturbed mode for the GST series expansion are shown. (b) Starting with the perturbed $\mathrm{TM}_{0,10,0}$ mode, the dominant mode is at least one index higher than the unperturbed mode.

dominant unperturbed modes depending on the *mode index* i_{mode} for a set of $\mathrm{TM}_{0,n,0}$ modes. By rising index i_{mode}, unperturbed and perturbed frequencies increasingly diverge, as Fig. 5.27(a) displays. In a sense, the frequencies of the dominant modes follow the perturbed frequencies by skipping certain indices in the sequence of unperturbed mode indices. Fig. 5.27(b) emphasizes this for the perturbed $\mathrm{TM}_{0,10,0}$ mode ($i_{\mathrm{mode}} = 10$). Here, the corresponding dominant expansion mode is the unperturbed $\mathrm{TM}_{0,11,0}$ mode instead of the skipped $\mathrm{TM}_{0,10,0}$ mode. Thus, the n-indices of the unperturbed and dominant expansion modes start to differ from the 10th mode on. The skipping repeats every 20 indices in accordance to (5.1). Figure 5.28(a) illustrates why the phenomenon occurs the first time for the 10th mode (or more general the $\lceil \xi/(2\Delta\xi) \rceil$) by means of the ratio of the unperturbed and perturbed wavelengths. It it obvious that the wavelength of the 10th perturbed mode is exactly the mean value of wavelengths of the 10th and 11th unperturbed mode. As a consequence, the 11th unperturbed mode becomes the dominant expansion mode for the 10th perturbed mode which thus may not be sufficiently expanded without the 11th unperturbed mode. The same principle applies to the unperturbed $\mathrm{TE}_{0,1,19}$ (10th mode for odd p) and the perturbed $\mathrm{TE}_{0,1,17}$ (ninth mode for odd p) for a symmetric longitudinal 5% perturbation where the perturbed volume $\mathrm{d}V$ is split into two sub-volumes (see Fig. 5.1(b)). So both, frequencies and stationary fields elucidate the repetitive anomalies due to the shifting between unperturbed and perturbed mode indices. As just explained, this shifting results in a reduced number $\widetilde{N}_{\mathrm{modes}}$ of computable perturbed modes, compared to the number N_{modes} of unperturbed modes, if a certain mode index is exceeded. The series expansion can only yield reasonable results for perturbed modes whose wavelength $\widetilde{\lambda}_i$ is larger than the minimal unperturbed wavelength λ_{min}, as previously expounded in 3.3

(a)

(b)
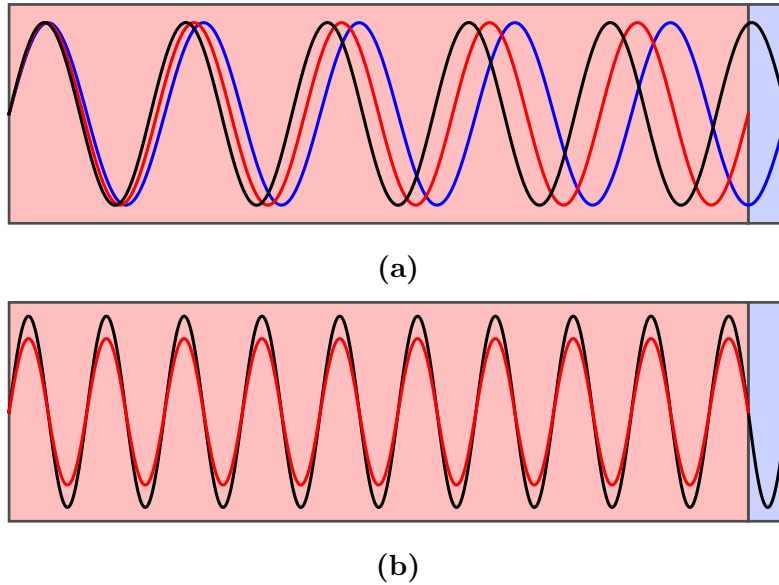
Figure 5.28: Illustration of the wavelength shifting using a simple 1D example subject to a 5% perturbation: (a) The 10th perturbed wavelength (red curve) lies exactly between the 10th (blue curve) and 11th (black curve) unperturbed wavelength. (b) Since one half-wave of 20th unperturbed mode (black curve) fits precisely into the volume ΔV removed by the perturbation (light blue), the 20th unperturbed wavelength equals the 19th perturbed one (red curve).

(see (3.83)). Derived from the irregular GST mode indices (5.1) the actual number $\widetilde{N}_{\mathrm{modes}}$ of perturbed modes can be approximated by

$$\widetilde{N}_{\mathrm{modes}} \approx \left\lfloor N_{\mathrm{modes}} \left(1 - \frac{\Delta\xi}{\xi} \right) \right\rfloor . \tag{5.4}$$

From this conclusion the question arises how GST is affected by this phenomenon since the method nevertheless inherently yields N_{modes} perturbed modes. A detailed examination revealed that, in contrast to the *regular* GST modes, for each irregular perturbed mode index i_{GSTirr} a pair of two *irregular* GST modes exists which constitutes just one perturbed mode. As a consequence, the actual number of perturbed modes is smaller than N_{modes}. So, GST provides a sort of compensatory mechanism to fulfill the requirement of a reduced number $\widetilde{N}_{\mathrm{modes}}$ of expandable perturbed modes. For instance, for a 5 % perturbation, the 10th and 11th, 30th and 31st, 50th and 51st mode form such pairs. Thus, just 51 perturbed modes may be computed for $N_{\mathrm{modes}} = 54$ and the 10th, 29th and 38th perturbed mode are the resulting irregular modes, as Fig. 5.26(a) depicts. Unexpectedly, the frequencies and expansion coefficients of these irregular mode pairs may have not only real but also complex values. Their domain changes depending on the number of used expansion modes, as Fig. 5.29 shows by the distribution of complex-valued frequencies depending on the GST mode index i_{GST} and N_{modes} for different types of perturbations. The subfigures 5.29 (a) to (c) prove that for 1D perturbations, pairs of complex frequencies only occur for i_{GSTirr} and the respective subsequent mode in a repetitive sequence. In the context of resonator eigenmodes (see Section 2.2), complex-valued frequencies would represent lossy modes. However, this violates the Helmholtz equations since purely PEC and PMC boundaries force lossless eigenmodes and thereby real-valued frequencies. In contrast, the complex GST frequencies and expansion coefficients seems to be an aliasing effect [95, Ch. 3] of the compensatory mechanism inherent to the method. The simultaneous existence of real- and complex-valued frequencies for the same perturbed mode based on different N_{modes} values substantiates this hypothesis. In a mathematical sense too, the existence of complex eigenvalues and eigenvectors cannot be excluded since the matrices $\mathbf{A}$ and $\mathbf{B}$ that form the eigenvalue problem of GST are non-symmetric matrices (see (3.75), (3.76)). Also, a universally valid similarity transformation [81] for $\mathbf{A}$ and $\mathbf{B}$ with $N_{\mathrm{modes}} > 4$ could not be found. The frequencies $f_{i_{\mathrm{GSTirr}}}$ and $f_{i_{\mathrm{GSTirr}}+1}$ as well as the expansion coefficients $\boldsymbol{\alpha}_{i_{\mathrm{GSTirr}}}$ and $\boldsymbol{\alpha}_{i_{\mathrm{GSTirr}}+1}$, $\boldsymbol{\beta}_{i_{\mathrm{GSTirr}}}$ and $\boldsymbol{\beta}_{i_{\mathrm{GSTirr}}+1}$ of a real-valued mode pair have different values without a distinct mathematical relation. The complex-valued mode pairs always have conjugate complex frequencies and coefficients with

$$\Re\left\{\underline{f}_{i_{\mathrm{GSTirr}}}\right\} = \Re\left\{\underline{f}_{i_{\mathrm{GSTirr}}+1}\right\} \quad , \quad \Im\left\{\underline{f}_{i_{\mathrm{GSTirr}}}\right\} = -\Im\left\{\underline{f}_{i_{\mathrm{GSTirr}}+1}\right\} , \tag{5.5}$$

$$\Re\left\{\underline{\boldsymbol{\alpha}}_{i_{\mathrm{GSTirr}}}\right\} = \Re\left\{\underline{\boldsymbol{\alpha}}_{i_{\mathrm{GSTirr}}+1}\right\} \quad , \quad \Im\left\{\underline{\boldsymbol{\alpha}}_{i_{\mathrm{GSTirr}}}\right\} = -\Im\left\{\underline{\boldsymbol{\alpha}}_{i_{\mathrm{GSTirr}}+1}\right\} , \tag{5.6}$$

$$\Re\left\{\underline{\boldsymbol{\beta}}_{i_{\mathrm{GSTirr}}}\right\} = \Re\left\{\underline{\boldsymbol{\beta}}_{i_{\mathrm{GSTirr}}+1}\right\} \quad , \quad \Im\left\{\underline{\boldsymbol{\beta}}_{i_{\mathrm{GSTirr}}}\right\} = -\Im\left\{\underline{\boldsymbol{\beta}}_{i_{\mathrm{GSTirr}}+1}\right\} , \tag{5.7}$$

since the matrices $\mathbf{A}$ and $\mathbf{B}$ have exclusively real-valued entries. So they only differ in the sign of the imaginary part. Examining the frequency convergence of an irregular GST mode pair reveals that the imaginary part of the complex frequencies $\underline{f}_{i_{\mathrm{GSTirr}}}$, $\underline{f}_{i_{\mathrm{GSTirr}}+1}$ in a way adds up to their real part resulting in a nearly regularly oscillating behavior, in combination with the real-valued $f_{i_{\mathrm{GSTirr}}}$, $f_{i_{\mathrm{GSTirr}}+1}$. Figure 5.30 demonstrates this for the
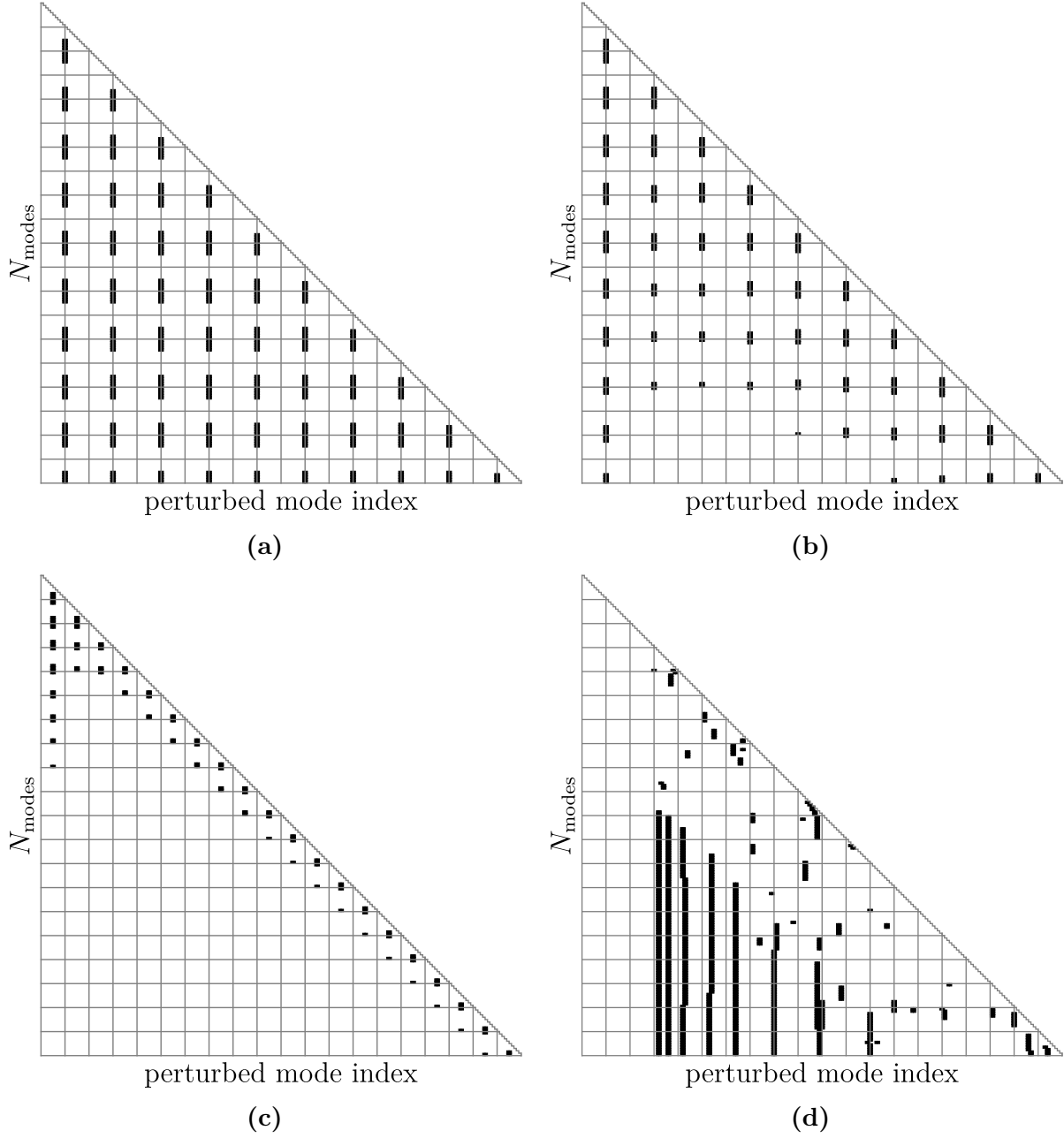
Figure 5.29: Domain of GST frequencies depending on the perturbed GST mode index i_{GST} and the number N_{modes} of unperturbed modes up to 200 modes: The left top square in each subfigure matches $N_{\mathrm{modes}} = 1$ and $i_{\mathrm{GST}} = 1$. White squares indicate real values and black squares complex values (gray auxiliary lines are plotted every ten modes). (a) Symmetric longitudinal perturbation of $\Delta L/L = 5\,\%$. (b) Radial perturbation of $\Delta R/R = 5\,\%$. (c) Radial perturbation of $\Delta R/R = 10\,\%$. (d) Radial and longitudinal perturbation of $\Delta R/R = 5\,\%$ and $\Delta L/L = 5\,\%$.

first irregular mode of a symmetric longitudinal perturbation of 5 %. But it depicts also that the frequencies converge noticeably slower than regular GST frequencies. The *mean irregular frequency* $\overline{f}_{i_{\mathrm{GSTirr}}}$ of both modes

$$\overline{f}_{i_{\mathrm{GSTirr}}} = \left(\underline{f}_{i_{\mathrm{GSTirr}}} + \underline{f}_{i_{\mathrm{GSTirr}}+1}\right)/2, \tag{5.8}$$

complex- or real-valued, oscillates smoothly around the correct frequency, and has an accuracy even better than the one of a regular mode. In case of complex-valued $\underline{f}_{i_{\mathrm{GSTirr}}}$,
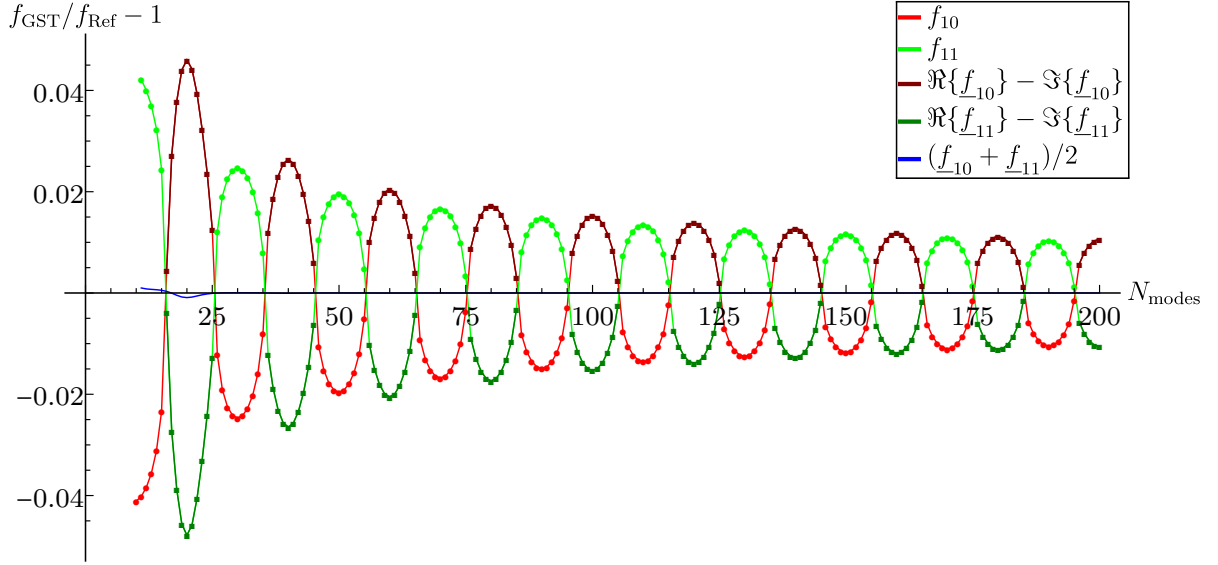
Figure 5.30: Relative frequency error depending on the number N_{modes} of unper. modes for the $TE_{0,1,19}$ mode subject to a symmetric longitudinal perturbation $\Delta L/L = 5\,\%$: Real-/complex-valued and mean frequency of the 10th and 11th GST mode (p: odd).
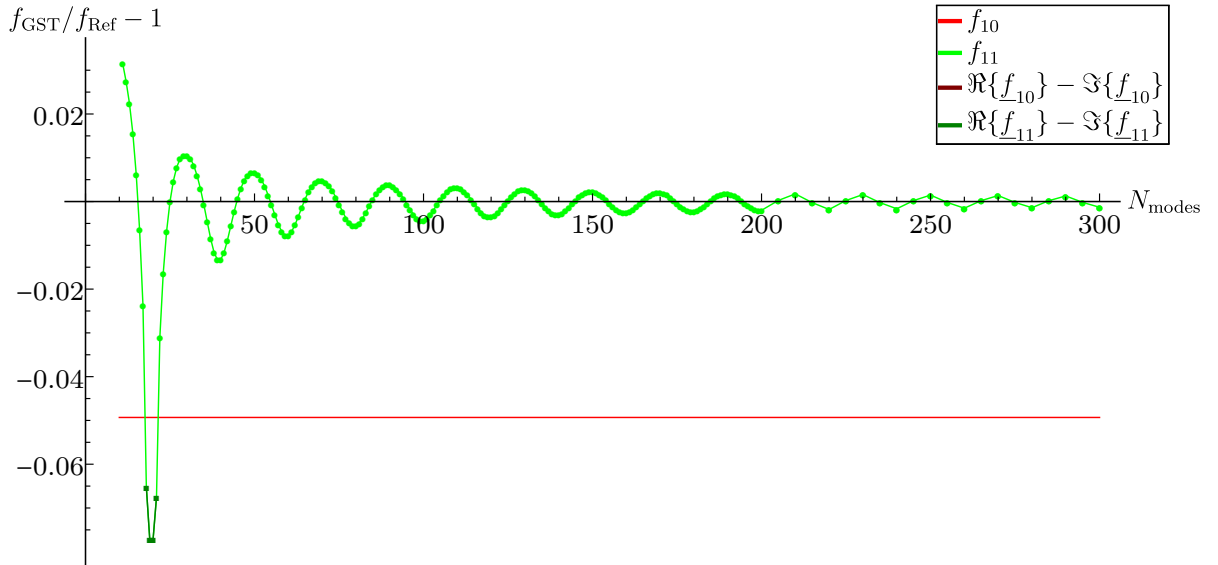
Figure 5.31: Relative frequency error depending on the number N_{modes} of unperturbed modes for the $TE_{0,1,10}$ mode subject to an asymmetric longitudinal perturbation of $\Delta L/L = 5\,\%$ based on the 10th and 11th GST mode.

$\underline{f}_{i\mathrm{GSTirr}+1}$ their mean value is identical to their real part. So, the mean irregular frequency $\overline{f}_{i\mathrm{GSTirr}}$ is exclusively real-valued, guaranteeing consistently valid results. The irregular mode pairs of an asymmetric longitudinal perturbation show a completely different behavior. Instead of two complementary modes, one mode of the pair constitutes the correct solution whereas the other mode is a sort of artifact, identical to the corresponding unperturbed mode, i.e. its frequency is the unperturbed one, and only one expansion coefficient differs from zero. Figure 5.31 illustrates this by the $TE_{0,1,10}$ mode. In addition, complex-valued results solely occur for three pairs of the first irregular mode. However, the example of an asymmetric perturbed cylinder is irrelevant for practice since it is actually a symmetric perturbation deliberately made asymmetric. Therefore, it is very unlikely that such GST results will occur for real-life structures. A radial perturbation presents the most probable way how the irregular GST modes will look like for real-life resonators. In contrast to longitudinal perturbations that are expanded in terms of sine functions, radial perturbations are expanded in terms of Bessel functions whose roots are not equidistant. As Fig. 5.32 demonstrates for the first two irregular mode pairs, each pair again consists of two complementary modes. However, $\overline{f}_{i\mathrm{GSTirr}}$ does not approach the correct solution but displays a perceptible offset. The first irregular mode pair converges towards a relative error of $7.87 \cdot 10^{-3}$ (see Fig. 5.32(a)), a value by an order of magnitude higher than the error of regular GST modes. Advantageously, the relative error reduces for irregular mode pairs of higher order since the absolute frequency offset is approximately constant. For the second irregular mode pair, it already decreases to $3.80 \cdot 10^{-3}$ (see Fig. 5.32(b)). Hence, primarily the accuracy of lower order modes is impaired by the aliasing phenomenon. The investigations of the irregular GST frequencies showed that asymmetric and symmetric longitudinal perturbations demonstrate the two extreme cases for the mannerism of GST while radial perturbations present a rather medial and more realistic case. Therefore, the frequencies of irregular modes of real-life cavity structures should be determined based on their mean frequency $\overline{f}_{i\mathrm{GSTirr}}$ to guarantee a smooth convergence. Since an error offset cannot be detected without knowing the true frequency, the possibly higher error cannot be evaded and should always be taken into consideration.

The real and imaginary part of any complex eigenvector may be changed by multiplying it by an arbitrary complex value without losing the eigenvector's validity. Thus, the expansion coefficients resulting from a complex-valued irregular mode pair have to be exclusively related to their absolute values to guarantee consistent field results. Since the single components α_{ik} (β_{ik}) of a real-valued coefficient $\boldsymbol{\alpha}_i$ ($\boldsymbol{\beta}_i$) differ in their sign, a signed absolute value is introduced for the complex-valued coefficients $\underline{\boldsymbol{\alpha}}_i$ ($\underline{\boldsymbol{\beta}}_i$) to preserve a correctly alternating sign. The sign of each $\underline{\alpha}_{ik}$ ($\underline{\beta}_{ik}$) can easily be determined from its phase since "positive" and "negative" values have a phase difference of approximately π. For a pair of real-valued irregular modes, the resulting coefficients are again formed by the *mean irregular electric expansion coefficient* $\overline{\boldsymbol{\alpha}}_{i\mathrm{GSTirr}}$ and *mean irregular magnetic expansion coefficient* $\overline{\boldsymbol{\beta}}_{i\mathrm{GSTirr}}$

$$\overline{\boldsymbol{\alpha}}_{i\mathrm{GSTirr}} = \frac{\boldsymbol{\alpha}_{i\mathrm{GSTirr}} + \boldsymbol{\alpha}_{i\mathrm{GSTirr}+1}}{2}, \tag{5.9}$$

$$\overline{\boldsymbol{\beta}}_{i\mathrm{GSTirr}} = \frac{\boldsymbol{\beta}_{i\mathrm{GSTirr}} + \boldsymbol{\beta}_{i\mathrm{GSTirr}+1}}{2}. \tag{5.10}$$

For longitudinal perturbations the EM fields of the irregular GST modes fit the refer-

ence fields equally well as regular GST modes. Figure 5.33(a) exemplarily depicts the absolute error of the electric field of the first irregular mode pair based on a pair of real-valued expansion coefficients $\boldsymbol{\alpha}_{i_{\mathrm{GSTirr}}}$, $\boldsymbol{\alpha}_{i_{\mathrm{GSTirr}}+1}$, their mean value $\overline{\boldsymbol{\alpha}}_{i_{\mathrm{GSTirr}}}$ and the signed absolute value of a complex $\underline{\boldsymbol{\alpha}}_{i_{\mathrm{GSTirr}}}$. It is apparent that $\overline{\boldsymbol{\alpha}}_{i_{\mathrm{GSTirr}}}$ and the signed absolute value of $\underline{\boldsymbol{\alpha}}_{i_{\mathrm{GSTirr}}}$ provide the fields with the lowest error of similar magnitude. Their errors amount to $5.41 \cdot 10^{-2}$ V/m and $5.19 \cdot 10^{-2}$ V/m at maximum and $2.44 \cdot 10^{-3}$ V/m and $1.30 \cdot 10^{-3}$ V/m on average. Figure 5.34 plots the corresponding well matching field pattern. As to be expected from the frequency results, the irregular mode fields subject to

(a)

(b)
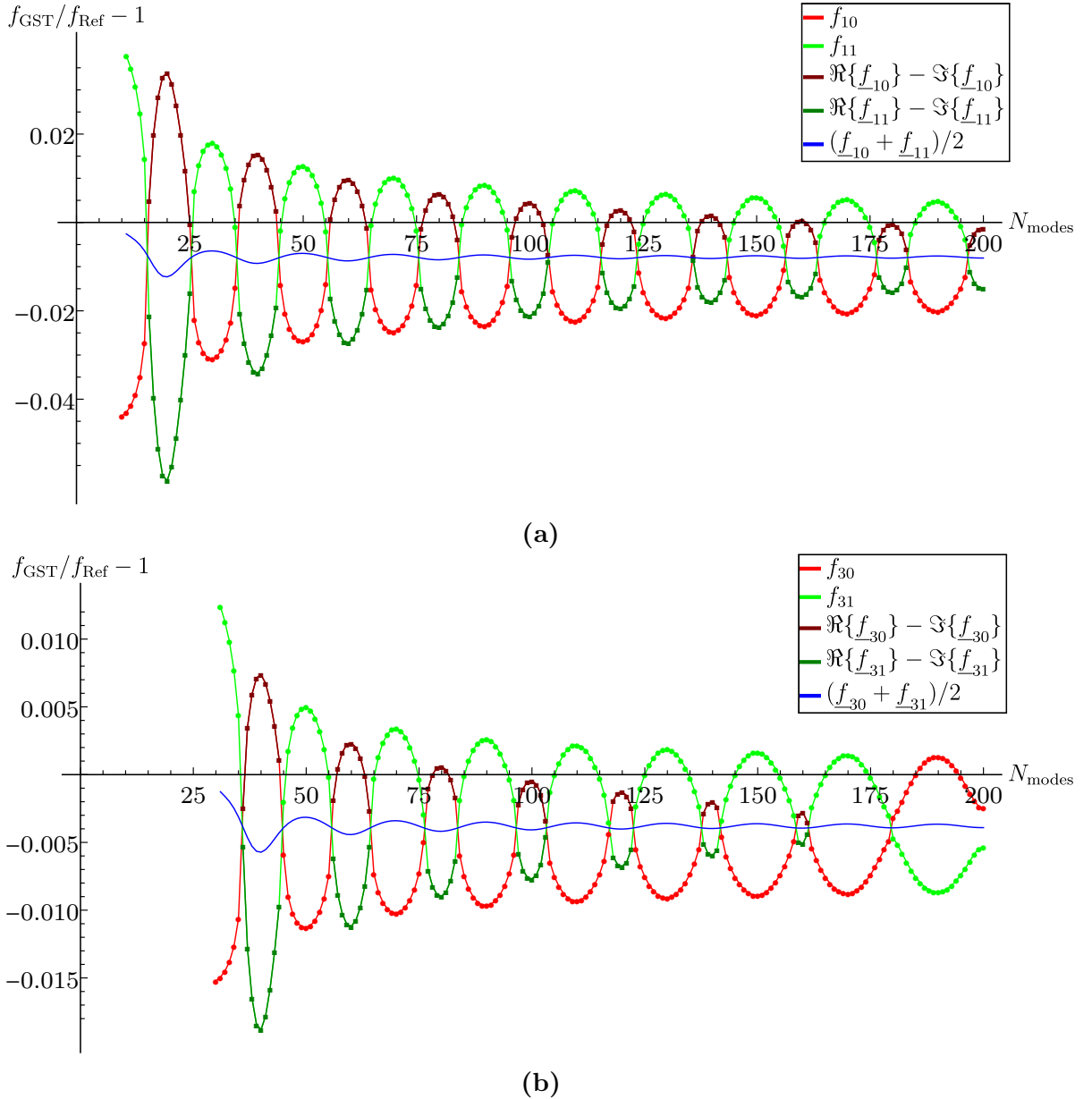
**Figure 5.32:** Relative frequency error depending on the number N_{modes} of unperturbed modes for irregular $\mathrm{TM}_{0,n,0}$ modes subject to a radial perturbation of $\Delta R/R = 5\,\%$: (a) $\mathrm{TM}_{0,10,0}$ based on real and complex frequencies of the 10th and 11th GST mode. (b) $\mathrm{TM}_{0,29,0}$ based on real and complex frequencies of the 30th and 31st GST mode.

(a)

(b)
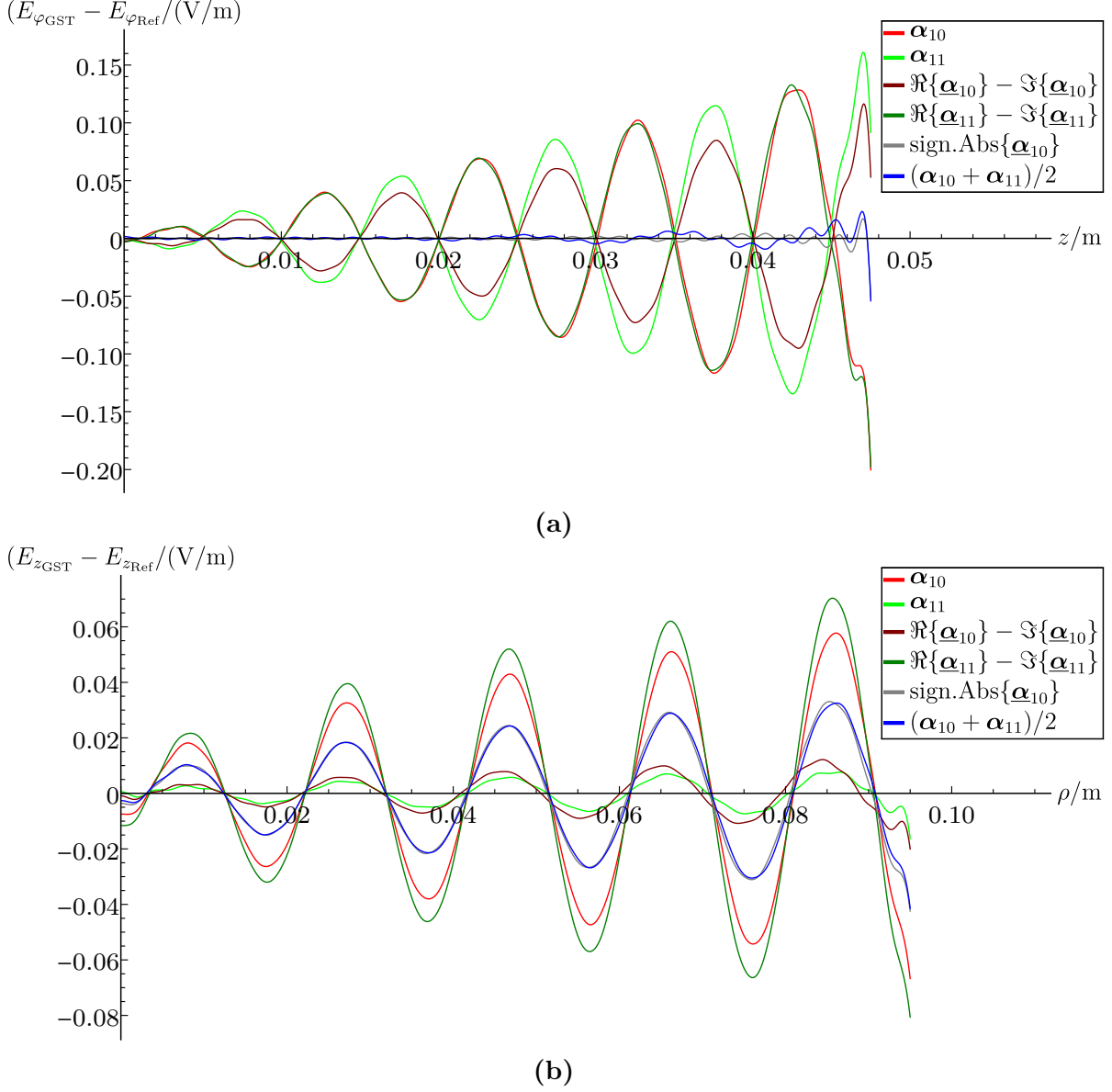
Figure 5.33: Absolute error of perturbed electric fields of irregular GST modes: (a) E_φ field of the $TE_{0,1,19}$ mode along the perturbed coordinate direction z based on real ($N_{modes} = 55$) and complex ($N_{modes} = 65$) expansion coefficients of the 10th and 11th GST mode (p: odd) for $\Delta L/L = 5\%$. (b) E_z field of the $TM_{0,10,0}$ mode along the perturbed coordinate direction ρ based on real ($N_{modes} = 55$) and complex ($N_{modes} = 64$) expansion coefficients of the 10th and 11th GST mode for $\Delta R/R = 5\%$.

a radial perturbation display a perceptible increased error. The mean coefficient $\overline{\boldsymbol{\alpha}}_{i_{\mathrm{GSTirr}}}$ and the signed absolute value of $\underline{\boldsymbol{\alpha}}_{i_{\mathrm{GSTirr}}}$ do not constitute the best fitting field due to the error offset, as Fig. 5.33(b) depicts. Their mean absolute errors are $1.46 \cdot 10^{-2}$ V/m and $1.48 \cdot 10^{-2}$ V/m and hence by an order of magnitude higher. The increased error primarily expresses in a shift of the zero crossings and has only a small impact on the local minima and maxima of the field pattern, as Fig. 5.35 demonstrates for the first two irregular mode pairs. A comparison of Fig. 5.35(a) and Fig. 5.35(b) further illustrates that the shift of the higher $\mathrm{TM}_{0,29,0}$ mode is less pronounced than the one of the $\mathrm{TM}_{0,10,0}$ mode. While the GST frequencies give no hint if an irregular mode has an error offset the EM fields clearly indicate the offset by the mismatched boundary conditions, as can be seen from both figures too. Thus, field components that need to be zero according to the applied boundary conditions can be used as an indicator of the accuracy. This, of course, is equally valid for all of the GST modes. As follows from (5.1), smaller perturbations create not only less frequent irregular modes but also increase the mode order of their
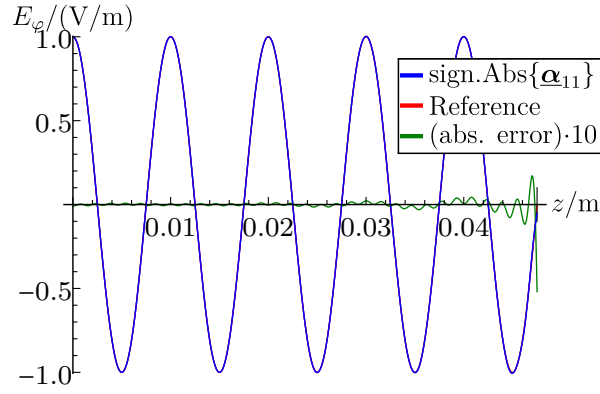
Figure 5.34: Perturbed E_φ field of the $\mathrm{TE}_{0,1,19}$ mode along the perturbed coordinate direction z based on signed absolute value of complex-valued 11th GST mode (p: odd) for $\Delta L/L = 5\,\%$ and $N_{\mathrm{modes}} = 65$.
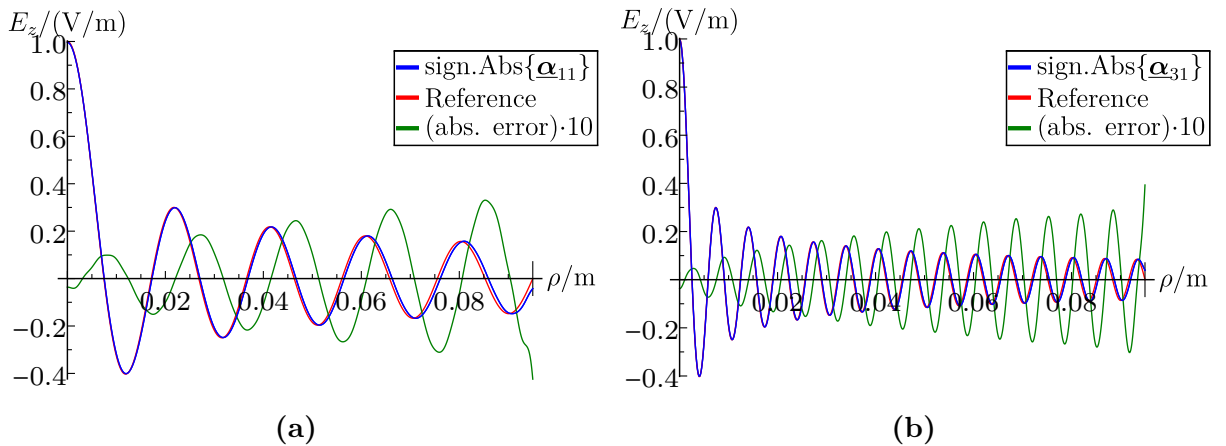
Figure 5.35: Perturbed E_z fields based on signed absolute value of irregular complex-valued GST modes ($N_{\mathrm{modes}} = 64$) along the perturbed coordinate direction ρ for $\Delta R/R = 5\,\%$: (a) E_z field of the $\mathrm{TM}_{0,10,0}$ mode (11th GST mode). (b) E_z field of the $\mathrm{TM}_{0,29,0}$ mode (31th GST mode).

first occurrence. Hence, the expectable error of irregular modes reduces. For instance, the first two irregular mode pairs for a radial perturbation of $\Delta R/R = 2\,\%$ are by a factor 32 and 96 higher than the fundamental mode frequency. Their MREs have moderate values of $3.17 \cdot 10^{-3}$ and $1.53 \cdot 10^{-3}$ which are about 0.4 times the errors for $\Delta R/R = 5\,\%$. So, the error of irregular GST modes is inverse proportional to the extent of the perturbation.

For 2D perturbations no such simple regularity of the irregular mode indices i_{GSTirr} can be found, as Fig. 5.29(d) shows. As a basic rule again applies that the first irregular mode arises if one entire half-wave of the corresponding unperturbed field fits into the volume ΔV. A similar behavior is to be expected for arbitrary shaped perturbations, i.e. irregular modes occur if their wave numbers undercut a certain value related to the perturbation extent. Advantageously, irregular modes can be detected by the existence of complex GST frequencies. In this context, it should be mentioned that the GST indices of an irregular mode pair may change depending on N_{modes}. The GST indices especially vary for N_{modes} that are small compared to the perturbed mode index, as Fig. 5.29(d) also illustrates. The cause is that the frequencies of neighboring modes can intersect by increasing N_{modes} due to a different progression. By default, the eigenmode solver sorts the results by increasing eigenvalue magnitude. Thus, two intersecting frequencies may be associated with different GST indices, as Fig. 5.36(a) demonstrates. The correct order can be derived from the expansion coefficients (see Fig. 5.36(b)) since the dominant coefficients $\alpha_{i_{\mathrm{dom}}}$ and $\beta_{i_{\mathrm{dom}}}$ allow for an easy association. In addition, an adequately high N_{modes} facilitates to skip the initial transient state. However, by rising frequency and for complex structures a correct ordering becomes increasingly difficult. Therefore, a correct ordering, especially of the irregular modes, should always be ascertained.
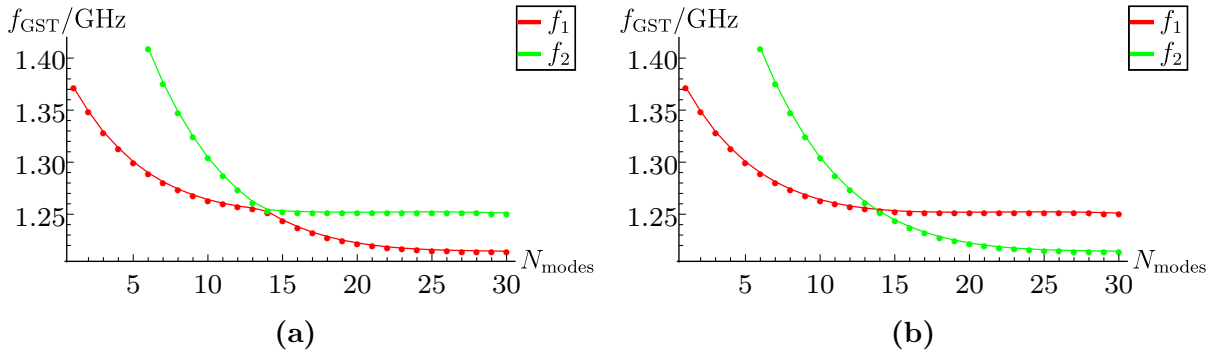

Figure 5.36: Two GST frequencies depending on the number N_{modes} of unperturbed modes: (a) Frequencies sorted by their magnitudes. (b) Correctly sorted frequencies, according to the magnitudes of their expansion coefficients.

5.2 Expansion of Reduced Eigenmode Set

The expansion of a reduced eigenmode set (ERES) is a perturbative method intentionally developed to avoid the inaccurate irregular modes emerging in GST. In contrast to GST, ERES yields a reduced number of perturbed modes $\widehat{N}_{\mathrm{modes}}$ and thereby inherently prevents a discrepancy of computed and actually computable eigenmodes. This section analyzes the achievable accuracy of ERES depending on the required effort by evaluating the frequencies and stationary electromagnetic fields of the perturbed eigenmodes exemplarily for a cylindrical resonator subject to topologically one-dimensional and two-dimensional perturbations. The presented results were partially published in [80].

5.2.1 Cylindrical Resonator

ERES has a fundamentally different convergence behavior than GST, as Fig. 5.37(a) demonstrates for a radial perturbation. While the GST frequencies have a uniform and approximately symmetrical convergence behavior, the ERES frequencies feature step-like changes. For 1D perturbations, these abrupt changes occur every time a deficient mode is removed from the set of computed perturbed modes, which means every time the difference $\Delta\widehat{N}_{\mathrm{modes}} = N_{\mathrm{modes}} - \widehat{N}_{\mathrm{modes}}$ increases. For all modes, the magnitude of the steps reduces by increasing N_{modes} and the ERES frequencies approach the correct perturbed frequencies. Like GST, ERES has a linear rate of convergence, as Fig. 5.37(b) depicts. However, it is also obvious that the error magnitude of the ERES frequencies is approximately by a factor eight higher than the one of the GST frequencies for the shown mode. Compared to GST, ERES has one additional free parameter ϵ_{EV} that influences the result accuracy. The eigenvalue truncation accuracy ϵ_{EV} determines the threshold value for the removal of deficient perturbed modes (see (3.123)) and hence regulates the reduced number $\widehat{N}_{\mathrm{modes}}$ of perturbed modes. One may expect that a low ϵ_{EV} yields the best results since it allows only small inaccuracies in the underlying ERES matrices. Though, a comparison of the
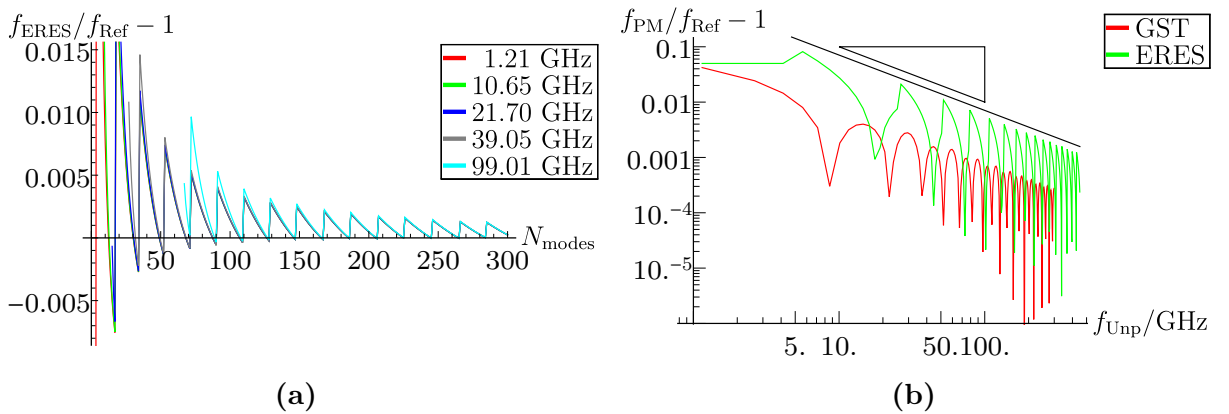
Figure 5.37: Relative ERES frequency error ($\epsilon_{\mathrm{EV}} = 0.01$) for $\mathrm{TM}_{0,n,0}$ modes subject to a radial perturbation of $\Delta R/R = 5\,\%$: (a) Error depending on the number N_{modes} of unperturbed mode for different mode orders ($n = 1, 7, 14, 25, 63$). (b) Error of the $\mathrm{TM}_{0,1,0}$ mode depending on the unperturbed frequency based on GST and ERES. The black line depicts a linear rate of convergence.

(a)

(b)
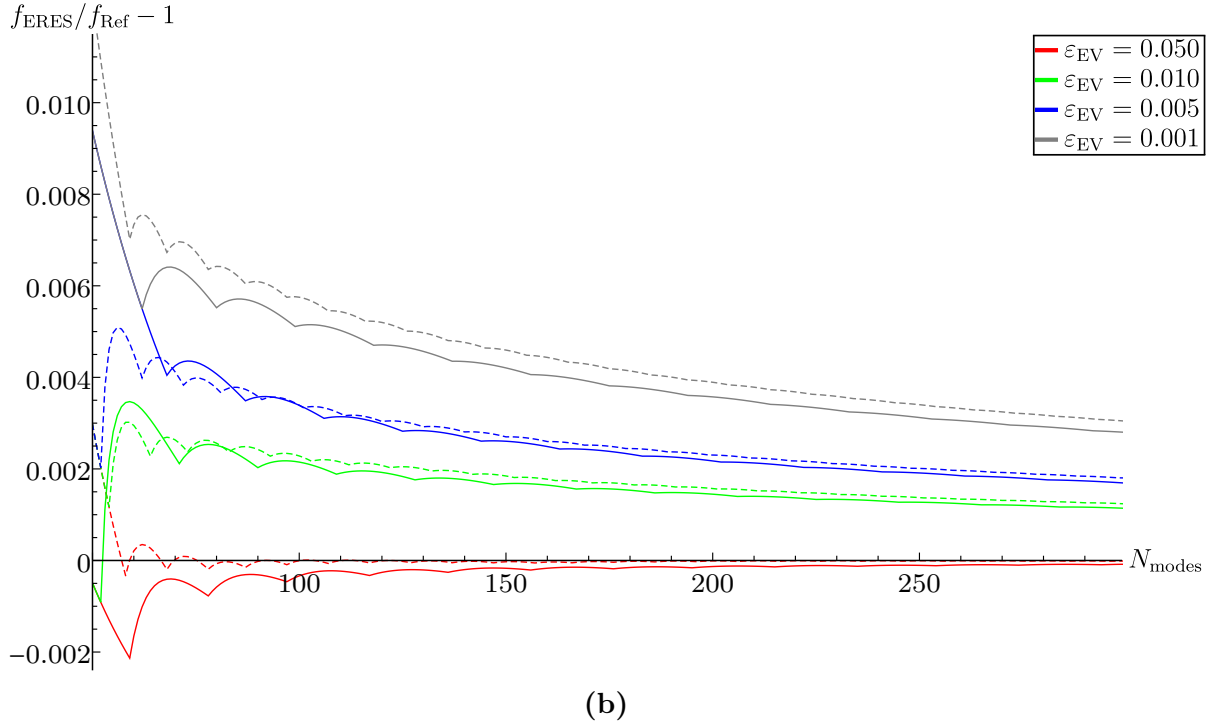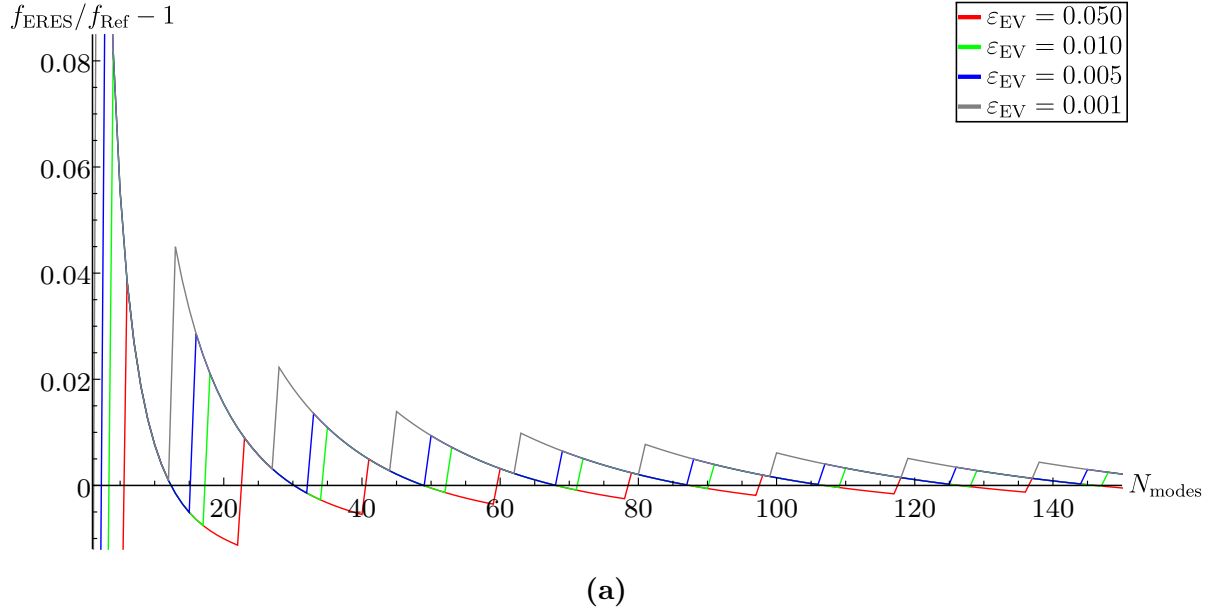
Figure 5.38: Relative frequency error depending on the number N_{modes} of unperturbed modes for the $\text{TM}_{0,1,0}$ mode subject to radial perturbations for different ϵ_{EV}: (a) $\Delta R/R = 5\,\%$ (b) Mean frequency $\overline{f}_{i_{\text{ERES}}}$ depending on N_{modes} ($N_{\text{modes}} \geq 50$) for $\Delta R/R = 5\,\%$ (continuous lines) and $\Delta R/R = 10\,\%$ (dashed lines). All frequencies f_{ERES} converge towards f_{Ref} but with a different initial error.

convergence for different ϵ_{EV} reveals that between two steps ($\Delta \widehat{N}_{\mathrm{modes}} = \mathrm{const.}$) the frequency continues along identical lines, independently of ϵ_{EV}, as Fig. 5.38(a) illustrates for the $\mathrm{TM}_{0,1,0}$ mode. The truncation accuracy ϵ_{EV} exclusively determines for which number N_{modes} the $\Delta \widehat{N}_{\mathrm{modes}}$ is increased and thus a step to the next line sets in. Consequently, the frequency error and thus naturally also the EM field accuracy may significantly vary for different values of ϵ_{EV}. For a relative low ϵ_{EV} of 10^{-3}, $\Delta \widehat{N}_{\mathrm{modes}}$ increases before the ERES frequency error crosses a value of zero, resulting in a comparatively high initial error. Even by using a very high number of unperturbed modes, the ERES frequency does not reach the correct frequency. A suitable raise of ϵ_{EV} noticeably shifts the onset of a $\Delta \widehat{N}_{\mathrm{modes}}$-increase and hence improves the overall error. This becomes particularly clear observing the mean value $\overline{f}_{i_{\mathrm{ERES}}}$ of the ERES frequency for a perturbed mode i depending on N_{modes}. Figure 5.38(b) shows that for a radial perturbation of $10\,\%$, a ϵ_{EV} of 0.05 provides a $\overline{f}_{i_{\mathrm{ERES}}}$ with a small error ranging around zero whereas the frequencies $\overline{f}_{i_{\mathrm{ERES}}}$ of lower (and higher) ϵ_{EV} only slowly approach the correct frequency. But Fig. 5.38(b) also demonstrates by means of a $5\,\%$ perturbation that the perturbation extent affects the convergence behavior and thereby the optimal value for ϵ_{EV}. In general, the step-like oscillating behavior of ERES impedes to determine the actual accuracy without knowing the true perturbed frequencies. The gradient of the mean frequencies $\overline{f}_{i_{\mathrm{ERES}}}$ gives an indication but no reliable proof for it. Figure 5.39 displays the relative frequency error for a constant N_{modes} depending on the mode order for an optimally chosen ϵ_{EV} of 0.05 and an only moderately adjusted ϵ_{EV} of 0.01. In both cases N_{modes} was defined in such a way that the frequencies $f_{i_{\mathrm{ERES}}}$ are as close as possible to the mean frequencies $\overline{f}_{i_{\mathrm{ERES}}}$. In contrast to GST, the ERES frequencies show no abrupt error growths but a steady progression. For an optimal ϵ_{EV}, the first 15 frequencies have a consistently better accuracy than the GST modes (see Fig. 5.39(a)). For modes of higher order, the error of the ERES frequencies progressively matches the error of the GST frequencies or even exceeds it (except for the second irregular mode). Especially the last 18 ERES frequencies have a noticeably higher error due to its steady growth while the GST frequencies are equally distributed around an error of zero. The relative error $|f_{\mathrm{ERES}}/f_{\mathrm{Ref}} - 1|$ has a maximum of $4.23 \cdot 10^{-3}$ and a mean value of $5.81 \cdot 10^{-4}$. So the average ERES error based on an optimally chosen ϵ_{EV}
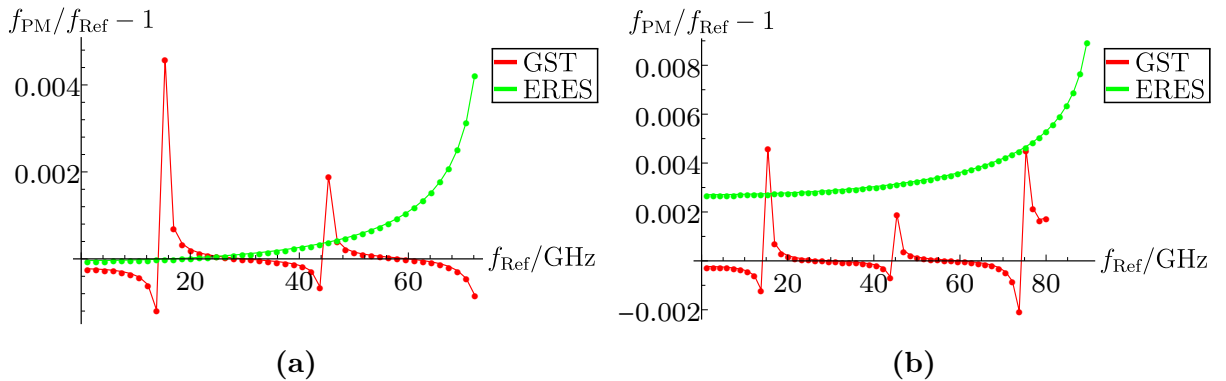
Figure 5.39: Relative error of ERES frequencies for $\mathrm{TM}_{0,n,0}$ modes depending on perturbed frequency for $\Delta R/R = 5\,\%$ in comparison to the corresponding GST frequencies ($N_{\mathrm{modes}} = 54$): (a) Optimal $\epsilon_{\mathrm{EV}} = 0.05$ for $N_{\mathrm{modes}} = 47$. (b) Moderate $\epsilon_{\mathrm{EV}} = 0.01$ for $N_{\mathrm{modes}} = 61$.

is similar to the one of GST. On the contrary, an only moderately adjusted ϵ_{EV} yields frequencies with a noticeably increased error, as Fig. 5.39(b) shows. All frequencies have a positive offset arising from the higher (initial) error and solely the first irregular GST mode has a worse accuracy than the corresponding ERES-based mode. The maximal relative error rises to $8.97 \cdot 10^{-3}$ and the MRE to $3.70 \cdot 10^{-3}$. The diminished accuracy is also clearly observable in the stationary fields, as exemplarily demonstrated for the electric field of $TM_{0,n,0}$ modes in Fig. 5.40. Table 5.2 lists the corresponding mean and maximal field errors. While the deviations for the lowest order mode $TM_{0,1,0}$ based on a ϵ_{EV} of 0.05 and 0.01 only slightly differ and both fields very well match the reference field, the E_z of the $TM_{0,7,0}$ mode already displays non-serious but apparent deviations for the moderate ϵ_{EV}. The field of the $TM_{0,29,0}$ yet has higher deviations, even noticeable in a shift of the zero crossings. Comparing Fig. 5.40(f) to Fig. 5.35(b) additionally illustrates that for $\epsilon_{EV} = 0.01$ the $TM_{0,29,0}$ ERES field is only as accurate as the corresponding GST field that represents one of the mismatched irregular GST modes. Thus, a suboptimal truncation accuracy ϵ_{EV} may significantly impair the accuracy of the eigenmodes.

The influence of the truncation accuracy ϵ_{EV} and the number N_{modes} of unperturbed modes on the accuracy of ERES becomes even more complicated applying two-dimensional perturbations. While for a 1D perturbation the abrupt frequency changes occur always for the same N_{modes}, each ERES frequency step-like changes for a different N_{modes} in case of a 2D perturbation. Figure 5.41 shows this for a set of $TE_{0,n,p}$ modes subject to a simultaneous radial and longitudinal perturbation. The differences arise from the fact that a perturbed mode is mainly affected by expansion modes with similar mode indices n and p. Therefore, each perturbed mode reacts differently to the truncation of the ERES matrices. As a consequence, each perturbed mode i has an individual optimal value for N_{modes} providing the $f_{i_{ERES}}$ closest to $\overline{f}_{i_{ERES}}$. It is also apparent from Fig. 5.41 that there is a smaller number of abrupt steps. Despite a relatively high number of 600 unperturbed modes, some ERES frequencies display no steps at all. In turn, this entails that even an optimal ϵ_{EV} does not guarantee that the $\overline{f}_{i_{ERES}}$ are close to the correct frequencies since a certain number of "oscillation cycles" (progression between two steps) is required for a reliable $\overline{f}_{i_{ERES}}$. Figure 5.42 demonstrates this for the mean ERES frequency $\overline{f}_{i_{ERES}}$ of the $TE_{0,1,1}$ mode. For an adjusted ϵ_{EV} of 0.05, $\overline{f}_{i_{ERES}}$ approaches the correct perturbed frequency within the second cycle ($N_{modes} > 187$) but diverges afterwards since the maximal N_{modes} of 600 modes is not sufficient for a third cycle. On the contrary,

Table 5.2: Mean and maximal values of the absolute error of the ERES-based electric field E_z for a radial perturbation of $\Delta R/R = 5\,\%$.

Mode	Error	$\epsilon_{EV} = 0.05$ ($N_{modes} = 49$)	$\epsilon_{EV} = 0.025$ ($N_{modes} = 47$)	$\epsilon_{EV} = 0.01$ ($N_{modes} = 61$)
$TM_{0,1,0}$	Mean	$2.68 \cdot 10^{-4}$ V/m	$6.13 \cdot 10^{-4}$ V/m	$1.53 \cdot 10^{-3}$ V/m
	Maximal	$1.97 \cdot 10^{-3}$ V/m	$3.44 \cdot 10^{-3}$ V/m	$5.29 \cdot 10^{-3}$ V/m
$TM_{0,7,0}$	Mean	$8.00 \cdot 10^{-4}$ V/m	$1.82 \cdot 10^{-3}$ V/m	$4.34 \cdot 10^{-3}$ V/m
	Maximal	$5.90 \cdot 10^{-3}$ V/m	$1.02 \cdot 10^{-2}$ V/m	$1.54 \cdot 10^{-2}$ V/m
$TM_{0,29,0}$	Mean	$2.57 \cdot 10^{-3}$ V/m	$6.19 \cdot 10^{-3}$ V/m	$1.04 \cdot 10^{-2}$ V/m
	Maximal	$1.65 \cdot 10^{-2}$ V/m	$2.37 \cdot 10^{-2}$ V/m	$2.98 \cdot 10^{-2}$ V/m
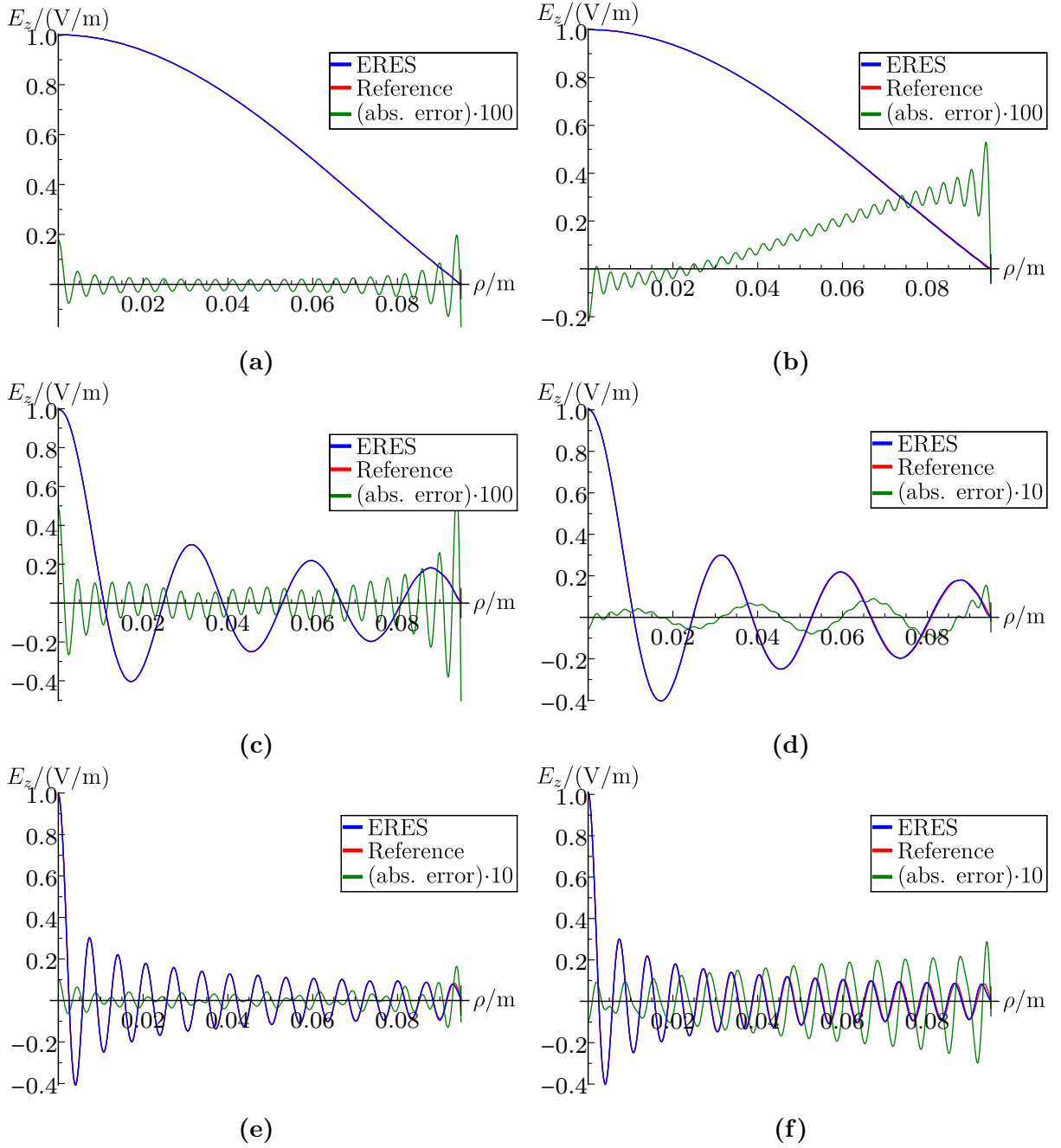
Figure 5.40: Perturbed electric field E_z of $\text{TM}_{0,n,0}$ modes along the perturbed coordinate direction ρ for $\Delta R/R = 5\,\%$: (a) $\text{TM}_{0,1,0}$ mode based on optimal $\epsilon_{\text{EV}} = 0.05$ ($N_{\text{modes}} = 47$). (b) $\text{TM}_{0,1,0}$ mode based on moderate $\epsilon_{\text{EV}} = 0.01$ ($N_{\text{modes}} = 61$). (c) $\text{TM}_{0,7,0}$ mode based on optimal $\epsilon_{\text{EV}} = 0.05$ ($N_{\text{modes}} = 47$). (d) $\text{TM}_{0,7,0}$ mode based on moderate $\epsilon_{\text{EV}} = 0.01$ ($N_{\text{modes}} = 61$). (e) $\text{TM}_{0,29,0}$ mode based on optimal $\epsilon_{\text{EV}} = 0.05$ ($N_{\text{modes}} = 47$). (f) $\text{TM}_{0,29,0}$ mode based on moderate $\epsilon_{\text{EV}} = 0.01$ ($N_{\text{modes}} = 61$).
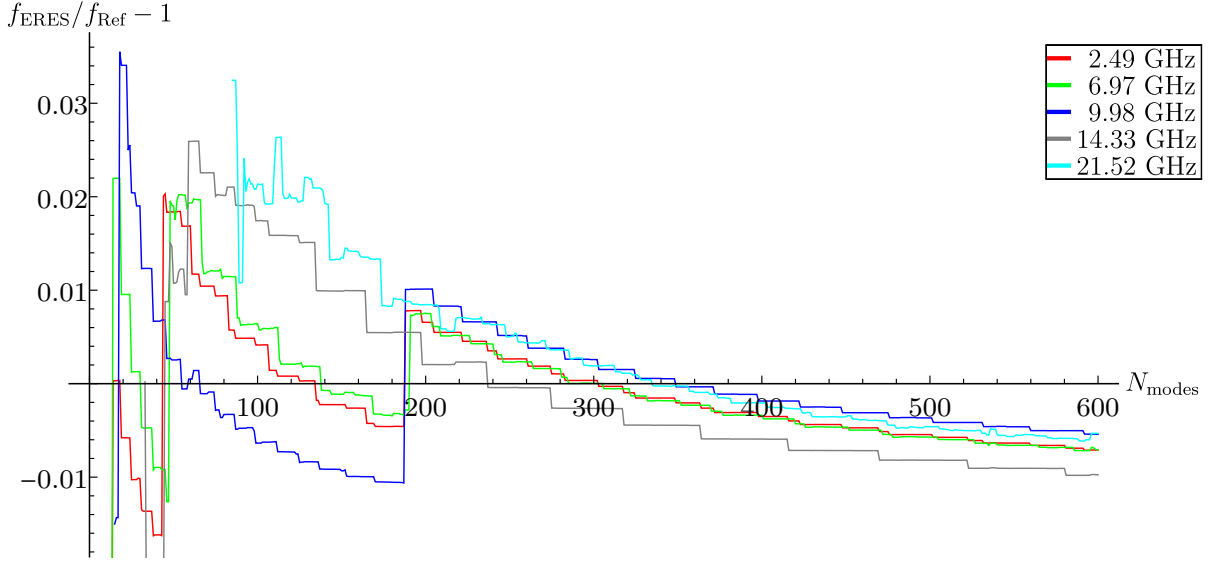
Figure 5.41: Relative ERES frequency error depending on the number N_{modes} of unperturbed modes for $\mathrm{TE}_{0,n,p}$ (p: odd) modes subject to a two-dimensional perturbation of $\Delta R/R = 5\,\%$ and $\Delta L/L = 5\,\%$ based on an optimal ϵ_{EV} of 0.05: $\mathrm{TE}_{0,1,1}$ (2.49 GHz), $\mathrm{TE}_{0,3,3}$ (6.97 GHz), $\mathrm{TE}_{0,6,1}$ (9.98 GHz), $\mathrm{TE}_{0,1,9}$ (14.33 GHz) and $\mathrm{TE}_{0,10,9}$ (21.52 GHz).
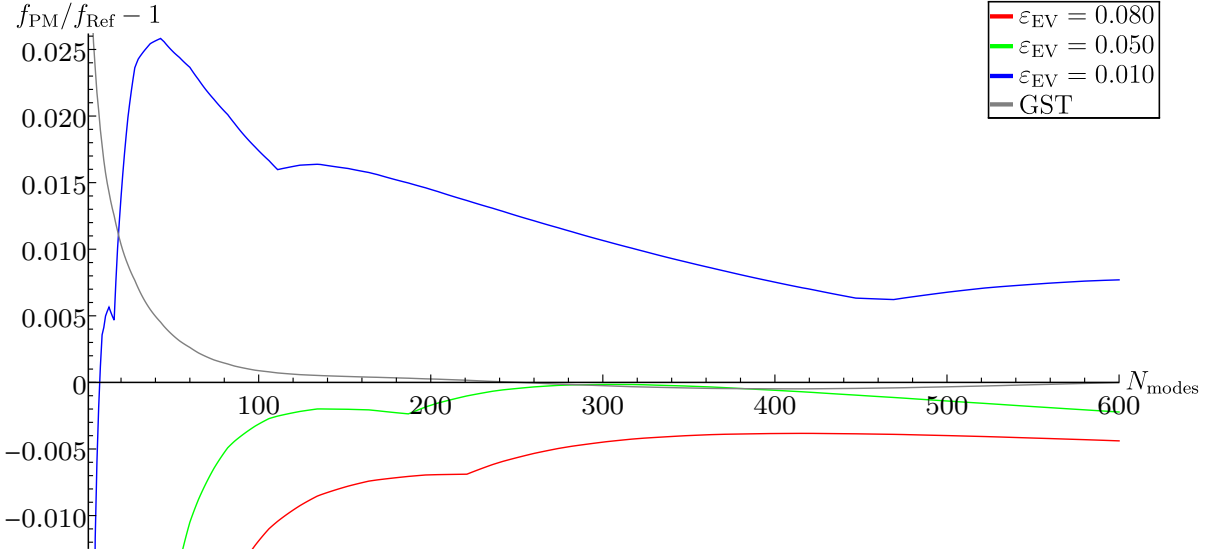
Figure 5.42: Relative error of the mean frequencies $\overline{f}_{i_{\mathrm{ERES}}}$ and $\overline{f}_{i_{\mathrm{GST}}}$ depending on the number N_{modes} of unperturbed modes for the $\mathrm{TE}_{0,1,1}$ mode based on GST and ERES with different ϵ_{EV}-values for a 2D perturbation of $\Delta R/R = 5\,\%$ and $\Delta L/L = 5\,\%$.

the GST frequency fluctuates far less once it reached a converging state. Suboptimal ϵ_{EV}-values (0.01 and 0.08), in general, result in a too slow and thereby inadequate error reduction. For comparison, the electric fields of the perturbed $TE_{0,1,1}$, $TE_{0,6,1}$, $TE_{0,1,9}$ and $TE_{0,10,9}$ mode that were already presented for GST in Fig. 5.14 – 5.17 are analyzed for an ϵ_{EV} of 0.05. To obtain the best possible accuracy, the ERES fields based on the $f_{i_{ERES}}$ closest to $\overline{f}_{i_{ERES}}$ were chosen. To additionally avoid a distortion of $\overline{f}_{i_{ERES}}$ by $f_{i_{ERES}}$ with a too small number of dominating unperturbed modes, $\overline{f}_{i_{ERES}}$ is determined only from the frequencies $f_{i_{ERES}}$ that base on at least 50 unperturbed modes with a higher frequency than the prime dominant expansion mode (see (5.2)). For instance, the mean frequency $\overline{f}_{69_{ERES}}$ of the $TE_{0,10,9}$ mode is computed from the frequencies $f_{69_{ERES}}$ with $N_{modes} \geq 119$. The fields of the $TE_{0,1,1}$ and $TE_{0,6,1}$ mode very well coincide with the reference fields and provide an equal accuracy as GST, as Fig. 5.43 and 5.44 depict. The field of the $TE_{0,1,9}$ mode in Fig. 5.45 still has a good agreement but the amplitude of E_φ observably deviates along the last half-wave close to $z = \widetilde{L}$. In contrast, the $TE_{0,10,9}$ field tremendously deviates from the correct field, as Fig. 5.46 displays. Especially along the radial direction ρ both the amplitude and the position of the zero crossings disagree. This
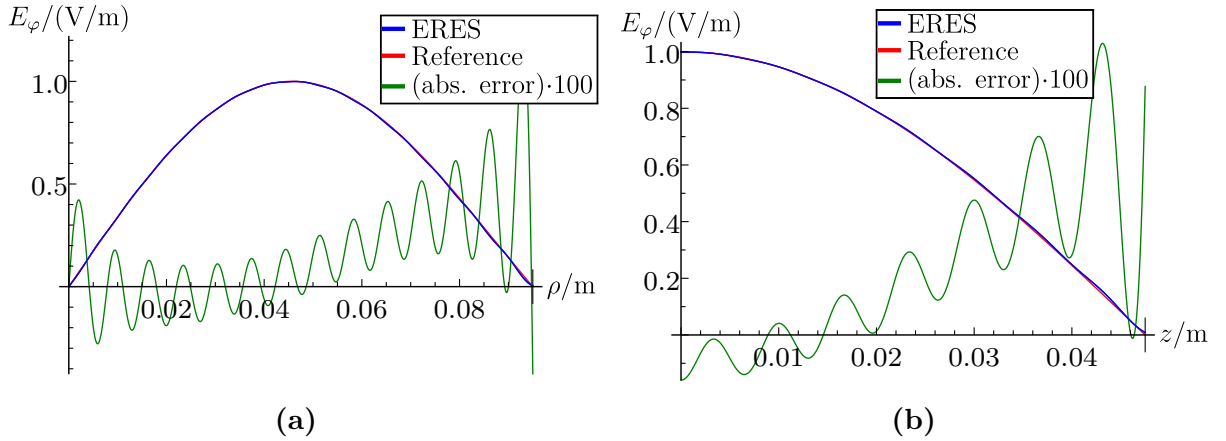
Figure 5.43: Perturbed electric field of the $TE_{0,1,1}$ mode along both perturbed coordinate directions ρ and z for $\Delta R/R = 5\,\%$, $\Delta L/L = 5\,\%$, $\epsilon_{EV} = 0.05$ and $N_{modes} = 318$.
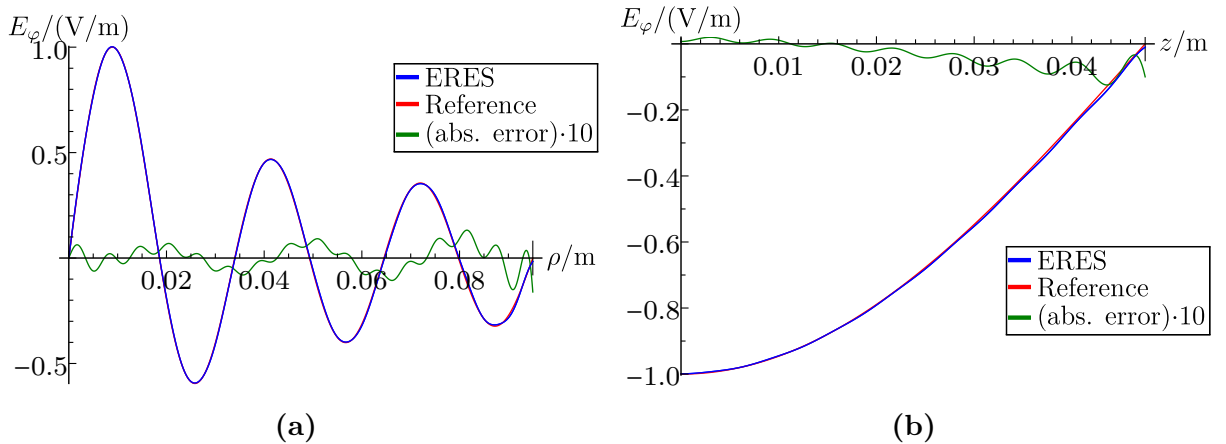
Figure 5.44: Perturbed electric field of the $TE_{0,6,1}$ mode along both perturbed coordinate directions ρ and z for $\Delta R/R = 5\,\%$, $\Delta L/L = 5\,\%$, $\epsilon_{EV} = 0.05$ and $N_{modes} = 398$.

arises from the fact that the mean frequency $\overline{f}_{69_{\text{ERES}}}$ does not correspond to the optimal ($N_{\text{modes}} \approx 344$, see Fig. 5.41) but a slightly smaller number of modes ($N_{\text{modes}} = 313$). Determining $\overline{f}_{69_{\text{ERES}}}$ from all frequencies $f_{69_{\text{ERES}}}$ with $N_{\text{modes}} \geq 1$ would create an even worse result. Hence, the $TE_{0,10,9}$ mode clearly elucidates that a suitable accuracy cannot be guaranteed without an adequate number of oscillation cycles even if a well adjusted truncation accuracy ϵ_{EV} is provided.

Figure 5.45: Perturbed electric field of the $TE_{0,1,9}$ mode along both perturbed coordinate directions ρ and z for $\Delta R/R = 5\%$, $\Delta L/L = 5\%$, $\epsilon_{\text{EV}} = 0.05$ and $N_{\text{modes}} = 274$.
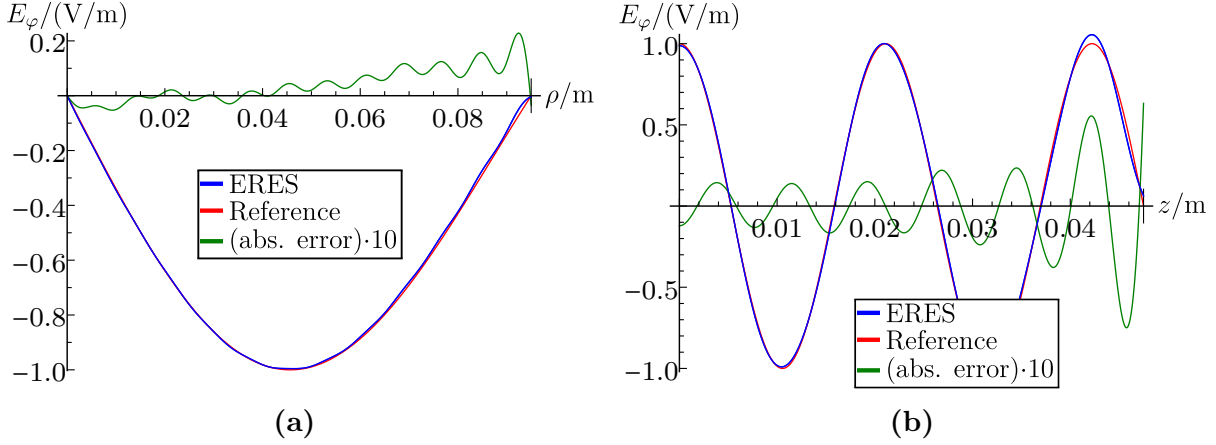

Figure 5.46: Perturbed electric field of the $TE_{0,10,9}$ mode along both perturbed coordinate directions ρ and z for $\Delta R/R = 5\%$, $\Delta L/L = 5\%$, $\epsilon_{\text{EV}} = 0.05$ and $N_{\text{modes}} = 313$.
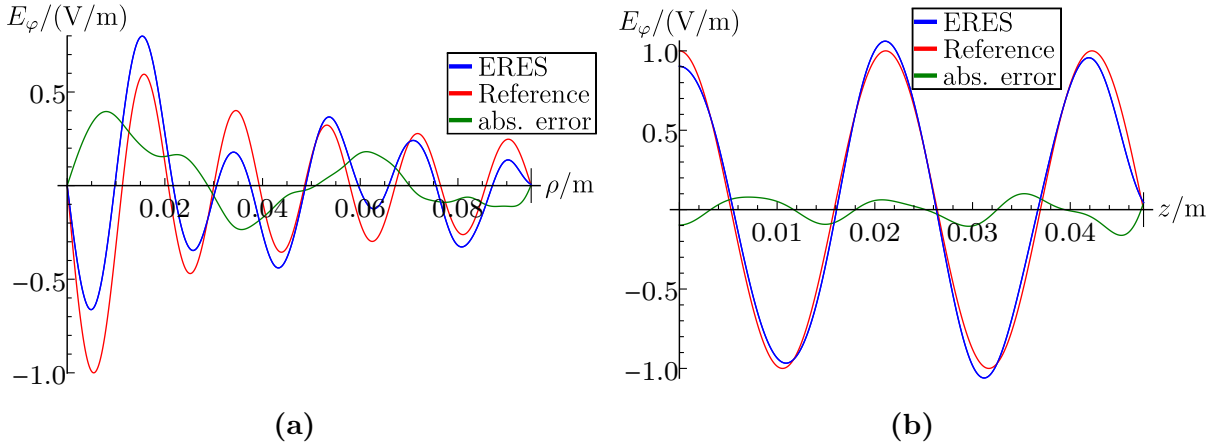
5.3   Comparison of Methods

Summarizing, GST allows for a very accurate computation of perturbed eigenmodes, on condition that each perturbed mode is expanded in terms of an adequate number of dominating unperturbed modes, guaranteeing a converging state of the normal mode expansion. A comparison of one-dimensional and two-dimensional perturbations evinced that the required number of dominating modes primarily depends on the type and extent of the perturbation. Since the order of the dominating modes rises with increasing perturbed mode order, N_{modes} always should exceed the desired number of perturbed modes by a corresponding amount. Considering these aspects, frequencies and stationary EM fields may be accurately computed over a wide frequency range. The clear drawback of GST is the repetitive occurrence of irregular modes with a diminished accuracy. The phenomenon may primarily impair irregular modes of lower order. The accuracy of irregular modes of higher order is less affected. A further important fact is, that the error of the GST modes reduces faster for larger perturbations but that the results are more affected by irregular modes whereas smaller perturbations produce a slower convergence but less and more accurate irregular modes. The major advantage of ERES is that it inherently prevents the generation of irregular modes. However, ERES possesses a generally higher error than GST and therefore requires a distinctly larger number N_{modes} of unperturbed modes. This is complicated by the free parameter ϵ_{EV} that may additionally perceptibly impair the convergence. The optimal setting of ϵ_{EV} depends on the extent and presumably on the type of perturbation and thus is difficult to assess in advance. In addition, the step-like changes of the error causes results with an unreliably accuracy for multi-dimensional and consequently realistic perturbations, that may only be avoided at the cost of a very high number N_{modes}.

One of the main restrictions for applying perturbative methods to real-life accelerating structures is the limited number of computable unperturbed modes N_{modes}. Thus, GST is the preferable PM since it provides a more reliable and mostly higher accuracy than ERES, requiring less unperturbed modes. In addition, realistic perturbations of accelerating cavities are relatively small as introduced in Section 1.3. Hence, the amount and impairment of irregular modes is to be expected comparatively small. Another consequence of this chapter is, that in any case a convergence study depending on N_{modes} should be performed. It involves only a minor additional computational effort but provides essential information considering converging state, mean perturbed frequencies and expectable accuracy, allowing to choose the optimal results.

Chapter 6

Application Examples

The applicability of perturbative methods to real-life accelerating cavities is of major significance for the methods' benefit. The EM fields in realistic resonators may not be determined analytically but require a numerical solution. Thus, the PMs have to be performed based on numerically computed unperturbed eigenmodes. This chapter analyzes the accuracy of GST-based eigenmodes for different elliptical single-cell resonators and a multicell structure. For the multicell resonator additionally an extensive parameter study is presented included a cavity characteristics optimization and a robustness analysis with respect to inevitable shape imperfections. Further, it was investigated if the harmonics of a cylindrical resonator can be utilized to expand the eigenmodes of an elliptical single-cell resonator, in order to avoid a numerical computation of the unperturbed eigenmodes. The second method ERES was not applied because of the disadvantages discussed in the previous chapter.

6.1 Elliptical Single-Cell Resonator

The shape of an elliptical cell is described by seven geometric parameters, as Fig. 6.1 shows. Exemplarily, the Cornell seven-cell SRF cavity design [4] with PEC boundaries was chosen as unperturbed geometric for the GST single-cell investigations. Table 6.1 lists the corresponding geometric parameters.

To assess the accuracy and computational demands of GST different types of rotationally symmetric perturbations and subsequently asymmetric perturbations were investigated. As rotationally symmetric perturbations different variations of the equator radius R_{eq} and the cell width were applied. The cell width variations were realized by an equal percentage modification of the longitudinal ellipse parameters $x_{Ell,eq}$ and $x_{Ell,iris}$. Com-

Table 6.1: Shape parameters of unperturbed single-cell resonator.

Parameter	R_{eq}	R_{iris}	L_{cell}	$x_{Ell,eq}$	$y_{Ell,eq}$	$x_{Ell,iris}$	$y_{Ell,iris}$
Value in mm	102.8797	17.99 [i]	115.384	41.35	35.57	12.35	21.14

---

[i] The actual iris radius R_{iris} of the Cornell design is 35.98 mm. Inadvertently, only half its value was used for the unperturbed and perturbed geometries. The correctness of the GST results is not affected.

pared to equator variations they are smaller. As asymmetric perturbation exemplarily a single circular dent was applied in order to create a fully symmetry breaking resonator. Figure 6.2 illustrates the different perturbations. All unperturbed modes were computed with CST MWS using all three symmetry planes. The simulation of 100 modes took about three hours of computational time (CPU: Intel Xeon E5-2643 $2 \times 3.30\,$GHz, RAM: 256 GB). The volume integral matrices $\mathbf{Q}_e$, $\mathbf{S}_e$, $\mathbf{Q}_h$, $\mathbf{S}_h$ of the EM fields were formed based on discrete 3D volume elements. In the following, the main relevant GST results for the PEC Cornell single-cell are discussed. Appendix C.2 presents a more extensive summary of result data concerning required volume discretization, convergence behavior, eigenmode accuracy and irregular modes. Some results were already published in [96].
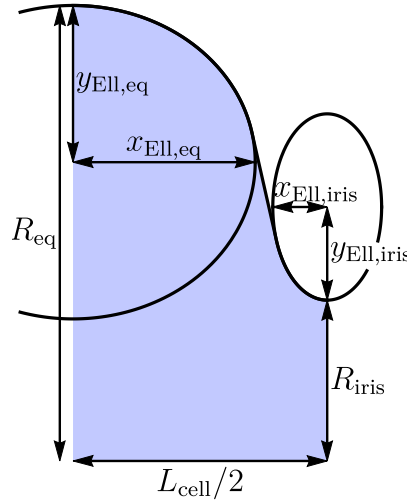
Figure 6.1: Rotationally symmetric elliptical single-cell (quarter view) with an equator radius R_{eq}, an iris radius R_{iris} and a cell length $L_{\mathrm{c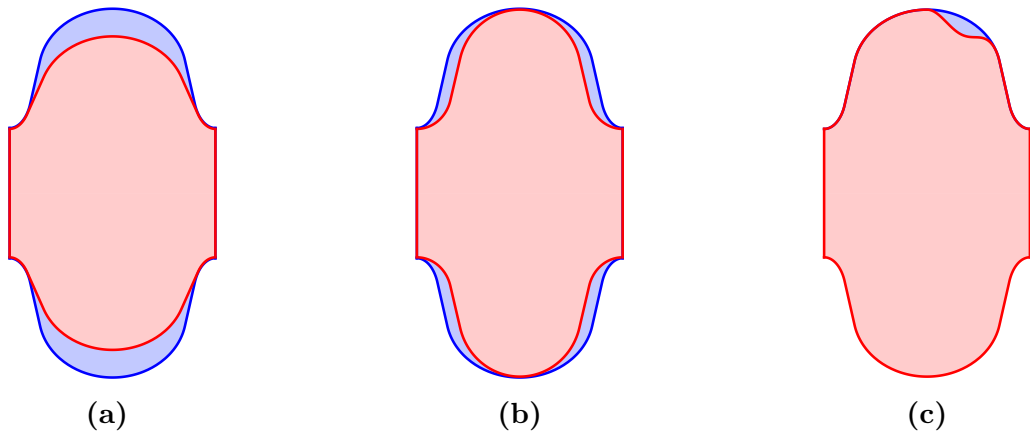ell}}$. Curvatures and the straight transition between equator and iris are set by the longitudinal ellipse parameters $x_{\mathrm{Ell,eq}}$, $x_{\mathrm{Ell,iris}}$ and the radial ellipse parameters $y_{\mathrm{Ell,eq}}$, $y_{\mathrm{Ell,iris}}$.


Figure 6.2: Types of perturbations applied to an elliptical single-cell resonator: (a) Reduction of cell equator R_{eq}. (a) Reduction of cell width by simultaneous increase of $x_{\mathrm{Ell,iris}}$ and decrease of $x_{\mathrm{Ell,eq}}$. (a) Circular dent.

6.1.1 Rotationally Symmetric Perturbations

For the rotationally symmetric perturbations exemplarily modes with an even azimuthal index m (monopole, quadrupole, etc.) were investigated based on 871 unperturbed modes within a frequency range of 1.24–20.83 GHz. The unperturbed modes were separated into subsets of interacting modes based on their azimuthal dependence. For example, TM_0-like modes form a set of 70, quadrupole modes a set of 118 modes. Depending on the perturbation extent, between $2 \cdot 10^4$ and $4 \cdot 10^4$ volume elements were necessary for a sufficient discretization of the removed volume ΔV. For this, larger perturbations required more elements conditioned by the minimal unperturbed wavelength λ_{min}. The computation of discrete volume integrals for a set of 50 modes took 50 to 120 s, the final algebraic GST operations lie in the range of some seconds (CPU: Intel Xeon X5650 2×2.66 GHz, RAM: 20 GB). Thus, the computation of the unperturbed modes is the most expensive part while the actual GST procedures require only a fraction of the effort.

All regular GST modes homogeneously converge toward the correct perturbed frequency. For all variation types, a rapid reduction of the frequency error is already achieved with a small number N_{modes} of modes. For large perturbations, a clear oscillating behavior around the correct solution is observable. A 10 % R_{eq}-reduction requires only about 24 modes to reach a converging state for the perturbed frequencies of TM_0-like modes up to 8.82 GHz, as Fig. 6.3(a) illustrates. For a 5 % reduction about 30 modes are needed. In case of small perturbations, GST does not reach an oscillating state, as Fig. 6.3(b) demonstrates for TM_0-like modes based on the maximal computed number N_{modes} of 70 modes. Thereby, all GST frequencies have a positive error offset and are not evenly distributed around an error of zero, in contrast to moderate and large perturbations. However, the frequency error is generally lower for a small variation so that the overall accuracy is similar. Table 6.2 demonstrates this by the respective mean and maximal relative frequency error for TM_0-like and quadrupole modes. Independent of the perturbation extent the MRE is lower than $3.28 \cdot 10^{-3}$. Appendix C.2.3 presents the respective frequency plots. GST also provides very precise perturbed fields for modes of lower order. For small and moderate perturbations, the maximal deviations are about two orders of magnitude lower than the
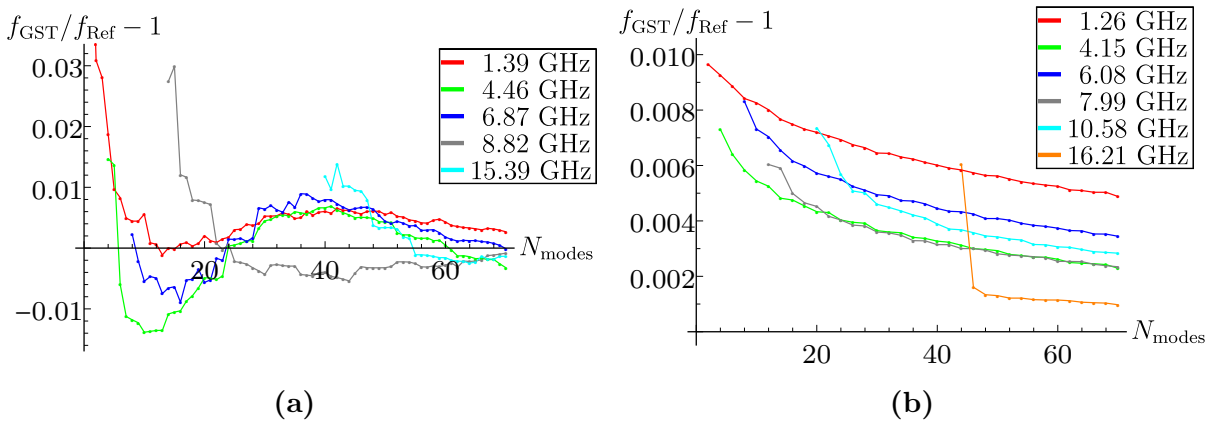

Figure 6.3: Relative frequency error depending on the number N_{modes} of unperturbed modes for TM_0-like modes for different equator perturbations. (a) Reduction of 10 %. (b) Reduction of 1 %.

Table 6.2: Mean and maximal value of relative frequency error of regular GST frequencies for TM_0-like and quadrupole modes: Irregular modes are excluded.

Perturbation		Freq. range	$|f_{GST}/f_{Ref} - 1|$	
Type	Extent	in GHz	Mean	Max
Equator	10 %	1.39–15.39	$2.88 \cdot 10^{-3}$	$7.77 \cdot 10^{-3}$
	5 %	1.32–14.85	$1.61 \cdot 10^{-3}$	$3.68 \cdot 10^{-3}$
	1 %	1.26–16.21	$2.71 \cdot 10^{-3}$	$4.88 \cdot 10^{-3}$
Width	10 %	1.27–11.62	$1.47 \cdot 10^{-3}$	$6.21 \cdot 10^{-3}$
	5 %	1.25–12.71	$3.28 \cdot 10^{-3}$	$5.98 \cdot 10^{-3}$
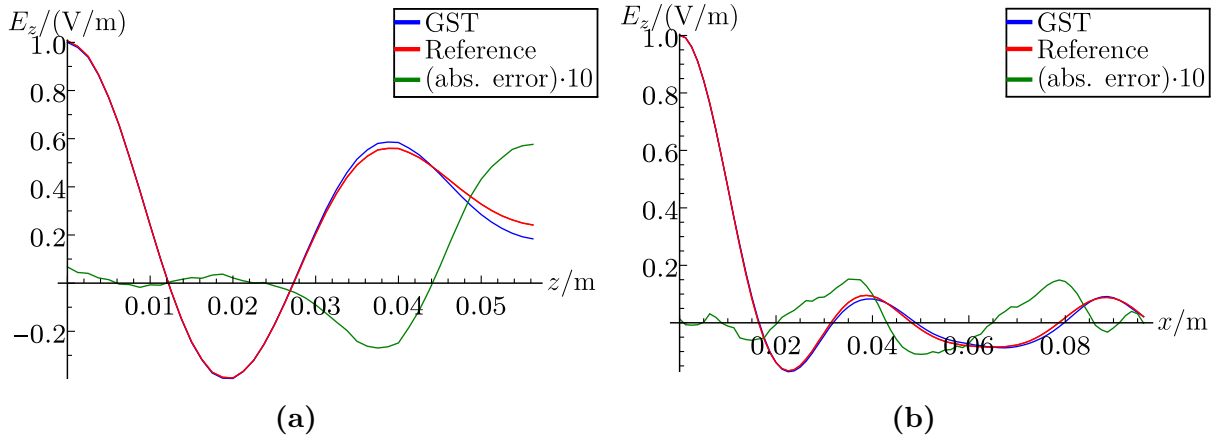
Figure 6.4: Perturbed electric field of TM_0-like mode with a frequency of $10.18\,GHz$ along the x- and z-axis for a reduction of R_{eq} by $5\,\%$ and $N_{modes} = 70$: Non-displayed field components are zero.

maximal absolute value of the respective fields. The mean deviations often are considerably smaller. The error just marginally increases by rising frequency. Even for modes with a frequency only half the maximal unperturbed frequency the GST fields coincide very well with the reference fields, as exemplarily shown for a $5\,\%$ equator reduction in Fig. 6.4. Beyond that frequency, the accuracy increasingly diminishes but the basic field patterns still have a good agreement. For relatively large perturbations, like the equator reduction of $10\,\%$, GST yields a slightly worse accuracy. Here, the mean absolute error of LOMs is already in the range of 10^{-2} while the maximal error is about $4 \cdot 10^{-2}$. Nevertheless, the field patterns match to a large extent. Table 6.3 lists the mean and maximal field error inside the complete perturbed domain $\widetilde{V}$ for a selection of modes. Appendix C.2.4 presents corresponding 1D field plots along the x- and z-axis.

As expected from the investigations of simple boundary value problems in Chapter 5, the GST results for elliptical resonators also contain irregular eigenmodes in form of partially complex-valued mode pairs. For a $1\,\%$ equator and a $5\,\%$ width reduction, no irregular modes were detected within the examined frequency range up to $20.83\,GHz$. Even for a medial equator perturbation of $5\,\%$ only a few irregular mode pairs exist. The first occurs for a very high frequency of $13.00\,GHz$, which is ten times higher than the fundamental frequency. Although its GST frequency matches the correct frequency very well (MRE: $4.03 \cdot 10^{-4}$) the field only moderately agrees with the reference field.

Table 6.3: Mean and maximal values of absolute field deviations between GST-based electric fields and reference fields for TM_0-like modes: The reference fields are scaled to a maximal value of $1\,\mathrm{V/m}$. The deviations are listed for E_z along the x- and z-axis as well as for the norm of the vector fields $\mathbf{E}$ [ii] inside the complete perturbed domain $\widetilde{V}$.

Reduction of equator R_{eq}

Per.	f_{Ref} in GHz	$|E_{z,\mathrm{GST}}(x) - E_{z,\mathrm{Ref}}(x)|$ in V/m		$|E_{z,\mathrm{GST}}(z) - E_{z,\mathrm{Ref}}(z)|$ in V/m		$\|\mathbf{E}_{\mathrm{GST}}(\mathbf{r}) - \mathbf{E}_{\mathrm{Ref}}(\mathbf{r})\|$ in V/m	
		Mean	Max	Mean	Max	Mean	Max
10 %	1.39	$1.04 \cdot 10^{-2}$	$3.08 \cdot 10^{-2}$	$3.66 \cdot 10^{-3}$	$8.61 \cdot 10^{-3}$	$1.23 \cdot 10^{-2}$	$3.86 \cdot 10^{-2}$
	8.07	$1.28 \cdot 10^{-2}$	$3.08 \cdot 10^{-2}$	$2.73 \cdot 10^{-2}$	$6.79 \cdot 10^{-2}$	$1.49 \cdot 10^{-2}$	$6.35 \cdot 10^{-2}$
	15.39	$9.88 \cdot 10^{-2}$	$2.98 \cdot 10^{-1}$	$3.84 \cdot 10^{-2}$	$9.70 \cdot 10^{-2}$	$1.02 \cdot 10^{-2}$	$9.29 \cdot 10^{-2}$
5 %	1.32	$5.09 \cdot 10^{-3}$	$1.80 \cdot 10^{-2}$	$2.58 \cdot 10^{-3}$	$5.31 \cdot 10^{-3}$	$6.10 \cdot 10^{-3}$	$1.87 \cdot 10^{-2}$
	10.18	$6.34 \cdot 10^{-3}$	$1.52 \cdot 10^{-2}$	$1.46 \cdot 10^{-2}$	$5.76 \cdot 10^{-2}$	$7.05 \cdot 10^{-3}$	$5.66 \cdot 10^{-2}$
	13.37	$4.92 \cdot 10^{-2}$	$1.23 \cdot 10^{-1}$	$1.06 \cdot 10^{-1}$	$3.26 \cdot 10^{-1}$	$2.64 \cdot 10^{-2}$	$2.99 \cdot 10^{-1}$
1 %	1.26	$4.02 \cdot 10^{-3}$	$1.19 \cdot 10^{-2}$	$1.45 \cdot 10^{-3}$	$3.89 \cdot 10^{-3}$	$4.57 \cdot 10^{-3}$	$1.19 \cdot 10^{-2}$
	7.99	$8.56 \cdot 10^{-3}$	$6.26 \cdot 10^{-2}$	$1.04 \cdot 10^{-2}$	$2.65 \cdot 10^{-2}$	$7.27 \cdot 10^{-3}$	$4.33 \cdot 10^{-2}$
	16.21	$2.25 \cdot 10^{-2}$	$6.16 \cdot 10^{-2}$	$6.97 \cdot 10^{-2}$	$1.47 \cdot 10^{-2}$	$1.40 \cdot 10^{-2}$	$1.56 \cdot 10^{-1}$

Cell width reduction

Per.	f_{Ref} in GHz	$|E_{z,\mathrm{GST}}(x) - E_{z,\mathrm{Ref}}(x)|$ in V/m		$|E_{z,\mathrm{GST}}(z) - E_{z,\mathrm{Ref}}(z)|$ in V/m		$\|\mathbf{E}_{\mathrm{GST}}(\mathbf{r}) - \mathbf{E}_{\mathrm{Ref}}(\mathbf{r})\|$ in V/m	
		Mean	Max	Mean	Max	Mean	Max
10 %	1.27	$7.15 \cdot 10^{-3}$	$1.37 \cdot 10^{-2}$	$1.38 \cdot 10^{-2}$	$3.11 \cdot 10^{-2}$	$9.46 \cdot 10^{-3}$	$4.35 \cdot 10^{-2}$
	11.62	$1.24 \cdot 10^{-1}$	$3.09 \cdot 10^{-1}$	$9.91 \cdot 10^{-2}$	$2.52 \cdot 10^{-1}$	$3.54 \cdot 10^{-2}$	$2.33 \cdot 10^{-1}$
5 %	1.25	$5.09 \cdot 10^{-3}$	$1.80 \cdot 10^{-2}$	$3.59 \cdot 10^{-3}$	$7.13 \cdot 10^{-3}$	$4.73 \cdot 10^{-3}$	$3.11 \cdot 10^{-2}$
	12.71	$2.93 \cdot 10^{-2}$	$1.68 \cdot 10^{-1}$	$2.81 \cdot 10^{-2}$	$7.56 \cdot 10^{-2}$	$6.72 \cdot 10^{-3}$	$8.46 \cdot 10^{-2}$

However, this arises not merely from the fact that the mode is an irregular one but also from its high order. Table 6.4 lists their occurrence. For a $10\,\%$ R_{eq}-reduction, the first irregular mode occurs at $7.76\,\mathrm{GHz}$. Disadvantageously, its EM field tremendously deviates from the correct one due to the fact that the average of the two respective frequencies does not converge towards the reference frequency but has an offset. The second irregular GST mode at $9.65\,\mathrm{GHz}$ possesses a better basic agreement despite the still increased quantitative deviations. Hence, only irregular modes of low order are seriously defective while the affected modes of higher order at least have a correct basic field pattern, as Subsection 5.1.3 already concluded. But a deterioration of the irregular GST modes can not be evaded. However, merely a small number of irregular modes exists even for such a relatively large perturbation. Due to the fact that realistic imperfections are in general comparatively small, irregular GST modes are largely negligible in the context of robustness analyses. For the purposes of a cavity optimization, they may be of relevance if the applied geometric modifications are accordingly large. But this is to be expected only in rare cases. It can be concluded that except for a potentially low number of irregular modes, GST provides accurate frequencies and fields over a wide frequency range.

[ii]The axial field may display larger deviations than the fields in the full domain. This arises from the fact that axial and 3D fields are scaled separately to a maximal value of $1\,\mathrm{V/m}$.

Table 6.4: Occurrence of irregular modes for different perturbations within a frequency range of 1.24–20.53 GHz.

Perturbation		Mode type	Irregular modes	
Type	Extent		Number	First modes: f_{Ref}/GHz
Equator	10 %	TM_0-like	7	7.76, 9.65, 11.55
	10 %	quadrupole	9	7.81, 9.09, 9.63
	5 %	TM_0-like	4	13.00, 14.31, 16.00
	1 %	TM_0-like	0	-
Cell width	10 %	TM_0-like	2	17.91, 20.37
	5 %	TM_0-like	0	-

6.1.2 Asymmetric Perturbations

Circular dents of different extent and position were applied to the single-cell resonator in order to investigate the application of GST to both small and asymmetric geometric variations. In the following, the results for a dent with a radius of 12 mm, a depth of about 9 mm (10 %) and a distance of 15 mm to the equator are discussed. Only about 6400 tetrahedral elements were required for determining the volume integrals. Although the dent is a fully symmetry breaking perturbation, the unperturbed modes can be computed using all symmetry planes. This noticeably reduces the computational effort. For it, solely the eigenmodes simulated with the different symmetry plane settings have to be recombined to the full modal spectrum. By doing so, 1167 modes within a frequency range of 1.24–11.63 GHz were computed.

Due to the fact that the deformed volume ΔV is very small and all unperturbed modes interact inside ΔV, the GST results converge relatively slow since the spread between the single unperturbed frequencies is fundamentally smaller compared to IA mode sets of symmetric perturbations. At least 750 modes are required for a converging state. But, the perturbed frequencies are already very precise using only a small number of modes since the frequency shift relatively to the unperturbed frequencies is very small.

(a)

(b)
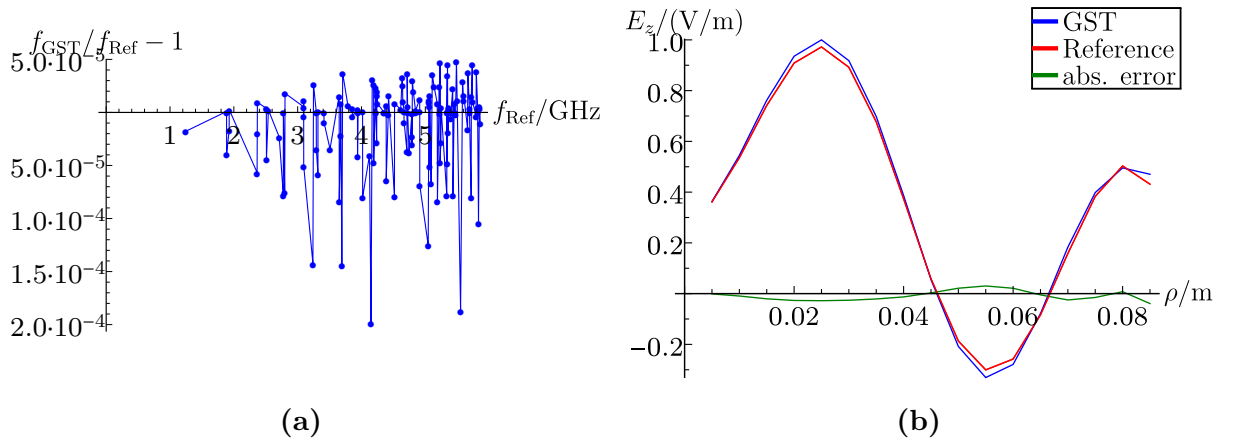
Figure 6.5: GST results for a 10 % dent for $N_{\text{modes}} = 1167$. (a) Relative frequency error depending on perturbed frequency f_{Ref}. (b) Longitudinal electric field of quadrupole mode at 5.86 GHz along radial direction ρ towards center of perturbation.

Table 6.5: Mean and maximal values of absolute field deviations between GST-based electric fields and reference fields inside the complete perturbed domain $\widetilde{V}$ for an elliptical resonator with a $10\,\%$ dent: The reference fields are scaled to a maximal value of $1\,\mathrm{V/m}$.

Mode type	$f_{\mathrm{Ref}}/\mathrm{GHz}$	$\|\mathbf{E}_{\mathrm{GST}}(\mathbf{r}) - \mathbf{E}_{\mathrm{Ref}}(\mathbf{r})\|\,/(\mathrm{V/m})$	
		Mean	Max
Monopole	1.24	$1.10 \cdot 10^{-3}$	$1.47 \cdot 10^{-1}$
Dipole	1.89	$1.61 \cdot 10^{-4}$	$3.89 \cdot 10^{-3}$
Quadrupole	5.86	$9.10 \cdot 10^{-3}$	$6.13 \cdot 10^{-1}$

Up to $5.87\,\mathrm{GHz}$, the relative frequency error is $2.78 \cdot 10^{-5}$ on average and $1.99 \cdot 10^{-4}$ at maximum, as Fig. 6.5(a) displays. Hence, the frequency accuracy is of minor relevance. Since the dent is relatively small and locally distinct, extremely short wavelengths are required for a precise reconstruction of the fields in direct vicinity of the dent. As a consequence, increased deviations arise close to the deformed boundary but inside the rest of $\widetilde{V}$ the fields accurately match. This is especially elucidated by the very low mean but partially high maximal field error within $\widetilde{V}$, as Table 6.5 exemplarily shows for three modes. Basically the field patterns only change to a minor degree. However, the dent causes a rotation of the mode polarization for $m > 0$ which can be adequately reproduced by the GST expansion. Figure 6.5(b) demonstrates this for a quadrupole mode of higher order. Within the full modal spectrum only two irregular modes occur at $10.92\,\mathrm{GHz}$ and $11.24\,\mathrm{GHz}$. Thus, their existence is likewise of little relevance.

6.2 Elliptical Single-Cell Resonator based on a Cylindrical Resonator

A question of interest is also whether the eigenmodes of a cylindrical resonator can be utilized to expand the eigenmodes of an arbitrarily shaped resonator. The great advantage of this approach is that the unperturbed modes are analytically known and thus an expensive numerical computation can be omitted. In addition, the number of expansion modes can significantly be increased if desired. The expected major drawback is a relatively high number of irregular GST modes due to the large perturbation extent. Exemplarily, the elliptical Cornell single-cell resonator with PEC boundaries was studied. Table 6.6 shows its geometric parameters. Its modes were computed based on a cylindrical resonator with the radius R_{eq} and the length L_{cell}. The perturbed modes were determined based on subsets of mono-, di-, quadru- and sextupole modes within an unperturbed frequency range of 1.12 up to $53.14\,\mathrm{GHz}$. Appendix C.4.1 lists the parameters of the individual IA sets of 600 modes each. The volume integral matrices $\mathbf{Q}_e$, $\mathbf{S}_e$, $\mathbf{Q}_h$, $\mathbf{S}_h$ were formed based on semi-analytical volume elements i.e. the integration over φ was done analytically and the remaining area integral was performed numerically (see Subsection 4.2.2). By doing so, solely 4627 area elements were required for an adequate discretization of the longitudinal plane. The evaluation of the IA terms of 100 modes took about $110\,\mathrm{s}$ (CPU: Intel Xeon E5-1630 $4 \times 3.70\,\mathrm{GHz}$, RAM: 32 GB). A fully analytical calculation was abstained from due to the only partially analytically integrable Bessel functions.

Table 6.6: Shape parameters of unperturbed elliptical single-cell resonator.

| Parameter	R_{eq}	R_{iris}	L_{cell}	$x_{\text{Ell,eq}}$	$y_{\text{Ell,eq}}$	$x_{\text{Ell,iris}}$	$y_{\text{Ell,iris}}$
Value in mm	102.8797	35.98	115.384	41.35	35.57	12.35	21.14

The initial error of perturbed frequencies very quickly reduces by increasing number of unperturbed modes. About 100 modes are sufficient to obtain accurate results. A few modes have a slight offset towards the correct solution but generally the frequencies are very precise. Figure 6.6 demonstrates this for a selection of regular GST modes. Excluding the irregular complex mode pairs, the frequencies have a MRE of $9.29 \cdot 10^{-4}$ and a maximal relative error of $3.83 \cdot 10^{-3}$. Table 6.7 lists the field error for a selection of regular and irregular modes. The Appendix C.4.3 presents 2D field plots for some of the modes. The majority of the regular fields matches the reference fields well, as exemplarily shown in Fig. 6.7. However, they are less accurate than the GST modes of the elliptical resonator subject to radial and width perturbations (see Section 6.1), as a comparison of Table 6.7 and Table 6.3 illustrates. The major deviations occur close to the deformed boundary. This is mainly a result of the emerging Gibbs phenomenon. In addition, GST cannot reproduce the boundary fields correctly at the transition between the iris faces and the elliptical lateral surface due to the local geometric discontinuity that necessarily is created if a cylindrical resonator is used as unperturbed geometry. Both orientation and amplitude of the GST fields are affected by this since the tangential electric and longitudinal magnetic fields of all unperturbed modes are zero at the discontinuity and can increase only with a finite gradient in its proximity. Thus, in that region the field error reduces more slowly than in the rest of the perturbed volume. The EM fields of most of the modes are relatively low in the corner between the iris and the lateral wall. So, their field accuracy is impaired only in direct vicinity of the discontinuity. Unfortunately, in particular the $TM_{0,1,0}$-like accelerating mode is one of the worst affected modes. The magnitude of its electric field $\mathbf{E}$ is relatively high in the iris corner since the field is maximal at the z-axis and reduces only slowly in radial direction, as Fig. 6.8(a) depicts. But in direct proximity of the discontinuity $\mathbf{E}$ is significantly lower. Thereby, deviations arising from the discontinuity affect the field at a greater distance. Figure 6.8(b) illustrates that the GST-based electric field is distinctly too high (by $40\,\%$) around the discontinuity and incorrectly oriented, mainly in the longitudinal direction. As a consequence, E_z also deviates up to $1.12 \cdot 10^{-1}$ V/m along the z-axis (see Fig. 6.9(a)), which means that the accelerating voltage may only be determined with a moderate accuracy. This is particularly disadvantageous for the applicability of GST, based on cylindrical harmonics, for the cavity optimization. The investigations substantiated that this accuracy deterioration occurs principally for modes with high field values in the iris corner. In total, only a few regular modes are affected by it. As expected, the first irregular GST mode pair occurs already at a relatively low frequency. The respective mode pair at $3.73\,$GHz is depicted in Fig. 6.10. It is obvious that the frequency of one of the two GST modes matches the correct frequency far better than the frequency of the other mode or their mean value. The MRE of their mean frequency is about $8.97 \cdot 10^{-3}$ and by an order of magnitude higher than the error of the regular GST modes. This reflects also in the field pattern, as shown for E_z in Fig. 6.10(b). The accuracy of the irregular modes rises by increasing frequency, as already observed for the previous application examples. Hence, a part of the irregular HOMs coincides relatively well with

(a)   **(b)**
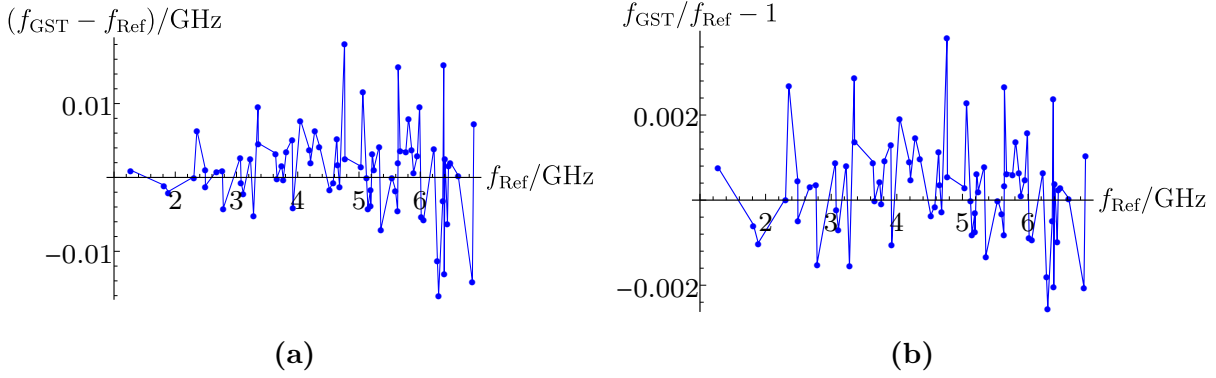
Figure 6.6: Absolute and relative frequency error depending on perturbed frequency f_{Ref} for a selection of 73 regular mono-, di-, quadru- and sextupole modes up to $6.88\,\text{GHz}$ ($N_{\text{modes}} = 360$): Irregular modes are excluded.

Table 6.7: Mean and maximal values of absolute field deviations between GST and reference fields: The reference fields are scaled to a maximal value of $1\,\text{V/m}$ or $1\,\text{A/m}$, respectively. The field deviations are listed along the x- and z-axis as well as inside the complete perturbed domain $\widetilde{V}$. Irregular GST modes are indicated by a star.
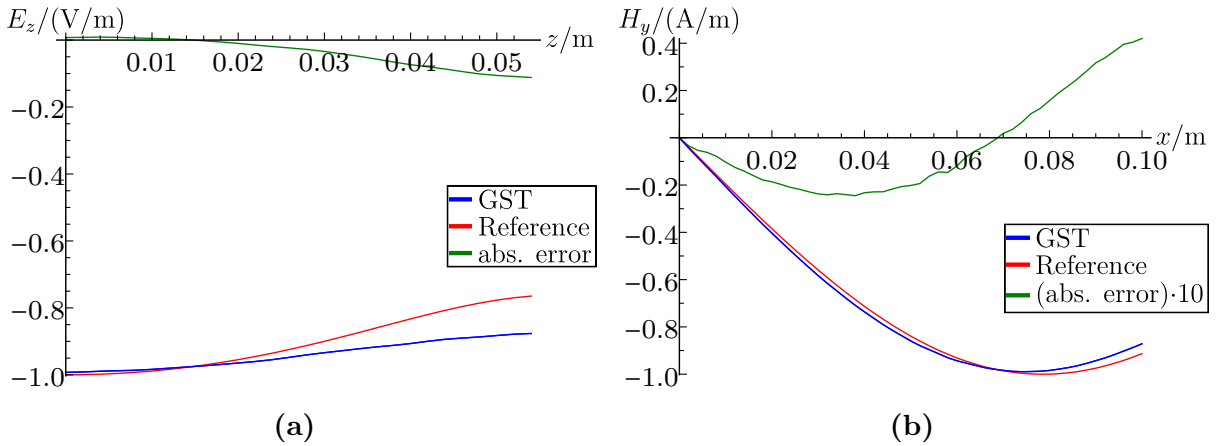
<div align="center">TM₀-like modes</div>

f_{Ref} in GHz	$\|\mathbf{E}_{\text{GST}}(x) - \mathbf{E}_{\text{Ref}}(x)\|$ in V/m		$\|\mathbf{E}_{\text{GST}}(z) - \mathbf{E}_{\text{Ref}}(z)\|$ in V/m		$\|\mathbf{E}_{\text{GST}}(\mathbf{r}) - \mathbf{E}_{\text{Ref}}(\mathbf{r})\|$ in V/m	
	Mean	Max	Mean	Max	Mean	Max
1.27	$2.70 \cdot 10^{-2}$	$4.22 \cdot 10^{-2}$	$4.14 \cdot 10^{-2}$	$1.12 \cdot 10^{-1}$	$3.91 \cdot 10^{-2}$	$4.34 \cdot 10^{-1}$
2.67	$3.64 \cdot 10^{-2}$	$5.23 \cdot 10^{-2}$	$8.55 \cdot 10^{-3}$	$1.47 \cdot 10^{-2}$	$3.51 \cdot 10^{-2}$	$1.32 \cdot 10^{-1}$
$\star$ 3.73	$2.27 \cdot 10^{-2}$	$5.32 \cdot 10^{-2}$	$7.02 \cdot 10^{-2}$	$8.18 \cdot 10^{-2}$	$2.09 \cdot 10^{-3}$	$1.00 \cdot 10^{-1}$
5.19	$1.80 \cdot 10^{-2}$	$4.63 \cdot 10^{-2}$	$7.01 \cdot 10^{-3}$	$1.61 \cdot 10^{-2}$	$1.17 \cdot 10^{-2}$	$2.13 \cdot 10^{-1}$

<div align="center">TE₀-like modes</div>

f_{Ref} in GHz	$\|\mathbf{H}_{\text{GST}}(x) - \mathbf{H}_{\text{Ref}}(x)\|$ in A/m		$\|\mathbf{H}_{\text{GST}}(z) - \mathbf{H}_{\text{Ref}}(z)\|$ in A/m		$\|\mathbf{H}_{\text{GST}}(\mathbf{r}) - \mathbf{H}_{\text{Ref}}(\mathbf{r})\|$ in A/m	
	Mean	Max	Mean	Max	Mean	Max
2.49	$7.80 \cdot 10^{-3}$	$2.89 \cdot 10^{-2}$	$7.22 \cdot 10^{-3}$	$1.23 \cdot 10^{-2}$	$1.66 \cdot 10^{-2}$	$2.10 \cdot 10^{-1}$
3.76	$6.63 \cdot 10^{-3}$	$1.34 \cdot 10^{-2}$	$3.71 \cdot 10^{-3}$	$7.12 \cdot 10^{-3}$	$1.41 \cdot 10^{-2}$	$3.68 \cdot 10^{-1}$
$\star$ 5.03	$1.65 \cdot 10^{-1}$	$6.03 \cdot 10^{-1}$	$9.65 \cdot 10^{-2}$	$2.39 \cdot 10^{-1}$	$3.87 \cdot 10^{-2}$	$2.24 \cdot 10^{-1}$
6.06	$1.07 \cdot 10^{-2}$	$1.60 \cdot 10^{-2}$	$7.22 \cdot 10^{-3}$	$1.24 \cdot 10^{-2}$	$9.81 \cdot 10^{-3}$	$1.91 \cdot 10^{-1}$

<div align="center">Dipole modes</div>

f_{Ref} in GHz	$\|\mathbf{E}_{\text{GST}}(x) - \mathbf{E}_{\text{Ref}}(x)\|$ in V/m		$\|\mathbf{E}_{\text{GST}}(z) - \mathbf{E}_{\text{Ref}}(z)\|$ in V/m		$\|\mathbf{E}_{\text{GST}}(\mathbf{r}) - \mathbf{E}_{\text{Ref}}(\mathbf{r})\|$ in V/m	
	Mean	Max	Mean	Max	Mean	Max
1.81	$2.01 \cdot 10^{-2}$	$7.35 \cdot 10^{-2}$	$6.32 \cdot 10^{-3}$	$1.26 \cdot 10^{-2}$	$2.07 \cdot 10^{-2}$	$1.98 \cdot 10^{-1}$
6.49	$2.80 \cdot 10^{-2}$	$1.08 \cdot 10^{-1}$	$2.30 \cdot 10^{-2}$	$5.64 \cdot 10^{-2}$	$1.70 \cdot 10^{-2}$	$1.60 \cdot 10^{-1}$
$\star$ 6.58	$6.38 \cdot 10^{-2}$	$1.63 \cdot 10^{-1}$	$6.20 \cdot 10^{-2}$	$1.21 \cdot 10^{-1}$	$6.05 \cdot 10^{-2}$	$2.53 \cdot 10^{-1}$
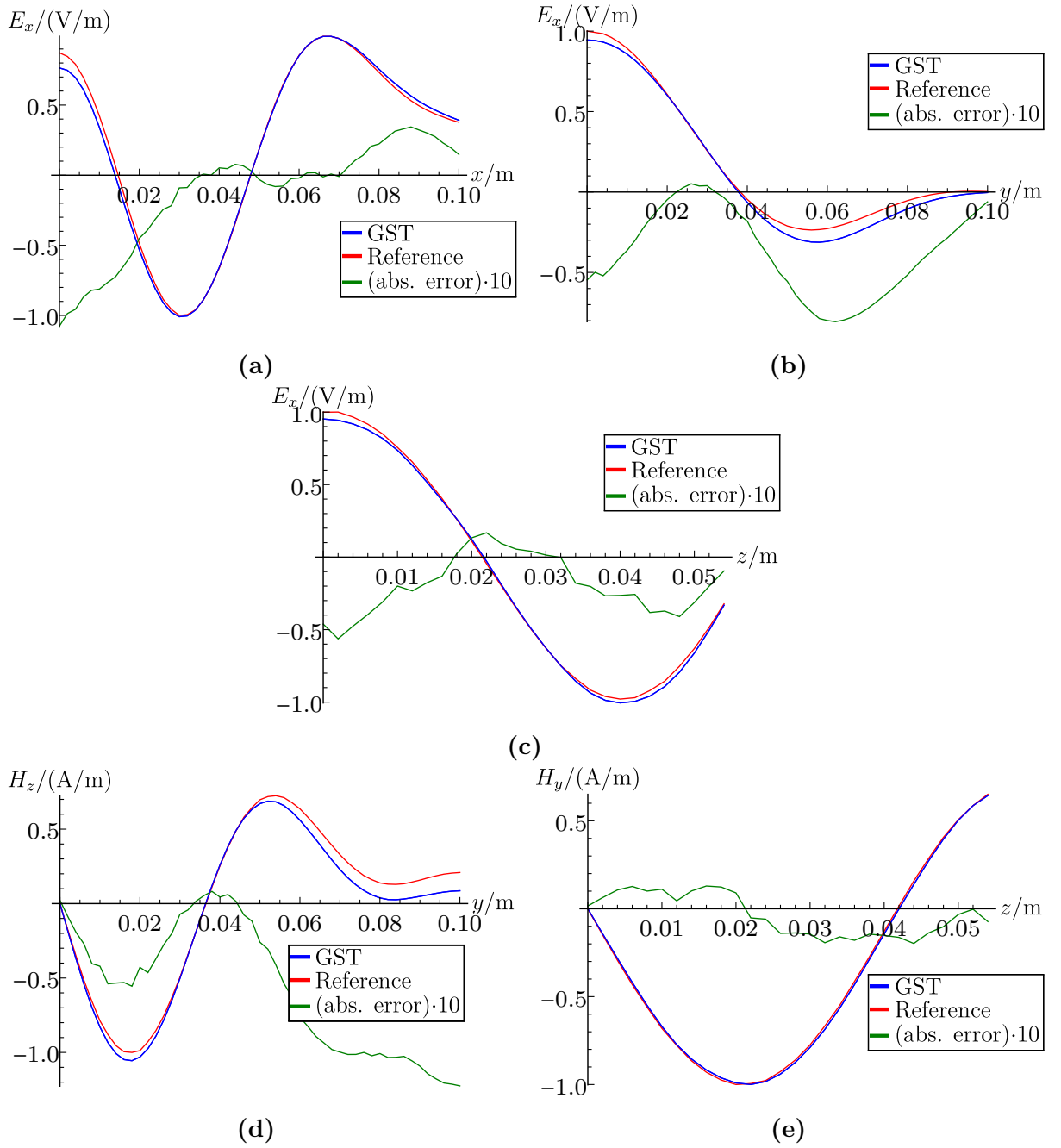
Figure 6.7: Perturbed EM field of a dipole mode at $6.49\,\text{GHz}$ along the coordinate axes ($N_{\text{modes}} = 375$): Only a selection of field components is displayed.

(a)   **(b)**   **(c)**
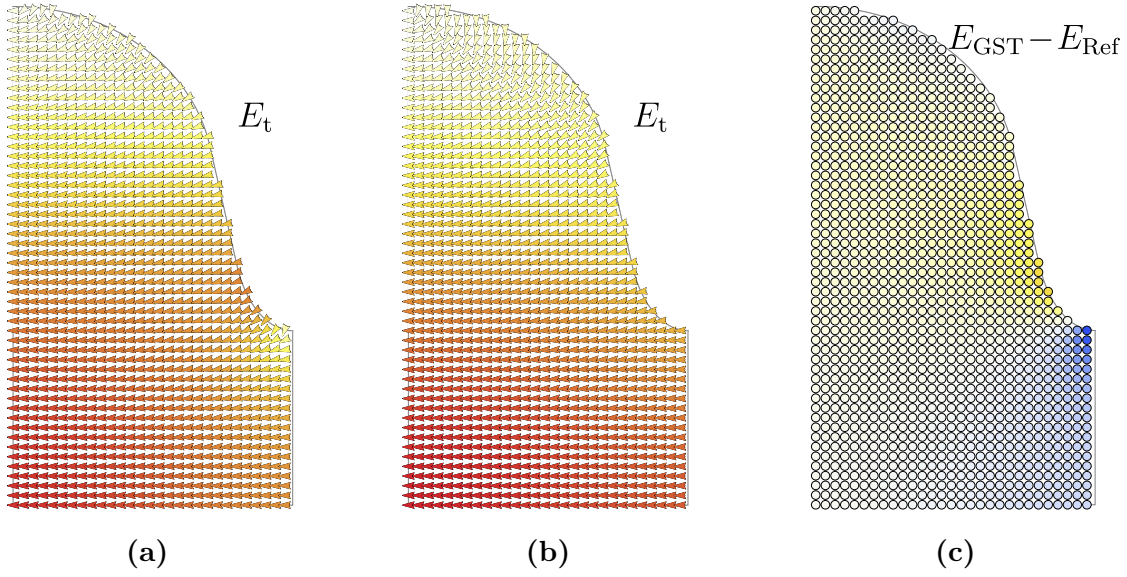
Figure 6.8: Electric field of $TM_{0,1,0}$-like accelerating mode at $1.27\,GHz$ in the x,z-plane: (a) Tangential reference field. (b) Tangential GST field. (c) Absolute error $E_{GST} - E_{Ref}$.


(a)   **(b)**

Figure 6.9: Perturbed EM field of $TM_{0,1,0}$-like mode at $1.27\,GHz$ ($N_{modes} = 430$): (a) Longitudinal electric field along the z-axis. (b) Azimuthal magnetic field along the x-axis.

the respective reference modes, as depicted for a dipole mode in Fig. 6.11. However, still a noticeable amount of HOMs possesses an inadequate accuracy. Up to a frequency of $10.0\,GHz$, in total 51 irregular mode pairs were detected within 308 GST modes (257 actual modes). So, about one fifth of the GST modes is affected.

Concluding, GST is rather unsuited for the eigenmode computation of arbitrarily shape single-cell resonators if a cylindrical resonator is used as unperturbed geometry. Although the frequencies are determined accurately, the precision of EM field of the accelerating mode is insufficient and a too high number of irregular modes arises. For further investigations, it would be of interest if the eigenmodes of a multicell resonator are expandable in terms of cylindrical harmonics. At this, the impairment by discontinuities may potentially be avoided by short additional beam pipes. Thereby, the discontinuities only occur at the beam pipe ends, shifting them away from of the region of interest.
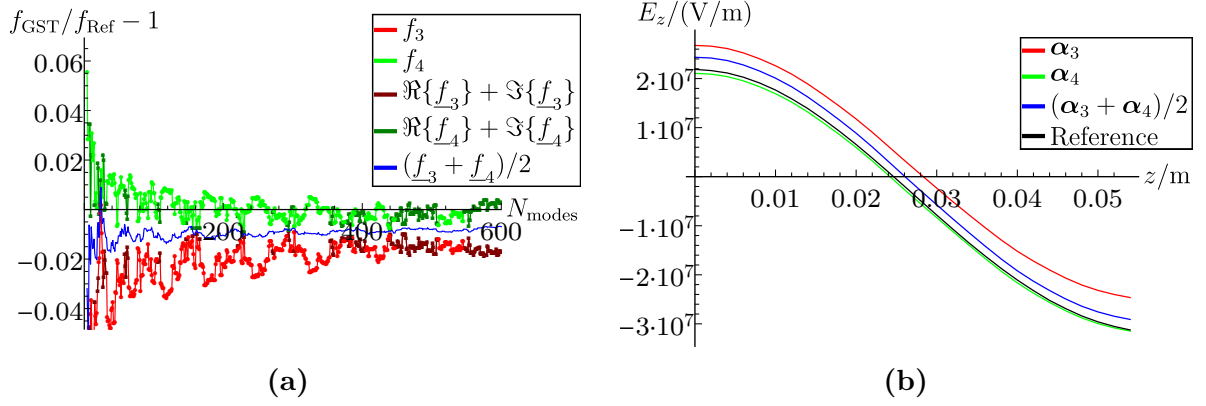
Figure 6.10: Real- and complex-valued GST mode pair for a TM_0-like mode at $3.73\,GHz$. (a): Relative frequency error depending on the number N_{modes} of modes. (b): Perturbed electric field E_z along the z-axis based on a real-valued GST mode pair ($N_{modes} = 430$).
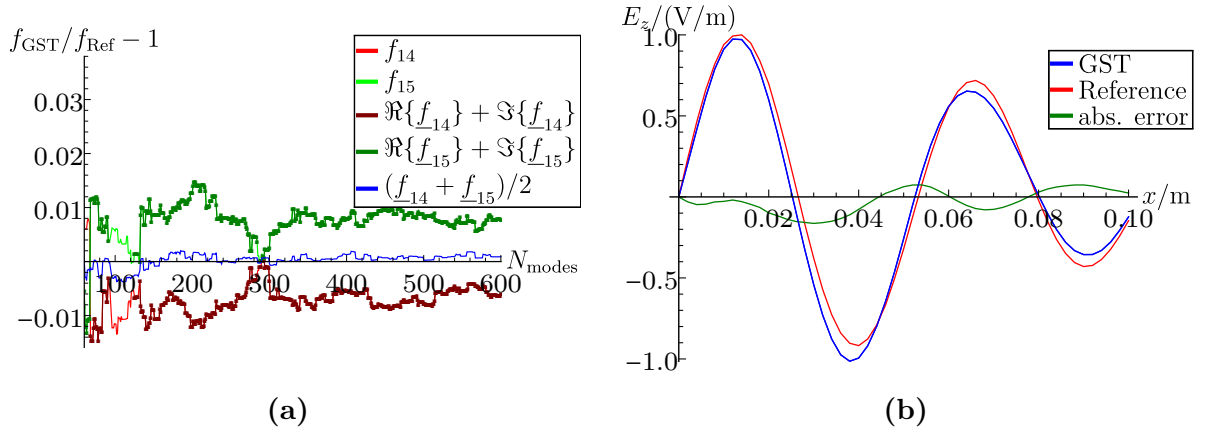
Figure 6.11: Real- and complex-valued GST mode pair for a dipole mode at $6.58\,GHz$. (a): Relative frequency error depending on the number N_{modes} of modes. (b): Perturbed E_z field along the x-axis based on signed absolute value of complex mode pair ($N_{modes} = 430$).

## 6.3 Multicell Resonator with Rotationally Symmetric Perturbations

Designing a multicell cavity implies the manipulation of various geometric parameters entailing a vast number of optimization steps. At this, computing the EM characteristics of only a single design already can be highly computationally demanding. If further the effects of inevitable shape imperfections are to be investigated, the resulting total effort is tremendous. For such extensive parameter studies, perturbative methods can provide an enormous efficiency improvement. Therefore, it is of major importance to examine the applicability of GST to a realistic multicell performance optimization with simultaneous consideration of shape deformations. Exemplarily, the main linac cavity of the Berlin Energy Recovery Linac Project (bERLinPro) [97] was studied. A part of the presented results were published in [83], [84] [iii].

[iii]The here presented R-over-Q values marginally differ from the values in [84] since in [84] the unperturbed mode energies were used instead of the perturbed ones.

6.3.1 Preliminary Considerations

The bERLinPro main linac cavity is a 1.3 GHz elliptical seven-cell cavity that bases on a modified Cornell ERL design [4]. In the following, eight different preliminary candidates for the final cavity design (state: middle of 2014) are compared and the effects of shape imperfections are investigated for each of them. The design candidates, referred to as C1 to C8, differ in length and equator ellipse parameters of their end-cells (see Table C.2 in Appendix C.3). The inevitable shape deformations are emulated by distinct equator and iris radii variations of the individual cells.

Since GST can exclusively be applied to deform the initial geometry inwardly, the unperturbed shape is defined in such a way that its end-cells comprise the shapes of all eight candidates C1 to C8, i.e. every candidate constitutes a perturbed resonator. In addition, the equator and iris radii of the unperturbed geometry are set 0.5 mm larger than the ones of the actual designs to allow for radial variations of ± 0.5 mm, as Fig. 6.12 illustrates. The shape is specified fully symmetric so that all three Cartesian symmetry planes can be used to speed up the CST MWS computations. In total 1405 unperturbed modes within a frequency range of 1.24 up to 7.43 GHz were computed. Since only modes with the same azimuthal type m interact, the modes are split into corresponding IA subsets before applying GST. Depending on the index m, one subset comprises just 40 up to 245 modes. The subsets can be processed separately and thereby in total faster (see Subsection 4.4.2). Furthermore, for the computation of the IA terms, the volume of the structure is partitioned into twelve half-cells (h) and two end-cell groups (eg), as shown in Fig. 6.13. This segmentation of ΔV into 14 sub-volumes (ΔV_{eg_-}, ΔV_{h6_-}, etc.) allows to process the IA terms of each segment separately, as described in Subsection 4.4.1. Thereby, each segment can be varied independently of the others. To investigate radial variations of 0.5, 0 and -0.5 mm for all candidates, only eight different subsets of IA terms for each half-cell and 24 subsets for each end-cell group have to be computed. In addition, only the IA terms of the six half-cells in the positive coordinate range ($\mathrm{h1}_+$ to $\mathrm{h6}_+$) are determined from CST MWS field data. The IA terms of the half-cells in the negative
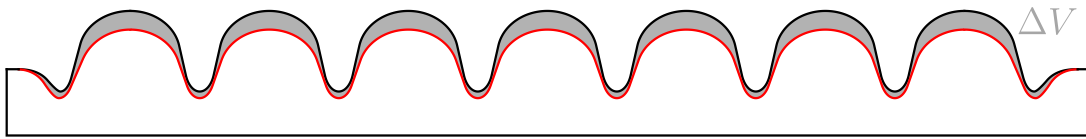
Figure 6.12: Rotationally symmetric unperturbed (black) and perturbed shape (red) of the bERLinPro main linac resonator: The deformed volume ΔV is highlighted in gray.
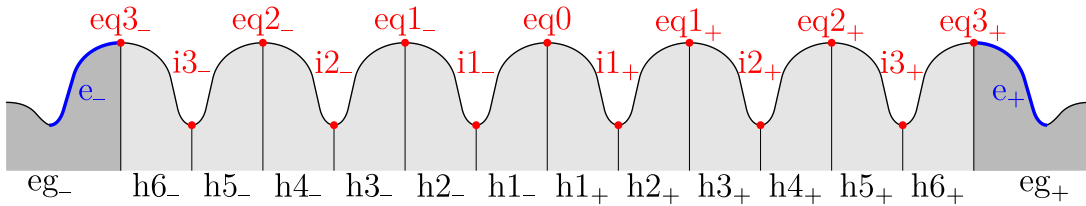
Figure 6.13: Segmentation of the unperturbed shape for the bERLinPro resonator into twelve half-cells (h) and two end-cell groups (eg) that allows for an individual variation of the equator radii (eq), iris radii (i) and end-cell shapes (e).

Table 6.8: Subsets of IA terms resulting from the segmentation of the deformed volume ΔV: For the total number of subsets, additionally, the number based on discrete volume integrals (d.) and based on mirroring (m.) is stated.

Segment type	Number of segments	Number of IA term subsets	
		Per segment	Total (d., m.)
Half-cell (h)	12 (h6_ to h6_+)	8 (equator and iris variation)	96 (48,48)
End-cell group (eg)	2 (eg_ & eg_+)	24 (eq. variation for C1–C8)	48 (48,0)

range (h1_ to h6_) are directly deduced from the ones in the positive range by mirroring, based on the applied symmetry settings. Eventually, only 96 subsets of IA terms have to be computed from discrete volume integrals, as Table 6.8 demonstrates. Combining the individual IA subsets of the 14 segments to the IA set of a full structure finally yields the eigenmodes of about $1.27 \cdot 10^7$ different designs, a remarkably large number. As to be expected from the single-cell investigations, the major computational effort in executing GST for the bERLinPro cavity was caused by the computation of the unperturbed modes. The simulation of 100 modes with CST MWS (Intel E5-2687W 3.4 GHz, 256 GB RAM) took, depending on the frequency range, between 4.5 and 5 hours (model with $4 \cdot 10^5$ up to $5 \cdot 10^5$ mesh cells). The computation of the IA terms of a set of 100 modes inside the sub-volume of a single half-cell segment took about 230 s. The final determination of the perturbed frequencies and expansion coefficients was done within some seconds.

6.3.2 Result Accuracy

6.3.2.1 Original GST

The GST frequencies do not reach a converging state based on the available set of unperturbed modes because of the very small geometric modifications. As Fig. 6.14(a) illustrates, the frequency error basically is relatively small but reduces too slowly to reach the correct frequencies. Disadvantageously, a major part of EM fields thus noticeably deviates from the correct reference fields (irregular modes were not detected). Even the accelerating mode displays severe deviations for the maximal amplitudes in the single cells, as shown in Fig. 6.14(b). This is of particular consequence for the applicability of GST since it generally forbids any kind of optimization. A slow error reduction was already observed in the context of the single-cell resonator (see Fig. 6.3(b)). However, there it had only a minor impact since the fields in a single-cell resonator generally only slightly vary if a small perturbation is applied. Hence, accurate GST results can be obtained for single-cell resonators even if the expansion error does not reach an oscillating state. In contrast, the fields of a multicell resonator, especially their amplitudes in each cell, may tremendously change depending on the cell-to-cell coupling. Due to this extreme sensitivity to geometric variations, GST imperatively requires a sufficiently high number of expansion modes for multicell resonators. This is furthermore compounded by the fact that for a N_{cell}-cell resonator, about N_{cell} times as many modes as for a similar single-cell resonator are necessary to obtain the same minimal unperturbed wavelength λ_{min}.
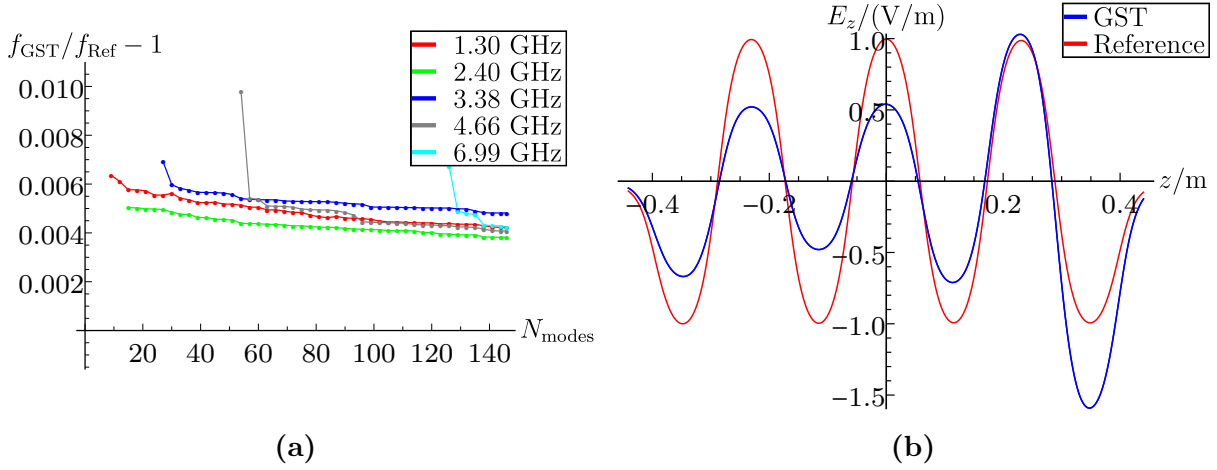
Figure 6.14: Original GST results for candidate C1: (a) Relative frequency error depending on the number N_{modes} of unperturbed modes for TM_0-like modes. (b) Longitudinal electric field of $\mathrm{TM}_{0,1,0_\pi}$-like accelerating mode with a frequency of $1.30\,\mathrm{GHz}$ along z-axis.

6.3.2.2   GST with Adjusted Interaction Terms

As already explained, the perturbation extent $\Delta\xi$ determines the minimal unperturbed wavelength λ_{min} that is at least required to reach a converging state. Figure 6.15(a) depicts the dependence of the necessary frequency from the ratio of the deformed volume ΔV to the unperturbed volume V. Evidently, there is an approximately proportional relation between the volume ratio $\Delta V/V$ and the required frequency range [iv]. Even different
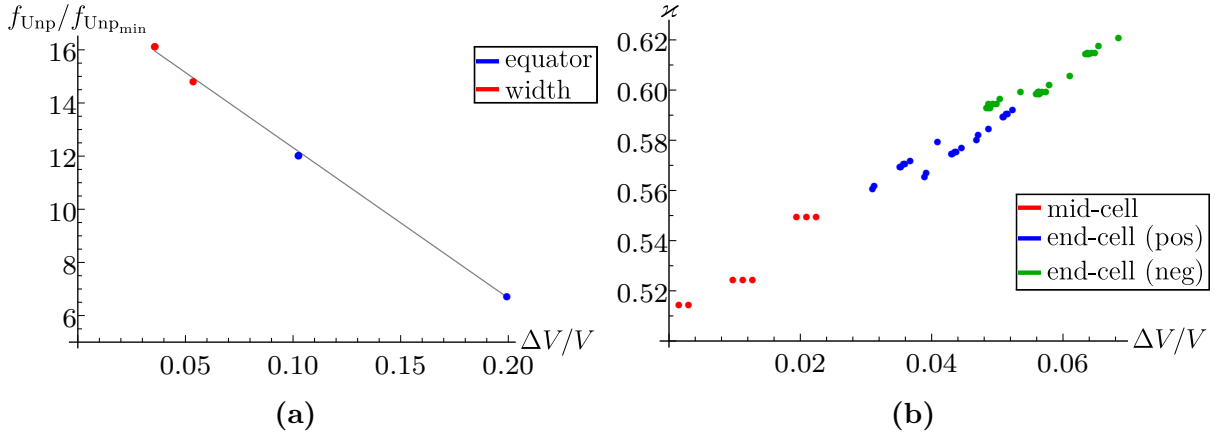
Figure 6.15: Relevance of the perturbation extent for convergence of GST: (a) Required unperturbed frequency (relative to frequency of lowest unperturbed mode) for reaching a converging state depending on the ratio of ΔV to V [v]. The diagram presents the data of a $\mathrm{TM}_{0,1,0}$-like mode in a single-cell and a three-cell elliptical resonator subject to different equator and cell width perturbations. (b) Applied adjustment constants $\varkappa_\nu$ for the bERLinPro resonator depending on the ratio of ΔV_ν to V_ν.

[iv]Strictly speaking, the required wavelength λ_{min} is related to the minimal dimension $\Delta\xi$ of the deformed volume ΔV (see (3.83)). But since an equator or width reduction is topologically rather a 1D perturbation, ΔV approximately scales proportionally with $\Delta\xi$.

[iv]The converging state is defined by the 1st local extrema of the GST frequencies depending on N_{modes}.

types of perturbations display a similar behavior. Deduced from this linear relation, it follows that the computed maximal unperturbed frequency of the regarded seven-cell resonator is almost by a factor of three too small. But computing the missing modes would be excessively expensive, if at all realizable. For this reason, a modification of GST was developed to overcome the necessity of very large unperturbed mode set in case of multicell resonators subject to small perturbations.

All application examples in this thesis indicate that the GST frequencies start to approach the correct solution from a higher frequency. This arises from two facts: Firstly, the perturbed frequencies are always higher than the unperturbed ones. And secondly, the majority of the interaction terms s_{kj} and q_{kj} reduces the wider the frequency spread between the two involved modes k and j becomes. So, the initial shift between the GST and unperturbed frequencies has to be larger than the correct (final) shift. Hence, the GST frequencies are invariably too high if the converging state is not reached (see Fig. 6.14(a)). This fact can be utilized to increase the GST convergence speed. Regarding the coupling matrices $\mathbf{A}$ and $\mathbf{B}$ (see Section 3.3) with

$$a_{kj} = \omega_k^2 \delta_{kj} + \omega_j \frac{s_{kj}}{U_k} - \omega_k \frac{q_{kj}}{U_k} - \sum_{l=1}^{\infty} \frac{s_{kl} q_{lj}}{U_k U_l}, \tag{6.1}$$

$$b_{kj} = \omega_k^2 \delta_{kj} - \omega_j \frac{q_{kj}}{U_k} + \omega_k \frac{s_{kj}}{U_k} - \sum_{l=1}^{\infty} \frac{q_{kl} s_{lj}}{U_k U_l}, \tag{6.2}$$

concerning perturbations of different extent $\Delta \xi$, it is evident that the alternation of their eigenvalues and eigenvectors, and thus also the convergence behavior of the GST modes, is determined by the IA terms q_{kj} and s_{kj}. The unperturbed frequencies are fixed and not affected by $\Delta \xi$. Consequently, the initial offset between the GST and reference frequencies can be reduced by diminishing the weight of the IA terms in the coupling matrices $\mathbf{A}$ and $\mathbf{B}$. For this purpose, all original matrix entries, except for the squared unperturbed frequencies in the diagonal entries, are multiplied by a *GST adjustment constant* $\varkappa$

$$a_{kj} = \omega_k^2 \delta_{kj} + \varkappa \left(\omega_j \frac{s_{kj}}{U_k} - \omega_k \frac{q_{kj}}{U_k} - \sum_{l=1}^{\infty} \frac{s_{kl} q_{lj}}{U_k U_l} \right), \tag{6.3}$$

$$b_{kj} = \omega_k^2 \delta_{kj} + \varkappa \left(-\omega_j \frac{q_{kj}}{U_k} + \omega_k \frac{s_{kj}}{U_k} - \sum_{l=1}^{\infty} \frac{q_{kl} s_{lj}}{U_k U_l} \right), \tag{6.4}$$

that lies between zero and one. Thereby, the GST frequency error faster reaches a value of zero. Figure 6.16(a) depicts that already a rough adjustment of the IA terms provides an appreciably improved accuracy. However, to obtain optimal results, the adjustment constant must deliberately be chosen. For a given unperturbed resonator geometry, the optimal $\varkappa$ value primarily depends on two parameters, the available unperturbed frequency range and the perturbation extent. For rotationally symmetric perturbations, the perturbation type again is only of small relevance. As initially explained, the ratio $\Delta V/V$ defines the necessary unperturbed frequency range. Taking additionally the ratio of the available maximal to the required frequency into account, a likewise linear relation between the adjustment factor $\varkappa$ and the volume ratio $\Delta V/V$ can be found, as Fig. 6.15(b) demonstrates. At this, the segmentation of the deformed volume ΔV into half-cells and
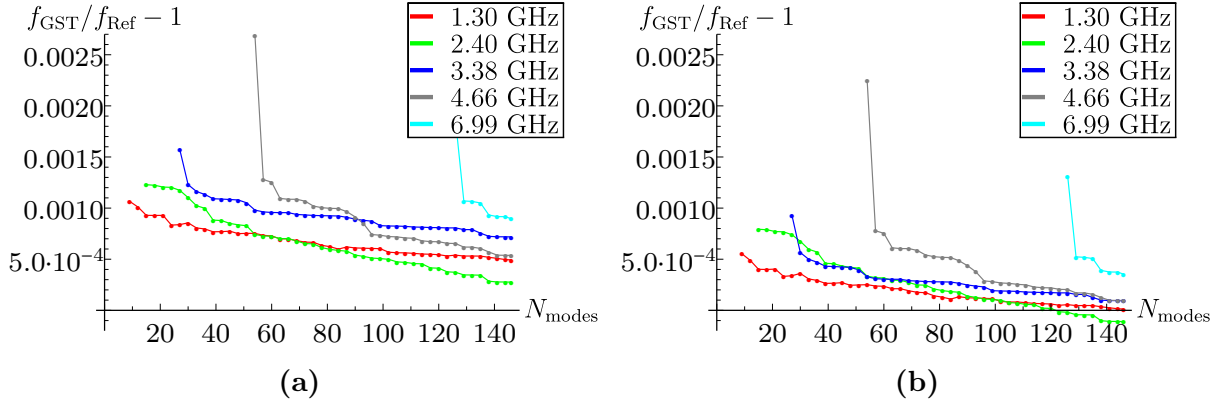
Figure 6.16: Relative frequency error depending on the number N_{modes} of unperturbed modes for TM_0-like modes of candidate C1 based on modified GST: (a) Uniform adjustment constant $\varkappa = 0.6$. (b) Segment-wise adjusted factors $\varkappa_\nu$ as specified in Fig. 6.15(b).

end-cell groups becomes of vital importance since it allows to assign an individual $\varkappa_\nu$ for each segment ν based on its volume ratio $\Delta V_\nu / V_\nu$. Applying these segment-wise GST adjustment constants $\varkappa_\nu$, all GST frequencies intersect the correct frequencies when all available expansion modes are used or for a slightly smaller or higher number of modes. Figure 6.16(b) illustrates the resulting convergence behavior. In general, small inaccuracies of the $\varkappa_\nu$ have only a marginal influence on the accuracy of the GST results. Due to generally slow convergence, the GST modes only slightly change if the number N_{modes} of used expansion modes is varied. The insensitivity is facilitated by the fact that the $\varkappa_\nu$ scale down the IA terms and thereby further reduce the speed of convergence. Consequently, the adjustment of the IA terms is relatively robust, so slight differences in the behavior of individual modes are compensated. Besides the adaption of the accuracy, the GST adjustment also modifies the EM field values at perturbed boundaries. As explained in Subsection 5.1.1, the boundary fields are subject to a form of Gibbs phenomenon that reduces the fields to half of their actual value. By the adjustment, the boundary values are again increased to $1/(2\varkappa_\nu)$ of their true value. This side effect beneficially reduces the unintended premature reduction of the GST fields in proximity of perturbed boundaries, especially when the respective adjustment constant $\varkappa_\nu$ is close to 0.5. In order to determine the relation between the optimal segment-wise $\varkappa_\nu$ and the respective volume ratio $\Delta V_\nu / V_\nu$, shown in Fig. 6.15(b), three reference computations of perturbed geometries had to be performed. The reference computations were necessary to provide correct benchmark frequencies. The first two perturbed resonators differed from the unperturbed resonator solely in the shape of their inner cells in order to identify the $\varkappa_\nu$ of the half-cells. For the first resonator, the radii eq0, i1$_-$ and i1$_+$ of the mid-cell were reduced by 1 mm. For the second one, the radii eq2$_-$ to eq2$_+$ and i3$_-$ to i3$_+$ of all five inner cells were diminished by 0.5 mm. Subsequently, the two $\varkappa_\nu$ constants of the end-cells were determined for the C1 geometry, using the previously ascertained $\varkappa_\nu$ of the half-cells. The rest of the adjustment constants were directly derived from these four known $\varkappa_\nu$ values. The reference computations obviously increase the computational effort of GST. However, a couple of LOMs are absolutely sufficient as benchmark. So, the required additional expense is relatively small. For future GST applications to similar basic cell types, like the elliptical cells discussed here, it would furthermore be conceivable to determine the adjustment constants directly

from the volume ratio $\Delta V_\nu / V_\nu$, the available maximal unperturbed frequency and if necessary from the type of the modified geometric parameters. This feasible approach would obviate the need for benchmark computations.

The accuracy of the modified GST was validated exemplarily for a selection of 65 reference modes for candidate C1 up to a frequency of $7.04\,\mathrm{GHz}$ (see Appendix C.3.3). The full spectrum was not simulated due to the computational expense. The relative frequency error is $6.91 \cdot 10^{-4}$ at maximum and $1.30 \cdot 10^{-4}$ on average. The axial GST field of the accelerating mode closely matches the reference field, as demonstrated in Fig. 6.17(a). On average, the field only deviates $5.11 \cdot 10^{-3}$ V/m. Solely in the region of the end-cells the error increases up to $2.53 \cdot 10^{-2}$ V/m. The HOMs coincide likewise well and have merely higher deviations. Figure 6.17(b) illustrates this for a HOM of C1 whose frequency is relatively close to the maximal unperturbed frequency. Appendix C.3.3 presents further EM field examples of the adjusted GST for different candidates and mode types. Table 6.9 shows that the GST field flatnesses η_{ff} of all eight candidates match the ones of the reference modes also very well. Solely for candidate C5 η_{ff} differs more than $1\,\%$. Consequently, the adjusted GST is suited for the design optimization and error estimation of multicell resonators, since it precisely reproduces the highly sensitive EM fields. Concluding, it must be pointed out that for an infinite number of modes, GST does not converge towards correct perturbed frequencies if the IA terms are modified. Hence, the adjustment may only be applied under the condition that the available unperturbed frequency range is distinctly too small. Further, a certain adjustment constant is only optimal for a specific number of unperturbed modes and a specific perturbation extent.

(a)   **(b)**
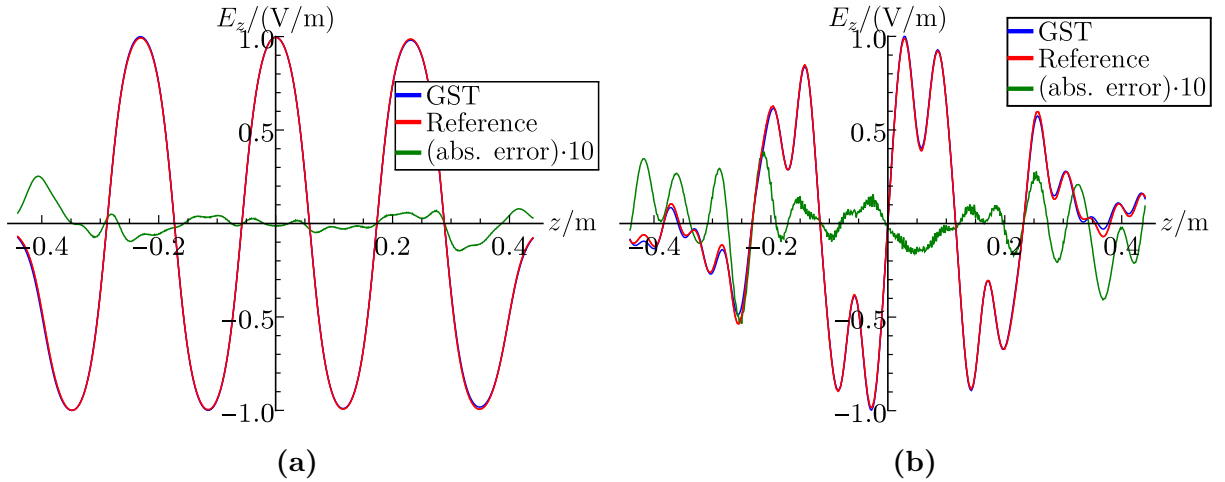
Figure 6.17: Longitudinal electric field of candidate C1 modes along z-axis based on segment-wise adjusted GST: (a) $\mathrm{TM}_{0,1,0_\pi}$-like accelerating mode with a frequency of $1.30\,\mathrm{GHz}$. (b) TM_0-like HOM with a frequency of $6.99\,\mathrm{GHz}$ (Mean and maximal absolute deviation: $1.27 \cdot 10^{-2}$ V/m and $5.36 \cdot 10^{-2}$ V/m)

Table 6.9: Field flatness η_{ff} of the design candidates C1 to C8.

| Candidate		1	2	3	4	5	6	7	8
η_{ff} in %	GST	98.07	97.32	97.21	98.17	97.69	98.37	96.59	98.27
	Reference	98.67	97.94	98.03	97.62	99.03	98.70	96.85	98.25

### 6.3.3   Study of Design Candidates and Geometric Imperfections

A major objective in cavity optimization is the maximization and flattening of the accelerating field for a given input power. However, for a reliable cavity operation, it is essential to also investigate the characteristics of its HOMs in order to identify potentially adverse modes and, if necessary, adapt the design. Starting with a comparison of the intended ideal designs of the candidates C1 to C8, Fig. 6.18 illustrates that already within the first ten passbands up to 2.79 GHz, frequency differences are observable. With the exception of the fundamental TM_0-like and the first TM_1-like band, all candidates and especially C6 (C5) and C7 show noticeable deviations up to 10 MHz. Although the frequencies do not provide an actual figure of merit, they may serve as a simple indicator of basic differences between the individual designs. The particularity of C6 and C7 can also clearly be seen from the longitudinal on-axis R-over-Q values. The accelerating mode only marginally varies for the different candidates and has an average R-over-Q of 781.11 Ω. Figure 6.19 shows that within a frequency range up to 7.04 GHz in total 15 HOMs with a $R_{\mathrm{sh}_i}/Q_{0_i}$ larger than 10 Ω exist. These modes may potentially interfere with the particle beam. For some of them, the designs C1 to C8 display considerable variances. The affected modes are depicted in detail in Fig. 6.20, where additionally the influence of geometric imperfections is considered. At first, only the ideal designs, denoted by variation 5, are compared. The potentially most harmful mode lies in the second TM_0 band at a frequency of about 2.43 GHz and has an average $R_{\mathrm{sh}_i}/Q_{0_i}$ of 126.37 Ω (see Fig. 6.20(b)). At this, C7 features the highest and C6 the lowest value with a difference of 4.6 %. For the mode with the second highest R-over-Q at 2.44 GHz in the same passband, in contrast, C7 plainly has the lowest $R_{\mathrm{sh}_i}/Q_{0_i}$ of 102.62 Ω while C5 and C6 have a 10.3 % higher value. For the third mode with a frequency of 2.42 GHz, again, C7 clearly states the largest $R_{\mathrm{sh}_i}/Q_{0_i}$ of 38.83 Ω (see Fig. 6.20(c)). So, candidate C6 and C7 constitute the designs with the most distinct characteristics, but demonstrate a contrary behavior concerning the most favorable design. These inherently contrary characteristics are even more apparent for the two modes between 3.82 and 3.86 GHz, shown in Fig. 6.20(d). While for C7 both modes have a similarly high R-over-Q of about 31.12 Ω and 19.18 Ω, C6 (and likewise C5) provides a significantly lower $R_{\mathrm{sh}_i}/Q_{0_i}$ of only 5.72 Ω for the first mode but at the same time a noticeably higher value of 40.44 Ω for the second mode. Since it is difficult to decide on a clearly preferable candidate solely based on the R-over-Q values, an investigation of additional characteristics, especially the external quality factors, may facilitate the decision.

Taking further the effects of geometric imperfections into consideration, the choice is even more complicated due to the enormous variety of probable deformations. Since not all $1.27 \cdot 10^7$ computed designs can be discussed here, exemplarily the effects arising from uniform variations of the equator and iris radii are presented at first. In this context, uniform means that the parameters of every half-cell are modified by the same extent. Table 6.10 lists the applied radii modifications. An iris radii increase reduces the maximal field amplitudes of the accelerating mode in the outer cells (see Fig. 6.22(a)) and thereby lowers its R-over-Q, as Fig. 6.20(a) depicts. A reduction of the equator radii has a similar but lower effect. In total, $R_{\mathrm{sh}_{\mathrm{acc}}}/Q_{0_{\mathrm{acc}}}$ may reduce up to 3.4 %. So, the accelerating mode is relatively robust against uniform geometric modifications. An iris decrease and equator enlargement may lead to an enhancement of $R_{\mathrm{sh}_i}/Q_{0_i}$, but only at the cost of a non-flat field, which should be avoided for maintaining a balanced acceleration of all particles.
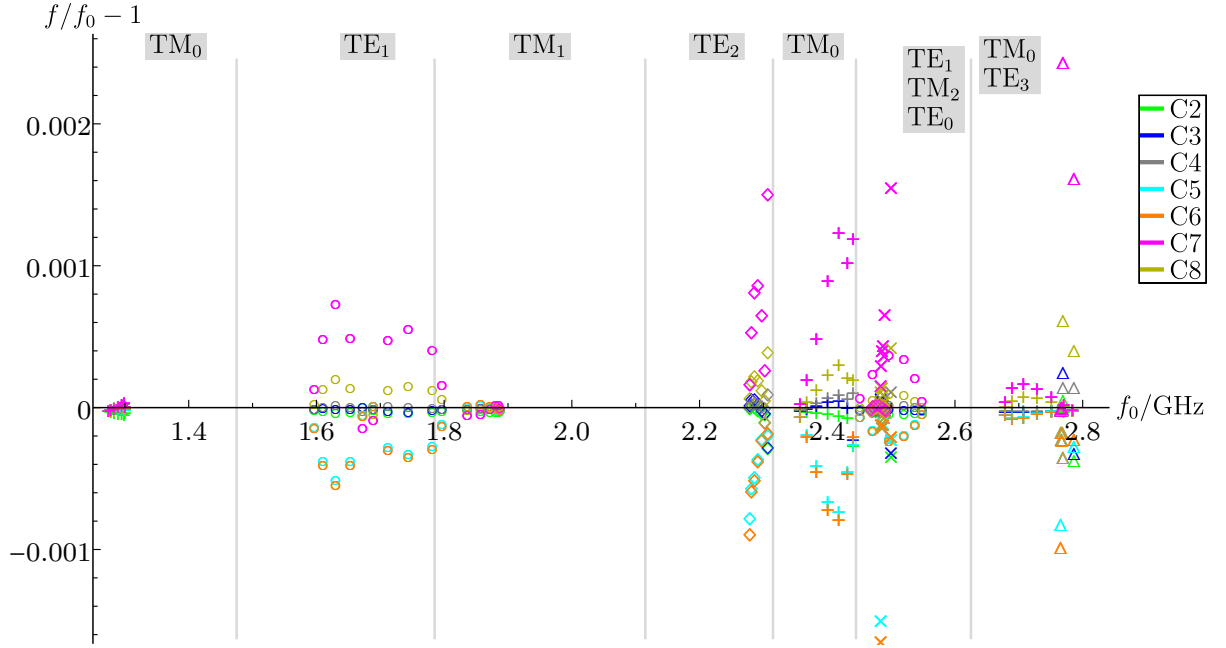
Figure 6.18: Relative frequency shift of the first ten passbands for the candidates C2 to C8 relatively to the frequencies f_0 of C1. Candidate C1 was chosen as comparative design since its frequencies f_0 are close to the average frequencies of all candidates. The different markers indicate the azimuthal mode type: TM_0-like ($+$), TE_0-like ($\times$), dipole ($\circ$), quadrupole ($\diamond$), sextupole ($\triangle$).
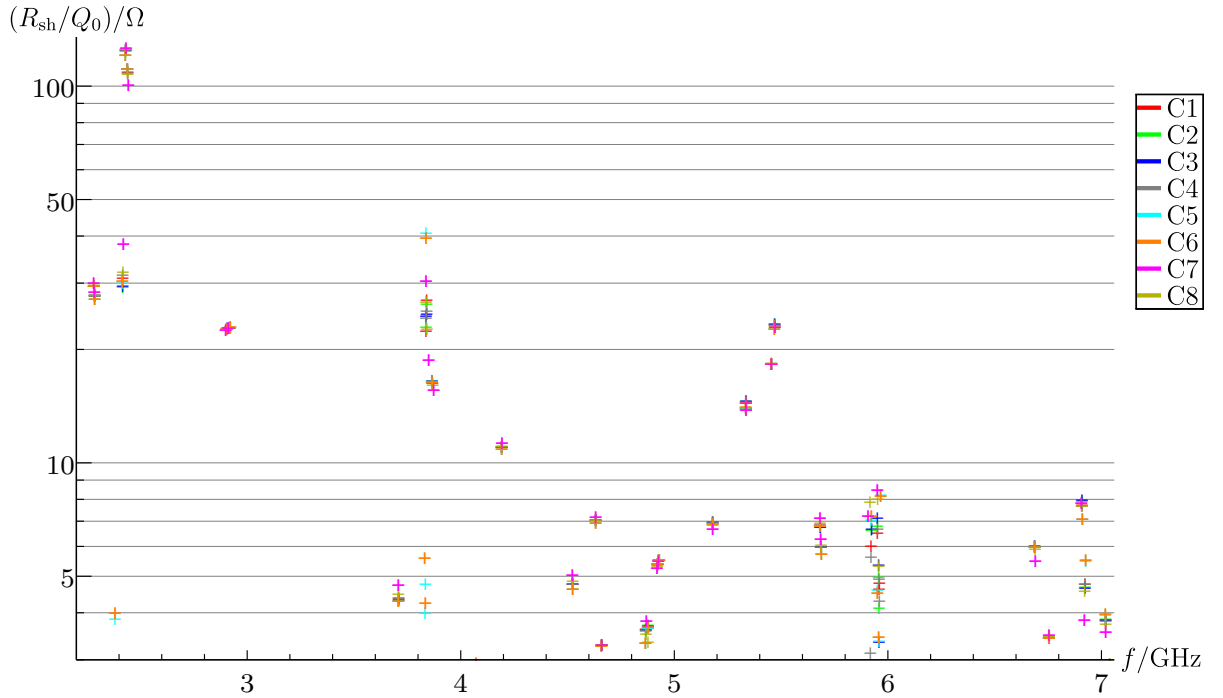
Figure 6.19: On-axis R-over-Q values of TM_0-like HOMs up to a frequency of $7.04\,\mathrm{GHz}$ for all design candidates. The $TM_{0,1,0}$-like band is not included and only modes with an R-over-Q value of at least $3\,\Omega$ are plotted.

The HOM with the highest $R_{\mathrm{sh}_i}/Q_{0_i}$ is relatively insensitive to geometric variations. Its $R_{\mathrm{sh}_i}/Q_{0_i}$ varies at most between $-6.4\,\%$ and $5.0\,\%$. The $R_{\mathrm{sh}_i}/Q_{0_i}$ of the neighboring HOM at $2.44\,\mathrm{GHz}$, however, may rise by $15.6\,\%$ by a simultaneous equator reduction and iris increase, or in turn decrease by $17.6\,\%$ by an opposite variation (see Fig. 6.20(b)). Thereby, it may have an R-over-Q yet higher than the first mode. The third mode with a frequency of $2.42\,\mathrm{GHz}$ has an even higher sensitivity to geometric imperfections and its $R_{\mathrm{sh}_i}/Q_{0_i}$ may rise by up to $30.0\,\%$, as Fig. 6.20(c). At this, the contrary behavior of both modes depending on the applied variations, again, is obvious. Thus, the influence of the varied parameters on the mode characteristics is in principle unpredictable, with regard to both
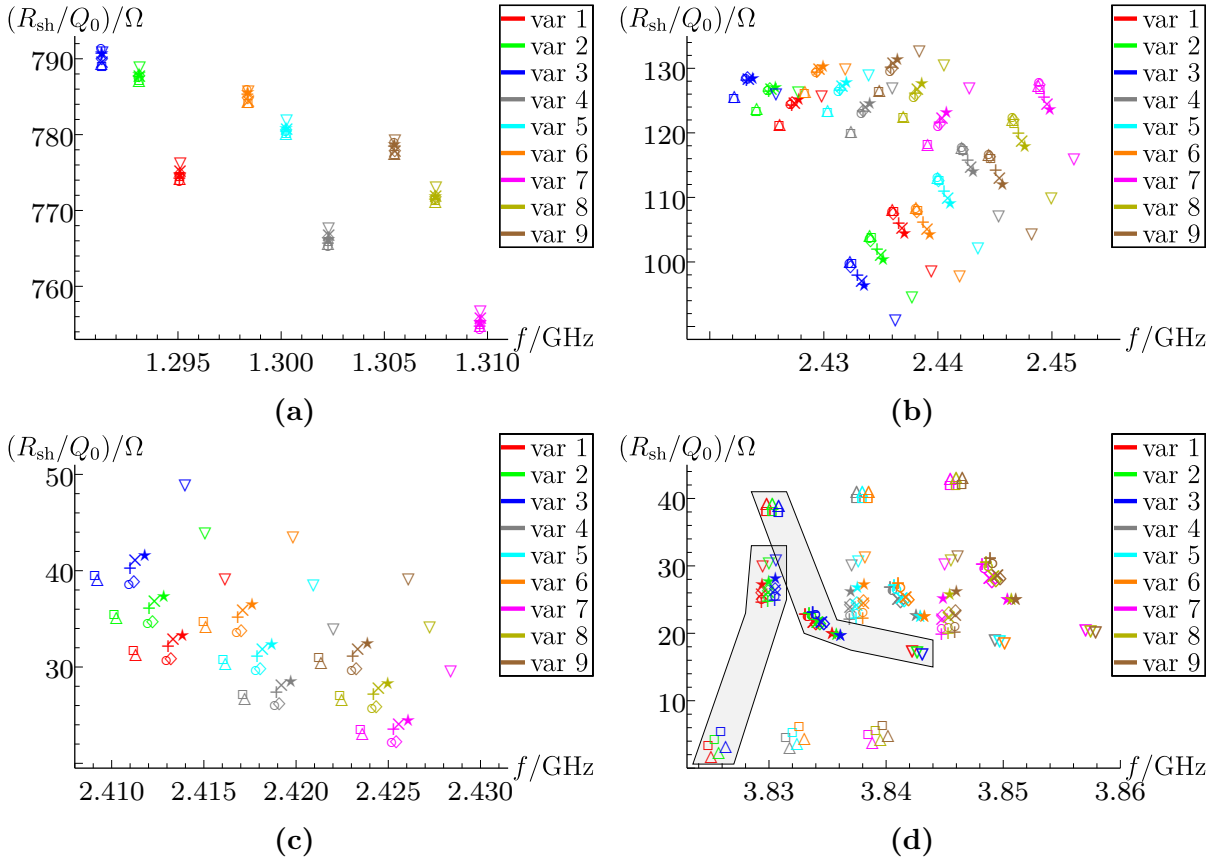
Figure 6.20: On-axis R-over-Q values of the $\mathrm{TM}_{0,1,0_\pi}$-like accelerating mode and a selection of TM_0-like HOMs with high R-over-Q for all candidates C1 (+), C2 (∘), C3 (◇), C4 (×), C5 (△), C6 (□), C7 (▽), C8 (⋆) subject to geometric imperfections: (a) Accelerating mode around $1.3\,\mathrm{GHz}$. (b) The two HOMs with the highest $R_{\mathrm{sh}_i}/Q_{0_i}$ around $2.44\,\mathrm{GHz}$. (c) HOM around $2.42\,\mathrm{GHz}$. (d) Two HOMs around $3.84\,\mathrm{GHz}$. The data points referring to the same mode are exemplarily highlighted for variations 1 to 3.

Table 6.10: Settings for uniform equator and iris radii variations: Variation 5 defines the ideal geometry of the respective design candidates.

| Variation	1	2	3	4	5	6	7	8	9
Equator variation in mm (eq3_ to eq3_+)	+0.5	+0.5	+0.5	0	0	0	-0.5	-0.5	-0.5
Iris variation in mm (i3_ to i3_+)	+0.5	0	-0.5	+0.5	0	-0.5	+0.5	0	-0.5
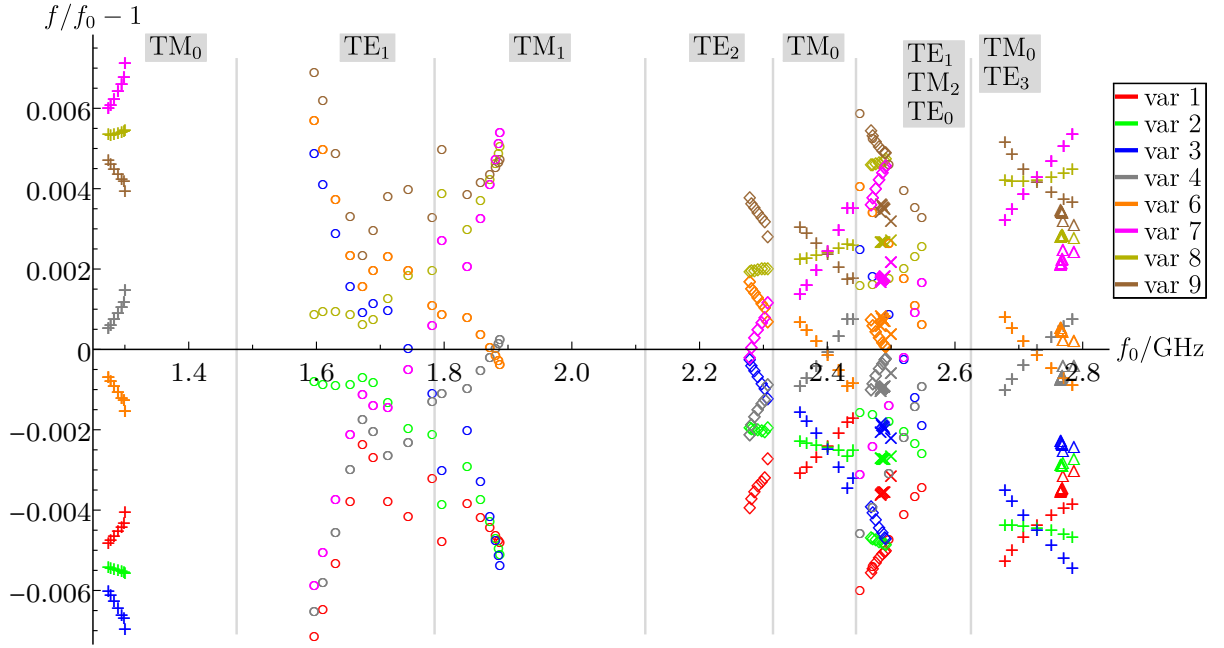
Figure 6.21: Relative frequency shift of the first ten passbands for candidate C1 subject to uniform geometric imperfections. The frequencies f_0 represent the respective frequencies for the ideal C1 shape (variation 5). The different markers indicate the azimuthal mode type: TM_0-like ($+$), TE_0-like ($\times$), dipole ($\circ$), quadrupole ($\diamond$), sextupole ($\triangle$).

geometric imperfections and the different designs C1 to C8. Appendix C.3.4.1 shows the R-over-Q values of the full frequency range for C6 and C7 subject to geometric imperfections. Additionally, the properties of C3 are presented, which is one of the candidates with the most moderate R-over-Q values. For the sake of completeness, Fig. 6.21 depicts the frequency changes that may arise from potential shape deviations. As to be expected, increasing the equator radii reduces the frequencies while decreasing them results in the exact opposite. Besides, the magnitude of the frequency shifts mainly depends on the equator radii and less on the iris radii, as it is particularly apparent for the TM_0-like modes. Since a shift in the frequency of the accelerating mode leads to a detuning of the mode, especially equator deformations may impair the energy transfer to the beam particles. In contrast, the iris radii influence the cell-to-cell coupling and thereby primarily affect the frequency spread within a passband. The comparison of the first TM_0-like and the first TE_1-like passband elucidates this effect. However, the spread also strongly depends on the field profile at the iris port faces. So, the frequency shift is rather a rough indicator for the sensitivity of the modes. The effects of arbitrary non-uniform imperfections are exemplarily demonstrated for the field profile of the accelerating mode for C1 by means of four different forms of variations, shown in Fig. 6.22. Although the R-over-Q value of the mode is only moderately affected by uniform variations, the field flatness is highly sensitive to it. A slight uniform increase of the iris radii (variation 4) already reduces the field flatness η_{ff} by a noticeable amount to 79.76 %, as Fig. 6.22(a) demonstrates. A deformation of solely the center mid-cell, by diminishing its equator and iris radii, results in an even worse η_{ff} of just 22.17 % (see Fig. 6.22(b)). Since this deformation is longitudinally symmetric, $R_{sh_{acc}}/Q_{0_{acc}}$ only lessens by 5.9 %. If further the imperfections are unevenly

distributed, the field profile may be tremendously impaired. For instance, an enlargement of two adjacent inner cells severely reduces the maximal field amplitudes from one end of the resonator to the other, as Fig. 6.22(c) illustrates. Thereby, the R-over-Q deteriorates by 23.5 % to 597.51 Ω. A deformation of a single end-cell is even worse. There, the field is mainly located in the deformed end-cell and its adjacent cell, diminishing $R_{\mathrm{sh_{acc}}}/Q_{0_{acc}}$ by 56.5 % to solely 340.15 Ω. The exemplarily presented parameter study results emphasize not only the high sensitivity of the EM fields to geometric variations, especially to non-uniform ones, but also the unpredictability of the individual mode behavior. This demonstrates that a detailed HOM analysis is vital for a reliable cavity design, favoring perturbative methods for the optimization process.
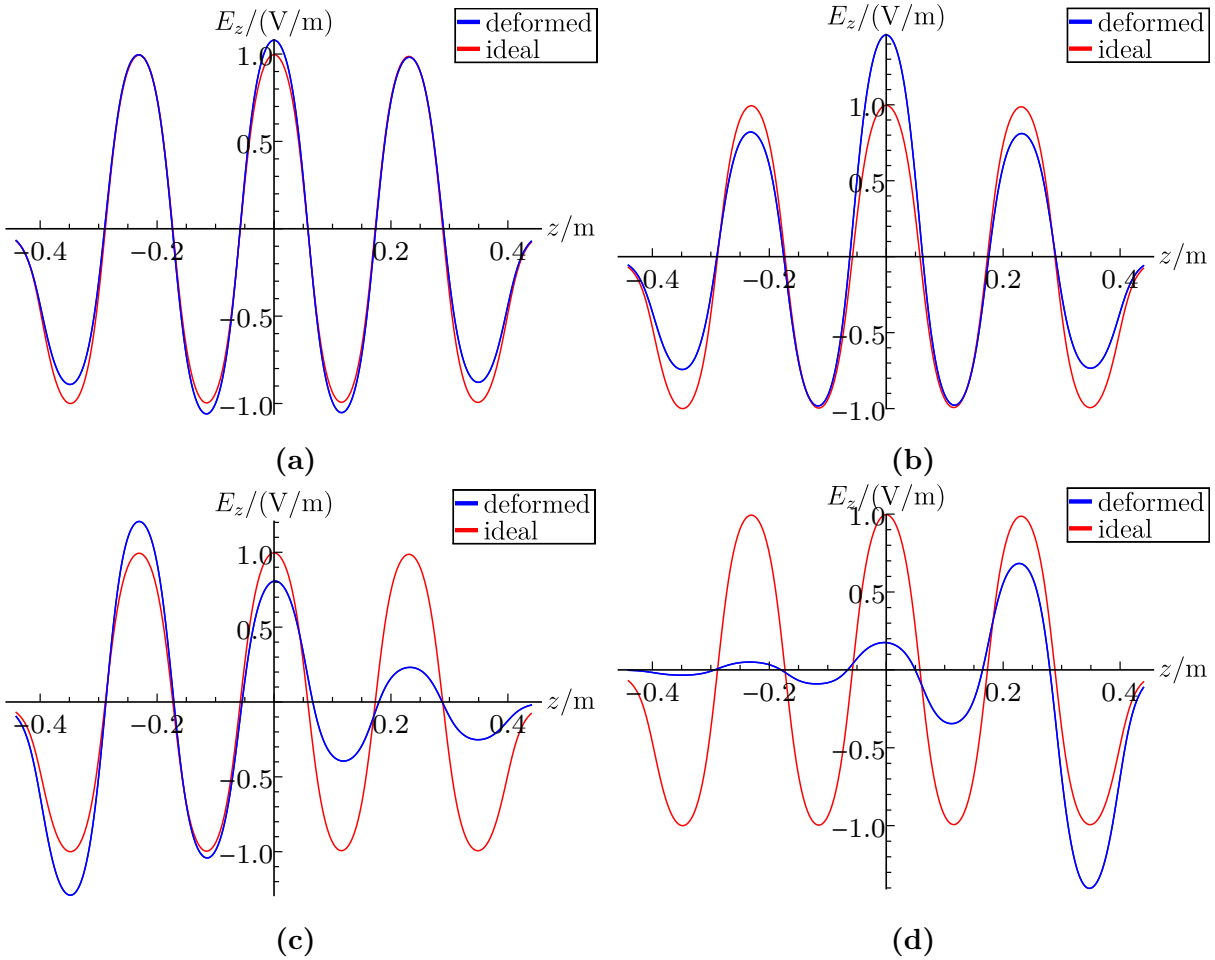
Figure 6.22: Longitudinal electric field of $TM_{0,1,0_{\pi}}$-like accelerating mode along z-axis for candidate C1 subject to geometric imperfections: (a) Uniformly deformed iris radii (i3$_-$ to i3$_+$: +0.5 mm). (b) Deformed mid-cell (eq0, i1$_-$, i1$_+$: −0.5 mm). (c) Two deformed inner cells (eq1$_+$, eq2$_+$, i1$_+$, i2$_+$: +0.5 mm). (c) Deformed end-cell (eq3$_+$: −0.5 mm).

Chapter 7

Discussion, Summary and Outlook

The objectives of this thesis were the introduction of two perturbative methods (PMs) for eigenmode computations, the generalization of Slater's theorem (GST) and the expansion of a reduced eigenmode set (ERES), as well as their effective and efficient implementation and a demonstration of suitable validation and application examples. The novel contributions of this work are the development of ERES, the extension of the GST algorithm and the complex implementation of an automated execution of both methods, including an interface to a direct 3D eigenmode solver and additional algorithms for an accuracy and efficiency enhancement. To motivate the work in a comprehensive manner, the thesis starts with an introduction to the subject of particle accelerators and the relevance of geometric variations in the context of the accelerating cavity design. The relevant basics of electromagnetic field theory are recounted before the fundamentals of GST and ERES are derived in detail. Subsequently, major aspects for the implementation of both methods are presented. The thesis concludes with a discussion of several validation and application examples. The here presented methods GST and ERES constitute efficient approaches for the eigenmode computation in RF structures with PEC or PMC boundaries in the context of geometric parameter studies. The eigenmodes of a so-called perturbed resonator with a modified geometry are expanded in terms of a set of consecutive eigenmodes of the initially defined unperturbed geometry. The energy-related mutual interactions of the complete set of unperturbed eigenmodes inside the volume that is removed by the perturbation form an electric and a magnetic coupling matrix. The eigensystems of the two matrices provide the frequencies and the expansion coefficients of the electric and magnetic fields for the corresponding perturbed geometry. The methods allow to investigate an arbitrary number of differently varied geometries based on the respective interaction terms, on condition that the unperturbed geometry completely encloses the perturbed one. The fundamental difference of GST and ERES lies in the number of computed perturbed eigenmodes. Generally, the number of computable perturbed modes is smaller or at most equal to the number of unperturbed modes. GST yields a number of perturbed modes that is equal to the number of unperturbed modes. The method compensates the excess of computed modes by the emergence of irregular mode pairs, each forming exactly one perturbed mode. In contrast, ERES inherently provides the correct number of actually computable modes by a truncation algorithm that adjusts the number of computed modes. The main advantage of both methods is that once a sufficient set of unperturbed modes is computed,

they allow for an eigenmode computation for a multitude of different perturbations with a very low effort. Besides, asymmetric structures can be derived from symmetric structures. This is especially of advantage in case of complex structures since it reduces the degrees of freedom for the unperturbed geometry. Chapter 4 demonstrated that the efficiency and accuracy of the methods was further enhanced by additional routines. The computational demands were particularly reduced by the generation of interacting mode subsets and a partitioning procedure for the unperturbed shape. The accuracy was improved by the application of so-called analytical volume elements or a semi-analytical integration for the determination of the interaction terms. Furthermore, it was pointed out that a precise computation of the unperturbed eigenmodes is essential for accurate results. At this, FEM combined with a tetrahedral mesh and curved elements of higher order proved to be the most suited algorithm because of the achievable precise boundary discretization.

The validation examples in Chapter 5 verified that both methods provide reasonable results over a wide frequency range. However, a comparison of identical examples revealed that ERES has a lower rate of convergence than GST and hence requires a noticeably larger number of unperturbed modes to achieve the same accuracy. In addition, the truncation algorithm of ERES creates step-like changes in the error progression. The algorithm is controlled by an additional free parameter, the eigenvalue truncation accuracy, which affects the emergence of the step-like changes, resulting in an unpredictable accuracy. In contrast, the frequencies of regular GST modes always oscillate symmetrically around the correct values. The drawback of GST is the occurrence of irregular mode pairs arising from the compensatory mechanism. The mode pairs can generally be detected by means of partially complex-valued results. The irregular modes very frequently do not converge towards the correct solution and are less accurate than the regular GST modes. For the investigated examples, it was observed that the frequency error can be by an order of magnitude higher than the error of the regular modes. However, this is only the case for relatively large perturbations that change the unperturbed volume by several percents. The smaller the perturbation is, the less irregular modes occur and the smaller their deviations are. Realistic geometric imperfections involve no or at most a few irregular modes. Consequently, GST is the preferred perturbative method. Using a just sufficient number of unperturbed, i.e. the expansion reached a converging state, the GST frequency error lies in the range of 10^{-4} up to 10^{-3}. The method provides very precise stationary fields for modes of lower order. As expected, the deviations slightly increase by rising mode order, but only for modes whose frequency is very close to the frequency of the highest unperturbed mode the accuracy noticeably reduces. Thus, accurate results can be obtained over a wide frequency range on condition that the minimal unperturbed wavelength is smaller than or at most equal to the size of the perturbation. The validation and application examples evinced that the required highest unperturbed frequency is indirectly proportional to the perturbation extent. Hence, the number of necessary expansion modes increases for smaller perturbations but also if the spread between the individual unperturbed frequencies reduces. As a consequence, especially multicell cavities subject to small geometric imperfections may require a hundred or several hundred modes for accurate results. But disadvantageously, in particular for such complex structures, the computation of the unperturbed modes is demanding. Consequently, the number of available expansion modes may be too small. To overcome this limitation, a modification of GST was developed that

reduces the number of necessary modes by an adjustment of the interaction terms with respect to the perturbation extent. The modified GST algorithm proved to provide precise results for both frequencies and EM fields allowing for a simultaneous performance optimization and shape imperfections consideration. In addition, it is advisable to define the unperturbed geometry deliberately larger to reduce the number of necessary modes. Such an unperturbed shape is also more flexible with regard to design modifications. Though the enlargement should be conducted in a reasonable manner taken in order to avoid, firstly, the emergence of irregular GST modes and, secondly, an excessive change of the unperturbed eigenmodes. The exemplarily presented results for the parameter study of the seven-cell bERLinPro resonator illustrated by means of the inherently contrary mode characteristics that a detailed broadband HOM analysis is vital for a reliable cavity design. Furthermore, the huge number of $1.27 \cdot 10^7$ investigated designs, taking also shape imperfections into account, demonstrated that perturbative methods are highly favorable for the optimization process. The attempt to expand the eigenmodes of an elliptical single-cell resonator in terms of the eigenmodes of a cylindrical resonator did not provide the desired results. Unfortunately, particularly the EM field of the accelerating mode can not be computed with a sufficient precision due to the discontinuity between the iris and the elliptical lateral surface.

The use of a 2.5D eigenmode solver [66], [67], [68] for the computation of the unperturbed modes would significantly reduce the computational demands and increase the computable frequency range. It would also allow to determine the interaction terms of the unperturbed modes invariably from semi-analytical volume integrals, requiring a discrete integration only for 2D surface integrals. Furthermore, symmetry breaking perturbations could nevertheless be applied to obtain asymmetric cavity geometries which conventionally can only be computed with 3D solvers. Therefore, the integration of a 2.5D eigenmode solver is highly preferred for future projects. In this context, the establishment of an extended or universal interface to other eigenmode solvers, for instance the open-source FEM package FEniCS [73] is also conceivable. Since a direct application of the PMs to multi-cavity structures is not advisable due to the immense number of degrees of freedom involved in the computation of the unperturbed modes, an interfacing with the state-space concatenation scheme [63] is planned. Thereby, an independent treatment of the single cavities by the PMs and a subsequent concatenation of multiple cavities and HOM couplers would be realizable. A successful combination of both methods would create unprecedented advances in the HOM analysis. Further investigations concerning the dependence of the GST adjustment constants $\varkappa_\nu$ from the perturbation type, its extent and the available unperturbed frequency range are advisable in order to develop an automated reliable GST adjustment algorithm. Moreover, a combination of GST and ERES is conceivable, allowing for a comparison and mutually improvement of both methods. The GST frequencies may provide a guidance for the choice of the eigenvalue truncation accuracy in ERES and thereby improve the accuracy and predictability of the ERES results. In turn, the so adapted ERES eigenmodes may yield better results than the irregular GST modes. The investigation of the bERLinPro resonator demonstrated the necessity of an efficient data processing algorithm for a comprehensive analysis of the PM-based EM cavity characteristics. Within the scope of an international cooperation funded by the German Research Foundation (Deutsche Forschungsgemeinschaft, DFG), it is planned to

link the PMs with a general-purpose framework for multi-objective optimization [98] to cope with the huge amount of different geometric designs and the likewise large number of modes that needs to be evaluated. Another general issue in a cavity robustness analysis is the acquirement of realistic input parameters for the geometric variations. Chapter 1 discussed the fundamental aspects arising in the manufacturing process and during operation. However, exact information can only be obtained from the databases of particle accelerator facilities. First attempts to utilize DESY's European XFEL Database [99] were made.

Chapter A

Analysis and Derivations

A.1 Vector Analysis

A.2 Vector Formulas

Magnitude of a real-valued vector (Euclidean norm) [78, Sec. 4.1.6]

$$\|\mathbf{F}\| = F = \sqrt{\mathbf{F} \cdot \mathbf{F}} \tag{A.1}$$

Magnitude of a complex-valued vector (Euclidean norm) [78, Sec. 4.1.6]

$$\|\underline{\mathbf{F}}\| = F = \sqrt{\underline{\mathbf{F}} \cdot \underline{\mathbf{F}}^*} \tag{A.2}$$

Divergence theorem (Gauss's theorem) [26, (B.47)]
d$\mathbf{A}$: outward-oriented normal vector of the infinitely small surface element dA

$$\oiint_{\partial V} \mathbf{F} \cdot \mathrm{d}\mathbf{A} = \iiint_V (\boldsymbol{\nabla} \cdot \mathbf{F}) \, \mathrm{d}V \tag{A.3}$$

Stokes's theorem [26, (B.52)]
d$\mathbf{s}$: infinitely small path element right-hand oriented to d$\mathbf{A}$

$$\oint_{\partial A} \mathbf{F} \cdot \mathrm{d}\mathbf{s} = \iint_A (\boldsymbol{\nabla} \times \mathbf{F}) \cdot \mathrm{d}\mathbf{A} \tag{A.4}$$

Vector algebraic formulas [26, Sec. B.2.1]

$$\mathbf{F}_1 \cdot (\mathbf{F}_2 \times \mathbf{F}_3) = \mathbf{F}_2 \cdot (\mathbf{F}_3 \times \mathbf{F}_1) = \mathbf{F}_3 \cdot (\mathbf{F}_1 \times \mathbf{F}_2) \tag{A.5}$$

Vector identities [26, Sec. B.2.2]

$$\boldsymbol{\nabla} \cdot (\boldsymbol{\nabla} \times \mathbf{F}) = 0 \tag{A.6}$$

$$\boldsymbol{\nabla} \cdot (\mathbf{F}_1 \times \mathbf{F}_2) = \mathbf{F}_2 \cdot (\boldsymbol{\nabla} \times \mathbf{F}_1) - \mathbf{F}_1 \cdot (\boldsymbol{\nabla} \times \mathbf{F}_2) \tag{A.7}$$

$$\boldsymbol{\nabla} \times \boldsymbol{\nabla} \times \mathbf{F} = \boldsymbol{\nabla}(\boldsymbol{\nabla} \cdot \mathbf{F}) - \Delta \mathbf{F} \tag{A.8}$$

A.3 Differential Equations

A.3.1 Differentiation rules

Product rule [78, Sec. 6.1.2.2]

$$\mathrm{d}(uv) = v\,\mathrm{d}u + u\,\mathrm{d}v \tag{A.9}$$

A.3.2 Integration rules

Integration by parts [78, Sec. 8.1.2.7]

$$\int u\,\mathrm{d}v = uv - \int v\,\mathrm{d}u \tag{A.10}$$

A.4 Analytical Derivations of Electromagnetic Field Theory

A.4.1 Separation of Spatial and Time Dependences for Time-Harmonic Electromagnetic Fields

Separation of variables for a complex EM field at a frequency ω:

$$\underline{\mathbf{E}}(\mathbf{r}, t) = \underline{e}^{\mathrm{t}}(t)\,\mathbf{E}(\mathbf{r}), \tag{2.46}$$
$$\underline{\mathbf{H}}(\mathbf{r}, t) = \underline{h}^{\mathrm{t}}(t)\,\mathbf{H}(\mathbf{r}) \tag{2.47}$$

Deliberate definition of time-dependences:

$$\underline{e}^{\mathrm{t}}(t) = \mathrm{e}^{\jmath\omega t}, \tag{A.13}$$
$$\underline{h}^{\mathrm{t}}(t) = \jmath\mathrm{e}^{\jmath\omega t} \tag{A.14}$$

Resulting temporal relation between electric and magnetic field:

$$\underset{\text{(A.13),(A.14)}}{\Longleftrightarrow} \qquad \underline{h}^{\mathrm{t}}(t) = \jmath\underline{e}^{\mathrm{t}}(t) \tag{2.48}$$

Elimination of time dependences in complex Maxwell's equations in a linear, isotropic, non-conducting, time-independent, charge- and source-free medium where $\rho(\mathbf{r}, t) = 0$, $\sigma = 0$, $\mathbf{J}_{\mathrm{ic}}(\mathbf{r}, t) = 0$ and ε and μ are constant scalars:

1. Elimination of time dependences in Gauss's law for the magnetic field:

$$\underset{\text{(2.18),(2.12)}}{\Longleftrightarrow} \qquad \boldsymbol{\nabla} \cdot (\mu\underline{\mathbf{H}}(\mathbf{r}, t)) = 0$$

$$\underset{\text{(2.47)}}{\Longleftrightarrow} \qquad \mu\boldsymbol{\nabla} \cdot (\underline{h}^{\mathrm{t}}(t)\,\mathbf{H}(\mathbf{r})) = 0$$

$$\Longleftrightarrow \qquad \boldsymbol{\nabla} \cdot \mathbf{H}(\mathbf{r}) = 0 \tag{2.49}$$

2. Elimination of time dependences in Gauss's law for the electric field:

$$\underset{(2.18),(2.11)}{\Longleftrightarrow} \qquad \boldsymbol{\nabla} \cdot (\varepsilon \underline{\mathbf{E}}(\mathbf{r}, t)) = 0$$

$$\underset{(2.46)}{\Longleftrightarrow} \qquad \varepsilon \boldsymbol{\nabla} \cdot (\underline{e}^{\mathrm{t}}(t) \, \mathbf{E}(\mathbf{r})) = 0$$

$$\Longleftrightarrow \qquad \boldsymbol{\nabla} \cdot \mathbf{E}(\mathbf{r}) = 0 \tag{2.50}$$

3. Elimination of time dependences in Faraday's law of induction:

$$\underset{(2.20),(2.12)}{\Longleftrightarrow} \qquad \boldsymbol{\nabla} \times \underline{\mathbf{E}}(\mathbf{r}, t) = -\jmath \omega \mu \underline{\mathbf{H}}(\mathbf{r}, t)$$

$$\underset{(2.46),(2.47)}{\Longleftrightarrow} \qquad \boldsymbol{\nabla} \times (\underline{e}^{\mathrm{t}}(t) \, \mathbf{E}(\mathbf{r})) = -\jmath \omega \mu (\underline{h}^{\mathrm{t}}(t) \, \mathbf{H}(\mathbf{r}))$$

$$\underset{(2.48)}{\Longleftrightarrow} \qquad \underline{e}^{\mathrm{t}}(t) \, (\boldsymbol{\nabla} \times \mathbf{E}(\mathbf{r})) = -\jmath \omega \mu \jmath \underline{e}^{\mathrm{t}}(t) \, \mathbf{H}(\mathbf{r})$$

$$\Longleftrightarrow \qquad \boldsymbol{\nabla} \times \mathbf{E}(\mathbf{r}) = \quad \omega \mu \mathbf{H}(\mathbf{r}) \tag{2.51}$$

4. Elimination of time dependences in Ampère's circuital law:

$$\underset{(2.21),(2.11)}{\Longleftrightarrow} \qquad \boldsymbol{\nabla} \times \underline{\mathbf{H}}(\mathbf{r}, t) = \jmath \omega \varepsilon \underline{\mathbf{E}}(\mathbf{r}, t)$$

$$\underset{(2.46),(2.47)}{\Longleftrightarrow} \qquad \boldsymbol{\nabla} \times (\underline{h}^{\mathrm{t}}(t) \, \mathbf{H}(\mathbf{r})) = \jmath \omega \varepsilon (\underline{e}^{\mathrm{t}}(t) \, \mathbf{E}(\mathbf{r}))$$

$$\underset{(2.48)}{\Longleftrightarrow} \qquad \jmath \underline{e}^{\mathrm{t}}(t) \, (\boldsymbol{\nabla} \times \mathbf{H}(\mathbf{r})) = \jmath \omega \varepsilon \underline{e}^{\mathrm{t}}(t) \, \mathbf{E}(\mathbf{r})$$

$$\Longleftrightarrow \qquad \boldsymbol{\nabla} \times \mathbf{H}(\mathbf{r}) = \varepsilon \omega \mathbf{E}(\mathbf{r}) \tag{2.52}$$

A.4.2 Poynting's Theorem

Note that the spatial and time dependences $(\mathbf{r}, t)$ of the quantities are not indicated in A.4.2 for reasons of clarity but are nevertheless valid.

Real Poynting vector in differential form

$$\underset{(A.7)}{\Longleftrightarrow} \qquad \boldsymbol{\nabla} \cdot (\mathbf{E} \times \mathbf{H}) = \quad \mathbf{H} \cdot (\boldsymbol{\nabla} \times \mathbf{E}) - \mathbf{E} \cdot (\boldsymbol{\nabla} \times \mathbf{H})$$

$$\underset{(2.7),(2.8)}{\Longleftrightarrow} \qquad \boldsymbol{\nabla} \cdot (\mathbf{E} \times \mathbf{H}) = -\mathbf{H} \cdot (\frac{\partial}{\partial t}\mathbf{B}) - \mathbf{E} \cdot (\frac{\partial}{\partial t}\mathbf{D} + \mathbf{J})$$

$$\Longleftrightarrow \qquad \boldsymbol{\nabla} \cdot (\mathbf{E} \times \mathbf{H}) = -\mathbf{H} \cdot \frac{\partial}{\partial t}\mathbf{B} - \mathbf{E} \cdot \frac{\partial}{\partial t}\mathbf{D} - \mathbf{E} \cdot \mathbf{J}$$

$$\underset{(2.10)}{\Longleftrightarrow} \qquad \boldsymbol{\nabla} \cdot (\mathbf{E} \times \mathbf{H}) = -\mathbf{H} \cdot \frac{\partial}{\partial t}\mathbf{B} - \mathbf{E} \cdot \frac{\partial}{\partial t}\mathbf{D} - \sigma E^2 - \mathbf{E} \cdot (\mathbf{J}_{\mathrm{cc}} + \mathbf{J}_{\mathrm{ic}}) \tag{A.20}$$

Real Poynting vector in integral form

$$\underset{(A.20),(A.3)}{\Longleftrightarrow} \oiint_{\partial \Omega} (\mathbf{E} \times \mathbf{H}) \cdot \mathrm{d}\mathbf{A} = - \iiint_{\Omega} \left(\mathbf{H} \cdot \frac{\partial}{\partial t}\mathbf{B} + \mathbf{E} \cdot \frac{\partial}{\partial t}\mathbf{D} + \sigma E^2 + \mathbf{E} \cdot (\mathbf{J}_{\mathrm{cc}} + \mathbf{J}_{\mathrm{ic}}) \right) \mathrm{d}V$$

$$\tag{2.22}$$

Differential electric and magnetic energy density [77, Sec. 1.7]:

$$\mathrm{d}u_{\mathrm{e}} = \mathbf{E} \cdot \mathrm{d}\mathbf{D}, \tag{A.22}$$
$$\mathrm{d}u_{\mathrm{m}} = \mathbf{H} \cdot \mathrm{d}\mathbf{B} \tag{A.23}$$

Differential electric and magnetic energy density for linear, homogeneous, isotropic, time-independent media:

$$\underset{(2.24)}{\Longleftrightarrow} \quad \mathrm{d}u_{\mathrm{e}} = \frac{1}{2}\mathrm{d}(\mathbf{E} \cdot \mathbf{D})$$

$$\underset{(\mathrm{A.9})}{\Longleftrightarrow} \quad \mathrm{d}u_{\mathrm{e}} = \frac{1}{2}(\mathbf{E} \cdot \mathrm{d}\mathbf{D} + \mathbf{D} \cdot \mathrm{d}\mathbf{E})$$

$$\underset{(2.11)}{\Longleftrightarrow} \quad \mathrm{d}u_{\mathrm{e}} = \frac{1}{2}(\mathbf{E} \cdot \mathrm{d}\mathbf{D} + \mathbf{E} \cdot \mathrm{d}(\varepsilon\mathbf{E}))$$

$$\Longleftrightarrow \quad \mathrm{d}u_{\mathrm{e}} = \mathbf{E} \cdot \mathrm{d}\mathbf{D} \tag{2.24}$$

$$\underset{(2.25),(\mathrm{A.23}),(\mathrm{A.9})}{\Longleftrightarrow} \mathrm{d}u_{\mathrm{m}} = \frac{1}{2}\mathrm{d}(\mathbf{H} \cdot \mathbf{B}) = \mathbf{H} \cdot \mathrm{d}\mathbf{B} \tag{2.25}$$

Complex Poynting vector in differential form

$$\underset{(\mathrm{A.7})}{\Longleftrightarrow} \quad \boldsymbol{\nabla} \cdot (\underline{\mathbf{E}} \times \underline{\mathbf{H}}^*) = \underline{\mathbf{H}}^* \cdot (\boldsymbol{\nabla} \times \underline{\mathbf{E}}) - \underline{\mathbf{E}} \cdot (\boldsymbol{\nabla} \times \underline{\mathbf{H}}^*)$$

$$\underset{(2.20),(2.21)}{\Longleftrightarrow} \quad \boldsymbol{\nabla} \cdot (\underline{\mathbf{E}} \times \underline{\mathbf{H}}^*) = \underline{\mathbf{H}}^* \cdot (-\jmath\omega\underline{\mathbf{B}}) - \underline{\mathbf{E}} \cdot (-\jmath\omega\underline{\mathbf{D}}^* + \underline{\mathbf{J}}^*)$$

$$\Longleftrightarrow \quad \boldsymbol{\nabla} \cdot (\frac{1}{2}\underline{\mathbf{E}} \times \underline{\mathbf{H}}^*) = -2\jmath\omega\left(\frac{\underline{\mathbf{H}}^* \cdot \underline{\mathbf{B}}}{4} - \frac{\underline{\mathbf{E}} \cdot \underline{\mathbf{D}}^*}{4}\right) - \frac{\underline{\mathbf{E}} \cdot \underline{\mathbf{J}}^*}{2}$$

$$\underset{(2.10)}{\Longleftrightarrow} \quad \boldsymbol{\nabla} \cdot (\frac{1}{2}\underline{\mathbf{E}} \times \underline{\mathbf{H}}^*) = -2\jmath\omega\left(\frac{\underline{\mathbf{H}}^* \cdot \underline{\mathbf{B}}}{4} - \frac{\underline{\mathbf{E}} \cdot \underline{\mathbf{D}}^*}{4}\right) - \frac{\sigma\underline{\mathbf{E}} \cdot \underline{\mathbf{E}}^*}{2} - \frac{\underline{\mathbf{E}} \cdot (\underline{\mathbf{J}}_{\mathrm{cc}}^* + \underline{\mathbf{J}}_{\mathrm{ic}}^*)}{2}$$

$$\tag{A.26}$$

Complex Poynting vector in integral form

$$\underset{(\mathrm{A.26}),(\mathrm{A.3})}{\Longleftrightarrow} \oiint_{\partial\Omega}(\frac{1}{2}\underline{\mathbf{E}} \times \underline{\mathbf{H}}^*)\cdot \mathrm{d}\mathbf{A} = -2\jmath\omega \iiint_{\Omega} \left(\frac{\underline{\mathbf{H}}^* \cdot \underline{\mathbf{B}}}{4} - \frac{\underline{\mathbf{E}} \cdot \underline{\mathbf{D}}^*}{4}\right) \mathrm{d}V$$

$$- \iiint_{\Omega} \frac{\sigma\underline{\mathbf{E}} \cdot \underline{\mathbf{E}}^*}{2} \, \mathrm{d}V - \iiint_{\Omega} \frac{\underline{\mathbf{E}} \cdot (\underline{\mathbf{J}}_{\mathrm{cc}}^* + \underline{\mathbf{J}}_{\mathrm{ic}}^*)}{2} \, \mathrm{d}V \tag{2.28}$$

A.4.3 Wave Equations

Inhomogeneous generalized wave equation for electric field

$$\underset{(A.8)}{\Longleftrightarrow} \qquad \boldsymbol{\nabla} \times \boldsymbol{\nabla} \times \mathbf{E}(\mathbf{r},t) = \boldsymbol{\nabla}(\boldsymbol{\nabla} \cdot \mathbf{E}(\mathbf{r},t)) - \Delta\mathbf{E}(\mathbf{r},t)$$

$$\underset{(2.7),(2.2),(2.11)}{\Longleftrightarrow} \qquad \boldsymbol{\nabla} \times (-\frac{\partial}{\partial t}\mathbf{B}(\mathbf{r},t)) = \boldsymbol{\nabla}\left(\frac{\rho(\mathbf{r},t)}{\varepsilon}\right) - \Delta\mathbf{E}(\mathbf{r},t)$$

$$\underset{(2.12)}{\Longleftrightarrow} \qquad -\mu\frac{\partial}{\partial t}\left(\boldsymbol{\nabla} \times \mathbf{H}(\mathbf{r},t)\right) = \frac{\boldsymbol{\nabla}\rho(\mathbf{r},t)}{\varepsilon} - \Delta\mathbf{E}(\mathbf{r},t)$$

$$\underset{(2.8),(2.11)}{\Longleftrightarrow} \qquad -\mu\frac{\partial}{\partial t}\left(\varepsilon\frac{\partial}{\partial t}\mathbf{E}(\mathbf{r},t) + \mathbf{J}(\mathbf{r},t)\right) = \frac{\boldsymbol{\nabla}\rho(\mathbf{r},t)}{\varepsilon} - \Delta\mathbf{E}(\mathbf{r},t)$$

$$\underset{(2.8),(2.10)}{\Longleftrightarrow} \Delta\mathbf{E}(\mathbf{r},t) - \mu\sigma\frac{\partial}{\partial t}\mathbf{E}(\mathbf{r},t) - \mu\varepsilon\frac{\partial^2}{\partial t^2}\mathbf{E}(\mathbf{r},t) = \frac{\boldsymbol{\nabla}\rho(\mathbf{r},t)}{\varepsilon} + \mu\frac{\partial}{\partial t}\left(\mathbf{J}_{\mathrm{cc}}(\mathbf{r},t) + \mathbf{J}_{\mathrm{ic}}(\mathbf{r},t)\right)$$

$$(2.30)$$

Inhomogeneous generalized wave equation for magnetic field

$$\underset{(A.8)}{\Longleftrightarrow} \qquad \boldsymbol{\nabla} \times \boldsymbol{\nabla} \times \mathbf{H}(\mathbf{r},t) = \boldsymbol{\nabla}(\boldsymbol{\nabla} \cdot \mathbf{H}(\mathbf{r},t)) - \Delta\mathbf{H}(\mathbf{r},t)$$

$$\underset{(2.8),(2.1)}{\Longleftrightarrow} \qquad \boldsymbol{\nabla} \times \left(\frac{\partial}{\partial t}\mathbf{D}(\mathbf{r},t) + \mathbf{J}(\mathbf{r},t)\right) = \boldsymbol{\nabla}0 - \Delta\mathbf{H}(\mathbf{r},t)$$

$$\underset{(2.11),(2.10)}{\Longleftrightarrow} \left(\varepsilon\frac{\partial}{\partial t} + \sigma\right)\left(\boldsymbol{\nabla} \times \mathbf{E}(\mathbf{r},t)\right) + \boldsymbol{\nabla} \times (\mathbf{J}_{\mathrm{cc}}(\mathbf{r},t) + \mathbf{J}_{\mathrm{ic}}(\mathbf{r},t)) = -\Delta\mathbf{H}(\mathbf{r},t)$$

$$\underset{(2.8),(2.11)}{\Longleftrightarrow} \quad \Delta\mathbf{H}(\mathbf{r},t) - \mu\sigma\frac{\partial}{\partial t}\mathbf{H}(\mathbf{r},t) - \mu\varepsilon\frac{\partial^2}{\partial t^2}\mathbf{H}(\mathbf{r},t) = -\boldsymbol{\nabla} \times (\mathbf{J}_{\mathrm{cc}}(\mathbf{r},t) + \mathbf{J}_{\mathrm{ic}}(\mathbf{r},t))$$

$$(2.31)$$

A.4.4 Orthogonality of EM Eigenmodes in an Ideal Resonator

Note that, the spatial dependences ($\mathbf{r}$) of the quantities are not indicated in A.4.4 for reasons of clarity but are nevertheless valid.

Orthogonality of stationary electric fields

Applying the vector identities (A.7)-(A.8) to the electric fields of two different eigenmodes i and k:

$$\boldsymbol{\nabla} \cdot \left(\mathbf{E}_k \times (\boldsymbol{\nabla} \times \mathbf{E}_i)\right) - \boldsymbol{\nabla} \cdot \left(\mathbf{E}_i \times (\boldsymbol{\nabla} \times \mathbf{E}_k)\right)$$
$$= (\boldsymbol{\nabla} \times \mathbf{E}_i) \cdot (\boldsymbol{\nabla} \times \mathbf{E}_k) - \mathbf{E}_k \cdot \left(\boldsymbol{\nabla} \times (\boldsymbol{\nabla} \times \mathbf{E}_i)\right) - (\boldsymbol{\nabla} \times \mathbf{E}_k) \cdot (\boldsymbol{\nabla} \times \mathbf{E}_i) + \mathbf{E}_i \cdot \left(\boldsymbol{\nabla} \times (\boldsymbol{\nabla} \times \mathbf{E}_k)\right)$$
$$= -\mathbf{E}_k \cdot \left(\boldsymbol{\nabla}(\boldsymbol{\nabla} \cdot \mathbf{E}_i) - \Delta\mathbf{E}_i\right) + \mathbf{E}_i \cdot \left(\boldsymbol{\nabla}(\boldsymbol{\nabla} \cdot \mathbf{E}_k) - \Delta\mathbf{E}_k\right) \tag{A.30}$$

Applying Maxwell's equations for the stationary EM field (2.49)-(2.52) and the Helmholtz equation (2.53) to (A.30):

$$\boldsymbol{\nabla} \cdot \left(\mathbf{E}_k \times (\boldsymbol{\nabla} \times \mathbf{E}_i)\right) - \boldsymbol{\nabla} \cdot \left(\mathbf{E}_i \times (\boldsymbol{\nabla} \times \mathbf{E}_k)\right) = -\mathbf{E}_k \cdot (0 + k_i^2\mathbf{E}_i) + \mathbf{E}_i \cdot (0 + k_k^2\mathbf{E}_k)$$
$$\boldsymbol{\nabla} \cdot \left(\mathbf{E}_k \times (\omega_i\mu\mathbf{H}_i)\right) - \boldsymbol{\nabla} \cdot \left(\mathbf{E}_i \times (\omega_k\varepsilon\mathbf{H}_k)\right) = (k_k^2 - k_i^2)\mathbf{E}_i \cdot \mathbf{E}_k$$

Finally applying Gauss's theorem (A.3):

$$\oiint_{\partial\Omega} \left(\omega_i \mu (\mathbf{E}_k \times \mathbf{H}_i) - \omega_k \varepsilon (\mathbf{E}_i \times \mathbf{H}_k) \right) \cdot \mathrm{d}\mathbf{A} = (k_k^2 - k_i^2) \iiint_{\Omega} \mathbf{E}_i \cdot \mathbf{E}_k \, \mathrm{d}V \tag{A.31}$$

Normal and tangential components of the electric and magnetic field at the resonator boundary:

$$\Longleftrightarrow \qquad (\mathbf{E}_k \times \mathbf{H}_i) \cdot \mathrm{d}\mathbf{A} = (\mathbf{E}_k \times \mathbf{H}_i) \cdot \mathbf{n} \, \mathrm{d}A$$

$$\underset{(2.43),(2.44)}{\Longleftrightarrow} \quad (\mathbf{E}_k \times \mathbf{H}_i) \cdot \mathrm{d}\mathbf{A} = \mathbf{E}_k \cdot \underbrace{(\mathbf{H}_i \times \mathbf{n})}_{\mathbf{0} \text{ at } \partial\Omega_{\mathrm{pmc}}} \cdot \mathrm{d}A = \underbrace{(\mathbf{n} \times \mathbf{E}_k)}_{\mathbf{0} \text{ at } \partial\Omega_{\mathrm{pec}}} \cdot \mathbf{H}_i \, \mathrm{d}A$$

$$\Longleftrightarrow \qquad \oiint_{\partial\Omega} (\mathbf{E}_k \times \mathbf{H}_i) \cdot \mathrm{d}\mathbf{A} = 0 \tag{A.32}$$

For an ideal resonator, whose boundary $\partial\Omega$ is either PEC or PMC, the cross product of any electric and any magnetic is zero as (A.32) shows. Consequently, the left-hand side of (A.31) becomes zero

$$0 = (k_k^2 - k_i^2) \iiint_{\Omega} \mathbf{E}_i \cdot \mathbf{E}_k \, \mathrm{d}V. \tag{A.33}$$

Since the eigenvalues k_i and k_k differ if $i \neq k$ (except in case of degeneracy where the electric fields are anyway orthogonal), (A.33) can only be valid if

$$0 = \iiint_{\Omega} \mathbf{E}_i \cdot \mathbf{E}_k \, \mathrm{d}V \quad \text{for } i \neq k. \tag{A.34}$$

Consequently, the electric fields of the eigenmodes are orthogonal.

Orthogonality of Stationary Magnetic Fields

The proof of orthogonality of the magnetic fields is made in an analogous manner to the one of the electric fields.

Chapter B

Resonator Eigenmodes

Eigenmodes in complex vector form:

$$\underline{\mathbf{E}}(\mathbf{r}, t) = \underline{e}^{\mathrm{t}}(t)\, \mathbf{E}(\mathbf{r})\,,$$
$$\underline{\mathbf{H}}(\mathbf{r}, t) = \underline{h}^{\mathrm{t}}(t)\, \mathbf{H}(\mathbf{r})$$

Time dependences:

$$\underline{e}^{\mathrm{t}}(t) = \mathrm{e}^{\jmath(\omega t + \phi_{\mathrm{e}})}\,,$$
$$\underline{h}^{\mathrm{t}}(t) = \mathrm{e}^{\jmath(\omega t + \phi_{\mathrm{e}} + \frac{\pi}{2})}$$

B.1 Rectangular Resonator with PEC Boundary

Table B.1: Parameters of rectangular resonator.

Dimensions	Width L_x
	Height L_y
	Length L_z
Rectangular coordinate system	$\mathbf{r} = (x, y, z)^T$
Mode indices	Transverse x-index m
	Transverse y-index n
	Longitudinal index p

B.1.1 Transverse Magnetic Modes

Wave numbers of $\mathrm{TM}_{m,n,p}$ mode:

$$k_x = \frac{m\pi}{L_x} \quad , \quad k_y = \frac{n\pi}{L_y} \quad , \quad k_z = \frac{p\pi}{L_z} \tag{B.1}$$

Resonant frequency of $\text{TM}_{m,n,p}$ mode:

$$\omega = \sqrt{\frac{\left(\frac{m\pi}{L_x}\right)^2 + \left(\frac{n\pi}{L_y}\right)^2 + \left(\frac{p\pi}{L_z}\right)^2}{\mu\varepsilon}} \qquad \text{(B.2)}$$

Stationary EM field of $\text{TM}_{m,n,p}$ mode:

$$
\begin{aligned}
E_x(\mathbf{r}) &= -E_0 k_x k_z \cos(k_x x)\sin(k_y y)\sin(k_z z)\,, & \text{(B.3)}\\
E_y(\mathbf{r}) &= -E_0 k_y k_z \sin(k_x x)\cos(k_y y)\sin(k_z z)\,, & \text{(B.4)}\\
E_z(\mathbf{r}) &= E_0 (k_x^2 + k_y^2) \sin(k_x x)\sin(k_y y)\cos(k_z z)\,, & \text{(B.5)}\\
H_x(\mathbf{r}) &= E_0 \varepsilon k_y\,\omega \sin(k_x x)\cos(k_y y)\cos(k_z z)\,, & \text{(B.6)}\\
H_y(\mathbf{r}) &= -E_0 \varepsilon k_x\,\omega \cos(k_x x)\sin(k_y y)\cos(k_z z)\,, & \text{(B.7)}\\
H_z(\mathbf{r}) &= 0 & \text{(B.8)}
\end{aligned}
$$

B.1.2 Transverse Electric Modes

Wave number of $\text{TE}_{m,n,p}$ mode:

$$k_x = \frac{m\pi}{L_x} \quad,\quad k_y = \frac{n\pi}{L_y} \quad,\quad k_z = \frac{p\pi}{L_z} \qquad \text{(B.9)}$$

Resonant frequency of $\text{TE}_{m,n,p}$ mode:

$$\omega = \sqrt{\frac{\left(\frac{m\pi}{L_x}\right)^2 + \left(\frac{n\pi}{L_y}\right)^2 + \left(\frac{p\pi}{L_z}\right)^2}{\mu\varepsilon}} \qquad \text{(B.10)}$$

Stationary EM field of $\text{TE}_{m,n,p}$ mode:

$$
\begin{aligned}
E_x(\mathbf{r}) &= H_0 \mu k_y\,\omega \cos(k_x x)\sin(k_y y)\sin(k_z z)\,, & \text{(B.11)}\\
E_y(\mathbf{r}) &= -H_0 \mu k_x\,\omega \sin(k_x x)\cos(k_y y)\sin(k_z z)\,, & \text{(B.12)}\\
E_z(\mathbf{r}) &= 0, & \text{(B.13)}\\
H_x(\mathbf{r}) &= -H_0 k_x k_z \sin(k_x x)\cos(k_y y)\cos(k_z z)\,, & \text{(B.14)}\\
H_y(\mathbf{r}) &= -H_0 k_y k_z \cos(k_x x)\sin(k_y y)\cos(k_z z)\,, & \text{(B.15)}\\
H_z(\mathbf{r}) &= H_0 (k_x^2 + k_y^2) \cos(k_x x)\cos(k_y y)\sin(k_z z) & \text{(B.16)}
\end{aligned}
$$

B.2 Cylindrical Resonator with PEC Boundary

Table B.2: Parameters of cylindrical resonator.

Dimensions	Radius R
	Length L
Circular-cylindrical coordinate system	$\mathbf{r} = (\rho, \varphi, z)^T$
Mode indices	Azimuthal index m
	Radial index n
	Longitudinal index p
Bessel function of m-th order	$J_m(x)$
First derivative of Bessel function of m-th order	$J'_m(x)$
n-th root of J_m	$x_{m,n}$
n-th root of J'_m	$x'_{m,n}$

B.2.1 Transverse Magnetic Modes

Wave number of $\mathrm{TM}_{m,n,p}$ mode:

$$k_T = \frac{x_{m,n}}{R} \quad , \quad k_z = \frac{p\pi}{L} \tag{B.17}$$

Resonant frequency of $\mathrm{TM}_{m,n,p}$ mode:

$$\omega = \sqrt{\frac{\left(\frac{x_{m,n}}{R}\right)^2 + \left(\frac{n\pi}{L}\right)^2}{\mu\varepsilon}} \tag{B.18}$$

Stationary EM field of $\mathrm{TM}_{m,n,p}$ mode:

$$E_\rho(\mathbf{r}) = -E_0 \frac{k_z}{k_T^2} J'_m(k_T\rho) \cos(m\varphi) \sin(k_z z) \,, \tag{B.19}$$

$$E_\varphi(\mathbf{r}) = E_0 \frac{m}{\rho} \frac{k_z}{k_T^2} J_m(k_T\rho) \sin(m\varphi) \sin(k_z z) \,, \tag{B.20}$$

$$E_z(\mathbf{r}) = E_0 J_m(k_T\rho) \cos(m\varphi) \cos(k_z z) \,, \tag{B.21}$$

$$H_\rho(\mathbf{r}) = -E_0\varepsilon \frac{m}{\rho} \frac{\omega}{k_T^2} J_m(k_T\rho) \sin(m\varphi) \cos(k_z z) \,, \tag{B.22}$$

$$H_\varphi(\mathbf{r}) = -E_0\varepsilon \frac{\omega}{k_T^2} J'_m(k_T\rho) \cos(m\varphi) \cos(k_z z) \,, \tag{B.23}$$

$$H_z(\mathbf{r}) = 0 \tag{B.24}$$

B.2.2 Transverse Electric Modes

Wave number of $\mathrm{TE}_{m,n,p}$ mode:

$$k_T = \frac{x'_{m,n}}{R} \quad , \quad k_z = \frac{p\pi}{L} \tag{B.25}$$

Resonant frequency of TE$_{m,n,p}$ mode:

$$\omega = \sqrt{\frac{\left(\frac{x'_{m,n}}{R}\right)^2 + \left(\frac{p\pi}{L}\right)^2}{\mu\varepsilon}} \tag{B.26}$$

Stationary EM field of TE$_{m,n,p}$ mode:

$$E_\rho(\mathbf{r}) = H_0\mu\frac{\omega}{k_T^2}J_m(k_T\rho)\sin(m\varphi)\sin(k_z z)\,, \tag{B.27}$$

$$E_\varphi(\mathbf{r}) = H_0\mu\frac{\omega}{k_T^2}J'_m(k_T\rho)\cos(m\varphi)\sin(k_z z)\,, \tag{B.28}$$

$$E_z(\mathbf{r}) = 0, \tag{B.29}$$

$$H_\rho(\mathbf{r}) = -H_0\frac{k_z}{k_T^2}J'_m(k_T\rho)\cos(m\varphi)\cos(k_z z)\,, \tag{B.30}$$

$$H_\varphi(\mathbf{r}) = H_0\frac{m}{\rho}\frac{k_z}{k_T^2}J_m(k_T\rho)\sin(m\varphi)\cos(k_z z)\,, \tag{B.31}$$

$$H_z(\mathbf{r}) = -H_0 J_m(k_T\rho)\cos(m\varphi)\sin(k_z z) \tag{B.32}$$

Chapter C

GST Eigenmode Results

C.1 Cylindrical Resonator with PEC Boundary

C.1.1 Longitudinal Perturbation: $TE_{0.1.p}$ and $TE_{1.1.p}$ modes

Relative error of perturbed frequencies of $TE_{0,1,p}$ and $TE_{1,1,p}$ modes (p: odd) subject to longitudinal perturbation
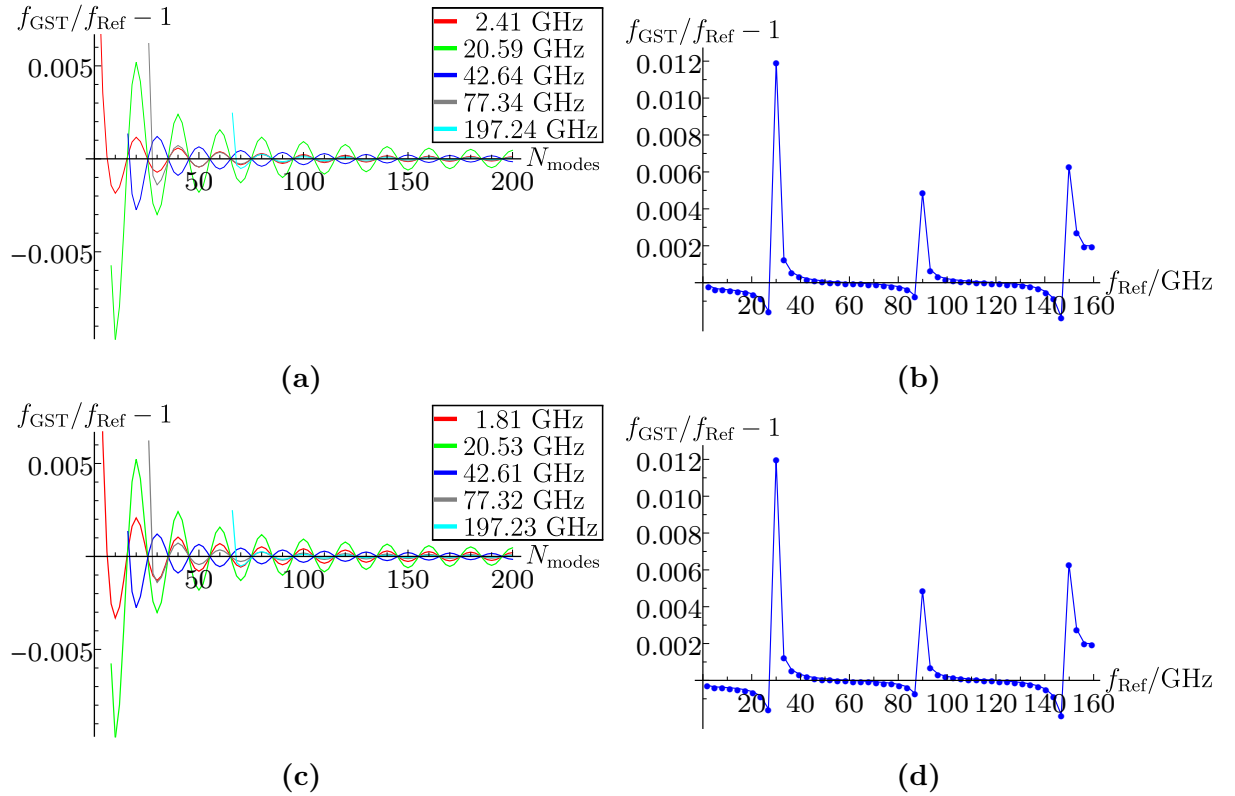
Figure C.1: Relative error of perturbed frequencies of $TE_{0,1,p}$ and $TE_{1,1,p}$ modes (p: odd) subject to longitudinal perturbation $\Delta L/L = 5\,\%$: (a), (c) Error depending on the number of unperturbed modes N_{modes} for modes of different order. (b), (d) Error depending on perturbed frequency for $N_{\mathrm{modes}} = 54$.
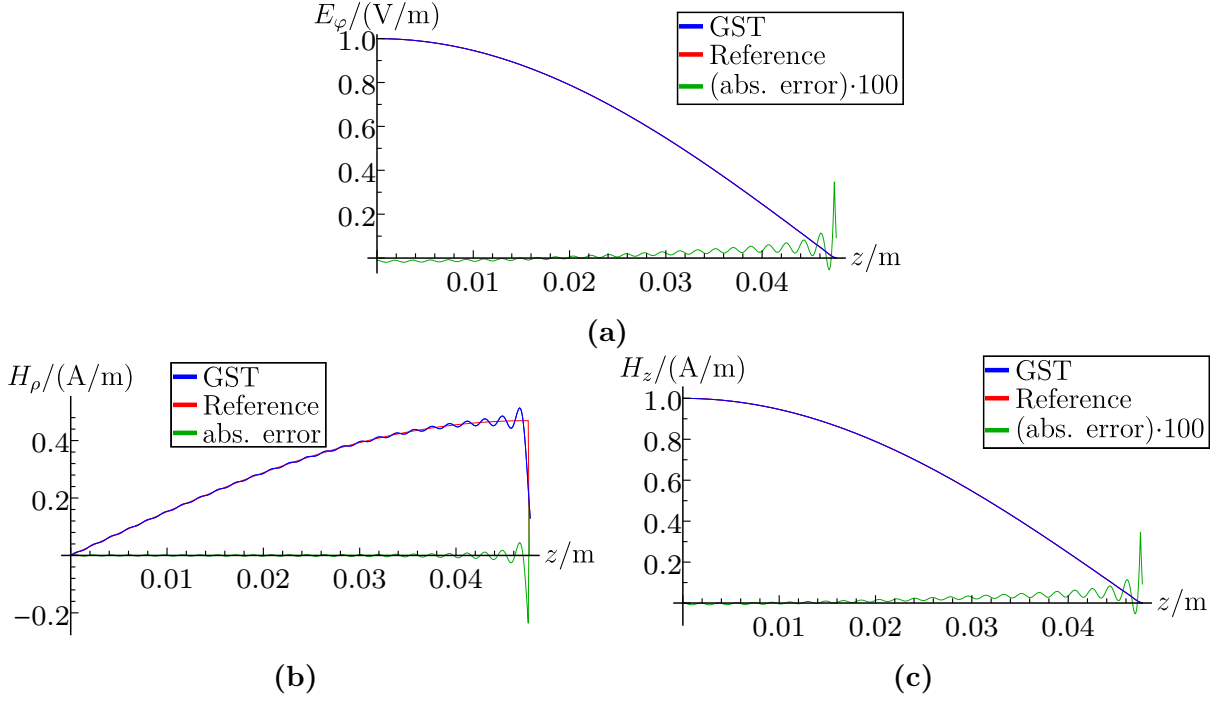
Figure C.2: Perturbed EM field of the $TE_{0,1,1}$ mode along the perturbed coordinate direction z for $\Delta L/L = 5\%$ and $N_{\text{modes}} = 54$: The field components E_ρ, E_z and H_φ are zero and therefore not displayed.
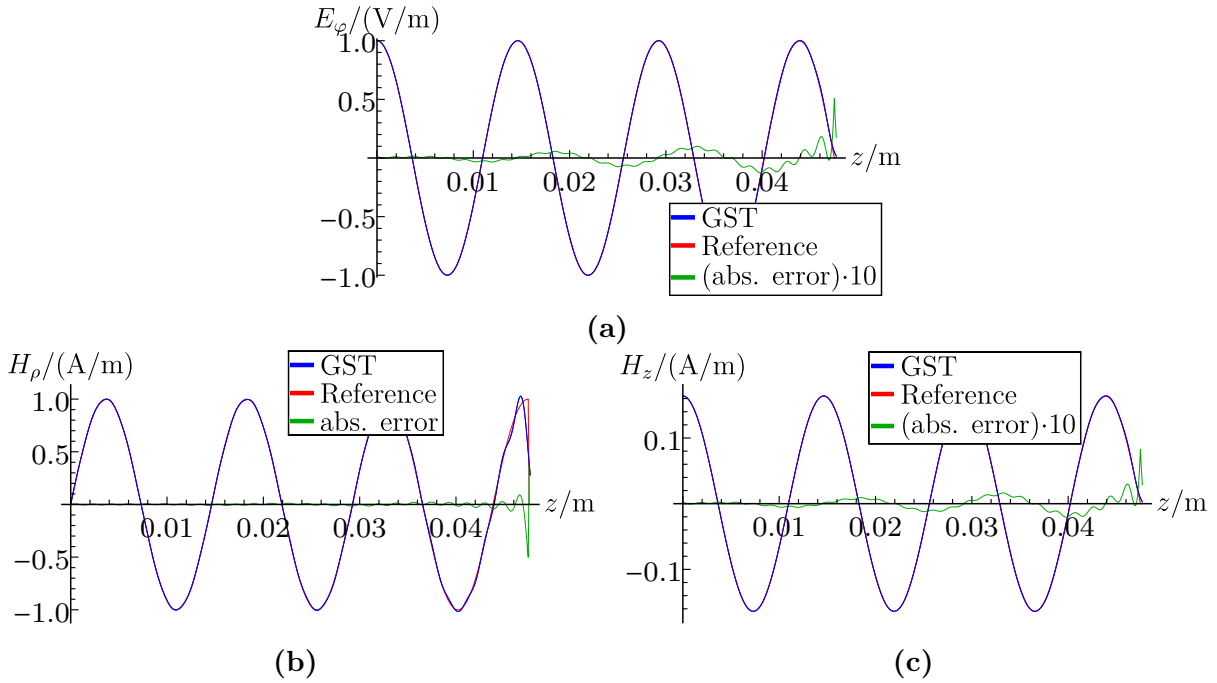
Figure C.3: Perturbed EM field of the $TE_{0,1,13}$ mode along the perturbed coordinate direction z for $\Delta L/L = 5\%$ and $N_{\text{modes}} = 54$: The field components E_ρ, E_z and H_φ are zero and therefore not displayed.
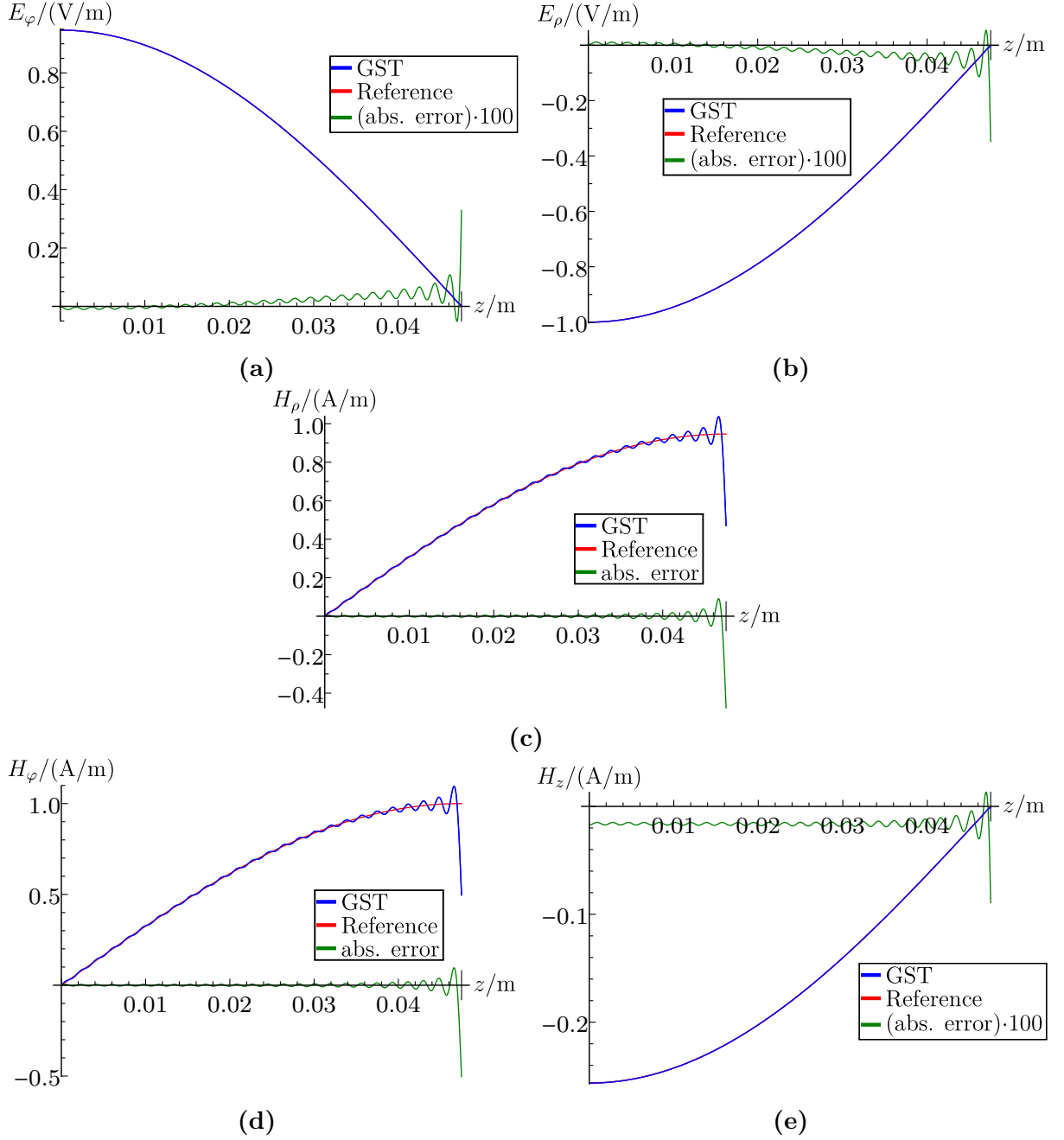
Figure C.4: Perturbed EM field of the $TE_{1,1,1}$ mode along the perturbed coordinate direction z for $\Delta L/L = 5\,\%$ and $N_{\text{modes}} = 54$: The field components E_z is zero and therefore not displayed.
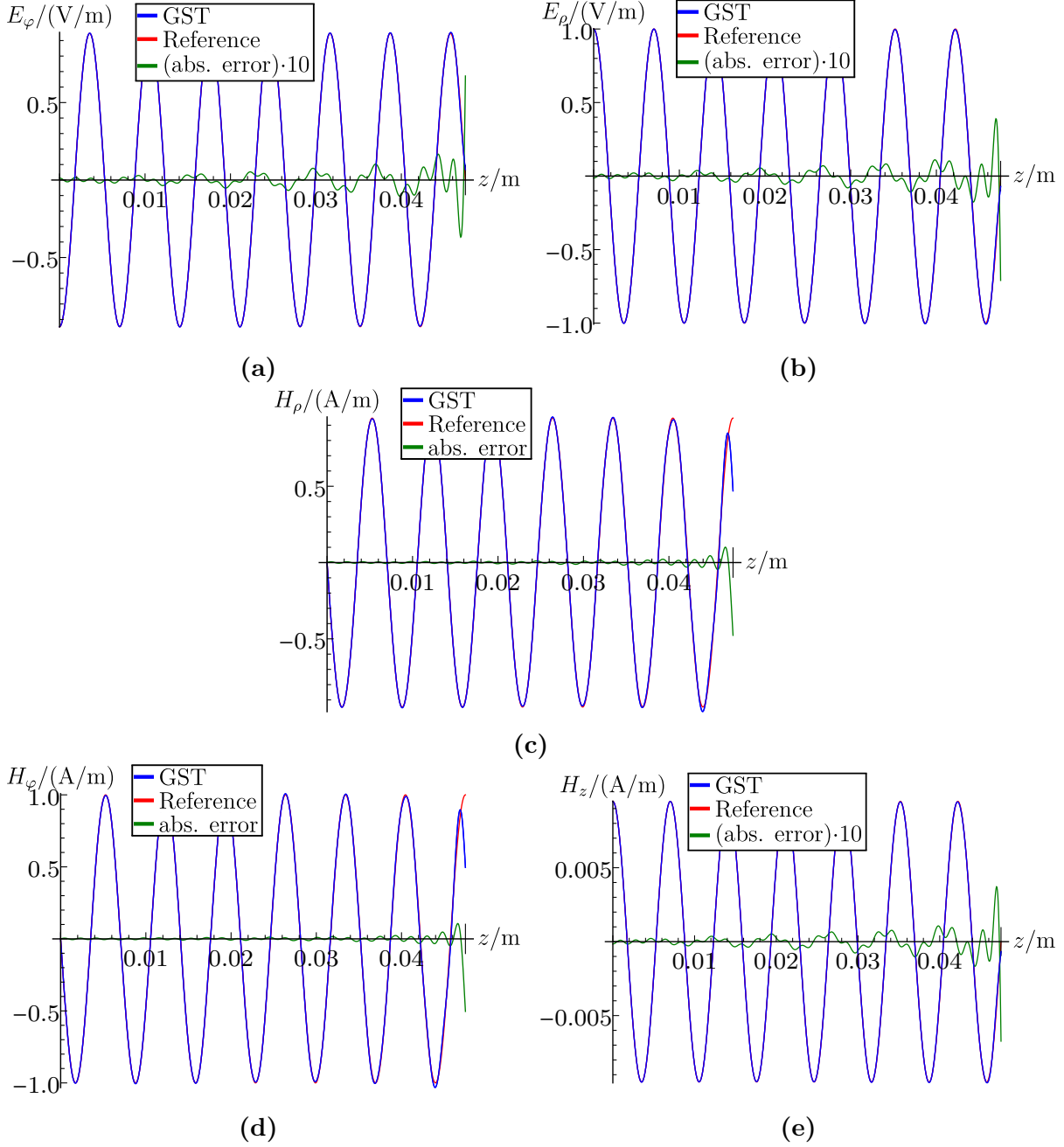
Figure C.5: Perturbed EM field of the $TE_{1,1,27}$ mode along the perturbed coordinate direction z for $\Delta L/L = 5\%$ and $N_{\mathrm{modes}} = 54$: The field components E_z is zero and therefore not displayed.

C.2 Elliptical Single-Cell PEC Resonator

C.2.1 Required Volume Element Discretization for IA Terms

Table C.1: Number N_{elem} of cylindrical ring elements depending on the radial step size $\Delta\rho$ and extent of an equator radius perturbation: For adequately fine step sizes additionally the reduced number of elements resulting from a combination of small adjacent elements (see section 4.2.2) is stated.

| Step size | Reduction of R_{eq} by 10 % | | Reduction of R_{eq} by 5 % | | Reduction of R_{eq} by 1 % | |
$\Delta\rho$/mm	N_{elem}	N_{elem} (comb.)	N_{elem}	N_{elem} (comb.)	N_{elem}	N_{elem} (comb.)
2.5	6023	-	4122	-	2577	-
1.75	16029	15135	10367	-	5588	-
1.25	40342	38356	25044	22236	12024	9686
1	-	-	45089	40967	20167	16698
0.8	-	-	-	-	34725	19858
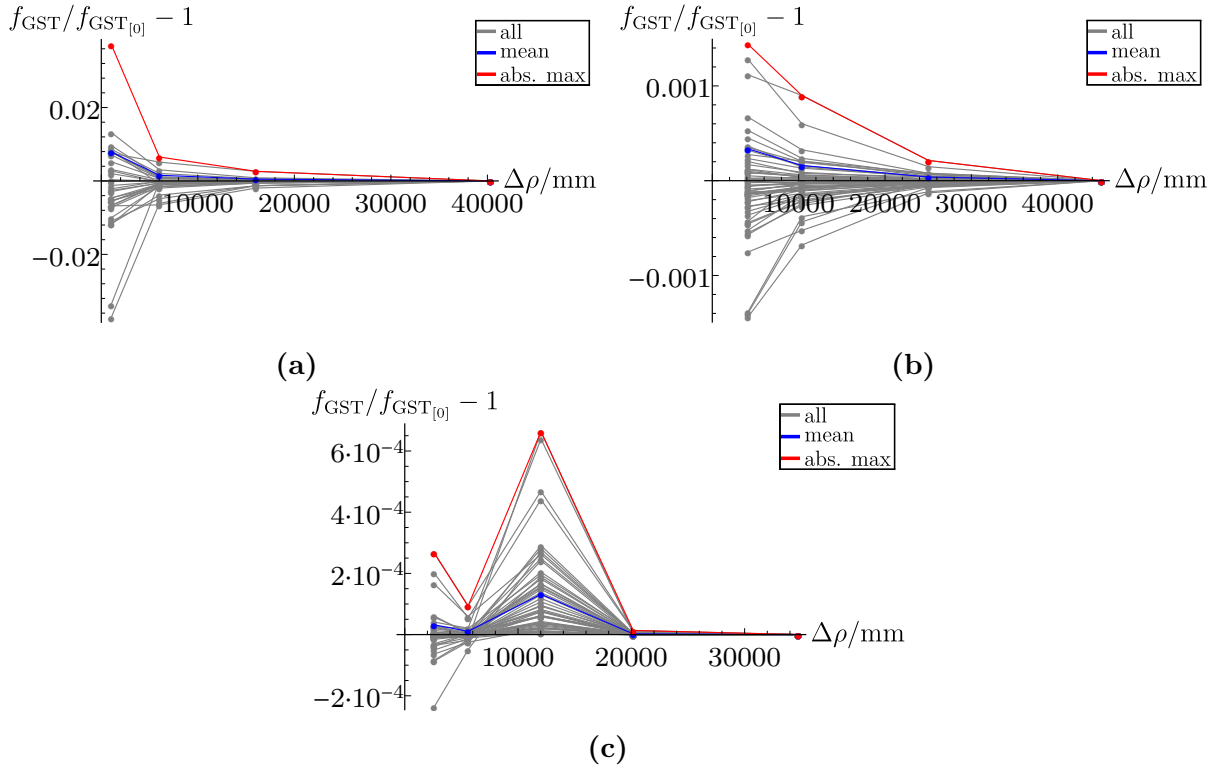
Figure C.6: Relative change of perturbed GST frequencies depending on the number N_{elem} of volume elements (compared to GST frequency with finest discretization): Each subfigure shows the changes for the first 70 TM$_0$-like modes within 1.24–20.53 GHz as well as their mean and maximal changing values. Irregular complex modes are not included. (a) Reduction of equator R_{eq} by 10 %. (b) Reduction of R_{eq} by 5 %. (c) Reduction of R_{eq} by 1 %.
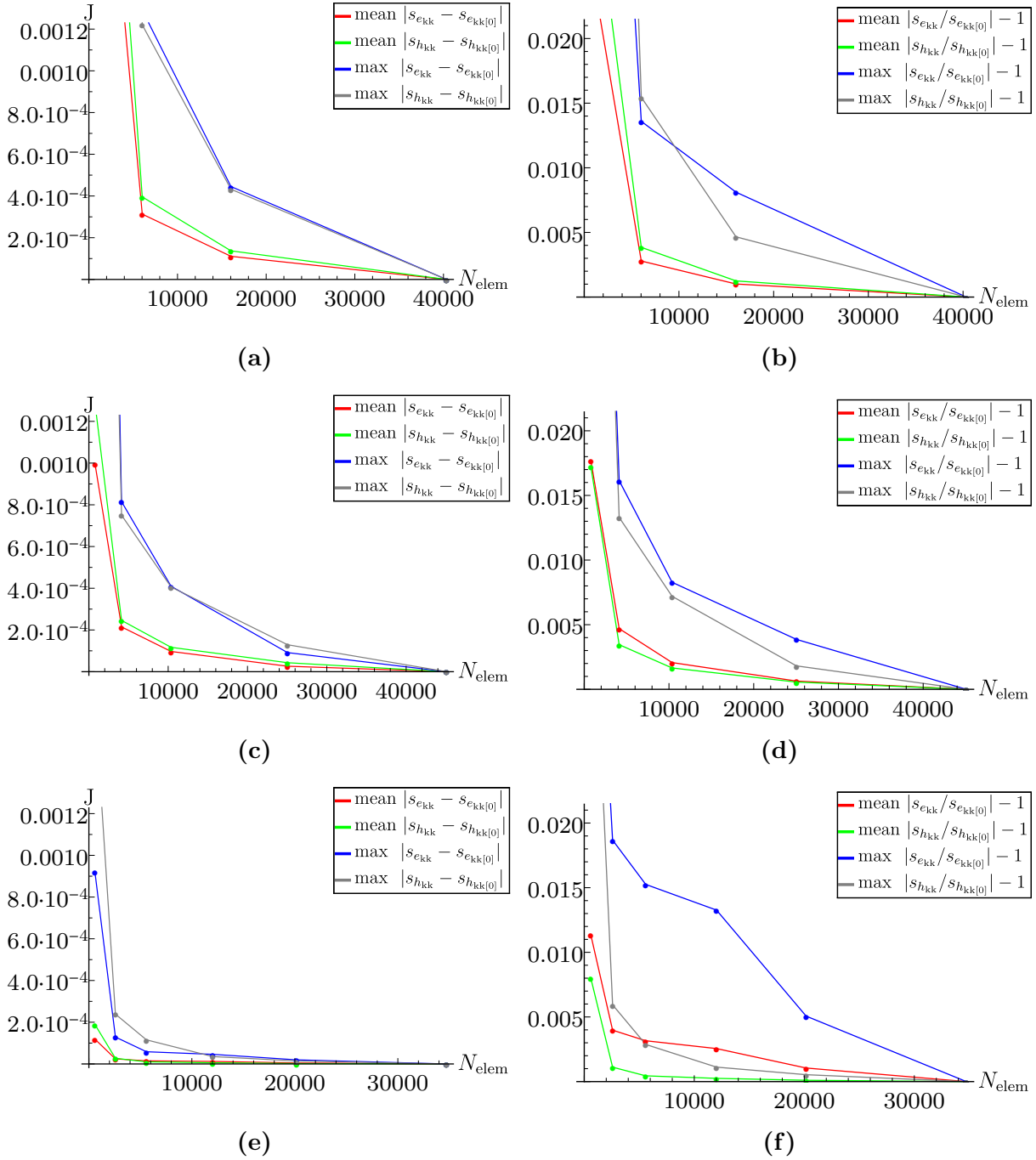
Figure C.7: Absolute and relative change of electric and magnetic interaction terms depending on the number N_{elem} of volume elements (compared to IA terms with finest discretization): Each subfigure shows the mean and maximal value of the changes for the first 70 unperturbed TM_0-like modes within 1.24–20.53 GHz. (a), (b) Reduction of R_{eq} by 10 %. (c), (d) Reduction of R_{eq} by 5 %. (e), (f) Reduction of R_{eq} by 1 %.

C.2.2   Convergence Depending on Number of Modes
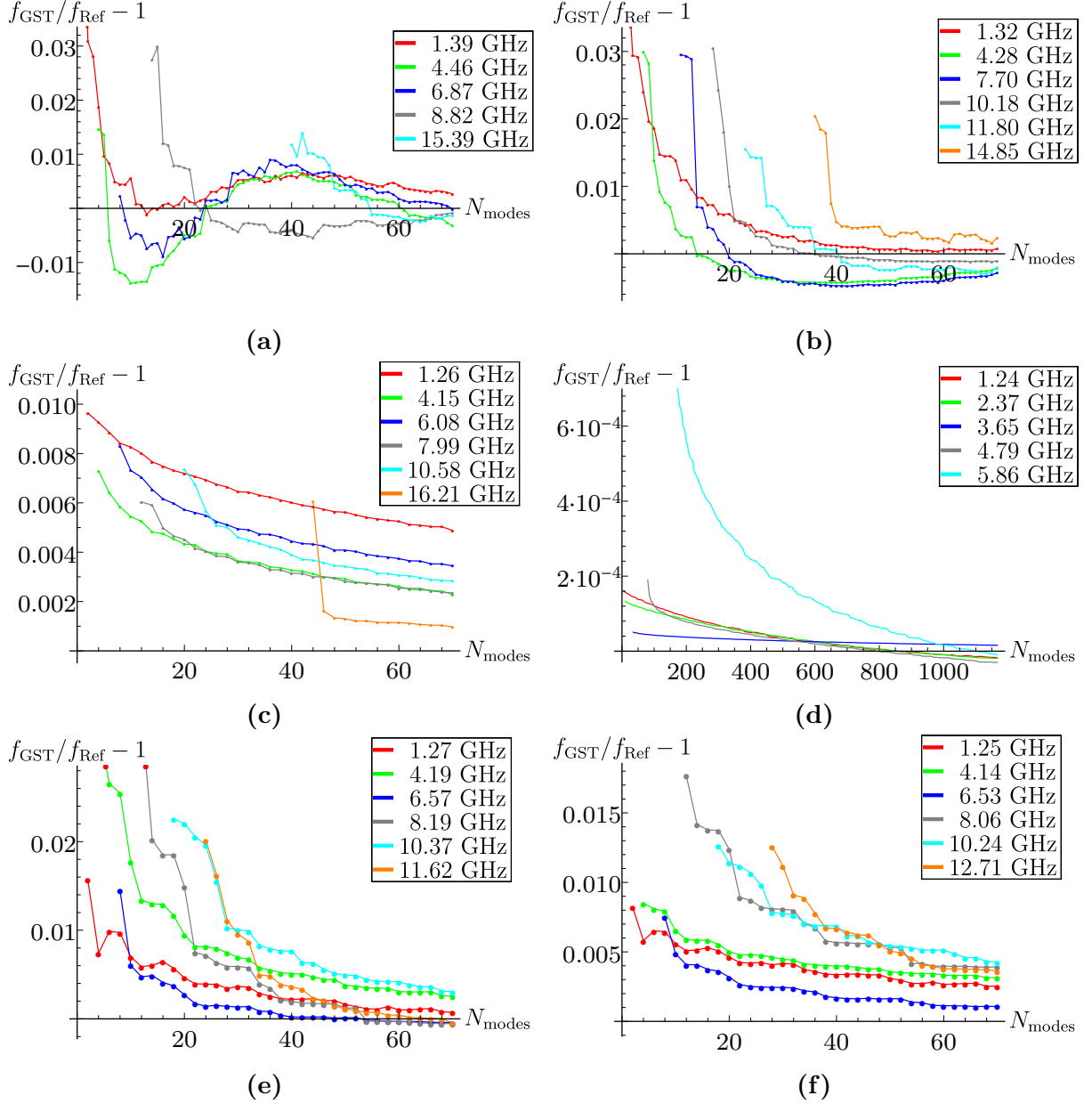
Figure C.8: Relative frequency error depending on the number N_{modes} of unperturbed modes for TM_0-like modes for different perturbations. (a) Equator reduction of 10 %. (b) Equator reduction of 5 %. (c) Equator reduction of 1 %. (d) 10 % dent. (e) Cell width reduction of 10 %. (f) Cell width reduction of 5 %.

C.2.3 Frequency Accuracy Depending on Perturbed Frequency
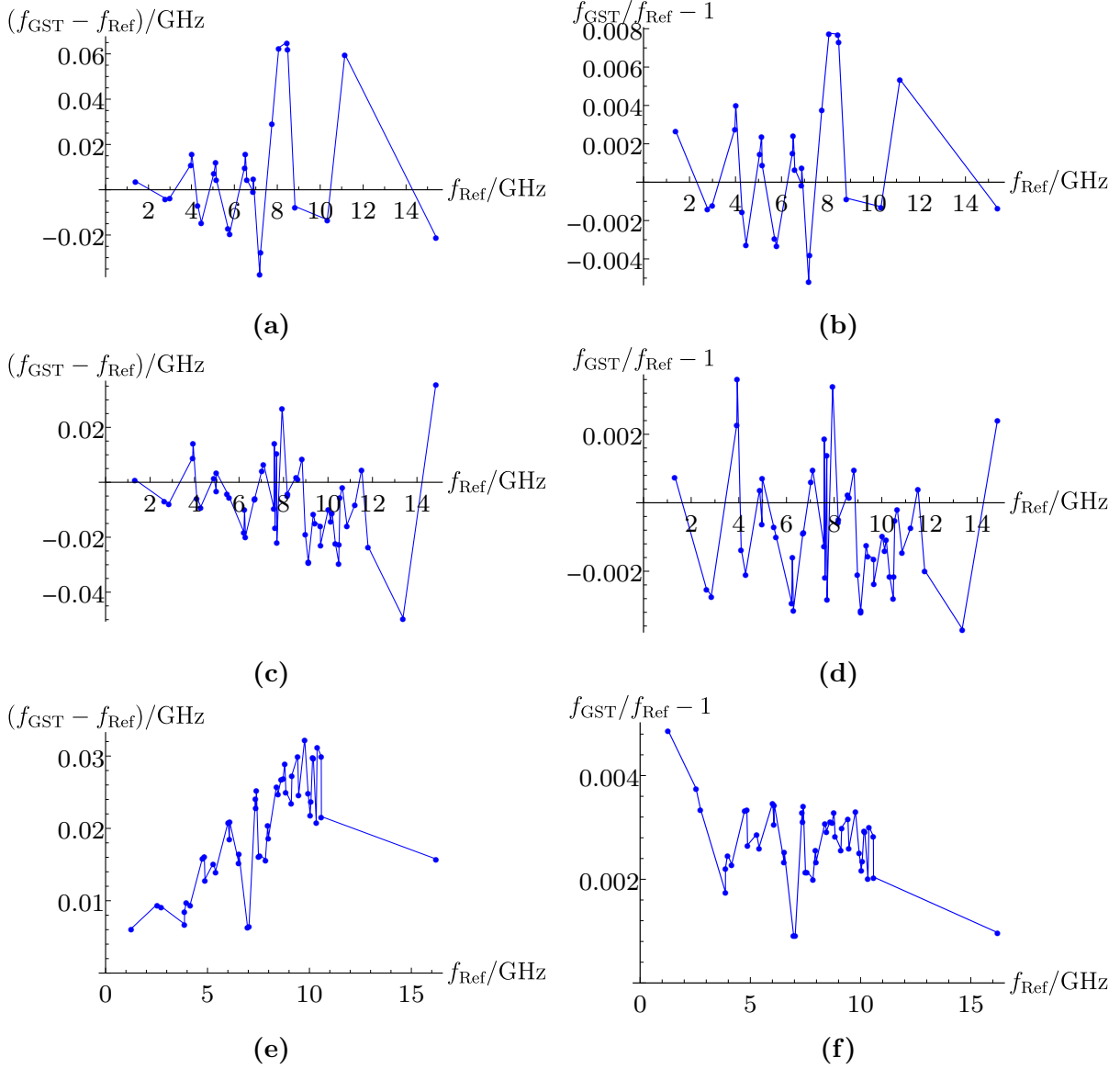
Figure C.9: Absolute and relative frequency error depending on perturbed frequency f_{Ref} for a selection of TM_0-like and quadrupole modes for different equator perturbations. (a), (b) Reduction of R_{eq} by 10 %. (c), (d) Reduction of R_{eq} by 5 %. (e), (f) Reduction of R_{eq} by 1 %.
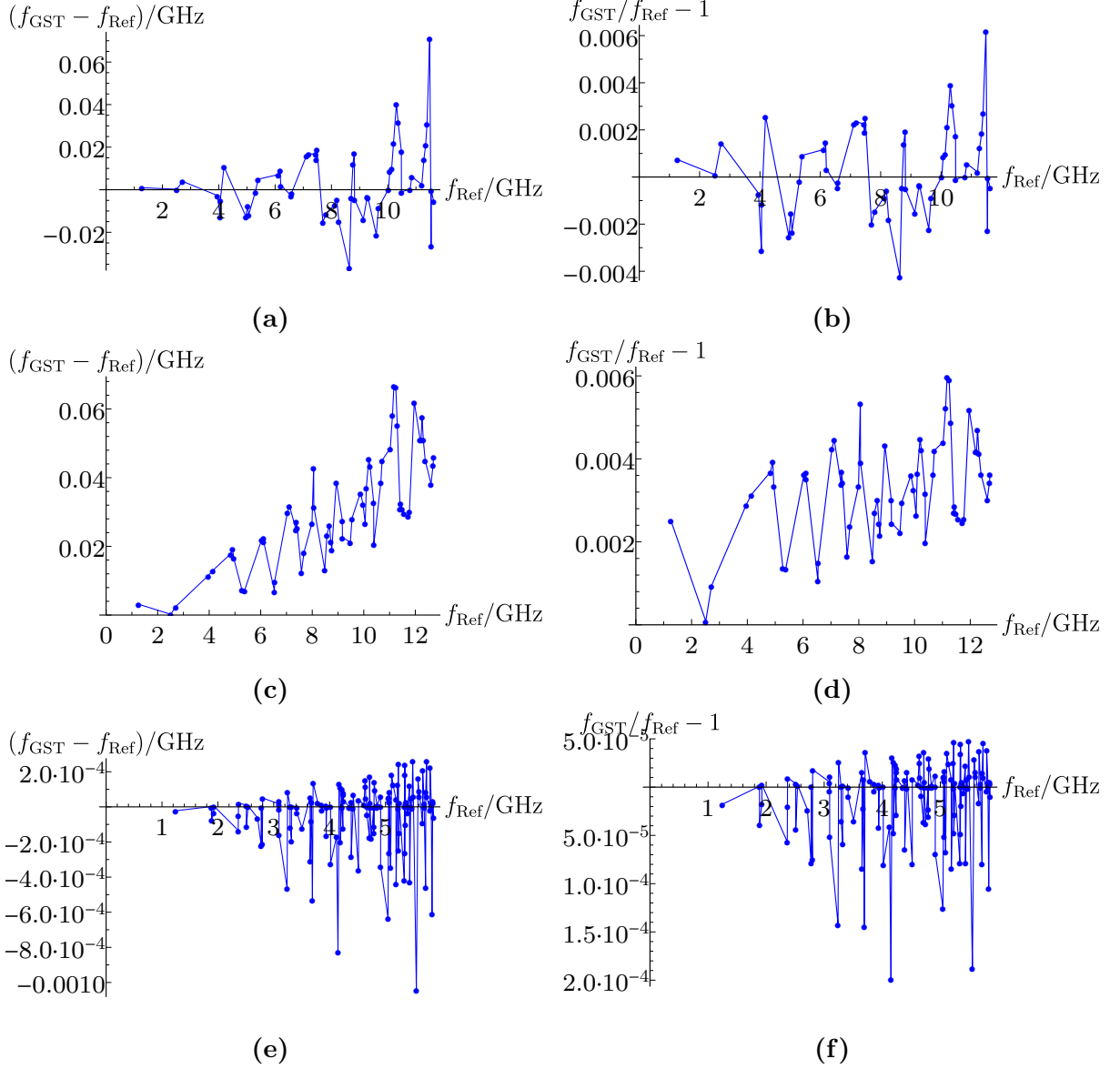
Figure C.10: Absolute and relative frequency error depending on perturbed frequency f_{Ref} for a selection of modes for different equator perturbations. (a), (b) Cell width reduction of $10\,\%$. (c), (d) Cell width reduction of $5\,\%$. (e), (f) $10\,\%$ dent.

C.2.4 Selected Electromagnetic Fields

C.2.4.1 Regular GST Fields
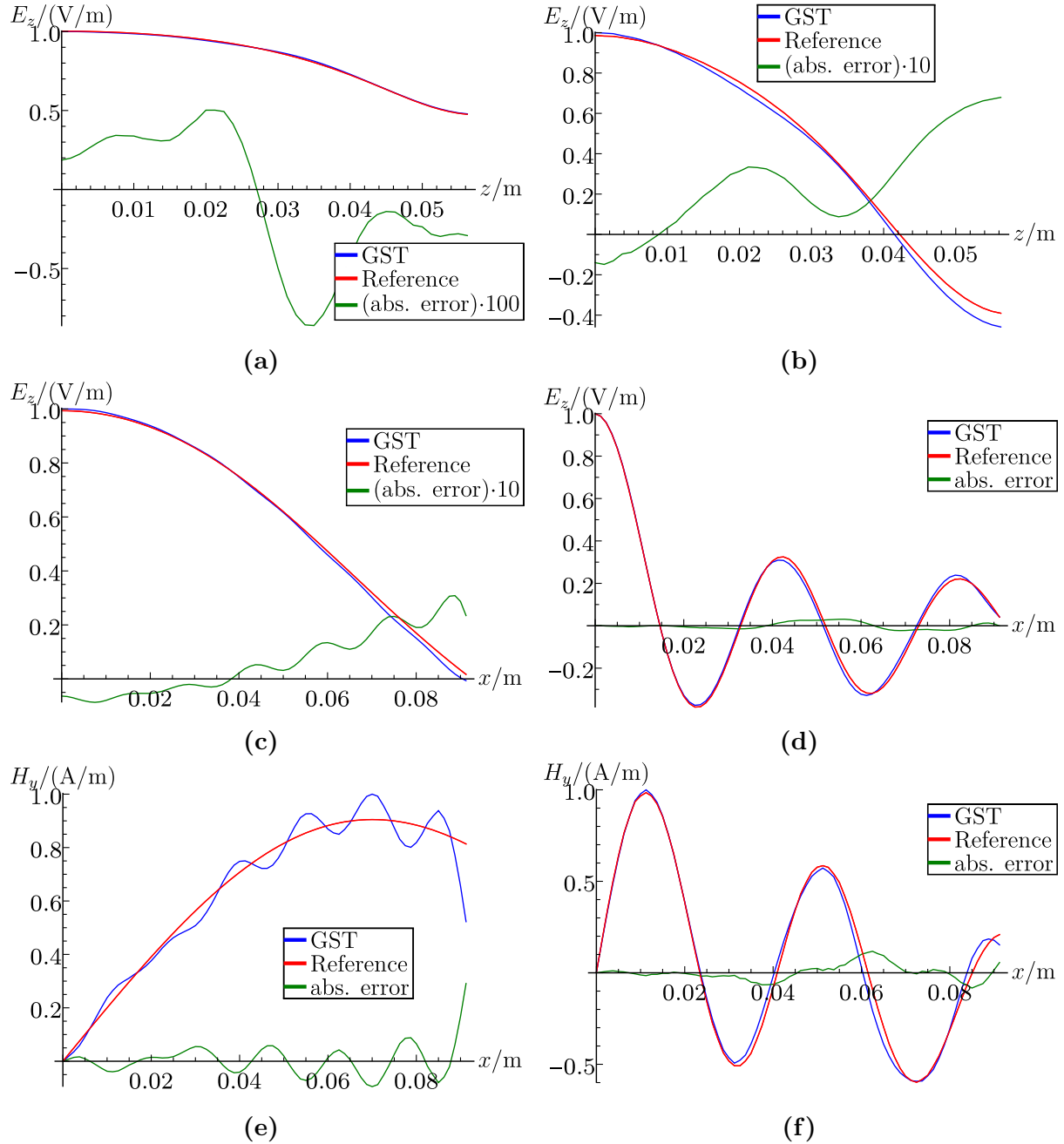

Figure C.11: Perturbed EM fields of TM_0-like modes along the x- and z-axis for a reduction of R_{eq} by 10% and $N_{modes} = 70$: Non-displayed field components are zero. (a), (c), (e) Fundamental mode at $1.39\,GHz$. (b), (d), (f) Mode at $8.07\,GHz$.
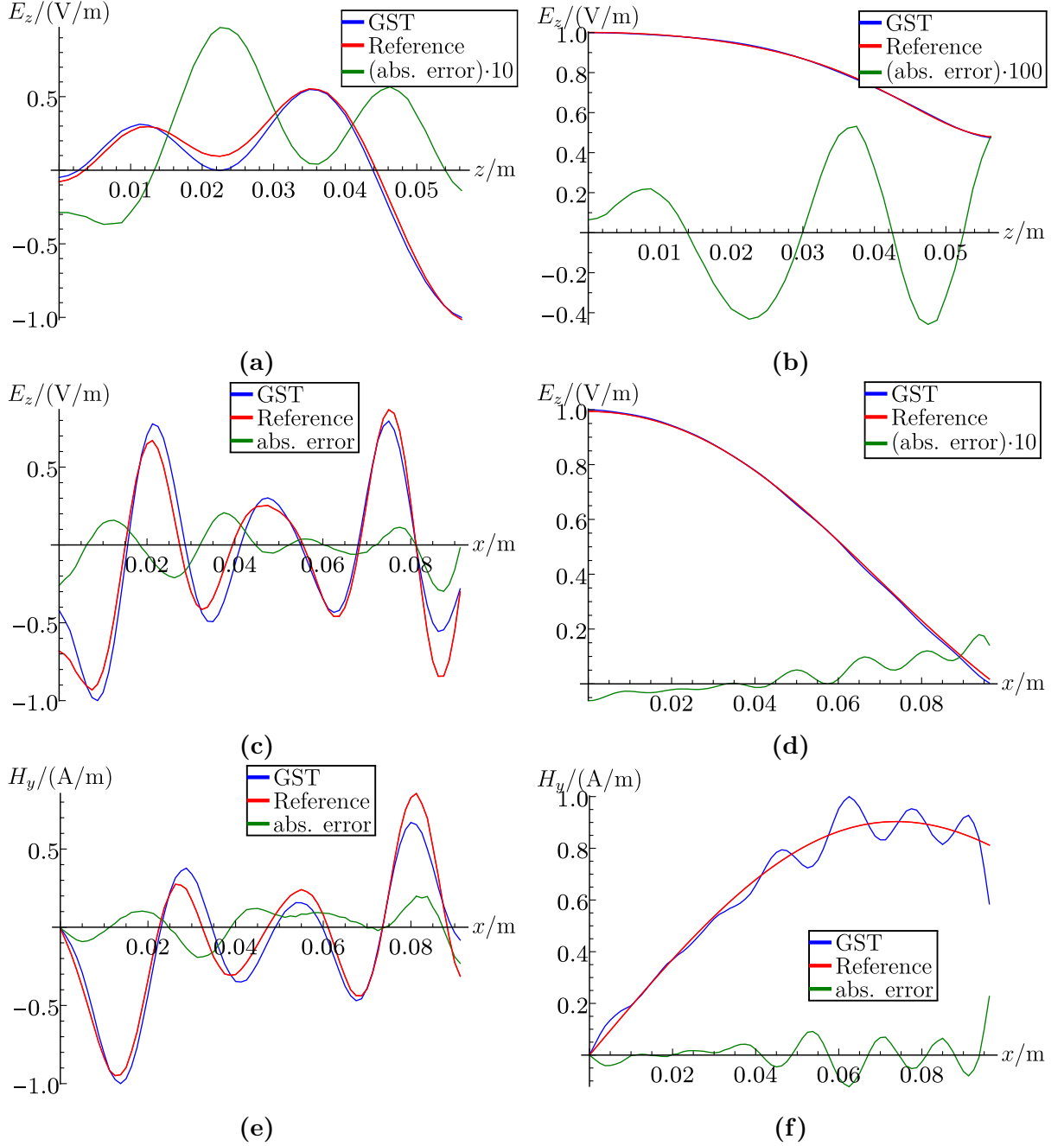
Figure C.12: Perturbed EM fields of TM_0-like modes along the x- and z-axis for $N_{\mathrm{modes}} = 70$: Non-displayed field components are zero. (a), (c), (e) Mode at $15.39\,\mathrm{GHz}$ for a reduction of R_{eq} by $10\,\%$. (b), (d), (f) Fundamental mode at $1.32\,\mathrm{GHz}$ for a reduction of R_{eq} by $5\,\%$.
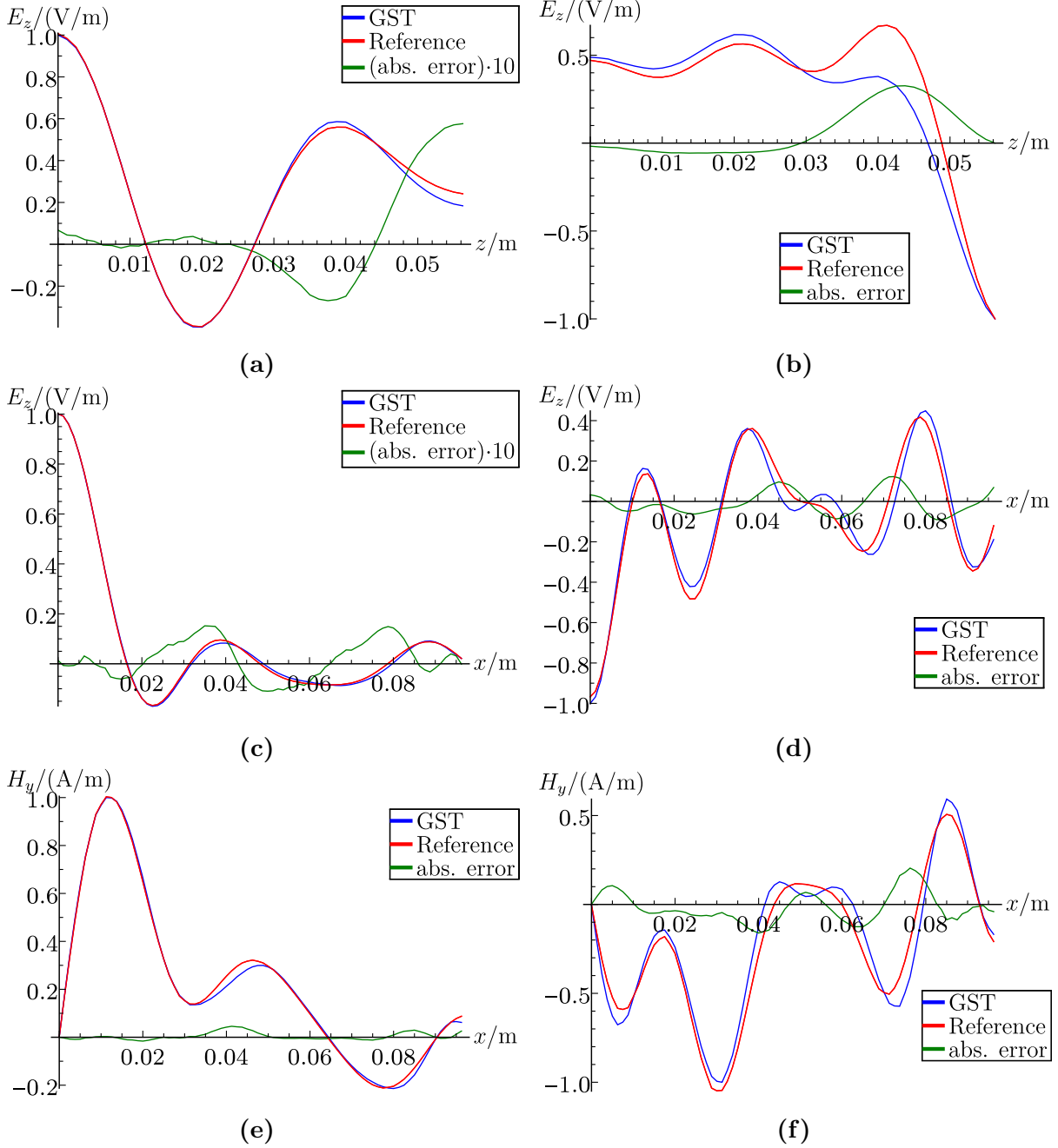
Figure C.13: Perturbed EM fields of TM$_0$-like modes along the x- and z-axis for a reduction of R_{eq} by 5% and $N_{\mathrm{modes}} = 70$: Non-displayed field components are zero. (a), (c), (e) Mode at $10.18\,\mathrm{GHz}$. (b), (d), (f) Mode at $13.37\,\mathrm{GHz}$.
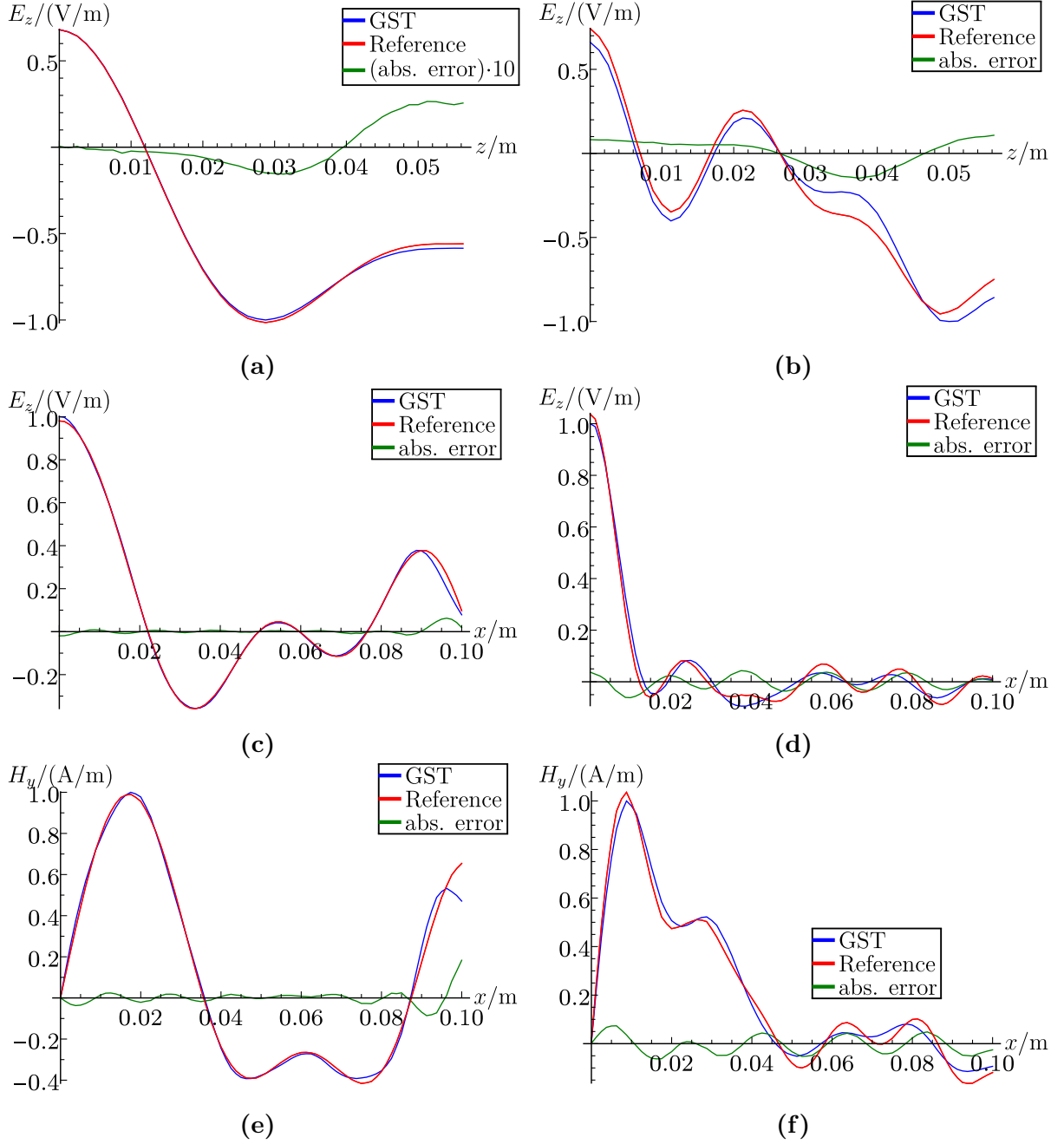
Figure C.14: Perturbed EM fields of TM$_0$-like modes along the x- and z-axis for a reduction of R_{eq} by 1% and $N_{\mathrm{modes}} = 70$: Non-displayed field components are zero. (a), (c), (e) Mode at $7.99\,\mathrm{GHz}$. (b), (d), (f) Mode at $16.21\,\mathrm{GHz}$.
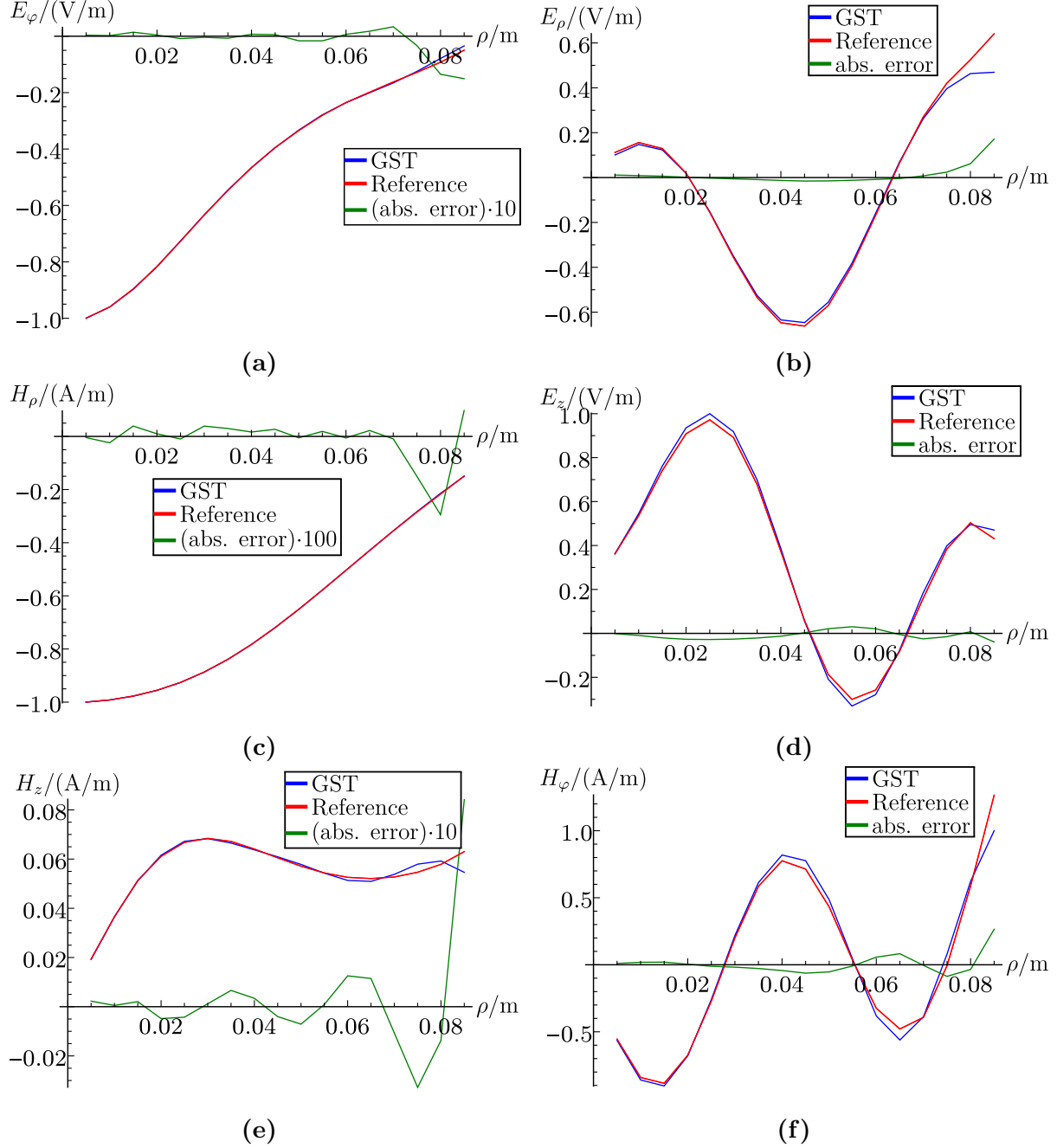
Figure C.15: Perturbed EM fields along radial direction ρ towards center of perturbation for a 10 % dent and $N_{\text{modes}} = 1167$: Non-displayed field components are zero. (a), (c), (e) Dipole mode at 1.89 GHz. (b), (d), (f) Quadrupole mode at 5.86 GHz.

C.2.4.2 Irregular GST Fields

(a)

(b)

(c)
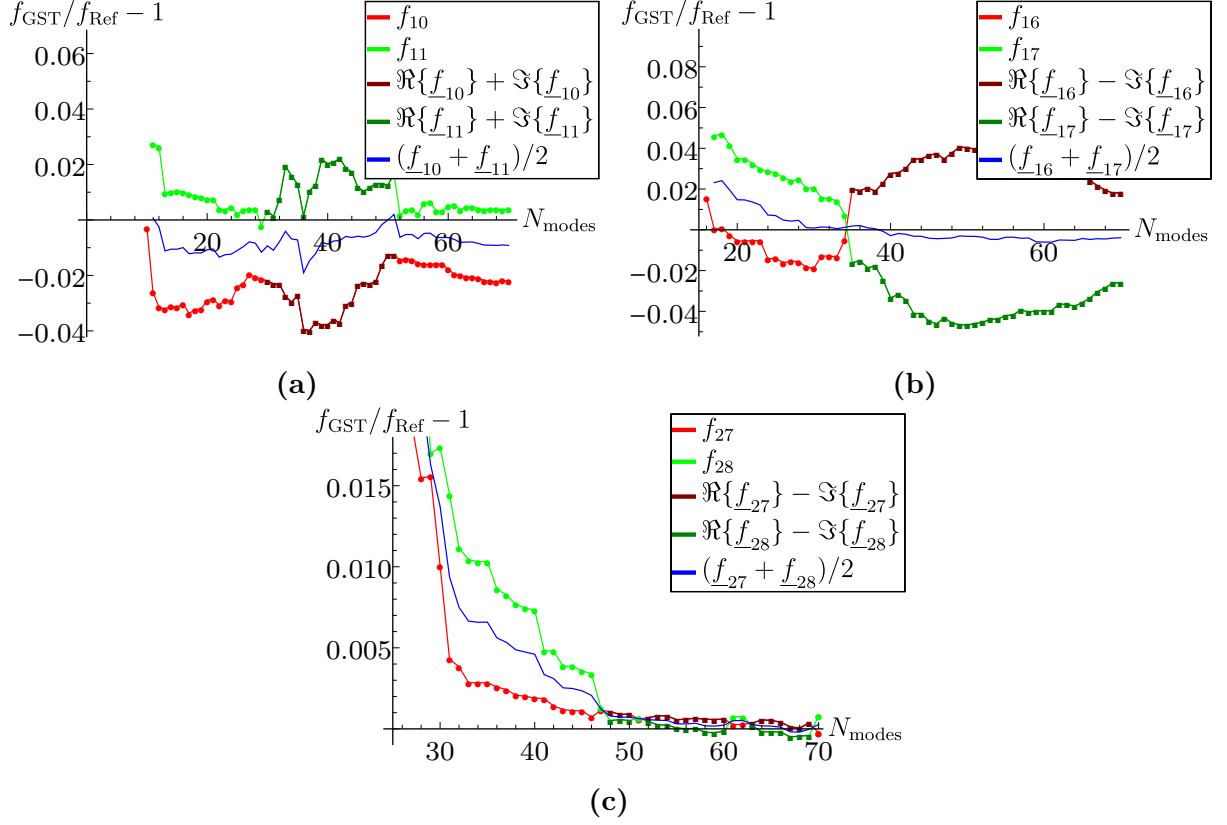
Figure C.16: Relative frequency error of irregular TM_0-like mode pairs depending on the number N_{modes} of unperturbed modes for different equator perturbations. (a) First irregular mode at $7.76\,\mathrm{GHz}$ for a reduction of $10\,\%$. (b) Second irregular mode at $9.65\,\mathrm{GHz}$ for a reduction of $10\,\%$. (c) First irregular mode at $13.00\,\mathrm{GHz}$ for a reduction of $5\,\%$.
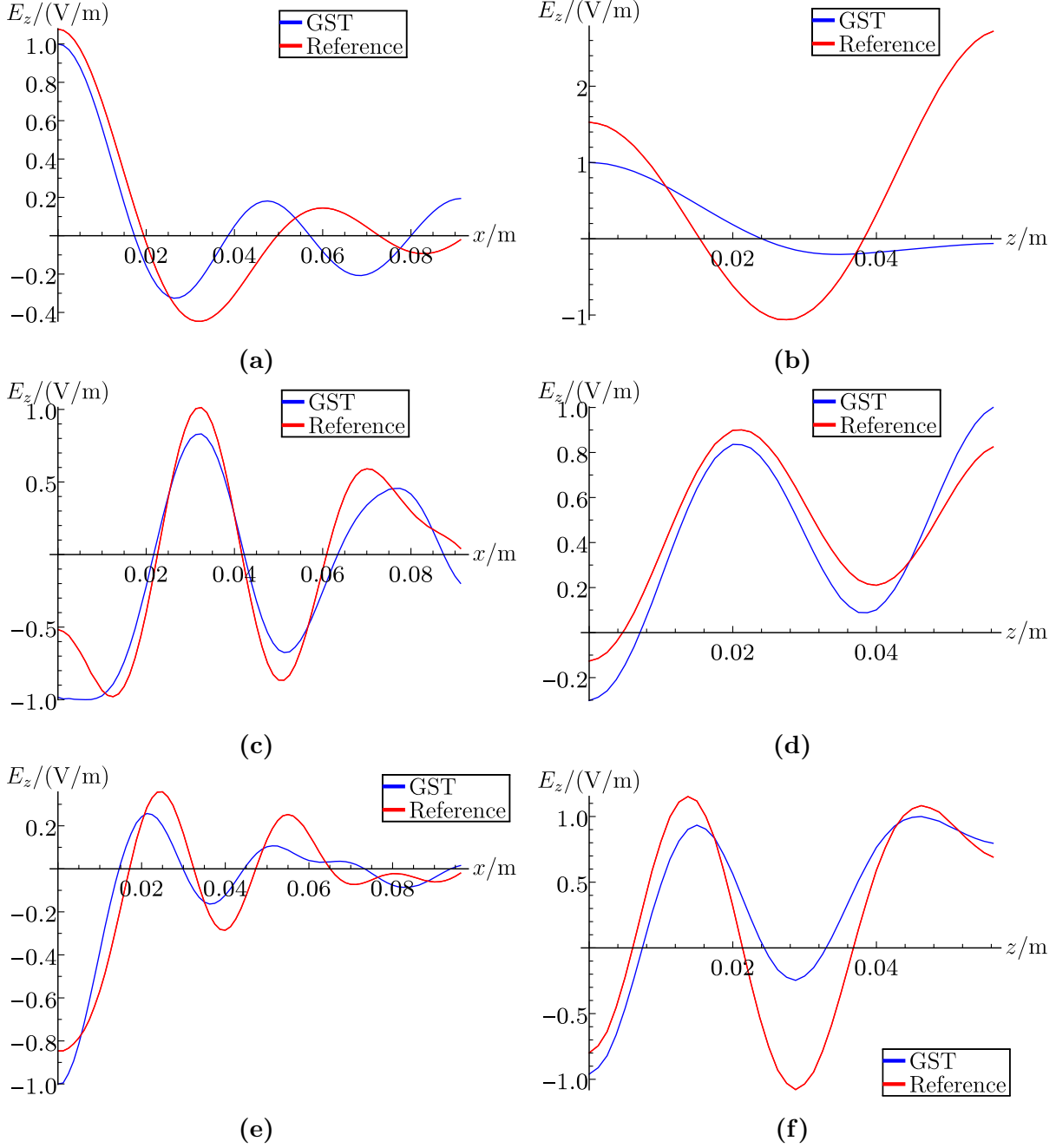
Figure C.17: Electric fields of irregular TM_0-like GST modes along the x- and z-axis for an equator reduction: Non-displayed field components are zero. (a), (b) First irregular mode at $7.76\,\mathrm{GHz}$ for a reduction of $10\,\%$. (c), (d) Second irregular mode at $9.65\,\mathrm{GHz}$ for a reduction of $10\,\%$. (e), (f) First irregular mode at $13.00\,\mathrm{GHz}$ for a reduction of $5\,\%$.

C.3 Elliptical seven-Cell bERLinPro Resonator

C.3.1 Resonator Parameters

Table C.2: End-cell shape parameters of the eight final design candidates C1 to C8 in the positive (e_+) and negative (e_-) longitudinal coordinate range.

| Candidate	Shape parameter in mm						
	R_{eq}	R_{iris}	L_{cell}	$x_{Ell,eq}$	$y_{Ell,eq}$	$x_{Ell,iris}$	$y_{Ell,iris}$
C1 (e_-)	102.8797	36	114.471	38.9516	35.0838	12.533	24.1615
C1 (e_+)	102.8797	36	117.492	41.8026	40.1715	12.533	24.1615
C2 (e_-)	102.8797	36	114.659	39.0114	35.0313	12.533	24.1615
C2 (e_+)	102.8797	36	117.414	41.7843	40.137	12.533	24.1615
C3 (e_-)	102.8797	36	114.689	39.0312	35.1895	12.533	24.1615
C3 (e_+)	102.8797	36	117.37	41.7342	40.1612	12.533	24.1615
C4 (e_-)	102.8797	36	114.414	38.9167	35.1253	12.533	24.1615
C4 (e_+)	102.8797	36	117.48	41.7272	40.1041	12.533	24.1615
C5 (e_-)	102.8797	36	114.536	39.2462	35.7844	12.533	24.1615
C5 (e_+)	102.8797	36	118.463	42.262	40.5968	12.533	24.1615
C6 (e_-)	102.8797	36	114.56	39.1314	35.5214	12.533	24.1615
C6 (e_+)	102.8797	36	118.517	42.4123	40.9864	12.533	24.1615
C7 (e_-)	102.8797	36	113.351	39.0463	36.334	12.533	24.1615
C7 (e_+)	102.8797	36	116.275	41.0051	39.2022	12.533	24.1615
C8 (e_-)	102.8797	36	114.066	39.3179	36.39	12.533	24.1615
C8 (e_+)	102.8797	36	117.175	41.5854	39.9098	12.533	24.1615

C.3.2 Frequency Accuracy Depending on Perturbed Frequency
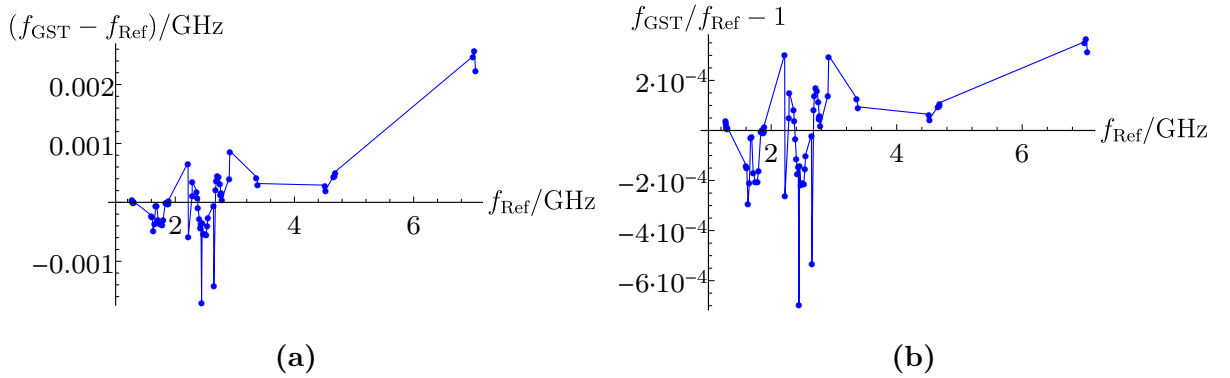
Figure C.18: Absolute and relative frequency error depending on perturbed frequency f_{Ref} for a selection of 65 TM_0-like, dipole and sextupole modes for candidate C1 based on segment-wise adjusted GST.

C.3.3   Selected Electromagnetic Fields

C.3.3.1   Accuracy of GST Fields with Adjusted Interaction Terms
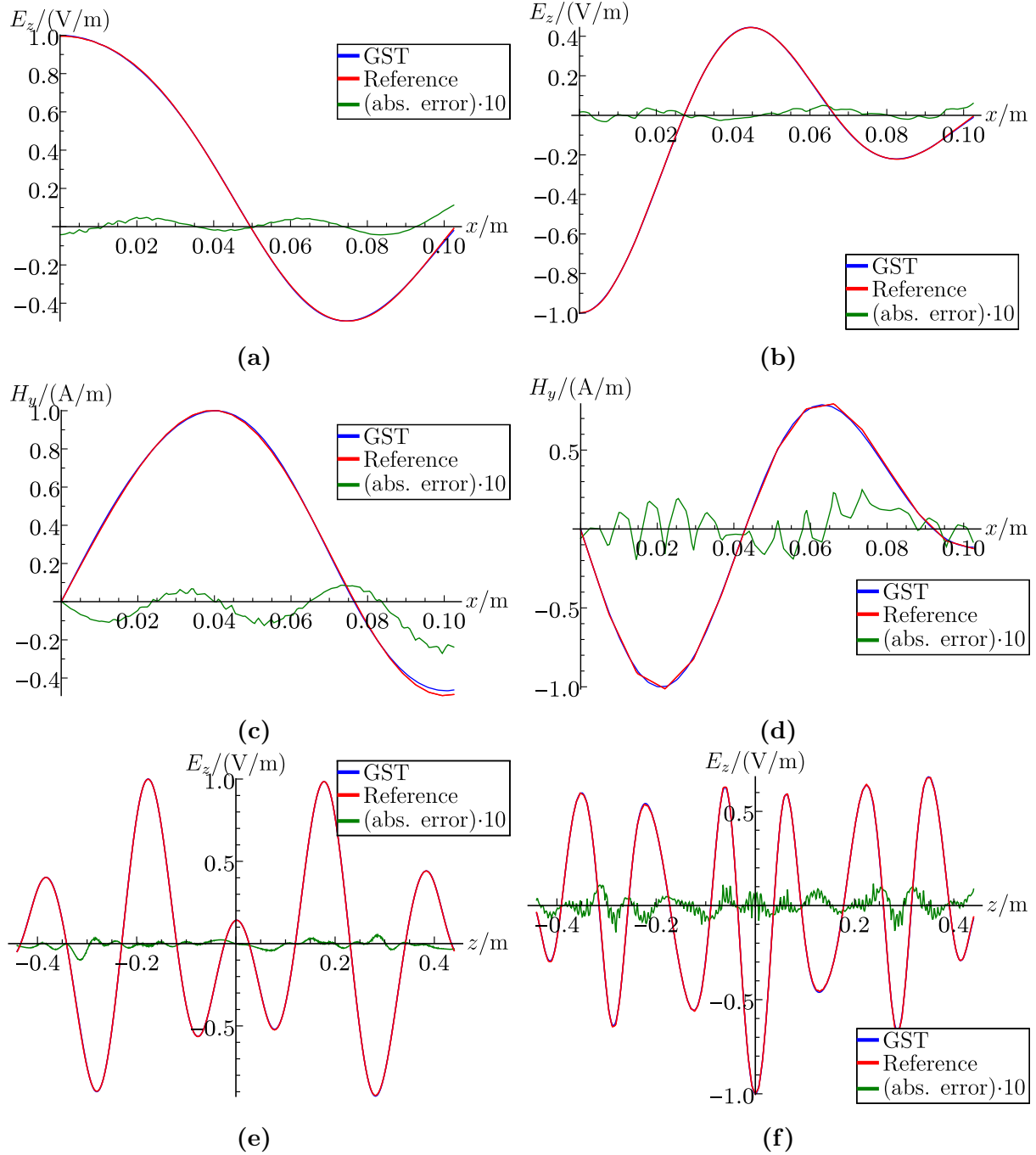
Figure C.19: EM fields along the x- and z-axis for candidate C1 ($N_{\text{modes}} = 146$): Non-displayed field components are zero. (a), (c), (e): TM$_0$-like HOM at 3.38 GHz. (b), (d), (f): TM$_0$-like HOM at 4.66 GHz.
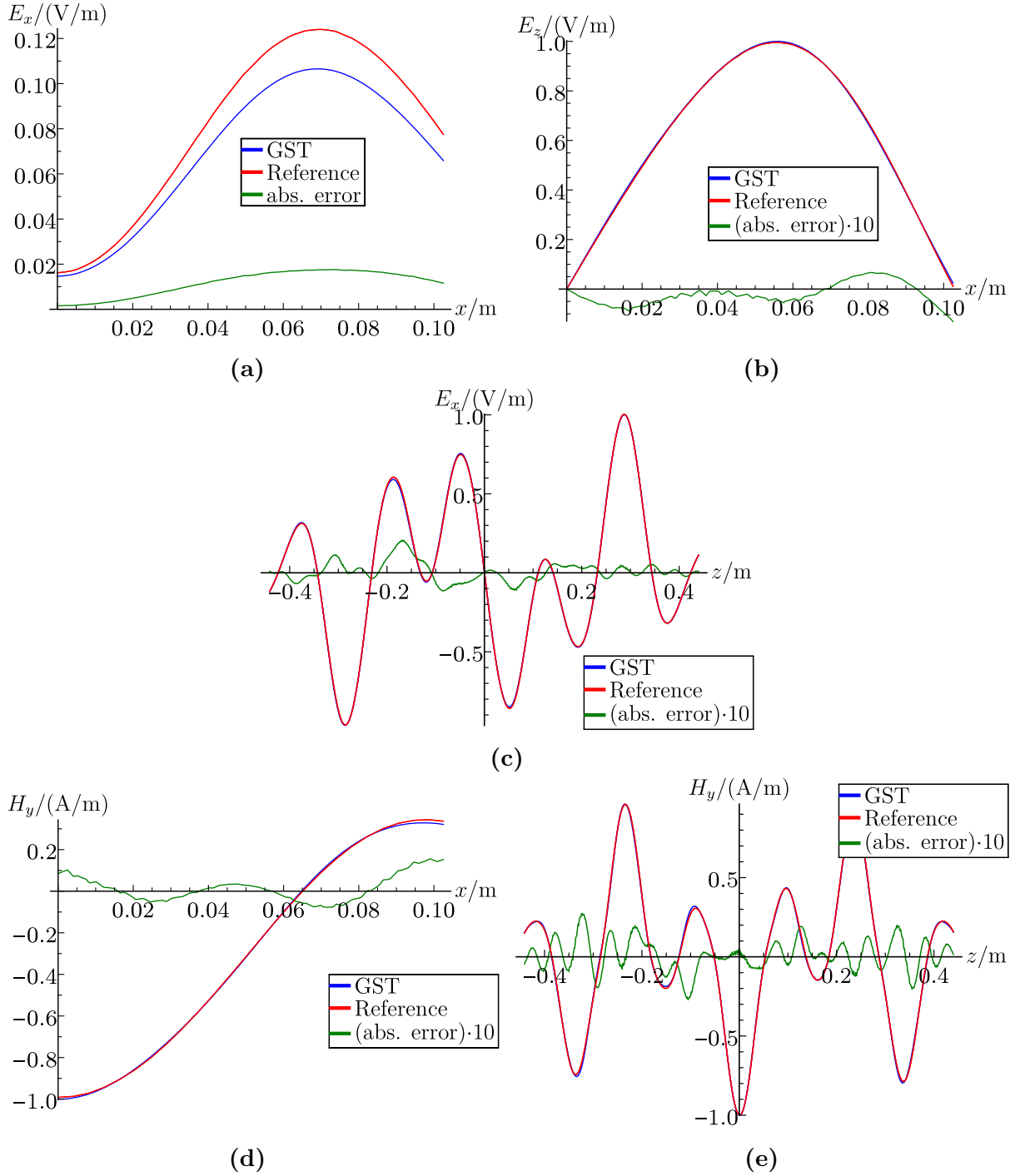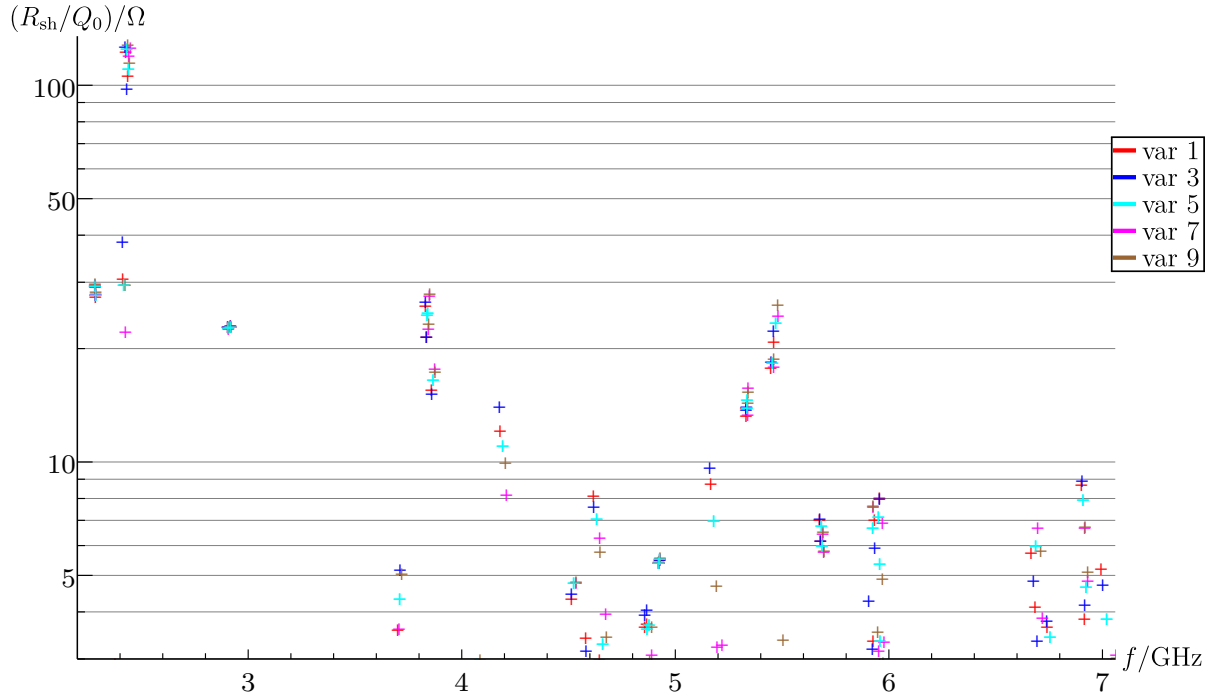
Figure C.20: EM field of dipole mode at $2.50\,\mathrm{GHz}$ along the x- and z-axis for candidate C1 ($N_\mathrm{modes} = 254$): Non-displayed field components are zero.
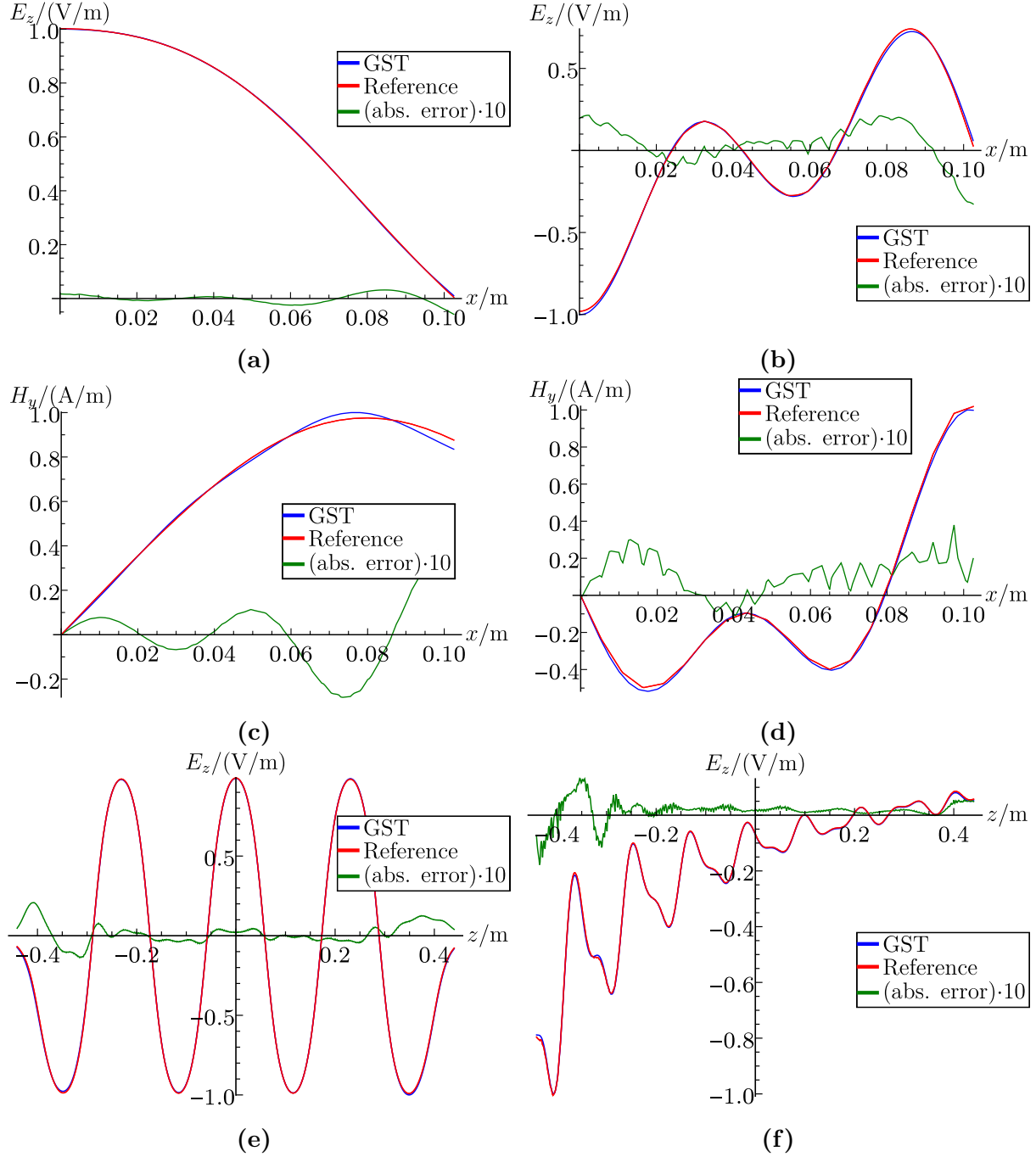
Figure C.21: EM fields along the x- and z-axis for candidate C5 ($N_{\mathrm{modes}} = 146$): Non-displayed field components are zero. (a), (c), (e): $\mathrm{TM}_{0,1,0_\pi}$-like accelerating mode at $1.30\,\mathrm{GHz}$. (b), (d), (f): TM_0-like HOM at $5.20\,\mathrm{GHz}$.

C.3.4   R-over-Q values

C.3.4.1   Geometric Imperfections

Figure C.22: On-axis R-over-Q values of TM_0-like HOMs up to a frequency of $7.04\,GHz$ for candidate C3 subject to different uniform geometric imperfections. The $TM_{0,1,0}$-like band is not included and only modes with an R-over-Q values of at least $3\,\Omega$ are plotted.
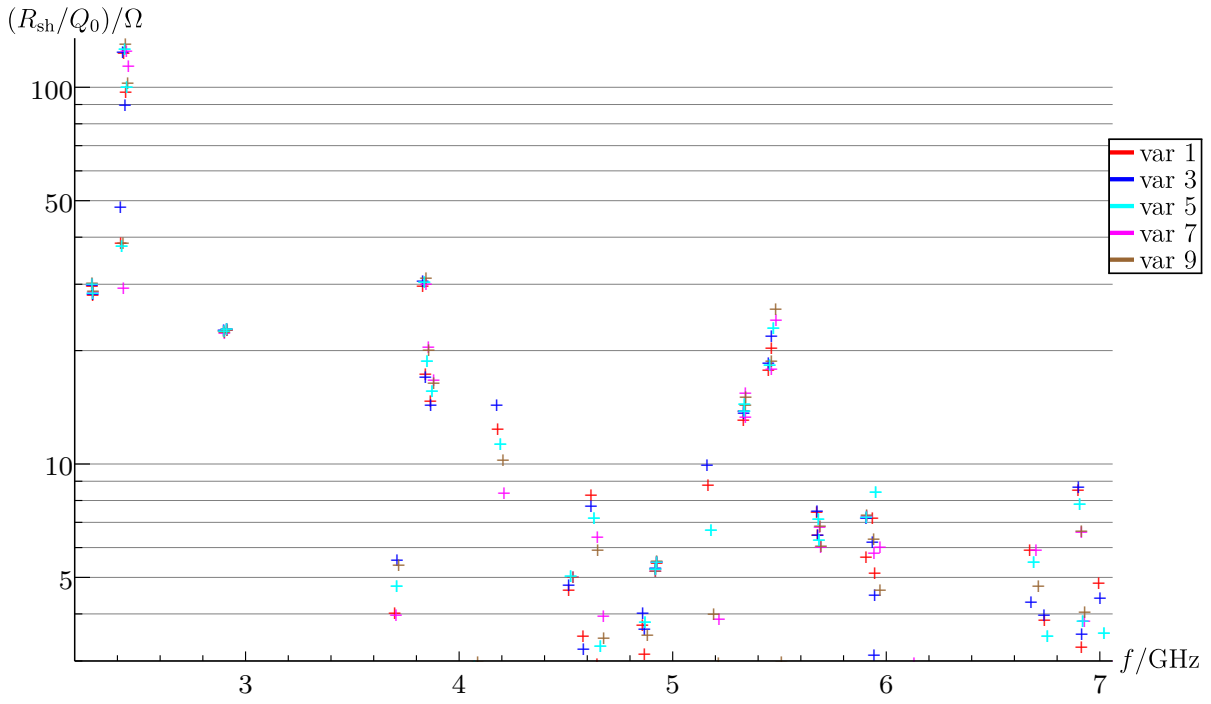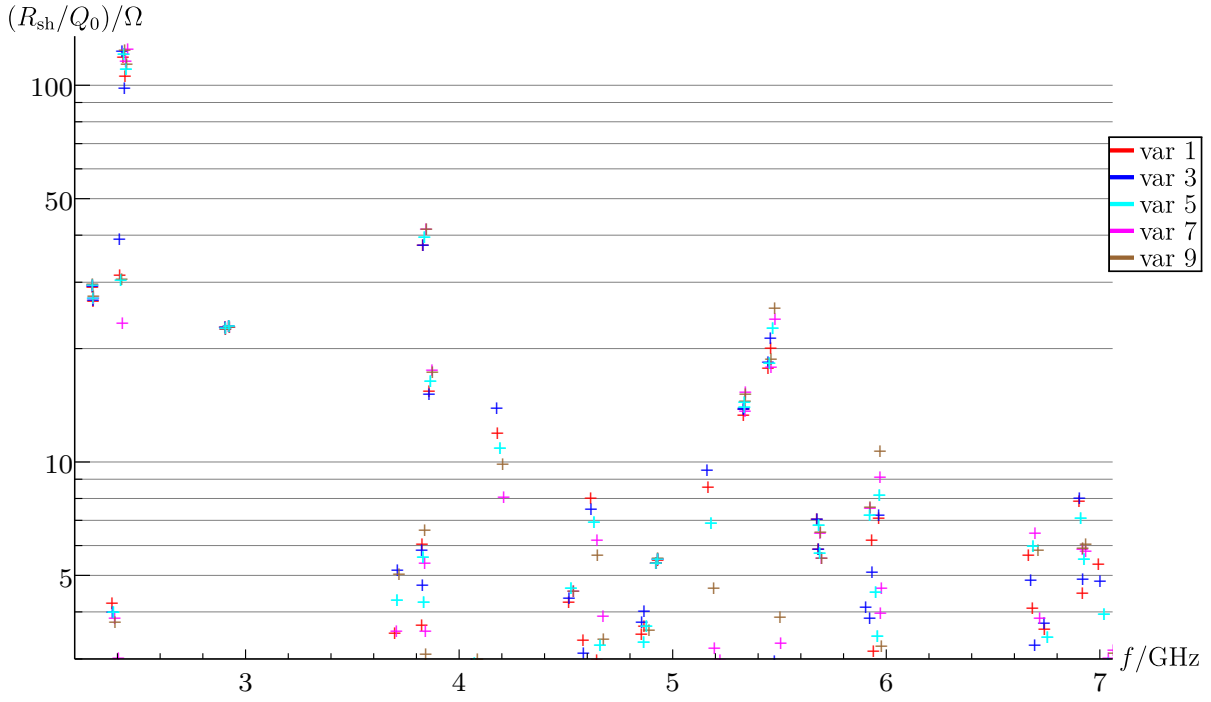
Figure C.23: On-axis R-over-Q values of TM_0-like HOMs up to a frequency of $7.04\,\mathrm{GHz}$ subject to different uniform geometric imperfections. The $TM_{0,1,0}$-like band is not included and only modes with an R-over-Q values of at least $3\,\Omega$ are plotted. (a): Candidate C6. (b): Candidate C7.

C.4 Elliptical Single-Cell Resonator based on Cylindrical Resonator

C.4.1 Interacting Mode Sets and Required Discretization

Table C.3: Required step size for semi-analytical area elements depending on frequency range of unperturbed IA mode sets: The step size satisfies ten samples per wavelength. Each set contains 600 modes.

IA mode set		Highest mode Type	f/GHz	Step size in mm
$TM_{0,n,p}$	(p: even)	$TM_{0,31,22}$	53.14	0.564
$TM_{1,n,p}$, $TE_{1,n,p}$	(p: odd)	$TE_{1,23,15}$	38.45	0.780
$TM_{0,n,p}$	(p: odd)	$TM_{0,6,41}$	53.92	0.556
$TM_{1,n,p}$, $TE_{1,n,p}$	(p: even)	$TE_{1,18,22}$	38.53	0.778
$TM_{2,n,p}$, $TE_{2,n,p}$	(p: odd)	$TM_{2,14,25}$	38.93	0.770
$TE_{0,n,p}$	(p: odd)	$TE_{0,37,3}$	54.41	0.551
$TM_{3,n,p}$, $TE_{3,n,p}$	(p: odd)	$TM_{3,11,27}$	39.33	0.762
$TM_{2,n,p}$, $TE_{2,n,p}$	(p: even)	$TE_{2,18,22}$	39.02	0.768
$TM_{4,n,p}$, $TE_{4,n,p}$	(p: odd)	$TE_{4,25,9}$	39.95	0.750
$TM_{3,n,p}$, $TE_{3,n,p}$	(p: even)	$TE_{3,21,18}$	39.36	0.762
$TE_{0,n,p}$	(p: even)	$TE_{0,37,8}$	55.25	0.543

All sets of interacting modes were determined based on a semi-analytical discretization with a step size of 0.54 mm. For this, 4627 area elements were needed. This corresponds to $1.065 \cdot 10^6$ 3D volume elements.
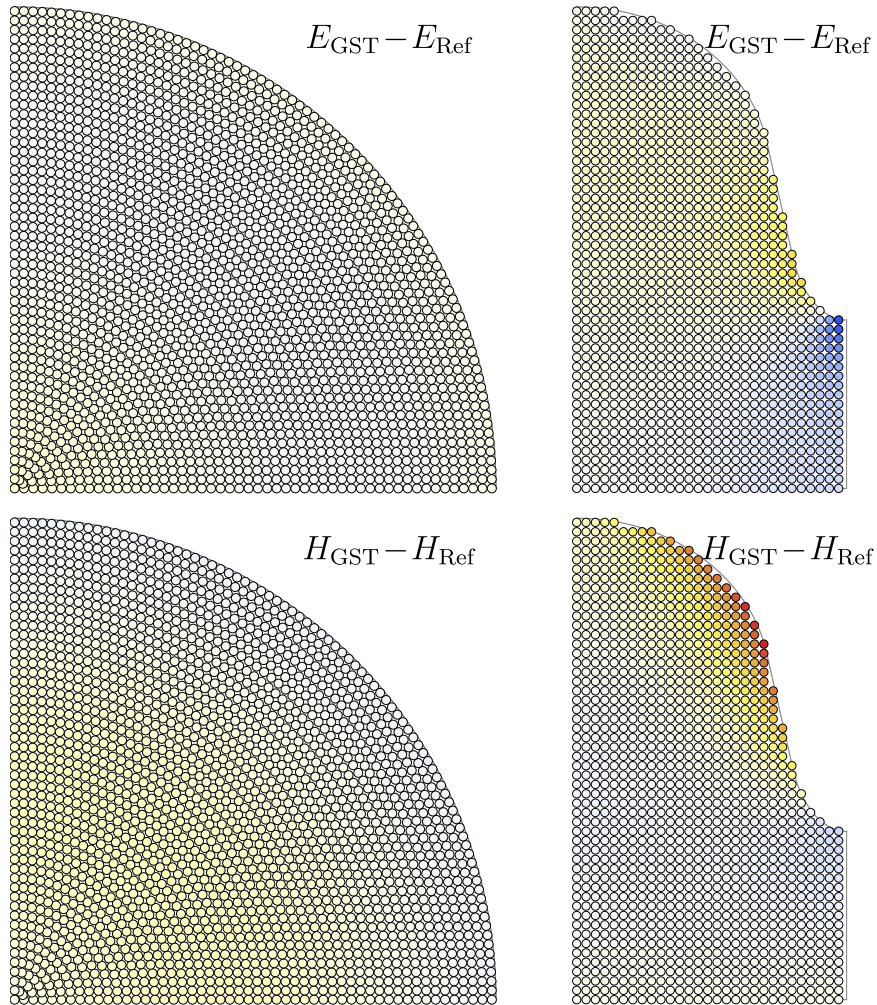
C.4.2 Convergence Depending on Number of Modes
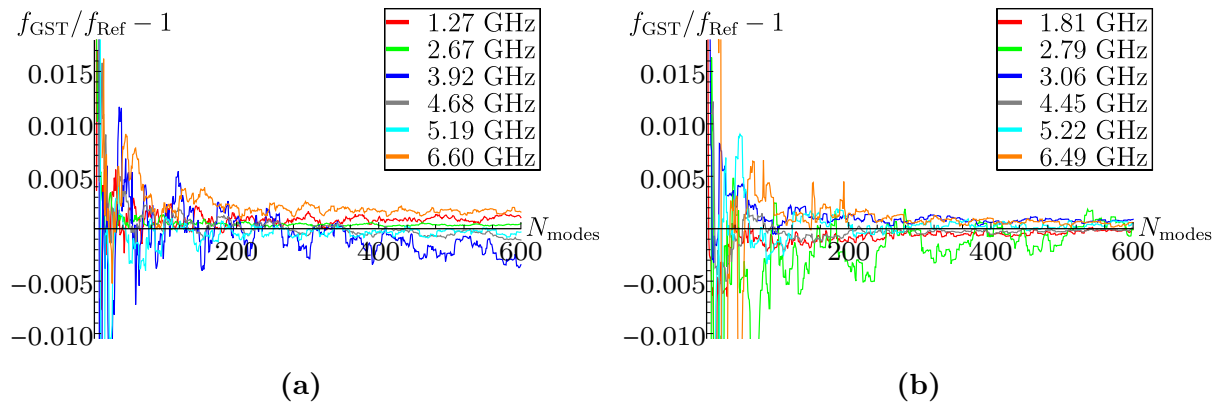
Figure C.24: Relative frequency error depending on the number N_{modes} of unperturbed modes: (a) TM_0-like modes. (b) HEM_1-like modes.

C.4.3 Selected Electromagnetic Fields
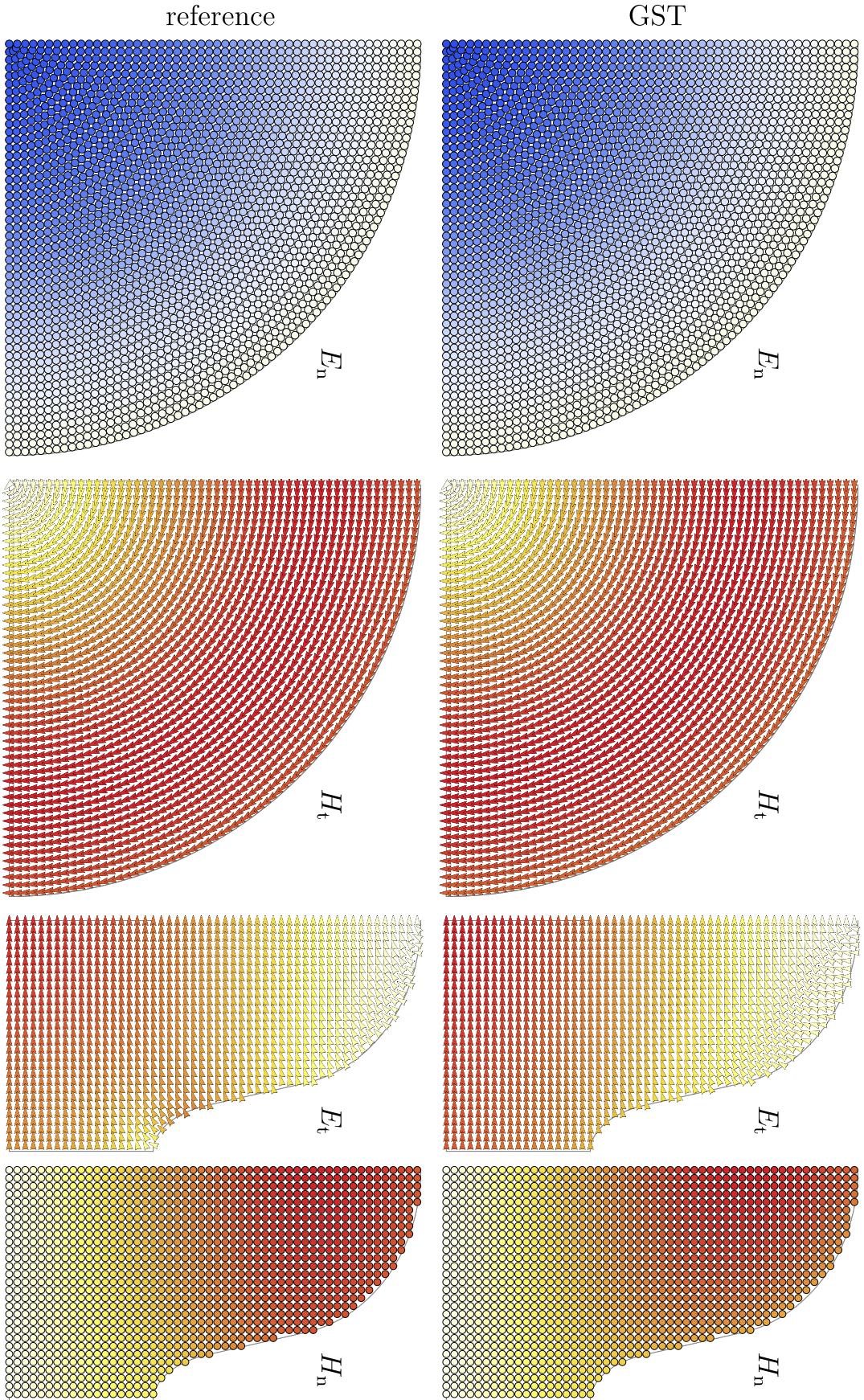
C.4.3.1 Regular GST Fields

Figure C.25: Absolute error of GST-based EM field (normalized to $1\,\text{V/m}$, $1\,\text{A/m}$) of $\text{TM}_{0,1,0}$-like accelerating mode at $1.27\,\text{GHz}$ in the x,y- and x,z-plane: Error range of $-220\,\text{mV/m}$ (blue) to $435\,\text{mV/m}$ (red) and $-239\,\text{mA/m}$ to $85\,\text{mA/m}$.
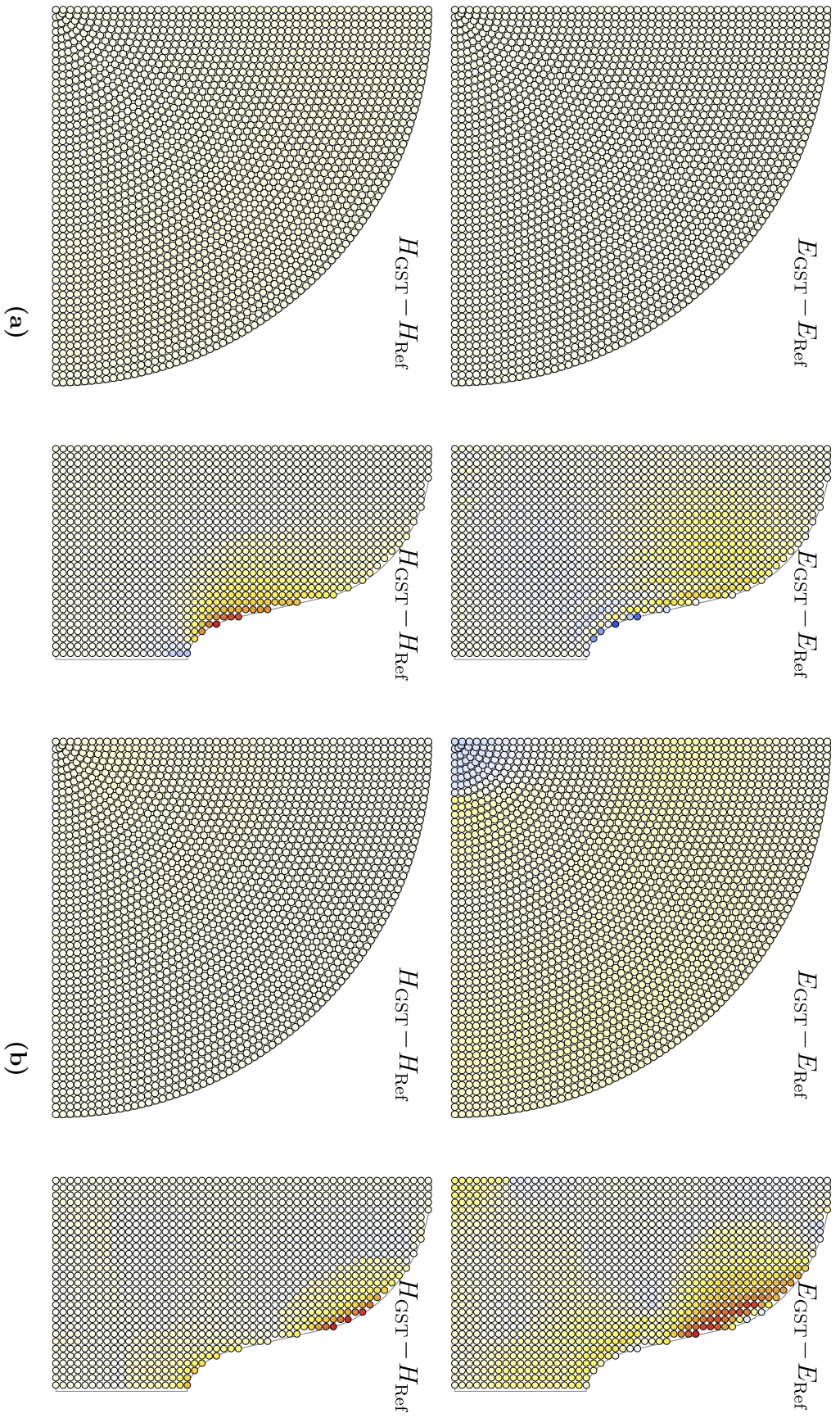
Figure C.26: Absolute error of GST-based EM fields (normalized to $1\,\mathrm{V/m}$, $1\,\mathrm{A/m}$) in the x,y- and x,z-plane: (a) $\mathrm{TE_0}$-like mode at $3.76\,\mathrm{GHz}$. Error range of $-24\,\mathrm{mV/m}$ (blue) to $12\,\mathrm{mV/m}$ (red) and $-368\,\mathrm{mA/m}$ to $161\,\mathrm{mA/m}$. (b) Dipole mode at $6.49\,\mathrm{GHz}$. Error range of $-160\,\mathrm{mV/m}$ to $45\,\mathrm{mV/m}$ and $-331\,\mathrm{mA/m}$ to $52\,\mathrm{mA/m}$.

Figure C.27: EM field of $TM_{0,1,0}$-like accelerating mode at 1.27 GHz in the x,y- and x,z-plane: First row: GST-based field. Second row: Reference field.
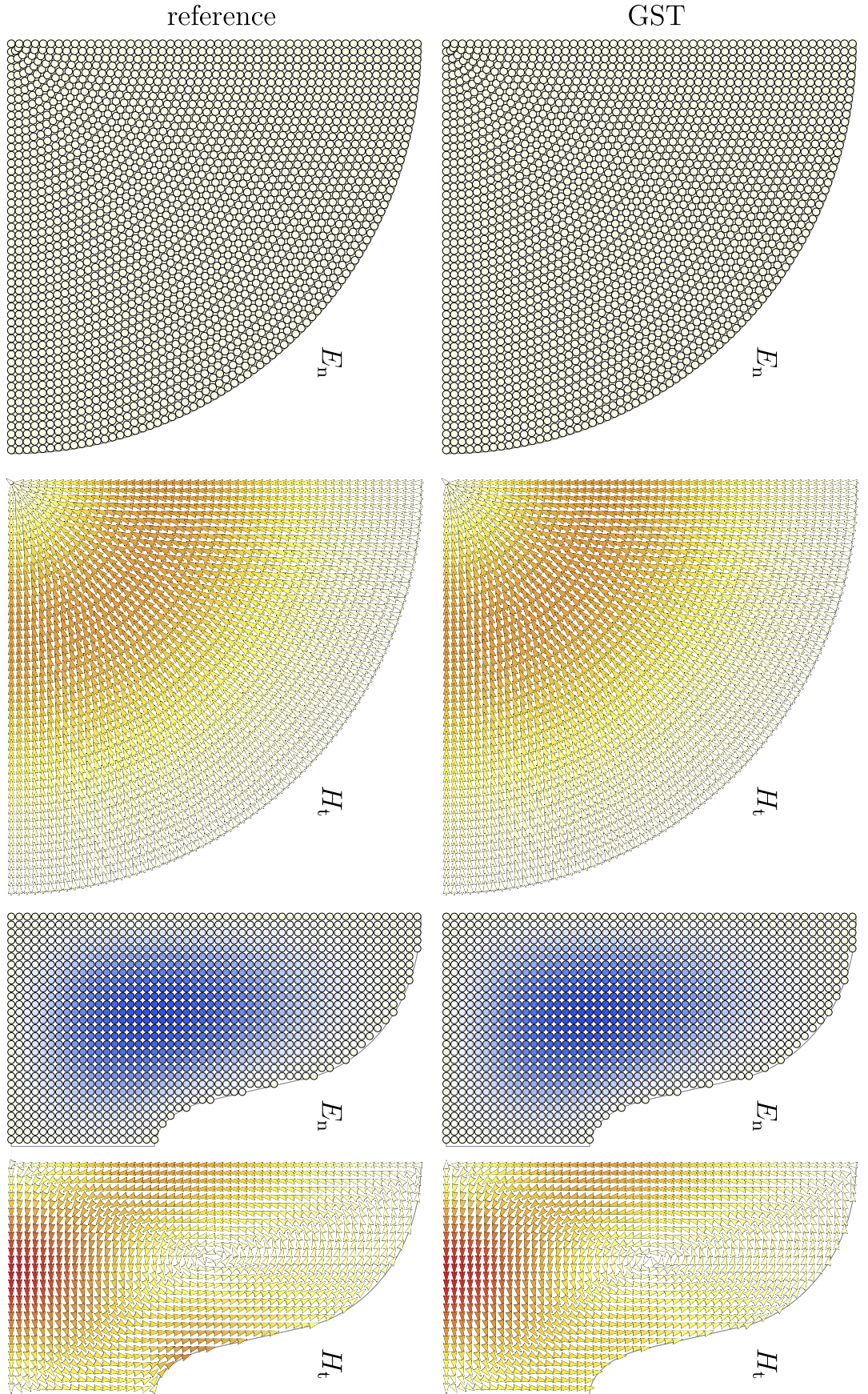
Figure C.28: EM field of TE_0–like mode at 3.76 GHz in the x,y- and x,z-plane: First row: GST-based field. Second row: Reference field.
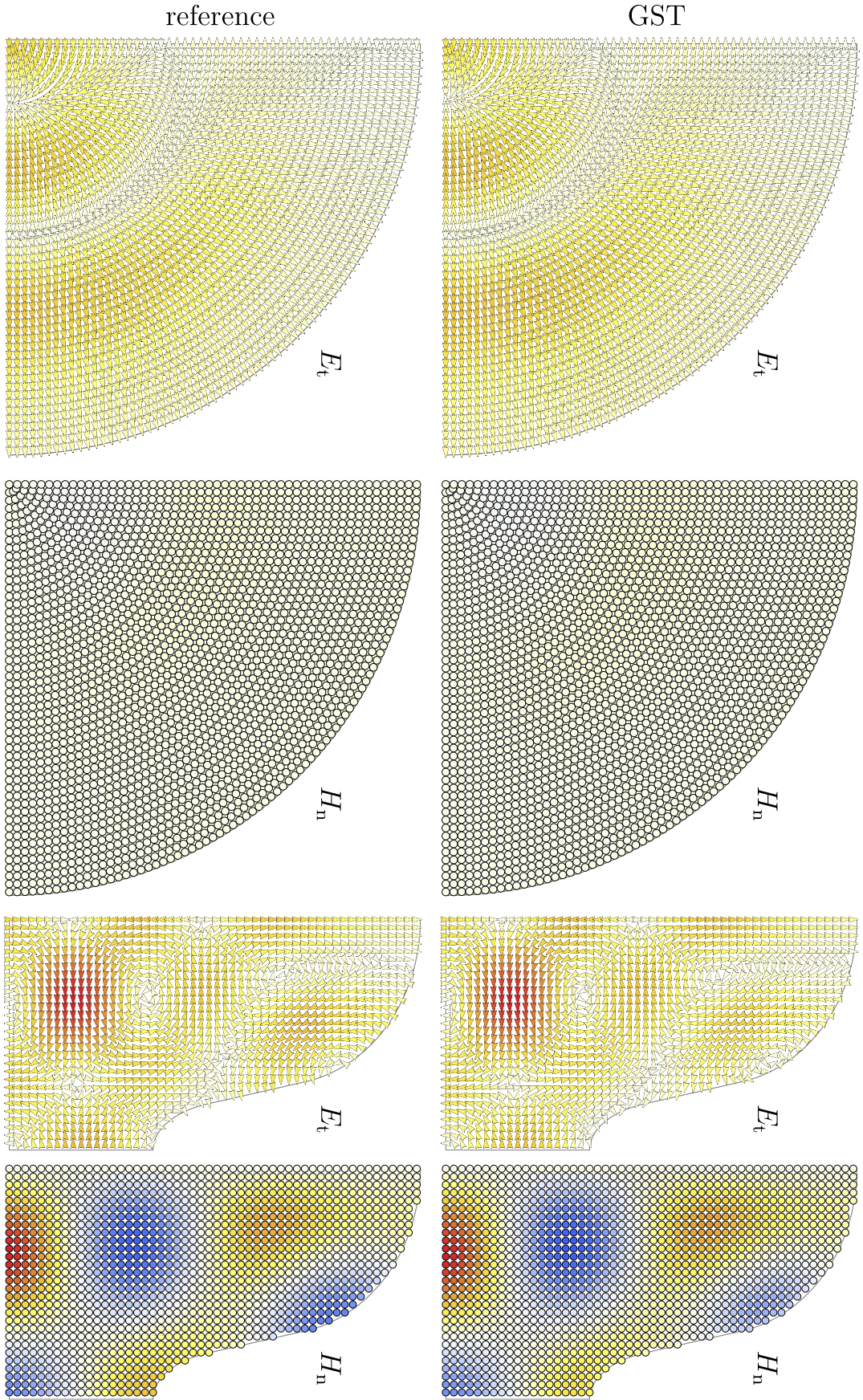
Figure C.29: EM field of dipole mode at 6.49 GHz in the x,y- and x,z-plane: First row: GST-based field. Second row: Reference field.

C.4.3.2   Irregular GST Fields

Figure C.30: Absolute error of EM fields (normalized to $1\,\mathrm{V/m}$, $1\,\mathrm{A/m}$) of irregular GST modes in the x,y- and x,z-plane: (a) $\mathrm{TM_0}$-like mode at $3.73\,\mathrm{GHz}$. Error range of $-100\,\mathrm{mV/m}$ (blue) to $67\,\mathrm{mV/m}$ (red) and $-303\,\mathrm{mA/m}$ to $116\,\mathrm{mA/m}$. (b) Dipole mode at $6.58\,\mathrm{GHz}$. Error range of $-107\,\mathrm{mV/m}$ to $169\,\mathrm{mV/m}$ and $-353\,\mathrm{mA/m}$ to $302\,\mathrm{mA/m}$.

Figure C.31: EM field of TM_0-like mode at 3.73 GHz in the x,y- and x,z-plane: First row: GST-based field. Second row: Reference field.
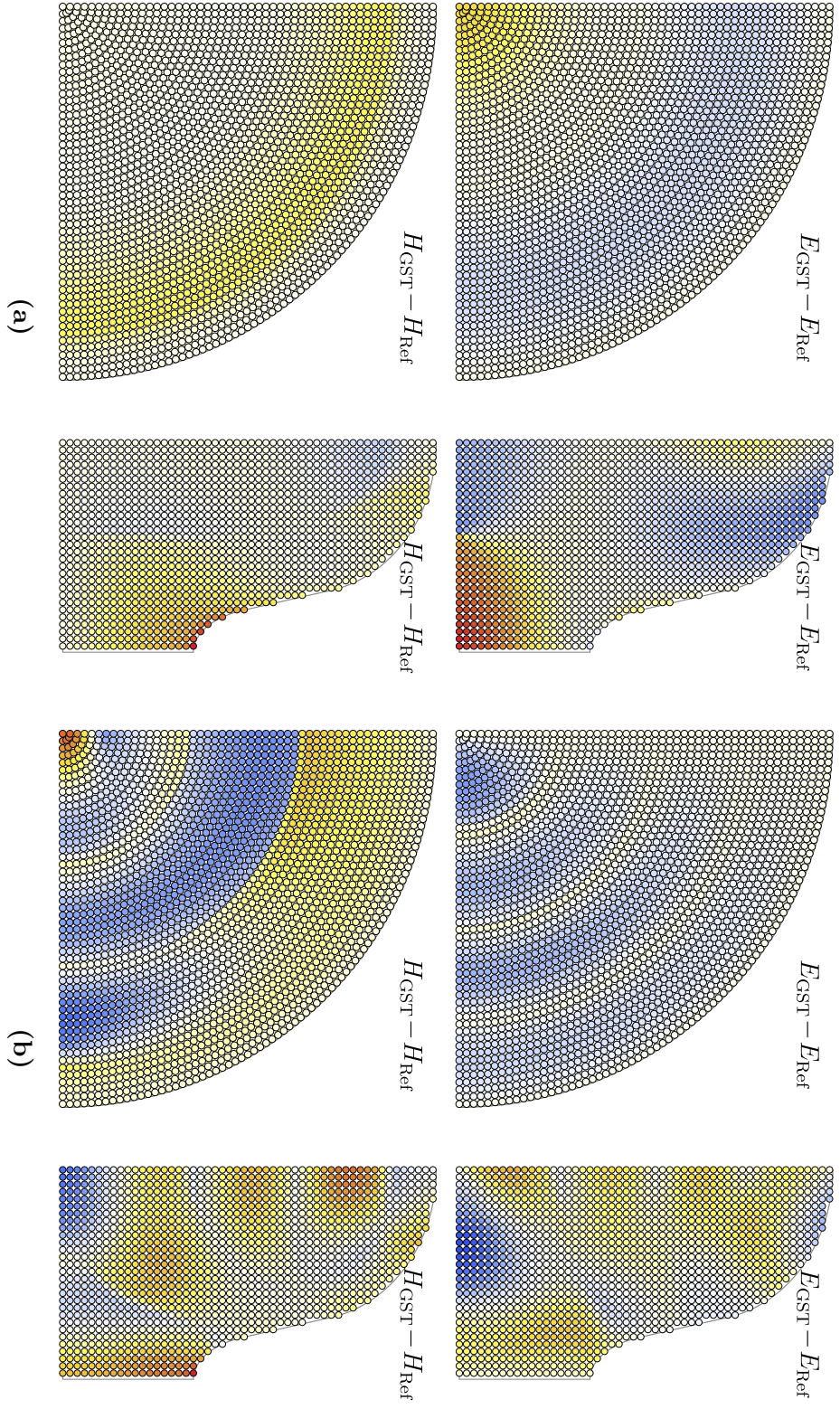
Figure C.32: EM field of dipole mode at 6.58 GHz in the x,y- and x,z-plane: First row: GST-based field. Second row: Reference field.
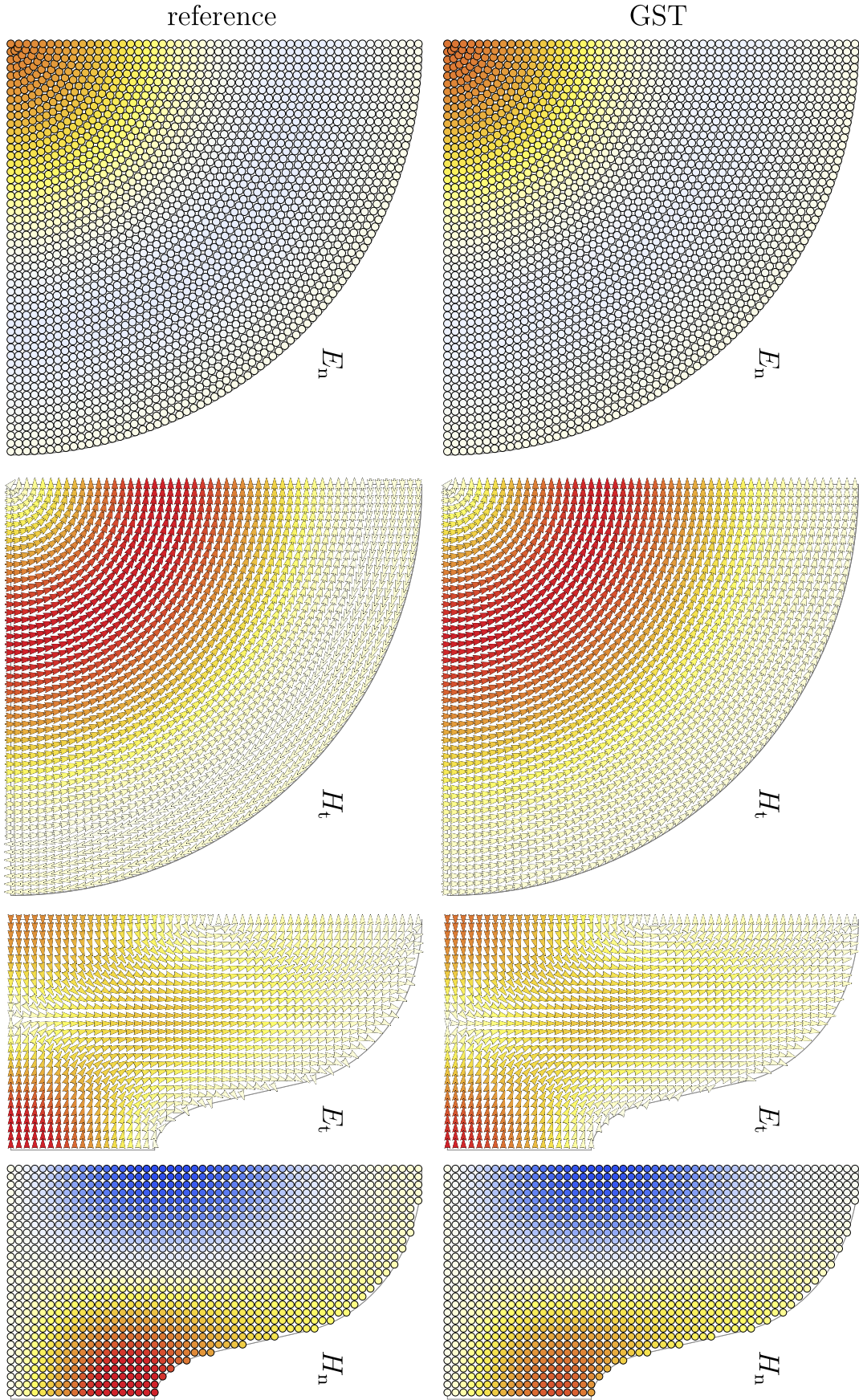
Bibliography

[1] H. Wiedemann. *Particle Accelerator Physics I: Basic Principles and Linear Beam Dynamics*, volume 2. Springer, 1999.

[2] H. Padamsee, J. Knobloch, and T. Hays. *RF Superconductivity for Accelerators*, volume 1. Wiley & Sons, 1998.

[3] B. Aune and et al. Superconducting TESLA cavities. *Phys. Rev. ST Accel. Beams*, September 2000. DOI: 10.1103/PhysRevSTAB.3.092001.

[4] N. R. A. Valles and M. Liepe. Seven-Cell Cavity Optimization for Cornell's Energy Recovery Linac. In *Proc. of SRF 2009*, pages 538–542, Berlin, Germany, 20–25 September 2009.

[5] V. D. Shemelin and G. H. Hoffstaetter. First Principle Approach for Optimization of Cavity Shape for High Gradient and Low Loss. In *Proc. of 3rd IPAC*, pages 3015–3017, New Orleans, USA, 20–25 May 2012.

[6] B. Riemann, T. Weis, and A. Neumann. Design of SRF Cavities with Cell Profiles Based on Bezier Splines. In *Proc. of 11th ICAP*, pages 167–169, Warnemünde, Germany, 19–24 August 2012.

[7] A. W. Chao. *Physics of Collective Beam Instabilities in High Energy Accelerators*, volume 1. Wiley & Sons, 1993.

[8] K. L. F. Bane, P. B. Wilson, and T. Weiland. Wake Fields and Wake Field Acceleration. In *Proc. of AIP*, volume 127, pages 875–928, 1984.

[9] P. B. Wilson. Introduction to Wakefields and Wake Potentials. In *Proc. of AIP*, volume 184, pages 525–564, 1989. SLAC-PUB-4547;SLAC-AP-66.

[10] T. Weiland and R. Wanzenberg. Wake Fields and Impedances. *Lect. Notes Phys.*, 400, 1992.

[11] H. Wiedemann. *Particle Accelerator Physics*, volume 3. Springer, 2007.

[12] E. Haebel. Couplers for Cavities. In *CERN Accelerator School*, pages 231–264, 1995. DOI: 10.5170/CERN-1996-003.231.

[13] R. F. Parodi. Couplers and HOM Dampers. In *CERN Accelerator School*, pages 253–264, 2002. DOI: 10.5170/CERN-2004-008.253.

[14] M. Dohlus, V. Kaljuzhny, and S. G. Wipf. Resonance Frequencies and Q-factors of Multi-Resonance Complex Electromagnetic Systems. Technical report, DESY, MHF-SL Group, 2002.

[15] R. Schuhmann and T. Weiland. Rigorous Analysis of Trapped Modes in Accelerating Cavities. *Physical Review Special Topics - Acclerators and Beams*, 3, 2000.

[16] D. A. Edwards and M. J. Syphers. *An Introduction to the Physics of High Energy Accelerators*, volume 1. Wiley-VCH, 2004.

[17] F. Furuta and K. Saito. Field Flatness Degradation Problems and Cure. In *Proc. of SRF 2009*, Berlin, Germany, 20–25 September 2009. THPPO083.

[18] L. Xiao, C. Adolphsen, V. Akcelik, A. Kabel, K. Ko, L. Lee, Z. Li, and C. Ng. Modeling Imperfection Effects on Dipole Modes in TESLA Cavity. In *Proc. of PAC 2007*, pages 2454–2456, Albuquerque, NM, USA, 25–29 June 2007.

[19] W. F. O. Müller and W. Koch. Numerical Calculation of Trapped Modes in TESLA Cavities Considering Production Tolerances. In *Proc. of EPAC 2002*, Paris, France, 2002.

[20] A. Lunin, T. Khabiboulline, and S. Yakovlev. Computational Needs for RF Design of Superconducting Cavities. In *Proc. of 11th ICAP*, pages 270–274, Warnemünde, Germany, 19–24 August 2012.

[21] A. Sulimov, G. Kreps, and J. Sekutowicz. Estimation of Small Geometry Deviation for TESLA-Shape Cavities due to Inner Surface Polishing. In *Proc. of SRF 2013*, Paris, France, 2013.

[22] F. Marhauser, K. Tian, and H. Wang. Critical Higher Order Modes in CEBAF Upgrade Cavities. Technical report, Jefferson Laboratory, 2009. JLAB-TN-09-50.

[23] G. R. Kreps and J. Sekutowicz. Tuning of TESLA Superconducting Cavities and Measurements of Higher Order Mode Damping. Technical report, DESY, 2009. JLAB-TN-09-50.

[24] C. Schmidt, T. Flisgen, J. Heller, and U. van Rienen. Comparison of Techniques for Uncertainty Quantification of SRF Cavities. In *Proc. of ICEAA*, pages 117–120, Palm Beach, Aruba, 2014.

[25] F. Marhauser, E. Weihreter, D. M. Dykes, P. McIntosh, S. A. Pande, K. R. Chu, Y. C. Tsaiand C. Wang, and R. A. Rimmer. Numerical simulations of a HOM Damped Cavity. In *Proc. of 7th EPAC*, pages 1972–1974, Vienna, Austria, 2000.

[26] K. Zhang and D. Li. *Electromagnetic Theory for Microwaves and Optoelectronics*, volume 2. Springer, 1998.

[27] D. M. Pozar. *Microwave Engineering*, volume 2. Wiley & Sons, 2003.

[28] J. C. Slater. Microwave Electronics. *Reviews of Modern Physics*, 18(4), October 1946.

[29] R. E. Collin. *Field Theory of Guided Waves*, volume 2. IEEE Press, 1991.

[30] R. Schuhmann, M. Clemens, P. Thoma, and T. Weiland. Frequency and Time Domain Computations of S-Parameters Using the Finite Integration Technique. In *Proc. of 12th ACES Conference*, pages 1295–1302, Monterey, USA, 1996.

[31] W. Ackermann and T. Weiland. High Precision Cavity Simulations. In *Proc. of 11th ICAP*, pages 43–47, Warnemünde, Germany, 19–24 August 2012.

[32] J. K. Sekutowicz. Superconducting Elliptical Cavities. Technical report, DESY, 2012. CERN Yellow Report CERN-2011-007.

[33] N. Juntong and R. M. Jones. High-Gradient SRF Cavity with Minimized Surface E.M. Fields and Superior Bandwidth for the ILC. In *Proc. of SRF 2009*, Berlin, Germany, 20–25 September 2009.

[34] J. K. Sekutowicz and et al. Design of a Low Loss SRF Cavity for the ILC. In *Proc. of PAC 2005*, Knoxville, Tennessee, USA, 12–16 May 2005.

[35] T. Khabiboulline, N. Solyak, and R. Wanzenberg. Higher Order Modes of a 3rd Harmonic Cavity with an Increased End-cup Iris. Technical report, DESY, Hamburg, Germany, 2003. TESLA-FEL Report: TESLA-FEL 2003-01.

[36] K. Ko and A. E. Candel. Advances in Parallel Computing Codes for Accelerator in Science and Development. In *Proc. of LINAC 2010*, Tsukuba, Japan, 2010.

[37] V. Akçelik, K. Ko, L. Lee, Z. Li, C. Ng, and L. Xiao. Shape Determination For Deformed Electromagnetic Cavities. *Journal of Computational Physics*, 227,3:1722–1738, 2008.

[38] L. Lee, V. Akçelik, S. Cheng, Z. Li, C. Ng, L. Xiao, and K. Ko. Shape Determination For Deformed Cavities. Technical report, Stanford Linear Accelerator Center, 2006. SLAC-PUB-12141.

[39] F. Deryckere, T. Roggen, B. Masschaele, and H. De Gersem. Stochastic Response Surface Method for Lorentz Detuning of Accelerator Cavities. In *Proc. of 11th ICAP*, pages 158–160, Warnemünde, Germany, 19–24 August 2012.

[40] S. Gorgi Zadeh. Application of Matrix Perturbation Theory for Generalized Eigenvalue Problems. Master's thesis, Universität Rostock, August 2015.

[41] J. C. Maxwell. *A Treatise on Electricity and Magnetism*, volume 1. Dover Publications, 1954.

[42] R. Plonsey and R. E. Collin. *Principles and Applications of Electromagnetic Fields.* McGraw-Hill, 1961.

[43] J. A. Kong. *Principles and Applications of Electromagnetic Wave Theory*, volume 2. Wiley & Sons, 1990.

[44] C. A. Balanis. *Advanced Engineering Electromagnetics.* Wiley & Sons, 1989.

[45] K. Klopfer, U. Niedermayer, H. Klingbeil, H. G. König W. Ackermann, and T. Weiland. Measurement of the Magnetic Material Properties for Ferrite-loaded Cavities. *Phys. Rev. ST Accel. Beams*, January 2015. DOI: 10.1103/PhysRevSTAB.18.010101.

[46] G. R. Eichhorn, J. Conway, Y. He, Y. Li, T. O'Connell, P. Quigley, J. Sears, V. D. Shemelin, and N. R. A. Valles. Cornell's Beam Line Higher Order Mode Absorbers. In *Proc. of International Conference on RF Superconductivity*, pages 1027–1030, Paris, France, 2013.

[47] V. Malka, J. Faure, Y. Glinec, and A. Lifschitz. Laser-plasma Wakefield Acceleration: Concepts, Tests and Premises. In *Proc. of EPAC 2006*, Edinburgh, Scotland, 2006.

[48] B. P. Antonyuk. *Light-Driven Alignment*. Springer Series in Optical Sciences, 2009.

[49] A. J. Jerri. *The Gibbs Phenomenon in Fourier Analysis, Splines and Wavelet Approximations*, volume 1. Kluwer Academic Publisher, 1998.

[50] N. Kroll and D. Yu. Computer Determination of the External Q and Frequency of Wave Guide Loaded Cavities. *Particle Accelerators*, 34, 1990.

[51] P. Balleyguier. External Q-Studies for APT SC-Cavity Couplers. In *Proc. of LINAC 2000*, pages 133–135, Monterey, USA, 2000.

[52] V. M. Papadopoulos. Propagation of Electromagnetic Waves in Cylindrical Wave-Guides with Imperfectly Conducting Walls. *Quarterly Journal of Mechanics and Applied Mathematics*, 7, 1953.

[53] J. Holzbauer. RF Theory and Design-Notes. Technical report, USPAS-Grand Rapids, 2012.

[54] F. Borgnis. Elektromagnetische Eingenschwingungen Dielektrischer Räume. *Annalen der Physik*, 427, 1939. DOI: 10.1002/andp.19394270408.

[55] L. A. Vainshtein. *Electromagnetic Waves*. Soviet Radio, 1957.

[56] S. Ramo, J. R. Whinnery, and T. Van Duzer. *Field and Waves in Communication*, volume 2. Wiley & Sons, 1984.

[57] P. M. Morse and H. Feshbach. *Methods of Theoretical Physics*. McGraw-Hill, 1953.

[58] J. G. Van Bladel. *Electromagnetic Fields*, volume 2. Wiley & Sons, 2007.

[59] B. W. Zotter and S. A. Kheifets. *Impedances and Wakes in High-Energy Particle Accelerators*, volume 1. World Scientific, 1998.

[60] J.R. Pierce. Coupling of Modes of Propagations. *Journal of Applied Physics*, 25, 1954.

[61] H.A. Haus and W.P. Huang. Coupled Mode Theory. *Proceedings of the IEEE*, pages 1505–1518, October 1991. DOI: 10.1109/5.104225.

[62] U. van Rienen. Higher Order Mode Analysis of Tapered Disc-Loaded Waveguides Using the Mode Matching Technique. *Particle Accelerators*, 41:173–201, 1993.

[63] T. Flisgen. *Compact State-Space Models for Complex Superconducting Radio-Frequency Structures based on Model Order Reduction and Concatenation Methods*. PhD thesis, Universität Rostock, April 2015.

[64] U. Lauströer, U. van Rienen, and T. Weiland. URMEL and URMEL-T User Guide (Modal Analysis of Cylindrically Symmetric Cavities; Evaluation of RF-Fields in Waveguides), 1987. DESY Report.

[65] U. van Rienen. Triangular discretization method for the evaluation of RF-fields in cylindrically symmetric cavities. *IEEE Transactions on Magnetics*, 21,6, 1993. DOI: 10.1109/TMAG.1985.1064183.

[66] M. T. Menzel and H. K. Stokes. User's Guide for the POISSON/SUPERFISH Group of Codes, 1987. Los Alamos, USA.

[67] D. G. Myakishev and V. P. Yakovlev. The New Possibilities of SuperLANS Code for Evaluation of Axisymmetric Cavities. *Proc. of 1995 Particle Accelerator Conference and International Conference on High-Energy Accelerators*, pages 2348–2350, 1–5 May 1995.

[68] B. D. Isbarn, B. Riemann, M. Sommer, and T. Weis. YACS - A New 2.5D FEM Eigenmode Solver for Axisymmetric RF-Structures. In *Proc. of 5th IPAC*, Richmond, VA, USA, 3–8 May 2015.

[69] T. Wangler. *Principles of RF Linear Accelerators*, volume 1. Wiley & Sons, 1998.

[70] K. Brackebusch and U. van Rienen. Automated Mode Recognition Algorithm for Accelerating Cavities. In *Proc. of 5th IPAC*, pages 409–411, Dresden, Germany, 15–20 June 2014.

[71] A. Bondeson, T. Rylander, and P. Ingelström. *Computational Electromagnetics*. Springer, 2005.

[72] G. R. Liu and S. S. Quek. *The Finite Element Method: A Practical Course*, volume 2. Butterworth-Heinemann, 2013.

[73] A. Logg, K.-A. Mardal, and G. N. Wells. *Automated Solution of Differential Equations by the Finite Element Method: The FEniCS Book*. Lecture Notes in Computational Science and Engineering. Springer, 2012.

[74] R. A. Shapiro. *Adaptive Finite Element Solution Algorithm for the Euler Equations*. Vieweg, 1991.

[75] J. J. Gustincic. A General Power Loss Method for Attenuation of Cavities and Waveguides. *IEEE Transactions on Microwave Theory and Techniques*, 11,1, 1963.

[76] D. Meidlinger. A General Perturbation Theory for Cavity Mode Field Patterns. In *Proc. of SRF 2009*, Berlin, Germany, 20–25 September 2009. THPPO005.

[77] K. Simonyi. *Theoretische Elektrotechnik*, volume 9. VEB Deutscher Verlag der Wissenschaften, 1989.

[78] I. N. Bronstein, K. A. Semendjajew, G. Musiol, and H. Mühlig. *Taschenbuch der Mathematik*, volume 5. Harri Deutsch, 2001.

[79] G. E. Dombrowski. Matrix Formulation of Slater's Cavity Perturbation Theorem. *Journal of Applied Physics*, 55(7):2648–2650, 1984.

[80] K. Brackebusch and U. van Rienen. Eigenmode Computation for Cavities with Perturbed Geometry based on a Series Expansion of Unperturbed Eigenmodes. In *Proc. of 3rd IPAC*, pages 277–279, New Orleans, USA, 20–25 May 2012.

[81] J. H. Wilkinson. *The Algebraic Eigenvalue Problem*, volume 1. Clarendon Press, 1988.

[82] K. Brackebusch and U. van Rienen. Implementational Aspects of Eigenmode Computation based on Perturbation Theory. In *Proc. of 11th ICAP*, pages 48–50, Warnemünde, Germany, 19–24 August 2012.

[83] K. Brackebusch and U. van Rienen. Investigation of Geometric Variations for Multicell Cavities using Perturbative Methods. In *Proc. of COMPUMAG 2015*, Montréal, Canada, June/July 2015.

[84] K. Brackebusch and U. van Rienen. Investigation of Geometric Variations for Multicell Cavities using Perturbative Methods. *Transaction on Magnetics*, October 2015. DOI: 10.1109/TMAG.2015.2487542.

[85] Inc. Wolfram Research. Mathematica, Version 8.0–10.3, 2010–2015. Champaign, USA.

[86] E. W. Cheney and D. R. Kincaid. *Numerical Mathematics and Computing*, volume 7. Brooks Cole, 2012.

[87] Computer Simulation Technology AG. Microwave Studio®, Version 2012–2015. Darmstadt, Germany.

[88] Computer Simulation Technology AG. CST Studio Suite® Help Documentation. Darmstadt, Germany.

[89] J. J. Leader. *Numerical Analysis and Scientific Computation*, volume 1. Pearson, 2004.

[90] R. P. Feynman, R. B. Leighton, and M. Sands. *Lectures on Physics*, volume 2. Addison-Wesley, 1964.

[91] H. Si. TetGen - A Quality Tetrahedral Mesh Generator and a 3D Delaunay Triangulator. Berlin, Germany.

[92] Inc. Wolfram Research. Wolfram Documentation center. http://www.wolfram.com/.

[93] E. Anderson, Z. Bai, C. Bischof, S. Blackford, J. Demmel, J. Dongarra, J. Du Croz, A. Greenbaum, S. Hammarling, A. McKenney, and D. Sorensen. *LAPACK Users' Guide*. Society for Industrial and Applied Mathematics, Philadelphia, PA, USA, 3 edition, 1999.

[94] K. Brackebusch, H.-W. Glock, and U. van Rienen. Calculation of High Frequency Fields in Resonant Cavities based on Perturbation Theory. In *Proc. of 2nd IPAC*, pages 2235–2237, San Sebastian, Spain, 4–6 September 2011.

[95] K. F. Warnick. *Numerical Analysis for Electromagnetic Integral Equations*, volume 1. Artech House, 2008.

[96] K. Brackebusch and U. van Rienen. Eigenmode Computation for Elliptical Cavities Subject to Geometric Variation using Perturbative Methods. In *Proc. of 4th IPAC*, pages 2331–2333, Shanghai, China, 12–17 May 2013.

[97] A. Neumann, J. Knobloch, B. Riemann, T. Weis, K. Brackebusch, T. Flisgen, T. Galek, and U. van Rienen. Final Design for the bERLinPro Main Linac Cavity. In *Proc. of LINAC14*, pages 217–220, Geneva, Switzerland, August/September 2014.

[98] Y. Ineichen. *Toward Massively Parallel Multi-Objective Optimization with Application to Particle Accelerators*. PhD thesis, ETH Zürich, 2013.

[99] DESY. European XFEL Database. http://xfel.desy.de/cavity_database/.

Selbstständigkeitserklärung

Hiermit erkläre ich, dass ich die vorliegende Dissertation mit dem Titel "Perturbative Methods for the Computation of Resonant Cavity Eigenmodes Subject to Geometric Variations" selbstständig und ohne fremde Hilfe verfasst, andere als die von mir angegebenen Quellen und Hilfsmittel nicht benutzt und die den benutzten Werken wörtlich oder inhaltlich entnommenen Stellen als solche kenntlich gemacht habe.

Rostock, 5. September 2016

Korinna Brackebusch